

# **Development of Semiconducting Tin Dinitridocarbonate Compounds by Solid-State Metathesis Reactions**

## **Dissertation**

der Mathematisch-Naturwissenschaftlichen Fakultät  
der Eberhard Karls Universität Tübingen  
zur Erlangung des Grades eines  
Doktors der Naturwissenschaften  
(Dr. rer. nat.)

vorgelegt von  
M. Sc. Manuel Löber  
aus Buchenbach

Tübingen  
2021



Gedruckt mit Genehmigung der Mathematisch-Naturwissenschaftlichen Fakultät der Eberhard Karls Universität Tübingen.

Tag der mündlichen Qualifikation:

10.12.2021

Dekan:

Prof. Dr. Thilo Stehle

1. Berichterstatter:

Prof. Dr. Hans-Jürgen Meyer

2. Berichterstatter:

Prof. Dr. Eberhard Schweda







# Acknowledgments

In particular, I would like to thank the supervisor of my project, Prof. Dr. Hans-Jürgen Meyer, for welcoming me into his research group, his complete confidence in me as a non-chemist, and for giving me the freedom to work independently on a topic I was passionate about. He has always supported me in this work with many suggestions and helpful comments.

Similarly, I would like to thank my second supervisor, Prof. Dr. Klaus G. Nickel, for the constant support.

My special thanks also go to Prof. Dr. Eberhard Schweda, who agreed to act as the second referee on short notice.

I would also like to express my special thanks to Dr. Markus Ströbele, who provided me with advice and support from the very beginning and solved and refined many crystal structures for me. I have always appreciated his many constructive bits of advice, and without him, I would not have been able to complete this PhD thesis.

Furthermore, I would also like to thank Dr. Carl Romao, who has supported me in numerous publications with calculations of various kinds, as well as many helpful pieces of advice.

In appreciation for all the support and the many pleasant moments we shared at work and in private, I would like to thank my entire research group and all former and present colleagues. To Florian Pachel, Patrick Schmidt, Paula Kallenbach, Jacqueline Händel, and Jonas Hiller in particular. Thank you very much! You are the best! Furthermore, I would like to thank Dr. Konstantin Dolabdjian, Robert Schmidt, Arin-Daniel Fuhrmann, Dr. Thorsten Hummel, Dr. David Schneider, Dr. Amira Siai, Albert Kraft, Angelika Rein, Peter Janoschek, and Ann-Kathrin Kaiser for their support. I am also very grateful for the help and support of Elaheh Bayat. You taught me how to use commas!

I would also like to thank all my friends and family, especially my parents, Uschi and Reinhard for their constant support and my wonderful girlfriend Franzi.

I am also very grateful for the work of the secretariat, the workshops, and all the other people who helped me.





**Für meine Eltern**



# Table of Contents

Acknowledgments .....	I
Table of Contents .....	V
Abbreviations.....	VI
Summary .....	VII
Zusammenfassung.....	IX
Publications .....	XI
Personal Contribution.....	XIII
1. Introduction.....	1
1.1 Solid-state reactions .....	2
1.2 Dinitridocarbonates .....	5
1.3 Tin compounds .....	13
2. Objective .....	17
3. Summary of the Main Results .....	19
3.1 Tin carbodiimide and tin chloride carbodiimide (Publ. 1) <sup>[24d]</sup> .....	20
3.2 $\text{Sn}_9\text{O}_5\text{Cl}_4(\text{CN}_2)_2$ (Publ. 2) <sup>[67]</sup> .....	24
3.3 $\text{Sn}_2\text{O}(\text{CN}_2)$ as photoanode (Publ. 3) <sup>[148]</sup> .....	28
3.4 Tin oxide halides (Publ. 4) <sup>[151]</sup> .....	29
3.5 Tungsten oxide iodides (Publ. 5) <sup>[153]</sup> .....	33
3.6 $\text{Pb}_{14.66}\text{Sn}_{7.34}\text{Br}_{26}(\text{CN}_2)_7\text{O}_2$ , a complex carbodiimide (Publ. 6) <sup>[15]</sup> .....	37
3.7 $\text{LiSn}_2\text{Br}_3(\text{CN}_2)$ and $\text{Sn}_4\text{Br}_2(\text{CN}_2)_3$ (Publ.7) <sup>[61]</sup> .....	40
3.8 The ternary lithium tin iodide $\text{LiSn}_3\text{I}_7$ (Publ. 8) <sup>[161]</sup> .....	44
3.9 Appendix .....	47
4. References .....	49
5. Publications .....	57

# Abbreviations

DFPT	density functional perturbation theory
DFT	density functional theory
DSC	differential scanning calorimetry
DTA	differential thermal analysis
EDX	energy-dispersive X-ray spectroscopy
ELF	electron localization function
HSAB	hard and soft acids and bases
IR	infrared
PEC	photoelectrochemical
PSC	perovskite solar cell
PXRD	powder X-ray diffraction
RE	rare earth
SSM	solid-state metathesis
ssNMR	solid-state nuclear magnetic resonance
XRD	X-ray diffraction

## Summary

This work focuses on solid-state syntheses of tin compounds and some of their properties. Most of these compounds were obtained by solid-state metathesis (SSM) reactions between lithium carbodiimide and tin halides. Furthermore, some halides and oxide halides have been synthesized. The majority of the described compounds have been characterized by single-crystal X-ray diffraction (XRD).

In the reaction of  $\text{Li}_2(\text{CN}_2)$  and  $\text{SnCl}_2$ ,  $\text{Sn}(\text{CN}_2)$  was produced, along with  $\text{Sn}_2\text{O}(\text{CN}_2)$ , as a byproduct. Further research has led to the discovery of  $\text{Sn}_4\text{Cl}_2(\text{CN}_2)_3$  and  $\text{Sn}_9\text{O}_5\text{Cl}_4(\text{CN}_2)_2$ . Moreover,  $\text{Sn}_4\text{Cl}_2(\text{CN}_2)_3$  was shown to act as a precursor compound in the syntheses of  $\text{Sn}(\text{CN}_2)$ ,  $\text{Sn}_2\text{O}(\text{CN}_2)$ , and  $\text{Sn}_9\text{O}_5\text{Cl}_4(\text{CN}_2)_2$ .  $\text{Sn}_4\text{Cl}_2(\text{CN}_2)_3$  is formed in these syntheses at temperatures below 200 °C and transforms into either  $\text{Sn}(\text{CN}_2)$ ,  $\text{Sn}_2\text{O}(\text{CN}_2)$ , or  $\text{Sn}_9\text{O}_5\text{Cl}_4(\text{CN}_2)_2$  at temperatures above 300 °C.  $\text{CuWO}_4$ -based photoanodes mixed with  $\text{Sn}_2\text{O}(\text{CN}_2)$  showed improved efficiencies compared to pure  $\text{CuWO}_4$  electrodes. Some tin carbodiimides were investigated by density functional theory (DFT) calculations, revealing their electronic structures, and indicating them to be semiconductors with band gaps on the order of 1 to 3 eV. The divalent tin carbodiimide compounds  $\text{Sn}_4\text{Cl}_2(\text{CN}_2)_3$ ,  $\text{Sn}_9\text{O}_5\text{Cl}_4(\text{CN}_2)_2$ , and  $\text{Sn}_2\text{O}(\text{CN}_2)$  were studied by Mössbauer spectroscopy to identify possible traces of  $\text{Sn}^{4+}$ . No tin IV could be detected in samples of  $\text{Sn}_4\text{Cl}_2(\text{CN}_2)_3$ ; however, samples of  $\text{Sn}_9\text{O}_5\text{Cl}_4(\text{CN}_2)_2$  and  $\text{Sn}_2\text{O}(\text{CN}_2)$  showed the presence of tetravalent tin. This  $\text{Sn}^{4+}$  presumably originates from the starting material  $\text{SnO}$ , which has also been shown to contain tin in the oxidation state IV.

Analogous reactions with  $\text{Li}_2(\text{CN}_2)$  and  $\text{SnBr}_2$  (instead of  $\text{SnCl}_2$ ) led to the discovery of two compounds,  $\text{Sn}_4\text{Br}_2(\text{CN}_2)_3$  and  $\text{LiSn}_2\text{Br}_3(\text{CN}_2)$ .  $\text{Sn}_4\text{Br}_2(\text{CN}_2)_3$  is isotopic to  $\text{Sn}_4\text{Cl}_2(\text{CN}_2)_3$ , whereas  $\text{LiSn}_2\text{Br}_3(\text{CN}_2)$  is isotopic to the mineral bideauxite ( $\text{AgPb}_2\text{Cl}_3(\text{F},\text{OH})_2$ ).  $\text{LiSn}_2\text{Br}_3(\text{CN}_2)$  is thought to show negative thermal expansion at temperatures below 25 K, as indicated by density functional perturbation theory (DFPT) calculations.

Reactions between tetravalent tin halides and lithium or sodium carbodiimide led to the formation of already known ternary compounds containing either Li or Na, e.g.,  $\text{A}_2\text{Sn}(\text{CN}_2)_3$ ,  $\text{A} = \text{Li}, \text{Na}$ . To avoid the formation of ternary Li/Na containing dinitridocarbonates, reactions of  $\text{Pb}(\text{CN}_2)$  and  $\text{SnBr}_4$  were carried out, leading to the formation of yellow single crystals, that were identified as  $\text{Pb}_{14.66}\text{Sn}_{7.34}\text{Br}_{26}(\text{CN}_2)_7\text{O}_2$ .

The compound containing only divalent tin has a complex crystal structure, where one metal site is occupied by both tin and lead. The tin to lead ratio could be determined by energy-dispersive X-ray spectroscopy (EDX) and is consistent with the crystal structure refinement.

In course of explorative syntheses in the system of  $\text{Li}_2(\text{CN}_2)$ ,  $\text{SnO}$ , and  $\text{SnX}_2$ , ( $X = \text{Cl}$ ,  $\text{Br}$ ,  $\text{I}$ ), three tin oxide halides,  $\text{Sn}_7\text{O}_4\text{Cl}_6$ ,  $\text{Sn}_7\text{O}_4\text{Br}_6$ , and  $\text{Sn}_4\text{OI}_6$ , were obtained. Since some tin oxide halides (in particular tin oxide chloride) were mentioned in the literature several decades ago, but without any crystal structure data, the discovery of these three compounds closed a long-standing gap between tin(II) oxide and tin halides.

From similar reactions with  $\text{Li}_2(\text{CN}_2)$  and  $\text{SnI}_2$ , a ternary lithium tin iodide,  $\text{LiSn}_3\text{I}_7$ , was obtained and later synthesized from  $\text{SnI}_2$  and  $\text{LiI}$ . Its crystal structure is closely related to  $\text{SnI}_2$ , but with one shared position of lithium and tin. Recorded  $^7\text{Li}$ ,  $^{119}\text{Sn}$ , and  $^{127}\text{I}$  solid-state nuclear magnetic resonance (ssNMR) spectra of  $\text{LiSn}_3\text{I}_7$  and some related compounds demonstrated the incorporation of  $\text{Li}$  into the structure and showed the presence of two distinct tin sites.

Besides syntheses with tin halides, reactions between lithium carbodiimide and tungsten oxide halides were carried out to synthesize a tungsten oxide carbodiimide. Since reactions with tungsten oxide chlorides and tungsten oxide bromide failed, a tungsten oxide iodide known from textbooks and articles,  $\text{WO}_2\text{I}_2$ , was synthesized to perform further reactions with it. Single crystals of  $\text{WO}_2\text{I}_2$  were synthesized and its previously unknown crystal structure was determined. In addition, a second compound with the composition  $\text{W}_2\text{O}_3\text{I}_4$  was obtained and structurally characterized.

$\text{WO}_2\text{I}_2$  was synthesized from a mixture of  $\text{WO}_3$ ,  $\text{W}$ , and  $\text{I}_2$  at a temperature gradient of 800 to 300 °C.  $\text{WO}_2\text{I}_2$  has been reported in the literature to play an important role in chemical transport reactions in tungsten halogen lamps, although its crystal structure was previously unknown. When heated above 400 °C,  $\text{WO}_2\text{I}_2$  transforms into  $\text{W}_2\text{O}_3\text{I}_4$ , a compound completely unknown in the literature so far.

# Zusammenfassung

Diese Arbeit konzentriert sich auf Festkörpersynthesen von Zinnverbindungen und einiger ihrer Eigenschaften. Der Großteil dieser Verbindungen konnte durch Festkörpermetathesereaktionen zwischen Lithiumcarbodiimid und Zinnhalogeniden dargestellt werden. Darüber hinaus wurden einige Halogenide und Oxidhalogenide synthetisiert. Die meisten der beschriebenen Verbindungen wurden durch Einkristall-Röntgenbeugung charakterisiert.

Bei der Reaktion von  $\text{Li}_2(\text{CN}_2)$  und  $\text{SnCl}_2$  entstand  $\text{Sn}(\text{CN}_2)$ , als Nebenphase bildete sich  $\text{Sn}_2\text{O}(\text{CN}_2)$ . Weitere Untersuchungen haben zur Entdeckung von  $\text{Sn}_4\text{Cl}_2(\text{CN}_2)_3$  und  $\text{Sn}_9\text{O}_5\text{Cl}_4(\text{CN}_2)_2$  geführt. Darüber hinaus konnte gezeigt werden, dass  $\text{Sn}_4\text{Cl}_2(\text{CN}_2)_3$  als Vorläuferverbindung bei den Synthesen von  $\text{Sn}(\text{CN}_2)$ ,  $\text{Sn}_2\text{O}(\text{CN}_2)$  und  $\text{Sn}_9\text{O}_5\text{Cl}_4(\text{CN}_2)_2$  dient.  $\text{Sn}_4\text{Cl}_2(\text{CN}_2)_3$  wird bei diesen Synthesen bei Temperaturen unter  $200\text{ }^\circ\text{C}$  gebildet und wandelt sich bei Temperaturen über  $300\text{ }^\circ\text{C}$  entweder in  $\text{Sn}(\text{CN}_2)$ ,  $\text{Sn}_2\text{O}(\text{CN}_2)$  oder  $\text{Sn}_9\text{O}_5\text{Cl}_4(\text{CN}_2)_2$  um. Photoanoden auf  $\text{CuWO}_4$ -Basis, die mit  $\text{Sn}_2\text{O}(\text{CN}_2)$  gemischt sind, zeigten im Vergleich zu reinen  $\text{CuWO}_4$ -Elektroden verbesserte Wirkungsgrade. Einige Zinncarbodiimide wurden mithilfe von DFT-Rechnungen untersucht, wodurch bei diesen Verbindungen die elektronischen Strukturen charakterisiert und sie als Halbleiter mit Bandlücken im Bereich von 1 bis 3 eV bestimmt werden konnten. Die zweiwertigen Zinncarbodiimid-Verbindungen  $\text{Sn}_4\text{Cl}_2(\text{CN}_2)_3$ ,  $\text{Sn}_9\text{O}_5\text{Cl}_4(\text{CN}_2)_2$  und  $\text{Sn}_2\text{O}(\text{CN}_2)$  wurden mittels Mößbauerspektroskopie untersucht, um mögliche Spuren von  $\text{Sn}^{4+}$  zu identifizieren. In Proben von  $\text{Sn}_4\text{Cl}_2(\text{CN}_2)_3$  konnte kein Zinn +IV nachgewiesen werden, jedoch zeigten Proben von  $\text{Sn}_9\text{O}_5\text{Cl}_4(\text{CN}_2)_2$  und  $\text{Sn}_2\text{O}(\text{CN}_2)$  das Vorhandensein von vierwertigem Zinn. Dieses  $\text{Sn}^{4+}$  stammt vermutlich aus dem Ausgangsmaterial  $\text{SnO}$ , in welchem auch Zinn in der Oxidationsstufe +IV nachgewiesen wurde.

Analoge Reaktionen mit  $\text{Li}_2(\text{CN}_2)$  und  $\text{SnBr}_2$  (anstelle von  $\text{SnCl}_2$ ) führten zur Entdeckung von zwei Verbindungen,  $\text{Sn}_4\text{Br}_2(\text{CN}_2)_3$  und  $\text{LiSn}_2\text{Br}_3(\text{CN}_2)$ .  $\text{Sn}_4\text{Br}_2(\text{CN}_2)_3$  ist isotyp zu  $\text{Sn}_4\text{Cl}_2(\text{CN}_2)_3$ , während  $\text{LiSn}_2\text{Br}_3(\text{CN}_2)$  isotyp zu dem Mineral Bideauxit ( $\text{AgPb}_2\text{Cl}_3(\text{F},\text{OH})_2$ ) ist. DFPT-Rechnungen von  $\text{LiSn}_2\text{Br}_3(\text{CN}_2)$  zeigen einen negativen Wärmeausdehnungskoeffizienten bei Temperaturen unter 25 K.

Reaktionen zwischen vierwertigen Zinnhalogeniden und Lithium- oder Natriumcarbodiimid führten zur Bildung von bereits bekannten ternären Verbindungen, die entweder Li oder Na enthalten, z. B.  $\text{A}_2\text{Sn}(\text{CN}_2)_3$ , A = Li, Na. Um die Entstehung

von ternären Li/Na-haltigen Dinitridocarbonaten zu vermeiden, wurden Reaktionen von  $\text{Pb}(\text{CN}_2)$  und  $\text{SnBr}_4$  durchgeführt, bei welchen gelbe Einkristalle gebildet wurden. Diese konnten als  $\text{Pb}_{14.66}\text{Sn}_{7.34}\text{Br}_{26}(\text{CN}_2)_7\text{O}_2$  identifiziert werden. Die Verbindung, die nur zweiwertiges Zinn enthält, weist eine komplexe Kristallstruktur auf, bei der eine Mischbesetzung von Zinn und Blei auf einer Atomposition auftritt. Das Verhältnis von Zinn zu Blei konnte durch EDX ermittelt werden und stimmt mit der Verfeinerung der Kristallstruktur überein.

Im Zuge explorativer Synthesen im System von  $\text{Li}_2(\text{CN}_2)$ ,  $\text{SnO}$  und  $\text{SnX}_2$  ( $X = \text{Cl}, \text{Br}, \text{I}$ ) entstanden die drei Zinnoxidhalogenide,  $\text{Sn}_7\text{O}_4\text{Cl}_6$ ,  $\text{Sn}_7\text{O}_4\text{Br}_6$  und  $\text{Sn}_4\text{OI}_6$ . Da einige Zinnoxidhalogenide (insbesondere Zinnoxidchlorid) bereits vor mehreren Jahrzehnten in der Literatur erwähnt wurden, jedoch ohne Kristallstrukturdaten, schloss die Entdeckung dieser drei Verbindungen eine seit langem bestehende Lücke zwischen Zinn(II)-oxid und Zinnhalogeniden.

Bei ähnlichen Reaktionen mit  $\text{Li}_2(\text{CN}_2)$  und  $\text{SnI}_2$  wurde ein ternäres Lithiumzinniodid,  $\text{LiSn}_3\text{I}_7$ , gebildet und später aus  $\text{SnI}_2$  und  $\text{LiI}$  synthetisiert. Seine Kristallstruktur ist eng mit der von  $\text{SnI}_2$  verwandt, jedoch mit einer gemischten Position von Lithium und Zinn. Die aufgezeichneten  $^7\text{Li}$ -,  $^{119}\text{Sn}$ - und  $^{127}\text{I}$ -Festkörper NMR-Spektren von  $\text{LiSn}_3\text{I}_7$  und einigen verwandten Verbindungen belegen den Einbau von Li in die Struktur und zeigen das Vorhandensein zweier verschiedener Zinnpositionen.

Neben Versuchen mit Zinnhalogeniden wurden Reaktionen zwischen Lithiumcarbodiimid und Wolframoxidhalogeniden durchgeführt, um ein Wolframoxidcarbodiimid zu synthetisieren. Da Reaktionen mit Wolframoxidchloriden und Wolframoxidbromid fehlschlugen, wurde ein aus Lehrbüchern und Artikeln bekanntes Wolframoxidiodid,  $\text{WO}_2\text{I}_2$ , hergestellt, um damit weitere Reaktionen durchzuführen. Dabei konnten Einkristalle von  $\text{WO}_2\text{I}_2$  synthetisiert und seine bis dato unbekannte Kristallstruktur bestimmt werden. Außerdem konnte eine zweite Verbindung mit der Zusammensetzung  $\text{W}_2\text{O}_3\text{I}_4$  dargestellt und ebenfalls strukturell charakterisiert werden.

$\text{WO}_2\text{I}_2$  wurde aus einer Mischung von  $\text{WO}_3$ , W und  $\text{I}_2$  bei einem Temperaturgradienten von 800 bis 300 °C gewonnen.  $\text{WO}_2\text{I}_2$  wird in der Literatur eine wichtige Rolle bei chemischen Transportreaktionen in Wolfram-Halogenlampen zugeschrieben, obwohl seine Kristallstruktur bislang unbekannt war.

Beim Erhitzen über 400 °C wandelt sich  $\text{WO}_2\text{I}_2$  in  $\text{W}_2\text{O}_3\text{I}_4$  um.  $\text{W}_2\text{O}_3\text{I}_4$  ist eine in der Literatur bisher völlig unbekannte Verbindung.



# Publications

## Publication 1:

*Synthesis, Structure, and Electronic Properties of Sn(CN<sub>2</sub>) and Sn<sub>4</sub>Cl<sub>2</sub>(CN<sub>2</sub>)<sub>3</sub>*

Manuel Löber, Konstantin Dolabdjian, Markus Ströbele, Carl P. Romao, and Hans-Jürgen Meyer

*Inorg. Chem.* **2019**, *58*, 7845–7851

<https://doi.org/10.1021/acs.inorgchem.9b00527>

## Publication 2:

*Synthesis, Structure, and Electronic Properties of Sn<sub>9</sub>O<sub>5</sub>Cl<sub>4</sub>(CN<sub>2</sub>)<sub>2</sub>*

Manuel Löber, Chris Steve Geißenhöner, Markus Ströbele, Sylvio Indris, Carl P. Romao, and Hans-Jürgen Meyer

*Inorg. Chem.* **2019**, *58*, 14560–14567

<https://doi.org/10.1021/acs.inorgchem.9b02229>

## Publication 3:

*Increased photocurrent of CuWO<sub>4</sub> photoanodes by modification with the oxide carbodiimide Sn<sub>2</sub>O(NCN)*

Zheng Chen, Manuel Löber, Anna Rokicińska, Zili Ma, Jianhong Chen, Piotr Kuśtrowski, Hans-Jürgen Meyer, Richard Dronskowski and Adam Slabon

*Dalton Trans.* **2020**, *49*, 3450–3456

<https://doi.org/10.1039/C9DT04752B>

## Publication 4:

*Synthesis, Structure and Electronic Properties of Three Tin Oxide Halides*

Manuel Löber, Chris Steve Geißenhöner, Markus Ströbele, Carl P. Romao, and Hans-Jürgen Meyer

*Eur. J. Inorg. Chem.* **2021**, *2021*, 283–288

<https://doi.org/10.1002/ejic.202000874>

## Publication 5:

*W<sub>2</sub>O<sub>3</sub>l<sub>4</sub> and WO<sub>2</sub>l<sub>2</sub>: metallic phases in the chemical transport reaction of tungsten*

Manuel Löber, Markus Ströbele, Carl P. Romao, and Hans-Jürgen Meyer

*Dalton Trans.* **2021**, *50*, 6789–6792

<https://doi.org/10.1039/D1DT01212F>

**Publication 6:**

*Synthesis and crystal structure of  $Pb_{14.66}Sn_{7.34}Br_{26}(CN_2)_7O_2$ , a complex member of group 14 carbodiimides*

Manuel Löber, Markus Ströbele and Hans-Jürgen Meyer

*Z. Anorg. Allg. Chem.* **2021**, 647, 1973–1977

<https://doi.org/10.1002/zaac.202100273>

**Publication 7:**

*Synthesis, Structure, and Thermoelastic Properties of  $LiSn_2Br_3(CN_2)$  and  $Sn_4Br_2(CN_2)_3$*

Manuel Löber, Markus Ströbele, Carl P. Romao, and Hans-Jürgen Meyer

*Eur. J. Inorg. Chem.* **2021**, 2021, 4572–4578

<https://doi.org/10.1002/ejic.202100660>

**Publication 8:**

*The Lithium Iodostannate  $LiSn_3I_7$ : Synthesis, Properties and its Relationship to  $SnI_2$*

Manuel Löber, Markus Ströbele, Klaus Eichele, Carl P. Romao, and Hans-Jürgen Meyer

*Eur. J. Inorg. Chem.* **2021**, 2021, 4929–4934

<https://doi.org/10.1002/ejic.202100771>

## Personal Contribution

**Publication 1:** The initial synthesis, as well as Rietveld refinement and infrared (IR) measurements of  $\text{Sn}(\text{CN}_2)$  were performed by Dr. Dolabdjian, but still with unknown side phases. I adjusted the synthesis so that only known side phases were present, Dr. Ströbele then refined the structure again from this synthesis. The compound  $\text{Sn}_4\text{Cl}_2(\text{CN}_2)_3$  was synthesized by me and I also performed the thermoanalytical measurements. A single crystal of the compound  $\text{Sn}_4\text{Cl}_2(\text{CN}_2)_3$  was measured by Mrs. Niquet and Dr. Maichle-Mössmer (University of Tübingen), the subsequent crystal structure refinement was also done by Dr. Ströbele. The DFT calculations on  $\text{Sn}(\text{CN}_2)$ , as well as  $\text{Sn}_4\text{Cl}_2(\text{CN}_2)_3$ , were performed by Dr. Romao. The optical reflectance measurements for  $\text{Sn}(\text{CN}_2)$ , as well as  $\text{Sn}_4\text{Cl}_2(\text{CN}_2)_3$ , were performed by Dr. Enseling (FH Münster) and evaluated by myself. The syntheses for these both were also performed by myself. Dr. Romao wrote the theoretical part in the manuscript. The draft for the manuscript was written by myself and completed by Prof. Meyer.

**Publication 2:** The synthesis, as well as the thermoanalytical investigation of  $\text{Sn}_9\text{O}_5\text{Cl}_4(\text{CN}_2)_2$ , were performed by myself. The Rietveld refinement was performed by Dr. Ströbele. Mr. Geißenhöner performed the DFT calculations under the supervision of Dr. Romao. Dr. Indris (KIT) recorded the Mössbauer spectra of  $\text{Sn}_9\text{O}_5\text{Cl}_4(\text{CN}_2)_2$ ,  $\text{Sn}_4\text{Cl}_2(\text{CN}_2)_3$ , and  $\text{SnO}$  and wrote the corresponding part in the manuscript. The optical reflectance measurements were recorded by Dr. Früh (University of Tübingen) and evaluated by me. Dr. Romao wrote the theoretical part in the manuscript. The draft for the manuscript was written by myself and completed by Prof. Meyer.

**Publication 3:** The  $\text{Sn}_2\text{O}(\text{CN}_2)$ , which was investigated as a photoanode, was prepared by myself. The electrochemistry was done by Zheng Cheng (RWTH Aachen), including the preparation of the electrodes, and the performance of the photochemical experiments. The XPS measurements and analysis were performed by Anna Rokicińska and Piotr Kuśtrowski. Jianhong Chen did the EDX analysis. Zili Ma co-performed the electrochemical experiments. Richard Dronskowski co-designed the analysis. Adam Slabon supervised the work and manuscript.

**Publication 4:** The three compounds,  $\text{Sn}_7\text{O}_4\text{Cl}_6$ ,  $\text{Sn}_7\text{O}_4\text{Br}_6$ , and  $\text{Sn}_4\text{O}_6$  were prepared by myself. I also conducted the single-crystal XRD experiments. The corresponding crystal structure refinements were performed by Dr. Ströbele. Mr. Geißenhöner and Dr. Romao did the DFT calculations and wrote the corresponding part in the manuscript. The draft for the manuscript was written by myself and completed by Prof. Meyer.

**Publication 5:** The syntheses of  $\text{WO}_2\text{I}_2$  and  $\text{W}_2\text{O}_3\text{I}_4$  as well as the single crystal measurements were performed by myself. Dr. Ströbele did the crystal structure refinement on both structures. Dr. Romao performed the DFT calculations and wrote the theoretical part in the manuscript. The draft for the manuscript was written by myself and completed by Prof. Meyer.

**Publication 6:** The synthesis and the single-crystal experiment were performed by myself. Dr. Ströbele did the structure refinement. Elke Nadler (University of Tübingen) performed the EDX measurements and recorded some SEM images. The EDX measurements were evaluated by me. The draft for the manuscript was written by myself and completed by Prof. Meyer.

**Publication 7:** The synthesis, single-crystal experiments, and the differential thermal analysis (DTA) were performed by myself. The structure refinement of  $\text{Sn}_4\text{Br}_2(\text{CN}_2)_3$  was performed by myself, the refinement of  $\text{LiSn}_2\text{Br}_3(\text{CN}_2)$  was performed by Dr. Ströbele. Dr. Romao performed the calculations on the electronic and vibrational properties of  $\text{LiSn}_2\text{Br}_3(\text{CN}_2)$  and some isotypic compounds. The draft for the manuscript was written by myself and completed by Prof. Meyer. The theoretical part was written by Dr. Romao.

**Publication 8:** The synthesis, single-crystal experiment, and the differential scanning calorimetry (DSC) measurement of  $\text{LiSn}_3\text{I}_7$  were performed by myself. The refinement was performed by Dr. Ströbele. Dr. Romao did the calculations and wrote the theoretical part of the manuscript. Dr. Eichele did the ssNMR measurements and wrote the corresponding part of the manuscript. The draft for the manuscript was written by myself and completed by Prof. Meyer.

# 1. Introduction

### 1.1 Solid-state reactions

Solid-state reactions can be used to synthesize a variety of different substances. The common approach for the synthesis of inorganic solids is to react either elements or solid compounds directly. In most cases, very high temperatures are required for this type of reaction, as many elements and compounds (e.g., oxides) have a high melting point, resulting in low reactivity due to low diffusion rates.<sup>[1]</sup> For example, the synthesis of  $\text{LaC}_2$  from lanthanum and carbon requires temperatures of 1200 to 2000 °C for 2–4h.<sup>[2]</sup> To synthesize the spinel  $\text{CoAl}_2\text{O}_4$  from the oxides  $\text{CoO}$  and  $\text{Al}_2\text{O}_3$ , temperatures of up to 1300 °C are necessary.<sup>[3]</sup> Precursors can be used to lower the required reaction temperatures, which is a common reaction path for the aforementioned synthesis of  $\text{CoAl}_2\text{O}_4$ , that can be performed at temperatures as low as 700 °C using sol-gel methods.<sup>[3]</sup> Furthermore, low melting fluxes such as eutectic salt mixtures can be used to increase the diffusion between the individual reactants (e.g.,  $\text{LiCl/KCl}$ , Mp. 355 °C). For solid-state reactions in general, it is essential to pestle the reactants, using an agate mortar or grinding them in a ball mill.<sup>[1]</sup>

Besides the type of reactants, the choice of the reaction vessel is also crucial for solid-state reactions. At first, it is important to know whether an open or a closed system is needed. Open systems are suitable when working in air, when a specific atmosphere is required for the reaction (solid-gas reaction, e.g.,  $\text{CO}_2$ ,  $\text{NH}_3$ , or  $\text{H}_2$ ),<sup>[4]</sup> when the pressure would be too high for a closed vessel, or a certain substance is to be removed. For example, such reactions can be carried out in corundum or platinum crucibles. Most of the reactions in closed containers are performed in silica ampules. For reactions at higher temperatures, pressures, or for glass-corrosive substances (such as alkali metals or fluorides), various metal ampules, e.g., made of niobium, tantalum, molybdenum, tungsten, or platinum are available. In addition to the above-mentioned benefit of low-melting salts as fluxes, melts can also be used as reaction partners, if the thermal stability is appropriate, e.g., for the synthesis of nitrogenous compounds, the use of molten  $\text{Li}_3\text{N}$  has proven to be effective.<sup>[1]</sup>

In ordinary solid-state reactions, such as synthesis from the elements, the most thermodynamically stable compounds are often formed due to the high activation energies of these reactions and the resulting high reaction temperatures.<sup>[1]</sup>

A diagram showing the principle of a thermodynamically controlled reaction is shown in Figure 1. In such a thermodynamically controlled reaction, metastable products can be formed, but this happens randomly rather than under controlled conditions.

# 1. Introduction

Suppose it is eventually possible to lower the activation energy of a reaction. In that case, a metastable product can be obtained, although it is not the thermodynamically most stable product, but is formed faster. Such a kinetically controlled reaction path is illustrated in Figure 2.<sup>[5]</sup>

Since solid-state reactions frequently suffer from low reactivity due to slow diffusion, different synthesis strategies with rather moderate reaction temperatures are needed. One of these different approaches is SSM reactions.<sup>[5]</sup>

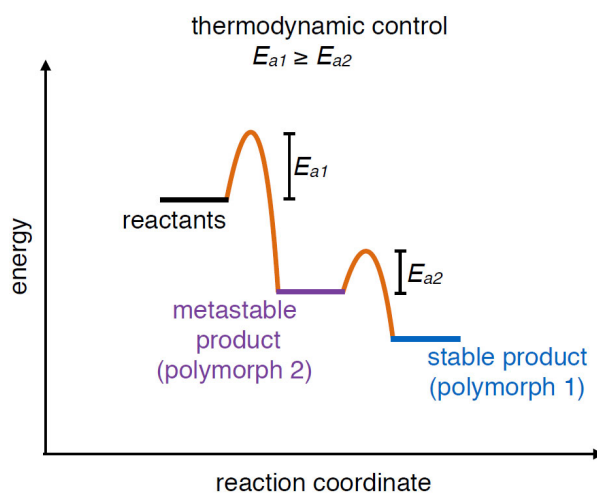


**Figure 1.** Schematic reaction diagram that illustrates a thermodynamically controlled reaction, in which the first activation energy  $E_{a1}$  is greater than or equal to  $E_{a2}$ . Reprinted (adapted) with permission from<sup>[6]</sup>. Copyright 2017 American Chemical Society.

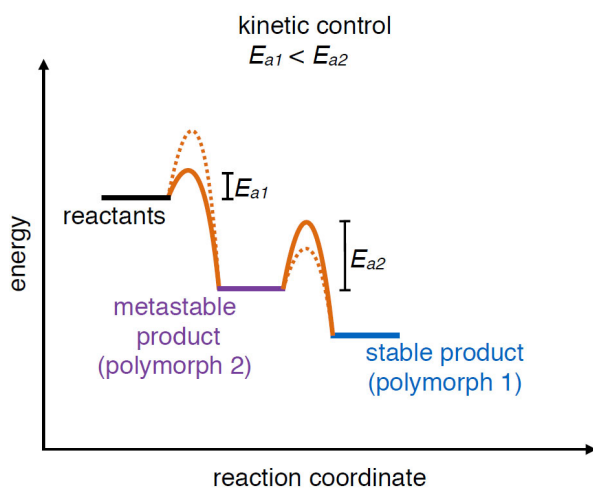


**Figure 2.** Schematic reaction diagram that illustrates a kinetically controlled reaction, where the first activation energy  $E_{a1}$  is smaller than  $E_{a2}$ . Reprinted (adapted) with permission from<sup>[6]</sup>. Copyright 2017 American Chemical Society.

The basic principle of SSM reactions is a pairwise ion exchange of (in the simplest case) two reaction partners, forming a new product and a corresponding metathesis salt, as can be seen in reaction (1), where the two starting materials AB and CD react to form a new product (AD) and a metathesis salt (BC). Such reactions are usually strongly exothermic and can be monitored thermoanalytically by DTA or DSC.<sup>[7]</sup>



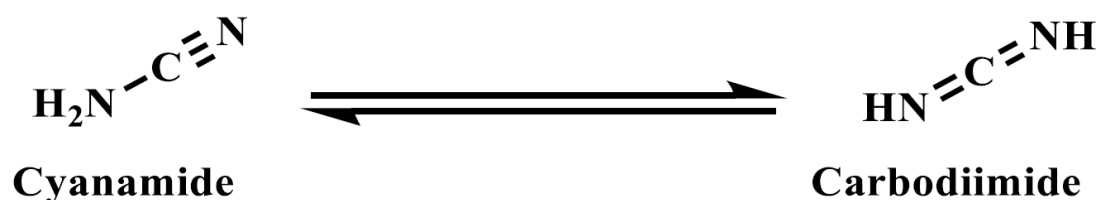
In addition, with SSM reactions, it is possible to transfer not only single but also polyatomic ions. SSM reactions have been explored for a wide variety of compounds, including nitrides, carbonates, carbides, and nitridoborates.<sup>[8]</sup> Besides the benefit of SSM reactions to capture metastable phases, it is also a useful tool for low-temperature syntheses compared to the classical solid-state approach. An example of this is the metathetic formation of  $\text{LaC}_2$  from  $\text{LaCl}_3$  and  $\text{Li}_2\text{C}_2$ , which occurs at 500 °C, whereas the above-mentioned synthesis from the elements requires more than 1200 °C.<sup>[8]</sup> The wide range of applications and benefits of these SSM reactions also becomes clear when looking at the substance class of dinitridocarbonates.



## 1.2 Dinitridocarbonates

Metal dinitridocarbonates are characterized by the  $[\text{NCN}]^{2-}$  anion, which exists in two different forms: the symmetric carbodiimide moiety and the asymmetric cyanamide form. Compounds containing the  $[\text{NCN}]^{2-}$  ion are referred to as NCN compounds in the following.

The protonated form  $\text{H}_2\text{CN}_2$  (cyanamide) was first synthesized in the 19<sup>th</sup> century and appears in two tautomeric forms, cyanamide and carbodiimide, of which the cyanamide moiety is heavily favored. The two different tautomers are depicted in Scheme 1. At room temperature, the cyanamide is unstable (without stabilizer) and tends to dimerize to dicyandiamide ( $\text{H}_2\text{C}_2\text{N}_4$ ) or even to trimerize to melamine ( $\text{C}_3\text{H}_6\text{N}_6$ ).<sup>[9]</sup>



**Scheme 1.** The two  $\text{H}_2\text{CN}_2$  tautomers, shown in chemical equilibrium. Reprinted (adapted) with permission from<sup>[9]</sup>.

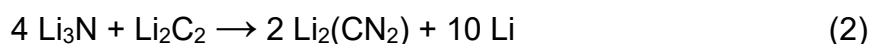
However, as a divalent anion in metal dinitridocarbonates, the carbodiimide or the cyanamide form can be present. An explanation for the presence of cyanamide or carbodiimide in a crystal structure is given by the hard and soft acids and bases (HSAB) concept, as shown between the harder oxide and the softer sulfide ion, where the  $[\text{NCN}]^{2-}$  ion can be placed in between.<sup>[10]</sup>

The same applies to the hardness and softness of cations. Soft cations, such as  $\text{Ag}^+$ ,  $\text{Pb}^{2+}$  or,  $\text{Hg}^{2+}$  support the asymmetric  $[\text{N}\equiv\text{C}-\text{N}]^{2-}$  cyanamide moiety,<sup>[11]</sup> whereas hard cations, such as  $\text{Li}^+$ ,<sup>[12]</sup>  $\text{Sm}^{3+}$ ,<sup>[13]</sup> or  $\text{Mg}^{2+}$ <sup>[14]</sup> support the symmetric  $[\text{N}=\text{C}=\text{N}]^{2-}$  carbodiimide form. However, the shape of the NCN unit is also determined by the coordination environment of the NCN ions.<sup>[15]</sup> In addition to distinguishing the two NCN moieties by XRD, IR spectroscopy provides a reliable differentiation method, since symmetric NCN stretching vibrations occur for the asymmetric cyanamide form and are IR-forbidden for the symmetric carbodiimide moiety.<sup>[14]</sup>

The first metal dinitridocarbonate discovered was  $\text{Ca}(\text{CN}_2)$ , obtained by Caro and Frank from  $\text{CaC}_2$  and  $\text{N}_2$  at temperatures of 1000 °C, which is called the Frank-Caro process.<sup>[16]</sup> Since then, calcium carbodiimide, called “nitrolime”, has been used as a fertilizer.<sup>[17]</sup>  $\text{Ca}(\text{CN}_2)$  decomposes into urea and  $\text{Ca}(\text{OH})_2$  when applied to soils; urea

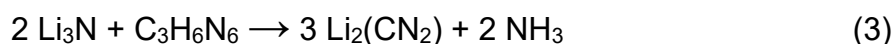
is further converted into ammonia and CO<sub>2</sub>.<sup>[18]</sup> The dicyandiamide formed as an intermediate acts as a nitrification inhibitor in the soil and could prevent the bacterial formation of N<sub>2</sub>O, which is a very potent greenhouse gas.<sup>[17]</sup> The trigonal crystal structure of Ca(CN<sub>2</sub>) was first determined in 1927 by Dehlinger<sup>[19]</sup> and revised later by improved measurements<sup>[20]</sup>. Since the discovery of calcium carbodiimide, many more NCN compounds have been synthesized. Among them are pseudobinary dinitridocarbonates of the alkali metals (Li,<sup>[12]</sup> Na,<sup>[21]</sup> K<sup>[22]</sup>), alkaline earth metals (Mg,<sup>[14]</sup> Sr,<sup>[14, 23]</sup> Ba<sup>[14]</sup>), some more main group metals,<sup>[24]</sup> the transition metals of 3d elements except Ti and V<sup>[25]</sup> and further d-elements<sup>[26]</sup>. In addition, the existence of pseudobinary compounds of all rare earth (RE) elements except La and Pm<sup>[13, 27]</sup> has been reported. More complex NCN compounds are also common and may contain additional anions (like Cl<sup>-</sup> or O<sup>2-</sup>)<sup>[28]</sup> or several cations like in LiM(CN<sub>2</sub>)<sub>2</sub>, (M = La, Ce)<sup>[29]</sup>.

During the last decades, many different approaches for the synthesis of NCN compounds have been reported. Among the earliest is the synthesis of lithium carbodiimide, Li<sub>2</sub>(CN<sub>2</sub>), which was prepared in the 1970<sup>th</sup> by reacting Li<sub>3</sub>N with Li<sub>2</sub>C<sub>2</sub> at 600 °C, according to reaction (2).<sup>[12]</sup>

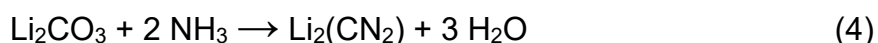


The sodium<sup>[21]</sup> and potassium<sup>[22]</sup> carbodiimides have been prepared by the reaction of their amides with the previously reported hydrogen-containing compounds Na(HCN<sub>2</sub>),<sup>[30]</sup> K(HCN<sub>2</sub>)<sup>[31]</sup>. For rubidium, only the hydrogenated compound Rb(HCN<sub>2</sub>) is reported, which was synthesized from the reaction of RbNH<sub>2</sub> and H<sub>2</sub>CN<sub>2</sub> in liquid ammonia.<sup>[32]</sup>

The alkaline earth metal carbodiimides Mg(CN<sub>2</sub>), Sr(CN<sub>2</sub>), and Ba(CN<sub>2</sub>) were synthesized, using metal nitrides and melamine (melamine route) at temperatures ranging from 740 to 850 °C,<sup>[14]</sup> a method that can also be used for the synthesis of Li<sub>2</sub>(CN<sub>2</sub>) in accordance with reaction (3)<sup>[33]</sup>.



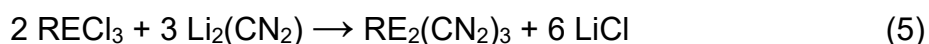
Some NCN compounds could be synthesized by ammonolysis using the metal carbonates and ammonia, as exemplified for the synthesis of Li<sub>2</sub>(CN<sub>2</sub>) in reaction (4).<sup>[34]</sup>



A rather inconvenient reaction pathway has been described for the synthesis of M<sub>2</sub>Cl<sub>2</sub>(CN<sub>2</sub>) (M = Eu, Sr),<sup>[35]</sup> which was obtained from the reactions of MCl<sub>2</sub>, NaN<sub>3</sub>, and

NaCN in tantalum ampules. This synthetic pathway will be referred to as azide-cyanide below.

A wide spectrum of NCN compounds could be obtained using SSM reactions. Among these are many different compounds of the group of RE elements as pseudobinary, ternary, or quaternary compounds. The reaction scheme for the synthesis of pseudobinary RE carbodiimides is shown in reaction (5).



More complex RE carbodiimide compounds containing additional anions and/or cations were also successfully synthesized, as exemplified for the compounds  $\text{La}_2\text{O}(\text{CN}_2)_2$ ,<sup>[36]</sup>  $\text{LaCl}(\text{CN}_2)$ ,<sup>[28b]</sup>  $\text{LiLa}(\text{CN}_2)_2$ ,<sup>[29]</sup>  $\text{La}_2\text{Cl}(\text{CN}_2)\text{N}$ ,<sup>[33]</sup>  $\text{LaSr}_3\text{F}_5(\text{CN}_2)_2$ <sup>[37]</sup>.

These reactions could be mostly performed in silica ampules at temperatures between 500 °C and 650 °C.<sup>[13]</sup>

Besides the solid-state approach, some of the NCN compounds have been synthesized from an aqueous solution.  $\text{Fe}(\text{CN}_2)$  was prepared from  $[(\text{NH}_4)_2\text{Fe}(\text{SO}_4)_2] \cdot 6\text{H}_2\text{O}$ ,  $\text{H}_2\text{CN}_2$ , and ammonia solution<sup>[25e]</sup>. Solutions of metal chlorides, cyanamide, and ammonia led to the formation of  $\text{Co}(\text{CN}_2)$ ,  $\text{Ni}(\text{CN}_2)$ ,<sup>[25d]</sup>  $\text{Cu}(\text{CN}_2)$ ,<sup>[25b]</sup> and  $\text{Cd}(\text{CN}_2)$ <sup>[26d]</sup>.  $\text{Zn}(\text{CN}_2)$  was precipitated from an aqueous solution of  $\text{ZnSO}_4$  and  $\text{Na}_2(\text{CN}_2)$ .<sup>[25a]</sup>  $\text{Ag}_2(\text{CN}_2)$  could be precipitated using  $\text{H}_2\text{CN}_2$ ,  $\text{AgNO}_3$ , and ammonia solution,<sup>[26a]</sup>  $\text{Pb}(\text{CN}_2)$  was prepared by mixing cyanamide, lead acetate, and ammonia solution,<sup>[24c]</sup>  $\text{Tl}_2(\text{CN}_2)$  was precipitated from a solution of  $\text{Tl}_2\text{CO}_3$  and  $\text{Na}(\text{CN}_2)$ ,<sup>[26e]</sup> and  $\text{Hg}(\text{CN}_2)$  was obtained by mixing  $\text{HgCl}_2$ ,  $\text{H}_2\text{CN}_2$ , and  $\text{NaOH}$ <sup>[26b]</sup>. Some of these compounds were first synthesized as hydrogenated species and later decomposed to hydrogen-free ones by heating.

Despite the many different approaches to synthesize NCN compounds, new synthetic routes are still being reported.<sup>[38]</sup>

An overview of all existing (to the author's knowledge) inorganic NCN compounds is presented in Tables 1–7. The year of publication, the molecular formula, the space group, and the type of synthesis used for preparation are given. A similar tabular overview of all known NCN compounds can be found in the PhD thesis of Dr. Konstantin Dolabdjian,<sup>[39]</sup> which has been expanded and supplemented in the present work. As shown in Tables 1–7, most of the metal dinitridocarbonates have been prepared by SSM reactions, especially in recent years. The large number of NCN compounds that have been prepared and characterized during the last decades is accompanied by many interesting properties and resulting applications, which will be

discussed in more detail in the following. Among the many different NCN compounds of RE elements that have been synthesized in the past, several have been investigated for their properties, in particular luminescence. As the first reported carbodiimide of the RE elements,  $\text{La}_2\text{O}_2(\text{CN}_2)$  has been studied as phosphor using different dopants, such as  $\text{Eu}^{3+}$ ,<sup>[40]</sup>  $\text{Pr}^{3+}$ ,<sup>[41]</sup>  $\text{Er}^{3+}/\text{Yb}^{3+}$ ,<sup>[42]</sup> or  $\text{Tb}^{3+}$ .<sup>[43]</sup> Furthermore, the potential use of  $\text{La}_2\text{O}_2(\text{CN}_2)$  nanofibers as photocatalyst was investigated.<sup>[42]</sup> Luminescence properties were reported and studied for the pseudobinary RE carbodiimide,  $\text{Gd}_2(\text{CN}_2)_3$  using  $\text{Ce}^{3+}$  and  $\text{Tb}^{3+}$  as dopants, revealing a strong luminescence comparable to that of doped yttrium aluminum garnet.<sup>[27c]</sup>

**Table 1.** Pseudobinary NCN compounds containing only one cation.

Year of discovery	Molecular formula	Space group	Synthetic route
1942 <sup>[20a]</sup>	$\text{Ca}(\text{CN}_2)$	$R\bar{3}m$ (166)	$\text{CaC}_2 + \text{N}_2$
1978 <sup>[12]</sup>	$\text{Li}_2(\text{CN}_2)$	$I4/mmm$ (139)	solid-state reaction
1994 <sup>[14]</sup>	$\text{Mg}(\text{CN}_2)$	$R\bar{3}m$ (166)	melamine route
1994 <sup>[14]</sup>	$\alpha\text{-Sr}(\text{CN}_2)$	$Pnma$ (62)	melamine route
2010 <sup>[23]</sup>	$\beta\text{-Sr}(\text{CN}_2)$	$R\bar{3}m$ (166)	SSM reaction
1994 <sup>[14]</sup>	$\text{Ba}(\text{CN}_2)$	$R\bar{3}c$ (167)	melamine route
1995 <sup>[24a]</sup>	$\text{In}_{2.24}(\text{CN}_2)_3$	$R\bar{3}c$ (167)	solid-state reaction
1997 <sup>[24b]</sup>	$\text{Si}(\text{CN}_2)_2$	$Pn\bar{3}m$ (224)	liquid-liquid reaction
2000 <sup>[24c]</sup>	$\text{Pb}(\text{CN}_2)^*$	$Pnma$ (62)	aqueous solution
2000 <sup>[26a]</sup>	$\text{Ag}_2(\text{CN}_2)$	$P2_1/c$ (14)	aqueous solution
2000 <sup>[26b]</sup>	$\text{Hg}(\text{CN}_2)$	$Pbca$ (61)	aqueous solution
2002 <sup>[26c]</sup>	$\text{Hg}(\text{CN}_2)$	$P2_1/a$ (14)	
2000 <sup>[22]</sup>	$\text{K}_2(\text{CN}_2)$	$C2/m$ (12)	liquid ammonia
2000 <sup>[21]</sup>	$\text{Na}_2(\text{CN}_2)$	$C2/m$ (12)	solid-state reaction
2001 <sup>[25a]</sup>	$\text{Zn}(\text{CN}_2)$	$I\bar{4}2d$ (122)	aqueous solution
2002 <sup>[26d]</sup>	$\text{Cd}(\text{CN}_2)$	$R\bar{3}m$ (166)	aqueous solution
2003 <sup>[27a]</sup>	$\text{Eu}(\text{CN}_2)$	$Pnma$ (62)	solid-state reaction
2005 <sup>[25c]</sup>	$\text{Mn}(\text{CN}_2)$	$R\bar{3}m$ (166)	SSM reaction
2005 <sup>[25b]</sup>	$\text{Cu}(\text{CN}_2)$	$Cmcm$ (63)	aqueous solution
2006 <sup>[13]</sup> 2008 <sup>[27c]</sup>	$\text{RE}_2(\text{CN}_2)_3$ $\text{RE} =$ Y, Pr, Nd, Sm, Gd–Er $\text{RE} = \text{Tm–Lu}$	$C2/m$ (12)  $R\bar{3}c$ (167)	SSM reaction
2007 <sup>[27b]</sup>	$\text{Yb}_2(\text{CN}_2)_3$	$R\bar{3}c$ (167)	solid-state reaction
2007 <sup>[25d]</sup>	$\text{Co}(\text{CN}_2)$ , $\text{Ni}(\text{CN}_2)$	$P6_3/mmc$ (194)	aqueous solution
2007 <sup>[26e]</sup>	$\text{Tl}_2(\text{CN}_2)$	$P\bar{1}$ (2)	aqueous solution
2009 <sup>[25e]</sup>	$\text{Fe}(\text{CN}_2)$	$P6_3/mmc$ (194)	aqueous solution
2010 <sup>[44]</sup>	$\text{Cr}_2(\text{CN}_2)_3$	$R\bar{3}c$ (167)	SSM reaction

## 1. Introduction

2016 <sup>[27d]</sup>	$\text{Eu}_2(\text{CN}_2)_3$	$C2/m$ (12)	SSM reaction
2018 <sup>[26f]</sup>	$\text{Zr}(\text{CN}_2)_2$ , $\text{Hf}(\text{CN}_2)_2$	$Pbcn$ (60)	SSM reaction
2019 <sup>[24d]</sup>	$\text{Sn}(\text{CN}_2)$	$I2/a$ (15)	SSM reaction
2020 <sup>[27e]</sup>	$\text{Sc}_2(\text{CN}_2)_3$	$R\bar{3}c$ (167)	SSM reaction
2021 <sup>[45]</sup>	$\text{Bi}_2(\text{CN}_2)_3$ $\text{Bi}_2(\text{CN}_2)_3 \cdot \text{NH}_3$	$C2/c$ $Cc$	diethyl ether solution

\* First described in the wrong space group  $Pna2_1$  in the 1960th.<sup>[46]</sup>

**Table 2.** Pseudoternary NCN compounds containing one cation and one additional anion.

Year of discovery	Molecular formula	Space group	Synthetic route
1995 <sup>[28a]</sup>	$\text{La}_2\text{O}_2(\text{CN}_2)$	$I4/mmm$ (139)	ammonia atm.
1995 <sup>[47]</sup>	$\text{EA}_2(\text{CN}_2)(\text{CN})_2$ $\text{EA} = \text{Sr}, \text{Ba}$	$P6_3/mmc$ (194)	HCN atm.
1996 <sup>[48]</sup> 2007 <sup>[49]</sup>	$\text{RE}_2\text{O}_2(\text{CN}_2)$ $\text{RE} = \text{Ce}, \text{Pr}, \text{Nd},$ $\text{Sm}, \text{Eu}, \text{Gd}$ $\text{RE} = \text{Dy} - \text{Yb}$	$P\bar{3}m1$ (164)	ammonia atm. melamine route
2000 <sup>[50]</sup>	$\text{Ca}_4\text{N}_2(\text{CN}_2)$ $\text{Ca}_{11}\text{N}_6(\text{CN}_2)_2$	$Pnma$ (62) $P4_2/mnm$ (136)	solid-state reaction (with $\text{NaN}_3$ )
2001 <sup>[51]</sup>	$\text{K}_5(\text{CN}_2)_2\text{H}$	$P4/ncc$ (130)	solid-state reaction
2004 <sup>[28b]</sup>	$\text{RECl}(\text{CN}_2)$ , $\text{RE}$ $= \text{La} - \text{Pr}$	$P2_1/m$ (11)	SSM reaction
2005 <sup>[36]</sup>	$\text{La}_2\text{O}(\text{CN}_2)_2$	$C2/c$ (15)	SSM reaction
2005 <sup>[52]</sup>	$\text{Eu}_8(\text{CN}_2)_{4.95}16.10$	$C2/m$ (12)	solid-state reaction
2005 <sup>[35]</sup>	$\text{M}_2\text{Cl}_2(\text{CN}_2)$ $\text{M} = \text{Sr}, \text{Eu}$	$C2/m$ (12)	azide-cyanide
2006 <sup>[53]</sup>	$\text{Eu}_2\text{I}_2(\text{CN}_2)$	$Pmma$ (51)	azide-cyanide
2007 <sup>[54]</sup>	$\text{Y}_2\text{O}_2(\text{CN}_2)$	$P6_3/mmc$ (194) $P\bar{3}m1$ (164)	SSM reaction
2009 <sup>[55]</sup>	$\text{LaF}(\text{CN}_2)$	$Cmcm$ (63)	SSM reaction
2009 <sup>[29]</sup> 2011 <sup>[56]</sup>	$\text{Ce}_3(\text{CN}_2)_3\text{N}$ $\text{La}_3(\text{CN}_2)_3\text{N}$	$P2_12_12_1$ (19)	SSM reaction
2010 <sup>[57]</sup>	$\text{Y}_2(\text{CN}_2)(\text{SiO}_4)$ $\text{La}_2(\text{CN}_2)(\text{SiO}_4)$ $\text{Pr}_2(\text{CN}_2)(\text{SiO}_4)$	$C2/m$ (12) $P2_1/c$ (14) $P\bar{1}$ (2)	SSM reaction
2011 <sup>[58]</sup>	$\text{Eu}_4\text{F}_5(\text{CN}_2)_2$	$P\bar{4}2_1c$ (114)	SSM reaction
2012 <sup>[59]</sup>	$\text{Na}_5(\text{CN}_2)_2(\text{CN})$ $(\text{Li}, \text{Na})_5(\text{CN}_2)_2(\text{CN})$	$I4/mmm$ (139) $Im\bar{3}m$ (229)	high pressure $\text{N}_2$ atm.
2018 <sup>[60]</sup>	$\text{Sn}_2\text{O}(\text{CN}_2)$	$Pccn$ (56)	SSM reaction
2019 <sup>[24d]</sup> 2021 <sup>[61]</sup>	$\text{Sn}_4\text{Cl}_2(\text{CN}_2)_3$ $\text{Sn}_4\text{Br}_2(\text{CN}_2)_3$	$P2_1/n$ (14)	SSM reaction
2019 <sup>[62]</sup>	$\text{Bi}_2\text{O}_2(\text{CN}_2)$	$I4/mmm$ (139)	SSM reaction

## 1. Introduction

2020 <sup>[27e]</sup>	Sc <sub>2</sub> O(CN <sub>2</sub> )	<i>Immm</i> (71)	SSM reaction
2020 <sup>[63]</sup>	LaI(CN <sub>2</sub> )	<i>Cmcm</i> (63)	SSM reaction
2020 <sup>[64]</sup>	Hg <sub>3</sub> Cl <sub>2</sub> (CN <sub>2</sub> ) <sub>2</sub>	<i>Pca2<sub>1</sub> (29)</i>	aqueous solution

**Table 3.** Pseudoquaternary NCN compounds containing one cation and two additional anions.

Year of discovery	Molecular formula	Space group	Synthetic route
2003 <sup>[33]</sup>	RE <sub>2</sub> Cl(CN <sub>2</sub> )N RE = La, Ce	<i>Cmmm</i> (65)	SSM reaction
2004 <sup>[65]</sup>	RE <sub>2</sub> Br(CN <sub>2</sub> )N, RE = La, Pr	<i>Cmmm</i> (65)	SSM reaction
2013 <sup>[66]</sup>	La <sub>3</sub> Cl(CN <sub>2</sub> )O <sub>3</sub>	<i>Cmcm</i> (63)	SSM reaction
2019 <sup>[67]</sup>	Sn <sub>9</sub> O <sub>5</sub> Cl <sub>4</sub> (CN <sub>2</sub> ) <sub>2</sub>	<i>C222<sub>1</sub> (20)</i>	SSM reaction
2019 <sup>[68]</sup>	Sr <sub>4</sub> N(CN <sub>2</sub> )(C <sub>2</sub> N)	<i>P2<sub>1</sub>/<i>c</i> (14)</i>	solid-state reaction
2020 <sup>[63]</sup>	RE <sub>2</sub> I(CN <sub>2</sub> )N RE = La, Gd	<i>Cmmm</i> (64)	SSM reaction

**Table 4.** Pseudoternary NCN compounds containing two different cations.

Year of discovery	Molecular formula	Space group	Synthetic route
1978 <sup>[69]</sup>	NaH(CN <sub>2</sub> )	<i>Pbcm</i> (57)	reaction in ethanol
1995 <sup>[24a]</sup>	NaIn(CN <sub>2</sub> ) <sub>2</sub>	<i>Cmcm</i> (63)	solid-state reaction
1998 <sup>[70]</sup>	Na <sub>5</sub> H(CN <sub>2</sub> ) <sub>3</sub>	<i>Im</i> $\bar{3}$ <i>m</i> (229)	decomposition
1998 <sup>[71]</sup>	K <sub>5</sub> H(CN <sub>2</sub> ) <sub>3</sub>	<i>Im</i> $\bar{3}$ <i>m</i> (229)	liquid ammonia
1999 <sup>[32]</sup>	RbH(CN <sub>2</sub> )	<i>P2<sub>1</sub><i>2</i><sub>1</sub> (19)</i>	liquid ammonia
2005 <sup>[72]</sup>	(NH <sub>4</sub> )H(CN <sub>2</sub> )	<i>P2<sub>1</sub><i>2</i><sub>1</sub> (19)</i>	liquid ammonia
2007 <sup>[73]</sup>	MH <sub>2</sub> (CN <sub>2</sub> ) <sub>2</sub> M = Co, Ni	<i>Pnmm</i>	aqueous solution
2011 <sup>[74]</sup>	M = Fe	<i>Pnmm</i>	
2009 <sup>[29]</sup>	LiM(CN <sub>2</sub> ) <sub>2</sub> M = La, Ce	<i>P2<sub>1</sub>/<i>m</i> (11)</i>	SSM reaction
2012 <sup>[75]</sup>	LiY(CN <sub>2</sub> ) <sub>2</sub>		SSM reaction
2015 <sup>[76]</sup>	LiM(CN <sub>2</sub> ) <sub>2</sub> M = Yb, Al, In	<i>Pbcn</i> (60)	
2017 <sup>[77]</sup>	SrZn(CN <sub>2</sub> ) <sub>2</sub>	<i>Cmcm</i> (63)	SSM reaction
2018 <sup>[78]</sup>	BaZn(CN <sub>2</sub> ) <sub>2</sub>	<i>Pbca</i> (61)	
2018 <sup>[79]</sup>	A <sub>2</sub> Sn(CN <sub>2</sub> ) <sub>3</sub> A = Li, Na	<i>Pnna</i> (52)	SSM reaction
2018 <sup>[24d]</sup>	Li <sub>2</sub> M(CN <sub>2</sub> ) <sub>3</sub> M = Zr, Hf	<i>R</i> $\bar{3}$ <i>c</i> (167)	SSM reaction
2020 <sup>[80]</sup>	NaSc(CN <sub>2</sub> ) <sub>2</sub>	<i>Pbcn</i> (60)	SSM reaction

## 1. Introduction

**Table 5.** Pseudoquaternary NCN compounds containing three different cations.

Year of discovery	Molecular formula	Space group	Synthetic route
2008 <sup>[81]</sup>	$KRE[Si(CN_2)_4]$ $RE = La-Gd$ (except Pm, Eu)	$P2_12_12$ (18)	SSM reaction
2016 <sup>[27d]</sup>	$RE = Eu$		
2008 <sup>[81]</sup>	$RbRE[Si(CN_2)_4]$ $RE = La-Gd$ (except Pm, Eu)	$\bar{I}4$ (82)	SSM reaction
2010 <sup>[82]</sup>	$RE = Y, Tb-Lu$		
2010 <sup>[82]</sup>	$CsRE[Si(CN_2)_4]$ $RE = Y, La-Lu$ (except Pm, Eu)	$\bar{I}4$ (82)	SSM reaction
2011 <sup>[83]</sup>	$LiM_2[Al(CN_2)_4]$ $M = Sr, Eu$	$C2/c$ (15)	SSM reaction
2013 <sup>[84]</sup>	$LiBa_2[Al(CN_2)_4]$	$P2_12_12_1$ (19)	SSM reaction
2013 <sup>[85]</sup>	$Li_2Gd_2Sr(CN_2)_5$	$C2/m$ (12)	SSM reaction
2013 <sup>[86]</sup>	$RbRE[Ge(CN_2)_4]$ $RE = La, Pr, Nd, Gd$	$\bar{I}4$ (82)	SSM reaction
2013 <sup>[87]</sup>	$LiSr_2[Ga(CN_2)_4]$	$C2/c$ (15)	SSM reaction
2017 <sup>[88]</sup>	$KRE[Ge(CN_2)_4]$ $RE = La-Gd$ (except Pm)	$P2_12_12$ (18)	SSM reaction
2017 <sup>[88]</sup>	$CsRE[Ge(CN_2)_4]$ $RE = La-Gd$ (except Pm)	$\bar{I}4$ (82)	SSM reaction
2019 <sup>[89]</sup>	$A_2MnSn_2(CN_2)_6$ $A = Li, Na$	$P\bar{3}1m$ (162)	SSM reaction
2021 <sup>[90]</sup>	$Li_2MgSn_2(CN_2)_6$		

**Table 6.** Pseudoquaternary NCN compounds containing two different cations and one additional anion.

Year of discovery	Molecular formula	Space group	Synthetic route
1996 <sup>[91]</sup>	$Ba_2Na(CN_2)(CN)_3$	$Fd\bar{3}m$ (227)	melamine route
2004 <sup>[92]</sup>	$LiEu_2(CN_2)I_3$	$Fd\bar{3}m$ (227)	azide-cyanide
2004 <sup>[93]</sup>	$LiSr_2(CN_2)I_3$		
2004 <sup>[92]</sup>	$LiEu_4(CN_2)_3I_3$	$P6_3/mmc$ (194)	azide-cyanide
2005 <sup>[94]</sup>	$LiM_2(CN_2)Br_3$ $M = Sr, Eu$	$Fd\bar{3}m$ (227)	azide-cyanide
2005 <sup>[95]</sup>	$Sr_4GaN_3(CN_2)$	$P2_1/c$ (14)	solid-state reaction
2006 <sup>[96]</sup>	$In_{0.08}Eu_4(CN_2)_3I_3$	$P6_3/mmc$ (194)	azide-cyanide
	$Eu_8I_9(CN)(CN_2)_3$	$P3m1$ (156)	
	$In_{0.28}Eu_{12}(CN_2)_5I_{14.91}$	$R\bar{3}m$ (166)	
2007 <sup>[97]</sup>	$(Sr_6N)(CoN_2)(CN_2)_2$	$P2_12_12$ (18)	solid-state reaction
2009 <sup>[98]</sup>	$(Sr_6N)(FeN_2)(CN_2)_2$	$P2_12_12$ (18)	
2020 <sup>[99]</sup>	$(Sr_6N)(CuN_2)(CN_2)_2$	$P2_1/c$ (14)	
2009 <sup>[55]</sup>	$LiRE_2F_3(CN_2)_2$ $RE = Ce-Gd$ (except Pm)	$C2/c$ (15)	SSM reaction

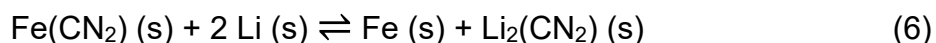
## 1. Introduction

<b>2012</b> <sup>[37]</sup>	LaSr <sub>3</sub> F <sub>5</sub> (CN <sub>2</sub> ) <sub>2</sub>	$\bar{I}42m$ (121)	SSM reaction
<b>2014</b> <sup>[100]</sup>	Ba <sub>4</sub> MgF <sub>2</sub> (CN <sub>2</sub> ) <sub>4</sub>	$P2_1/c$ (14)	SSM reaction
<b>2017</b> <sup>[101]</sup>	APb <sub>2</sub> Cl <sub>3</sub> (CN <sub>2</sub> ) A = Li, Na, Ag	$Fd\bar{3}m$ (227)	SSM reaction
<b>2017</b> <sup>[101]</sup>	LiPbCl(CN <sub>2</sub> )	$P2_1/m$ (11)	SSM reaction
<b>2019</b> <sup>[102]</sup>	K <sub>12</sub> Pb <sub>51</sub> (CN <sub>2</sub> ) <sub>30</sub> Cl <sub>54</sub>	$R\bar{3}m$ (166)	SSM reaction
<b>2021</b> <sup>[61]</sup>	LiSn <sub>2</sub> Br <sub>3</sub> (CN <sub>2</sub> )	$Fd\bar{3}m$ (227)	SSM reaction

**Table 7.** Other, more complex NCN compounds.

Year of discovery	Molecular formula	Space group	Synthetic route
<b>2011</b> <sup>[56]</sup>	Eu <sub>3</sub> [AlF <sub>2</sub> (CN <sub>2</sub> ) <sub>3</sub> (CN)]	$Pnma$ (62)	SSM reaction
<b>2013</b> <sup>[103]</sup>	CaBa <sub>8</sub> (CN <sub>2</sub> ) <sub>6</sub> O <sub>2</sub> (N <sub>0.5</sub> H <sub>0.5</sub> )	$R\bar{3}$ (148)	solid-state reaction
<b>2021</b> <sup>[15]</sup>	Pb <sub>14.66</sub> Sn <sub>7.34</sub> Br <sub>26</sub> (CN <sub>2</sub> ) <sub>7</sub> O <sub>2</sub>	$C2/m$ (12)	solid-state reaction

Transition metal dinitridocarbonates of the 3d series were reported to have several interesting properties, such as ferromagnetic behavior and a high resistivity against both acids and bases for Cr<sub>2</sub>(CN<sub>2</sub>)<sub>3</sub><sup>[25f, 44]</sup> and antiferromagnetic behavior for Mn(CN<sub>2</sub>)<sup>[25c]</sup>. In recent years several of those transition metal carbodiimides, such as Fe(CN<sub>2</sub>), Mn(CN<sub>2</sub>), Cr<sub>2</sub>(CN<sub>2</sub>)<sub>3</sub>, and Zn(CN<sub>2</sub>), were investigated for their potential use as anode materials in lithium- or sodium-ion batteries.<sup>[104]</sup> An equation of the conversion reaction of Fe(CN<sub>2</sub>) and Li is shown in reaction (6).<sup>[104b]</sup>



The compounds Ag<sub>2</sub>(CN<sub>2</sub>), Mn(CN<sub>2</sub>), and Bi<sub>2</sub>O<sub>2</sub>(CN<sub>2</sub>) have recently been investigated for photoelectrochemical (PEC) water oxidation and shown to improve the efficiency of CuWO<sub>4</sub> and WO<sub>3</sub> (tested with Bi<sub>2</sub>O<sub>2</sub>(CN<sub>2</sub>) only) photoanodes.<sup>[105]</sup> Silver cyanamide has furthermore been shown to be an effective photocatalyst for the reduction of CO<sub>2</sub> into CH<sub>4</sub>.<sup>[106]</sup>



### 1.3 Tin compounds

Many tin compounds are semiconductors, offering various applications for optical and electronic devices. Semiconductors are used in diodes, a simple electronic component in which the electric current can flow only in one direction while being blocked in the other, which is most commonly used for rectification. In addition to rectification, many other applications for diodes are known. Another important application of semiconductors is the conversion of light into electricity, which is used in photocatalysis, photodiodes, and solar cells. In addition, semiconductors can also be used to convert electricity into light, used for scintillators, light-emitting diodes, or lasers. Semiconductors are also essential for one of the most essential electronic devices, the transistor.<sup>[107]</sup>

The most prominent tin compounds are the tin oxides SnO and SnO<sub>2</sub>, representing both oxidation states that tin normally adopts (II and IV). SnO<sub>2</sub> occurs at standard pressure in two different modifications (tetragonal<sup>[108]</sup> and orthorhombic<sup>[109]</sup>) and, as a naturally occurring mineral cassiterite, it is one of the main tin ores<sup>[110]</sup>. Tin(IV) oxide is an n-type semiconductor with a direct band gap of 3.6 eV and belongs to the group of transparent conducting oxides.<sup>[111]</sup>

The main application of SnO<sub>2</sub> is its use for gas sensing since the electrical conductivity of SnO<sub>2</sub> is very sensitive to gas molecules adsorbed on its surface, such as CO,<sup>[112]</sup> O<sub>2</sub>,<sup>[113]</sup> NO<sub>2</sub>,<sup>[114]</sup> or H<sub>2</sub>S<sup>[115]</sup>. Another interesting application of SnO<sub>2</sub> is its potential use as anode material in Li- or Na-ion batteries.<sup>[116]</sup> Furthermore, tin dioxide is applied in perovskite solar cells (PSCs), (as will be discussed in more detail later), where it is used as the electron transport layer.<sup>[117]</sup> Additionally, SnO<sub>2</sub> is applied in optical sensors,<sup>[118]</sup> photoconductors,<sup>[119]</sup> and photocatalysis<sup>[120]</sup>.

To improve the properties of materials, doping can generally be used, as in the case of fluorine-doped tin oxide, which is used in many optoelectronic devices,<sup>[121]</sup> similarly to the even more common indium tin oxide that uses SnO<sub>2</sub> as dopant<sup>[122]</sup>.

Tin(II) oxide, SnO, crystallizes in two different modifications at standard pressure: as a tetragonal, black modification<sup>[123]</sup> and as a red orthorhombic modification, characterized recently<sup>[124]</sup>. SnO is a p-type semiconductor with an indirect band gap of 0.7 eV and a direct band gap of 2.7 eV.<sup>[125]</sup> SnO is investigated as a promising thin film transistor that can be used in displays.<sup>[126]</sup> Further application possibilities for SnO are electrocatalysis,<sup>[127]</sup> as anode material in Li-<sup>[128]</sup> or Na-ion<sup>[129]</sup> batteries or as a gas sensor<sup>[130]</sup>.

Besides tin(II) and tin(IV) oxide, several mixed valent tin oxides are reported in the literature, like  $\text{Sn}_2\text{O}_3$ ,  $\text{Sn}_3\text{O}_4$ ,  $\text{Sn}_4\text{O}_5$ , or  $\text{Sn}_5\text{O}_6$ .<sup>[131]</sup> However, only for  $\text{Sn}_3\text{O}_4$ , a crystal structure is available in the crystallographic databases<sup>[132]</sup>. The existence of this compound is not fully established, since the crystal structure was only determined by electron diffraction.

Apart from the important tin oxides, some tin chalcogenides of the elements S–Te should be mentioned here.  $\text{SnS}$ ,  $\text{SnS}_2$ , and  $\text{Sn}_2\text{S}_3$  are known tin sulfides.<sup>[133]</sup>  $\text{SnS}$  (orthorhombic modification) and  $\text{SnS}_2$  form both layered arrangements and are semiconductors with indirect band gaps of 1.8<sup>[134]</sup> and 2.2 eV<sup>[133b]</sup>, respectively.  $\text{SnS}$  is investigated as an anode material for Li-ion batteries,<sup>[135]</sup> for solar cell applications,<sup>[136]</sup> and for photocatalytic water splitting<sup>[137]</sup>. Tin(IV) sulfide is (besides its use as pigment) investigated as an anode material for Li-ion batteries<sup>[138]</sup> and for photochemical water oxidation<sup>[139]</sup>. Other tin chalcogenides such as  $\text{SnSe}$ ,  $\text{SnTe}$ , and  $\text{SnSe}_2$  are potential thermoelectric materials.<sup>[140]</sup> Moreover, for  $\text{SnSe}_2$  many applications are possible, including photoelectric detectors, nonlinear optics, IR photoelectric devices, and ultrafast photonics.<sup>[141]</sup>

To replace fossil fuels, intensive research is being conducted on solar cells to make them more efficient, more durable, less expensive, and less toxic. An alternative to conventional silicon solar cells is the PSC. In this type of solar cells, perovskite-structured halides are used as light absorbers,<sup>[142]</sup> and power conversion efficiencies of about 25 % for conventional PSCs,<sup>[143]</sup> and nearly 30 % for a perovskite/silicon tandem solar cell<sup>[144]</sup> have been reported. Most of the investigated compounds are organic-inorganic hybrid compounds like  $\text{MAPbI}_3$  with  $\text{MA}$  = methylammonium ( $[\text{CH}_3\text{NH}_3]^+$ ) or  $\text{FAPbI}_3$  with  $\text{FA}$  = formamidinium ( $[\text{CH}(\text{NH}_2)_2]^+$ ) and suffer from low thermal stability and toxicity.<sup>[145]</sup> Hence, many efforts are being made to overcome these problems, which may become possible with fully inorganic tin PSCs.<sup>[146]</sup>

In such compounds, the toxic lead is substituted by tin, the organic cation is substituted by Cs or Rb, like in  $\text{Rb}_y\text{Cs}_{1-y}\text{Sn}(\text{Br}_x\text{I}_{1-x})_3$ . However, compounds such as  $\text{CsSnI}_3$  suffer from oxidation of  $\text{Sn}^{2+}$ , leading to conversion to tin(IV) compounds like  $\text{Cs}_2\text{SnI}_6$ , which is a weakly light-absorbing material.<sup>[147]</sup>

## 1. Introduction

---

Inorganic tin compounds offer a variety of properties and applications, which can also be expected for tin dinitridocarbonates. Thanks to the work of Dr. Konstantin Dolabdjian, the first important tin dinitridocarbonates were synthesized. These are the two divalent compounds  $\text{Sn}_2\text{O}(\text{CN}_2)^{[60]}$  and  $\text{Sn}(\text{CN}_2)^{[39]}$  as well as two tetravalent compounds,  $\text{A}_2\text{Sn}(\text{CN}_2)_3$  ( $\text{A} = \text{Li}$  and  $\text{Na}$ )<sup>[79]</sup>.



## **2. Objective**

## 2. Objective

---

In times of resource scarcity, environmental destruction, and the pursuit of ever more technological progress, research is striving to find solutions to these problems, for example, by finding energy-efficient, simple, and cheap light sources or more efficient batteries for the rapidly growing e-mobility sector or new drive systems. The need for more efficient solar cells, for example, is also crucial in the field of renewable energies. For this purpose, known materials can be modified, and thus their properties adjusted, or the application itself can be developed more efficiently. Another approach is the synthesis and characterization of new materials, especially in groups of materials that have not yet been studied on a large scale. Hence, this work aimed to synthesize new compounds in the field of dinitridocarbonates and investigate their properties. These compounds have some advantages compared to related compounds such as oxides or nitrides with respect to chemical and thermal stability. Furthermore, new materials can be synthesized within the field of metal dinitridocarbonates, which is only possible to a very limited extent in the area of oxides or nitrides. Moreover, interesting properties of metal dinitridocarbonates have repeatedly emerged. It has been shown that inorganic tin compounds such as SnO, which is a semiconductor, have very fascinating properties that offer a wide range of applications, especially in the field of optoelectronics. Dinitridocarbonates are pseudo-chalcogenides and usually exhibit similar properties to their corresponding oxides. In recent decades, the diversity of metal dinitridocarbonates has been demonstrated, and SSM reactions have proven to be a valuable tool for the synthesis of such compounds.

### **3. Summary of the Main Results**

### 3.1 Tin carbodiimide and tin chloride carbodiimide (Publ. 1)<sup>[24d]</sup>

Due to preliminary work in the field of tin and NCN compounds that was conducted in our group, it was possible to continue and expand this research area.

The first reported tin carbodiimide compound  $\text{Sn}_2\text{O}(\text{CN}_2)$  was obtained as a side phase from the reaction of  $\text{SnCl}_2$  and  $\text{Li}_2(\text{CN}_2)$  by Dr. Dolabdjian.<sup>[60]</sup> The formation of brownish single crystals (attached to the ampule) already showed the tendency of this compound to be formed, even if no oxide phase is used in the reaction. This affinity of  $\text{SnCl}_2$  (and  $\text{Li}_2(\text{CN}_2)$ ) to form  $\text{Sn}_2\text{O}(\text{CN}_2)$  in the presence of oxygen was demonstrated, applying different metal oxides (such as  $\text{NiO}$ ,  $\text{FeO}$ , or  $\text{PtO}$ ) in the reaction with  $\text{SnCl}_2$  and  $\text{Li}_2(\text{CN}_2)$ , which always led to the formation of  $\text{Sn}_2\text{O}(\text{CN}_2)$ . Later, phase-pure tin oxide carbodiimide could be obtained by appropriate amounts of  $\text{SnCl}_2$ ,  $\text{Li}_2(\text{CN}_2)$ , and  $\text{SnO}$ .

Tin carbodiimide,  $\text{Sn}(\text{CN}_2)$ , was first obtained as a brownish powder from the reaction of  $\text{SnCl}_2$  and  $\text{Li}_2(\text{CN}_2)$ , contaminated with  $\text{Sn}_2\text{O}(\text{CN}_2)$ , elemental tin, and some unidentified side phases. Further attempts to synthesize a phase-pure sample of  $\text{Sn}(\text{CN}_2)$  failed. In order to have a more reliable Rietveld refinement (with only known phases), a reaction of equimolar amounts of  $\text{SnF}_2$  and  $\text{Li}_2(\text{CN}_2)$  was performed, using an arc-welded niobium container. The crystal structure of  $\text{Sn}(\text{CN}_2)$  could then be refined with two different side phases (elemental tin and  $\text{LiF}$ ). It crystallizes in the monoclinic space group  $I2/a$ , chosen due to the large monoclinic angle in the standard-setting  $C2/c$ . The crystal structure of  $\text{Sn}(\text{CN}_2)$  can be derived from the structure of tetragonal calcium carbide and of that of orthorhombic  $\text{FeS}_2$  (marcasite), as depicted in Figure 3. Here, the  $\text{C}_2^{2-}$  ions of  $\text{CaC}_2$  are tilted within the projection plane to the arrangement of  $\text{S}_2^{2-}$  ions in  $\text{FeS}_2$ . In the final  $\text{Sn}(\text{CN}_2)$  structure, the  $\text{NCN}^{2-}$  ions are tilted further out of the projection plane, resulting in a fourfold coordination environment, instead of sixfold, as in  $\text{CaC}_2$  and  $\text{FeS}_2$ .

The overall crystal structure of monoclinic  $\text{Sn}(\text{CN}_2)$  can be seen in Figure 4, where layers of metal atoms alternate with tilted layers of carbodiimide ions, forming a network-like structure. In order to get further insights into the electronic structure of  $\text{Sn}(\text{CN}_2)$ , the electron localization function (ELF) was calculated. When looking at the fourfold coordinated tin atom in  $\text{Sn}(\text{CN}_2)$ , it seems obvious that the  $\text{Sn}^{2+}$  lone pair is located somewhere above the  $\text{NCN}$  ions, as highlighted by a red asterisk in Figure 5a. Interestingly, the tin lone pair is distributed in a ring-shaped cloud (comparable to a



### 3. Summary of the Main Results

donut) around the Sn atom, as displayed in Figure 5b, showing electron delocalization that indicates covalent bonding.

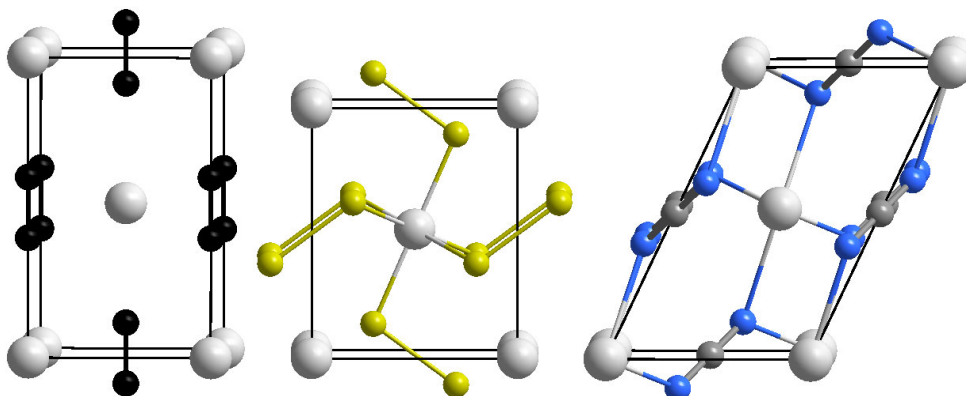


**Figure 3.** Comparison of the crystal structure of  $\text{Sn}(\text{CN}_2)$  with the structures of  $\text{CaC}_2$  (left) and  $\text{FeS}_2$ . Metals are shown in light gray, C in black, S in yellow, the  $\text{CN}_2$  units are displayed in dark gray (C) and blue (N).

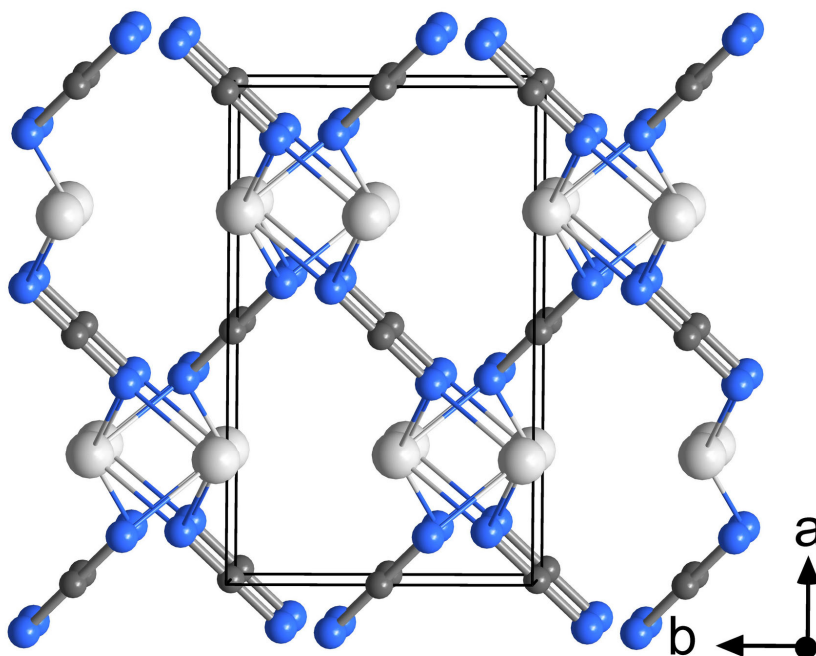


**Figure 4.** Perspective view of the  $ac$  plane of the structure of  $\text{Sn}(\text{CN}_2)$ .

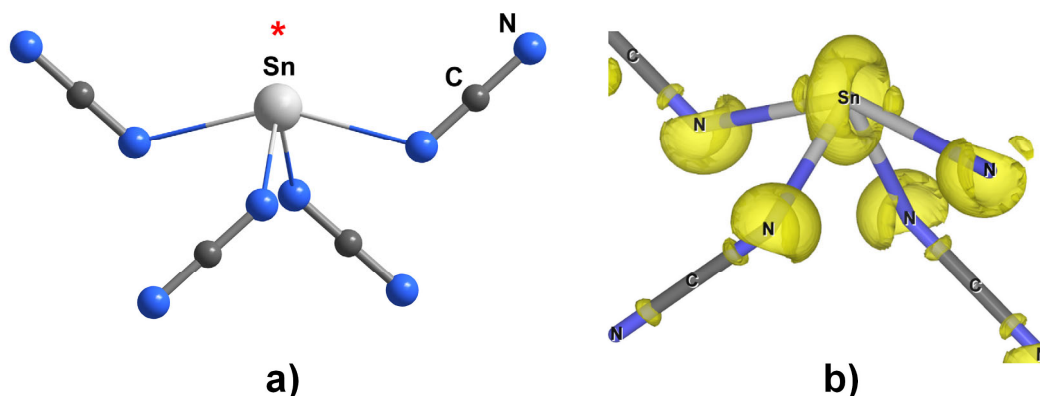
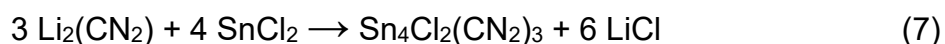


**Figure 5.** a) Coordination environment of tin in  $\text{Sn}(\text{CN}_2)$ . The red asterisk indicates the presumed position of the tin lone pair. b) A section of the ELF of  $\text{Sn}(\text{CN}_2)$  is shown as an isosurface at the 0.7 level.

In an attempt to optimize the synthesis of  $\text{Sn}(\text{CN}_2)$  by varying the reaction temperature, some unknown reflections appeared in the powder X-ray diffraction (PXRD) patterns at lower temperatures. Further investigations and variations of the used stoichiometries to 1:2 ( $\text{Li}_2(\text{CN}_2)$  to  $\text{SnCl}_2$ ) did not make these reflections disappear even at higher temperatures (as is the case with a 1 to 1 ratio). Appropriately long dwell times of the reaction mixtures at temperatures of around 350–400 °C and cooling rates of 0.1 K/min, resulted in transparent, platelet-shaped single crystals that were characterized as  $\text{Sn}_4\text{Cl}_2(\text{CN}_2)_3$ . Thermoanalytic studies of equimolar mixtures of  $\text{Li}_2(\text{CN}_2)$  and  $\text{SnCl}_2$  showed that  $\text{Sn}_4\text{Cl}_2(\text{CN}_2)_3$  is already formed slightly below 200 °C and transforms slowly into  $\text{Sn}(\text{CN}_2)$  during heating, without any detectable thermal effect (starting at around 300 °C).

Noteworthy,  $\text{Sn}_4\text{Cl}_2(\text{CN}_2)_3$  is also formed in the synthesis of  $\text{Sn}_2\text{O}(\text{CN}_2)$  at similarly low temperatures.

Phase-pure samples of  $\text{Sn}_4\text{Cl}_2(\text{CN}_2)_3$  (according to PXRD measurements) were obtained when heating a 3:4 molar mixture of  $\text{Li}_2(\text{CN}_2)$  and  $\text{SnCl}_2$  to 250 °C, in accordance with reaction (7).



The phase-pure  $\text{Sn}_4\text{Cl}_2(\text{CN}_2)_3$  remains stable up to 550 °C, which corresponds to a temperature range of 350 °C (from formation to decomposition). This is significantly more than for  $\text{Sn}(\text{CN}_2)$  or  $\text{Sn}_2\text{O}(\text{CN}_2)$ , which decompose about 100 to 150 °C after their formation. A DTA of reaction (7), revealing the exothermic formation of  $\text{Sn}_4\text{Cl}_2(\text{CN}_2)_3$  below 200 °C, also showed an endothermic effect upon heating and an exothermic effect upon cooling, that were assigned to be melting and recrystallization of  $\text{Sn}_4\text{Cl}_2(\text{CN}_2)_3$  and  $\text{LiCl}$  as depicted in Figure 6.

### 3. Summary of the Main Results

In contrast to the crystal structure of  $\text{Sn}(\text{CN}_2)$ , two distinct coordination environments of the carbodiimide ions are present in  $\text{Sn}_4\text{Cl}_2(\text{CN}_2)_3$ . One is planar coordinated and the other pseudotetrahedral. Tin is in a distorted trigonal prismatic coordination, surrounded by three Cl and three NCN ions. The overall crystal structure of  $\text{Sn}_4\text{Cl}_2(\text{CN}_2)_3$  is characterized by layers of tin alternating with mixed layers of NCN and Cl ions (see Figure 7). As already shown with  $\text{SnO}$ , tin compounds can have interesting electronic properties. These were investigated in more detail using DFT calculations. These calculations revealed both compounds to be semiconductors with indirect band gaps on the order of 1 eV ( $\text{Sn}(\text{CN}_2)$ ) and 2 eV ( $\text{Sn}_4\text{Cl}_2(\text{CN}_2)_3$ ), as confirmed by optical reflection measurements.

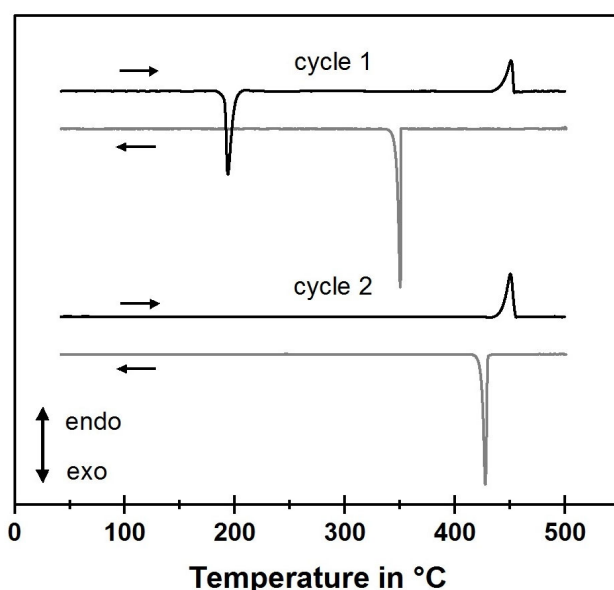


**Figure 6.** DTA of a 3:4 molar mixture of  $\text{Li}_2(\text{CN}_2)$  and  $\text{SnCl}_2$  performed from room temperature to 500 °C with two heating/cooling cycles.

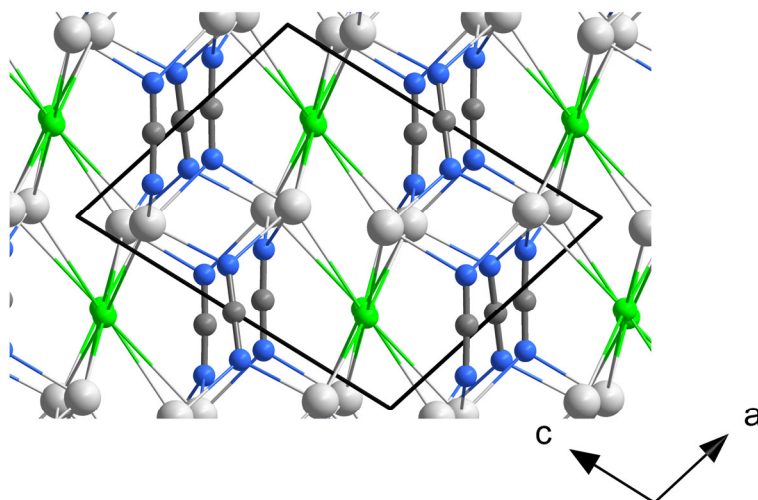


**Figure 7.** Section of the crystal structure of  $\text{Sn}_4\text{Cl}_2(\text{CN}_2)_3$ , showing the view along the *ac* plane. Tin is shown in light gray, chlorine in green, carbon in dark gray, and nitrogen in blue.

### 3.2 $\text{Sn}_9\text{O}_5\text{Cl}_4(\text{CN}_2)_2$ (Publ. 2)<sup>[67]</sup>

The reaction pathway of the first discovered tin carbodiimide  $\text{Sn}_2\text{O}(\text{CN}_2)$ , obtained from appropriate mixtures of  $\text{Li}_2(\text{CN}_2)$ ,  $\text{Na}_2\text{O}$ , and  $\text{SnCl}_2$ , was not fully elucidated when its synthesis and some properties were reported.<sup>[60]</sup> Thermal analysis (DTA) of a 1:1:2 molar mixture of  $\text{Li}_2(\text{CN}_2)$ ,  $\text{Na}_2\text{O}$ , and  $\text{SnCl}_2$  showed two exothermic effects and one endothermic effect upon heating, as illustrated in Figure 8. The first exothermic effect (1) could be assigned to the formation of  $\text{Sn}_4\text{Cl}_2(\text{CN}_2)_3$ , which forms, as in the synthesis of  $\text{Sn}(\text{CN}_2)$  at low temperatures ( $<200\text{ }^\circ\text{C}$ ) and transforms later into the target compound,  $\text{Sn}_2\text{O}(\text{CN}_2)$ . However, the second exothermic effect, which appeared upon heating at  $300\text{ }^\circ\text{C}$  (2), could not be assigned to the formation of  $\text{Sn}_2\text{O}(\text{CN}_2)$ ; instead, some unknown phase appeared in the PXRD pattern (recorded from reactions performed at  $300\text{ }^\circ\text{C}$ ).

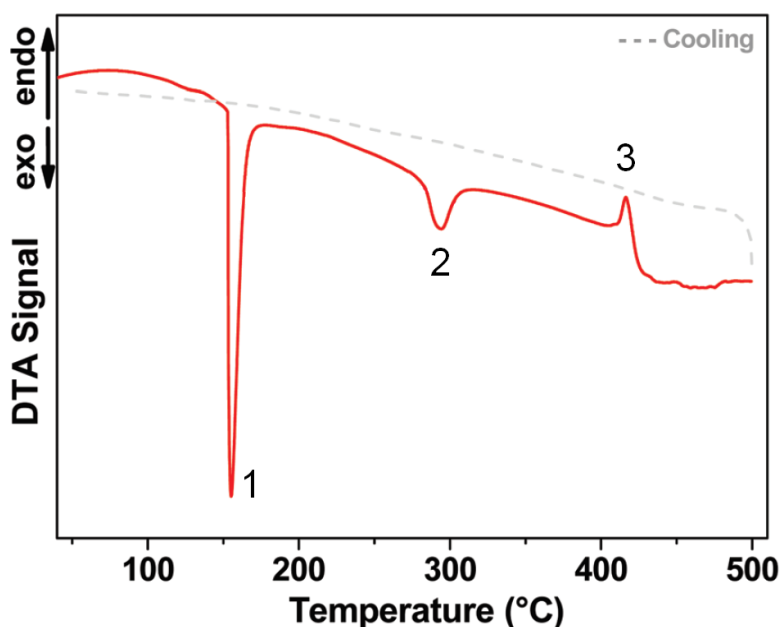


**Figure 8.** DTA of a 1:1:2 molar mixture of  $\text{Li}_2(\text{CN}_2)$ ,  $\text{Na}_2\text{O}$ , and  $\text{SnCl}_2$ . Reprinted (adapted) with permission from<sup>[60]</sup>. Copyright 2018 The Royal Society of Chemistry.

During heating, this unknown phase transforms into  $\text{Sn}_2\text{O}(\text{CN}_2)$ , to which the third (endothermic) effect at around  $420\text{ }^\circ\text{C}$  is attributed. When different molar mixtures of  $\text{Li}_2(\text{CN}_2)$ ,  $\text{SnO}$ , and  $\text{SnCl}_2$  were employed, this compound could finally be obtained at higher temperatures without transforming into  $\text{Sn}_2\text{O}(\text{CN}_2)$ . A phase-pure powder pattern of this unknown phase (additional  $\text{LiCl}$  was washed out with ethanol) could then be indexed and refined, revealing this unknown phase to have the composition  $\text{Sn}_9\text{O}_5\text{Cl}_4(\text{CN}_2)_2$ . It is obtained as a beige crystalline powder and crystallizes in the orthorhombic space group  $C222_1$ . The compound is stable up to  $450\text{ }^\circ\text{C}$  (less than

$\text{Sn}_2\text{O}(\text{CN}_2)$ ) and could be treated in air. Its crystal structure consists of the unique motif of a  $[\text{Sn}_8\text{O}_3]$  cluster, in which the tin atoms are organized in a hexagonal bipyramid, as depicted in Figure 9.

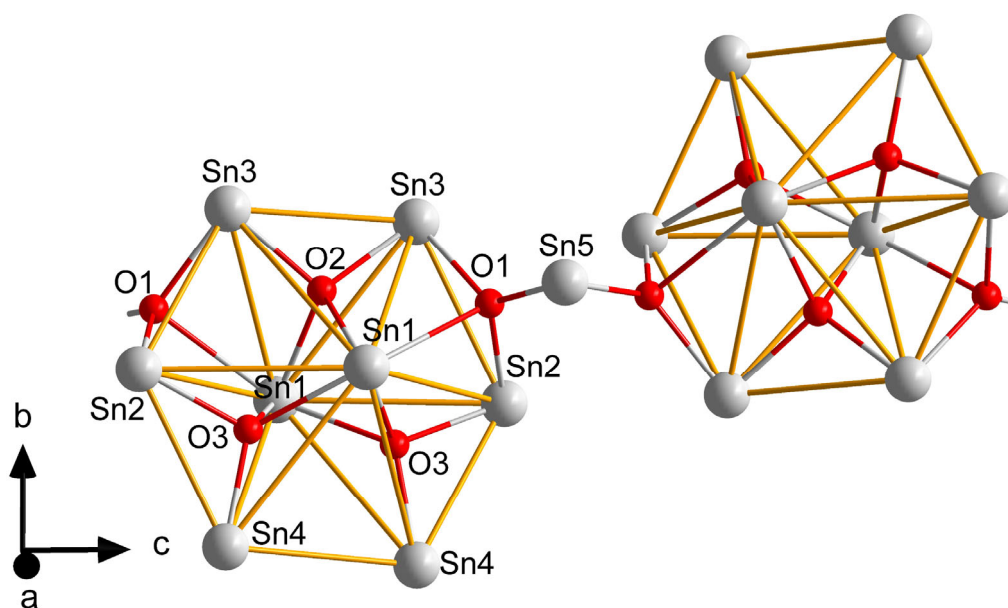


**Figure 9.** View of two crystallographically identical  $[\text{Sn}_8\text{O}_3]$  clusters, forming the motif of a hexagonal bipyramid. Note that the orange lines between the tin atoms are only meant to indicate the geometric figure, but do not represent real bonds.

The bond distances of the six in-plane tin atoms (Sn2, Sn3, Sn4) range from 3.36 to 3.89 Å and are too long to be considered genuine bonds. However, the distance between the tin atoms located at the two tips of the hexagonal bipyramid (Sn1) is shorter (3.17 Å). The bonding situation of tin atoms will be discussed in more detail later. The three oxygen atoms of the  $[\text{Sn}_8\text{O}_3]$  cluster (O2, O3) are tetrahedrally coordinated by Sn, as are the two additional oxygen atoms (O1), located on the outer sides of the hexagonal bipyramid, connecting the  $[\text{Sn}_8\text{O}_3]$  units to two other  $[\text{Sn}_8\text{O}_3]$  clusters via a bridging tin atom (Sn5). Those bonds are indicated in Figure 9. The hexagonal bipyramids form infinite chains along  $[001]$  by this linkage, as can be seen in Figure 10. The NCN ion is surrounded by four tin atoms and can be considered as carbodiimide, despite slight deviations in the C-N bond distances (1.25 and 1.29 Å). This was also confirmed by IR measurements. The bonding between Cl and Sn is not displayed in Figure 10 for clarity. The NCN units link the  $[\text{Sn}_8\text{O}_3]$  clusters and are slightly tilted out of the  $[100]$  direction.

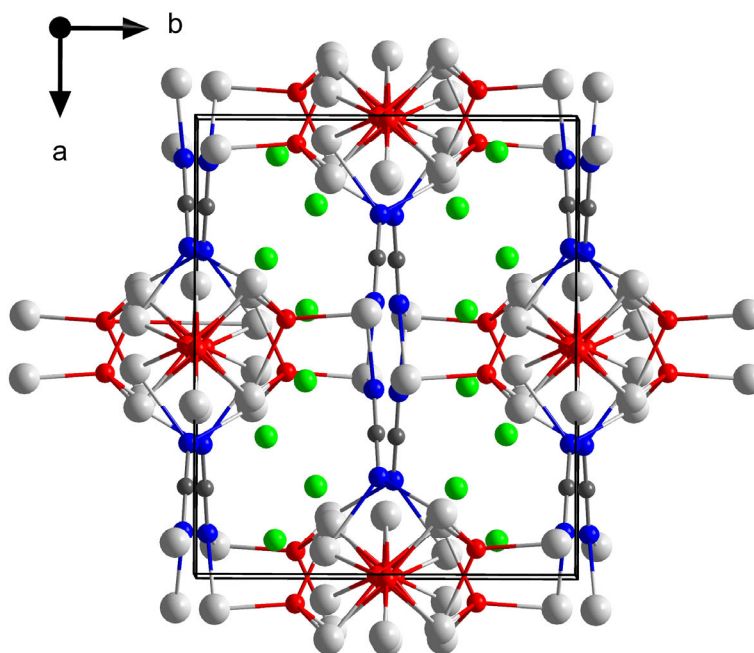


**Figure 10.** Perspective view along *c*. Tin is shown in light gray, oxygen in red, carbon in dark gray, nitrogen in blue, and chlorine in green.

As for the previously reported tin carbodiimide compounds, the electronic structure of this compound was studied in more detail, using DFT calculations. The calculated band structure reveals  $\text{Sn}_9\text{O}_5\text{Cl}_4(\text{CN}_2)_2$  to be a semiconductor with an indirect band gap on the order of 2 eV (the optical band gap was determined to be on the order of 3 eV).

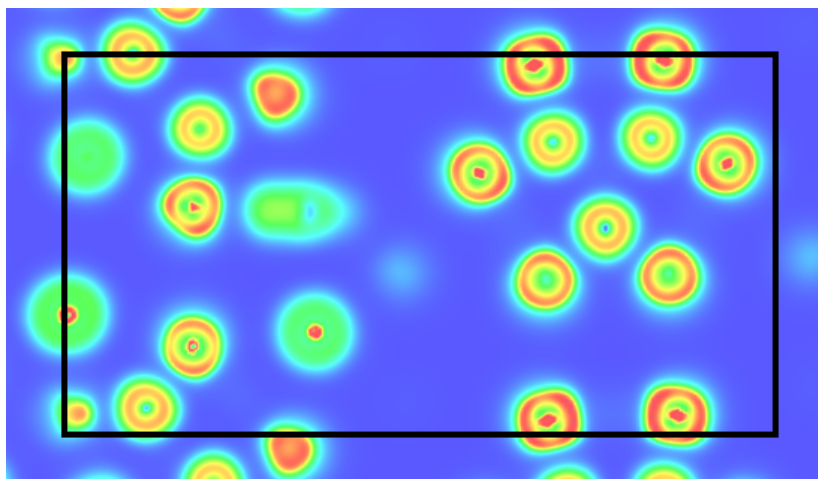


**Figure 11.** ELF of a section through the *bc* plane of the structure of  $\text{Sn}_9\text{O}_5\text{Cl}_4(\text{CN}_2)_2$ , showing the electronic structure of six tin atoms (upper-right corner) which are part of the hexagonal bipyramid, displayed in Figure 9. Additionally, three oxygen atoms are visible (inside the hexagon). Red color corresponds to a higher density of localized electrons, blue color corresponds to a lower density of localized electrons.

The ELF was calculated to further understand the electronic structure and the localization of the tin lone pair. Figure 11 indicates a section through the hexagonal bipyramid, depicted in the upper-right corner. It can be seen that the electron localization of the two lower tin atoms is more homogeneous than it is for the middle

### 3. Summary of the Main Results

---

and upper tin atoms, which supports a more ionic bonding nature (of the two lower ones) versus more covalent bonding nature between Sn and O (of the middle and upper ones), where the electron cloud is more distorted. However, no bonding between the tin atoms is indicated.

Since most tin carbodiimides remain stable for several days in air (except  $\text{Sn}(\text{CN}_2)$ ), tin Mössbauer spectroscopy measurements were performed to determine if  $\text{Sn}^{2+}$  is oxidized to  $\text{Sn}^{4+}$  during this air exposure. Hence, two different samples each of  $\text{Sn}_4\text{Cl}_2(\text{CN}_2)_3$ ,  $\text{Sn}_2\text{O}(\text{CN}_2)$ , and  $\text{Sn}_9\text{O}_5\text{Cl}_4(\text{CN}_2)_2$  were investigated. One sample that was kept in air for one day, and a sample that had no air contact. Interestingly, no obvious difference between those two differently treated samples of one compound could be determined. However, in samples of  $\text{Sn}_2\text{O}(\text{CN}_2)$  and  $\text{Sn}_9\text{O}_5\text{Cl}_4(\text{CN}_2)_2$ , tin(IV) could be detected, even in the samples without air contact (samples were stored and measured under argon). In contrast, both  $\text{Sn}_4\text{Cl}_2(\text{CN}_2)_3$  samples did not contain any  $\text{Sn}^{4+}$ . In order to trace the origin of this  $\text{Sn}^{4+}$  impurity, two different SnO samples (used to prepare the tin compounds and also stored under Ar) were analyzed by Mössbauer spectroscopy. Some tin(IV) was detected in both compounds, suggesting that the origin of the tin(IV) impurity in the two oxide-containing carbodiimides ( $\text{Sn}_2\text{O}(\text{CN}_2)$  and  $\text{Sn}_9\text{O}_5\text{Cl}_4(\text{CN}_2)_2$ ) was due to  $\text{Sn}^{4+}$  already present in the starting material SnO.

### 3.3 Sn<sub>2</sub>O(CN<sub>2</sub>) as photoanode (Publ. 3)<sup>[148]</sup>

Tin oxide carbodiimide appears as brownish crystals and (if phase-pure) as brick-red powder. It has been shown that this compound is stable in water and survives even temperatures of up to 400 °C in air (for at least 10 h). This chemical and thermal stability makes it an interesting candidate for further investigation of its properties. Band structure calculations, as well as optical reflection measurements, reveal Sn<sub>2</sub>O(CN<sub>2</sub>) to be a semiconductor with an indirect band gap of 1.6 eV and a direct band gap of 2 eV. Previous work on two other carbodiimide compounds, Ag<sub>2</sub>(CN<sub>2</sub>)<sup>[105a]</sup> and Mn(CN<sub>2</sub>)<sup>[105b]</sup> showed their potential as photoanodes for water splitting. Further investigation on the electronic properties showed that Sn<sub>2</sub>O(CN<sub>2</sub>) is an n-type semiconductor, similar to CuWO<sub>4</sub>. CuWO<sub>4</sub> has already been investigated as an effective photoanode for PEC water splitting in previous studies.<sup>[149]</sup> Hence, as for Ag<sub>2</sub>(CN<sub>2</sub>) and Mn(CN<sub>2</sub>), the effects of tin oxide carbodiimide on the photocatalytic water splitting efficiency of CuWO<sub>4</sub> was investigated. As illustrated in Figure 12, the photocurrent, generated by the mixed CuWO<sub>4</sub>/Sn<sub>2</sub>O(CN<sub>2</sub>) anode (60 μA·cm<sup>-2</sup>) is larger than the sum of the two individual ones. This photocurrent recorded with interrupted illumination remains constant over the tested period of 2 h.

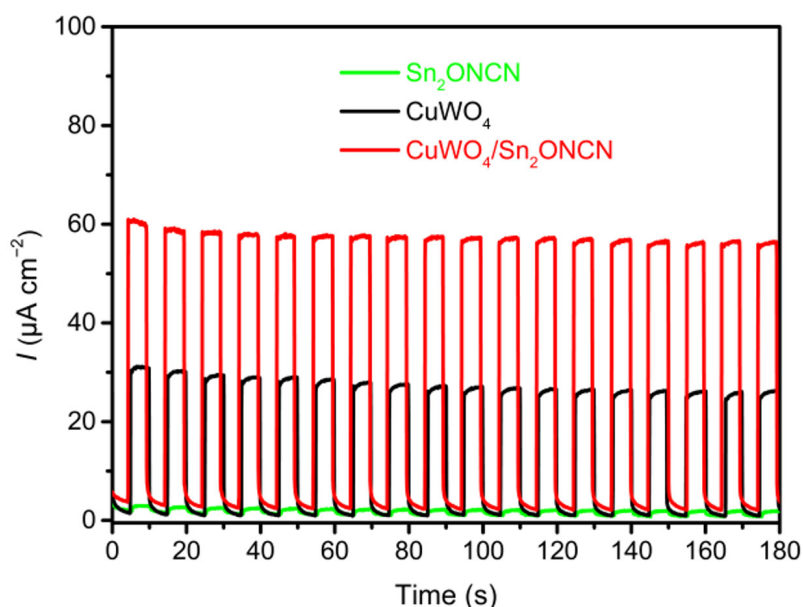


**Figure 12.** Chronoamperometry of Sn<sub>2</sub>O(CN<sub>2</sub>), CuWO<sub>4</sub>, and CuWO<sub>4</sub>/Sn<sub>2</sub>O(CN<sub>2</sub>) photoanodes. The measurements were performed at a constant voltage of 1.23 V vs. reversible hydrogen electrode under simulated illumination (100 mW·cm<sup>-2</sup>).

Recently, Sn<sub>2</sub>O(CN<sub>2</sub>) was investigated as anode material for Li-ion batteries and showed high capacity and cycling stability.<sup>[150]</sup>



### 3.4 Tin oxide halides (Publ. 4)<sup>[151]</sup>

In reactions with tin halides, tin(II) oxide, and lithium carbodiimide, which were employed to synthesize tin carbodiimide compounds, some peaks were observed in PXRD patterns at lower temperatures that could not be assigned to any known compounds. Experiments with only two of the three starting materials used in each case showed these unknown peaks in reactions with SnO and tin halides.

Further experiments with SnO and SnX<sub>2</sub> (X = Cl, Br, I) at longer reaction times and slow cooling rates led to the formation of colorless (SnCl<sub>2</sub>, SnBr<sub>2</sub>) and orange (SnI<sub>2</sub>) single crystals. The three hitherto unknown crystal structures of the compounds Sn<sub>7</sub>O<sub>4</sub>Cl<sub>6</sub>, Sn<sub>7</sub>O<sub>4</sub>Br<sub>6</sub>, and Sn<sub>4</sub>OI<sub>6</sub> could be determined from these crystals. All compounds are stable for several days under atmospheric conditions but decompose when in direct contact with water. Tin oxide chloride and tin oxide bromide both crystallize in the triclinic space group  $P\bar{1}$ , whereas tin oxide iodide crystallizes with a monoclinic lattice.

As a characteristic structural feature of both Sn<sub>7</sub>O<sub>4</sub>Cl<sub>6</sub> and Sn<sub>7</sub>O<sub>4</sub>Br<sub>6</sub>, a distorted, cubane-like [Sn<sub>4</sub>O<sub>4</sub>] unit can be emphasized, which forms a dimeric arrangement.

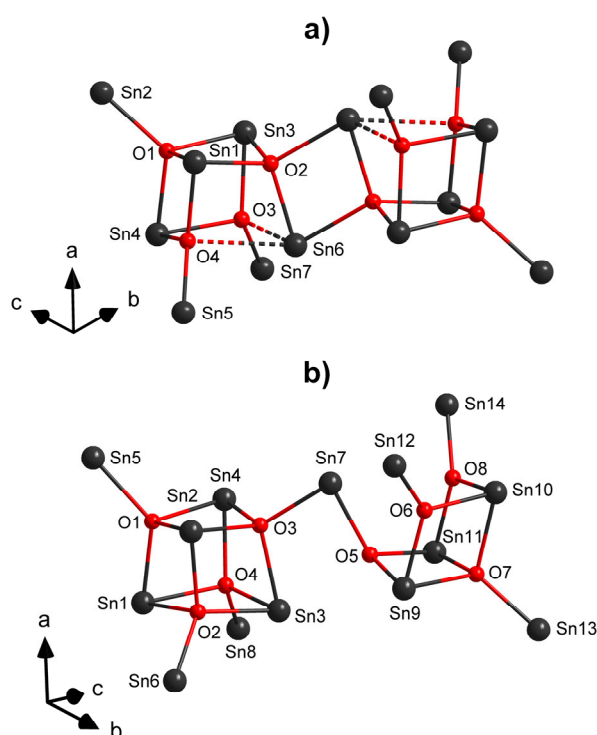


**Figure 13.** Cubane-like dimer as characteristic feature in the crystal structures of a) Sn<sub>7</sub>O<sub>4</sub>Cl<sub>6</sub> and b) Sn<sub>7</sub>O<sub>4</sub>Br<sub>6</sub>.

The [Sn<sub>4</sub>O<sub>4</sub>] unit in the crystal structure of Sn<sub>7</sub>O<sub>4</sub>Cl<sub>6</sub> deviates strongly from the geometric shape of a cube, as shown in Figure 13a. The two [Sn<sub>4</sub>O<sub>4</sub>] units are linked by two Sn-O bonds, between which a center of symmetry is situated that inverts one

### 3. Summary of the Main Results

[Sn<sub>4</sub>O<sub>4</sub>] unit into the other. Three additional tin atoms are attached to each of the two units (Sn2, Sn5, Sn7). The Sn-O bond distances vary between 2.10 and 2.74 Å. The two longest bonds (2.51 and 2.74 Å) between Sn6 and O3/O4 are indicated by dashed lines since they seem too long to be considered actual bonds and will be discussed later.

A similar motif can be found in Sn<sub>7</sub>O<sub>4</sub>Br<sub>6</sub>. However, a center of symmetry is missing here so that a dimer is present, which consists of a “complete” and an “incomplete” cubane-like [Sn<sub>4</sub>O<sub>4</sub>] unit (Figure 13b). The “incomplete” cubane-unit of Figure 13b (right part) contains longer Sn-O bonds with distances of 3.16 and 3.21 Å between Sn7 and O6/O8 and 2.81 Å between Sn3 and O5, which are too long to be considered bonds. The bond distances between the other tin and oxygen atoms vary between 2.1 and 2.4 Å and are similar to the shorter bonds in Sn<sub>7</sub>O<sub>4</sub>Cl<sub>6</sub> (no dashed lines).

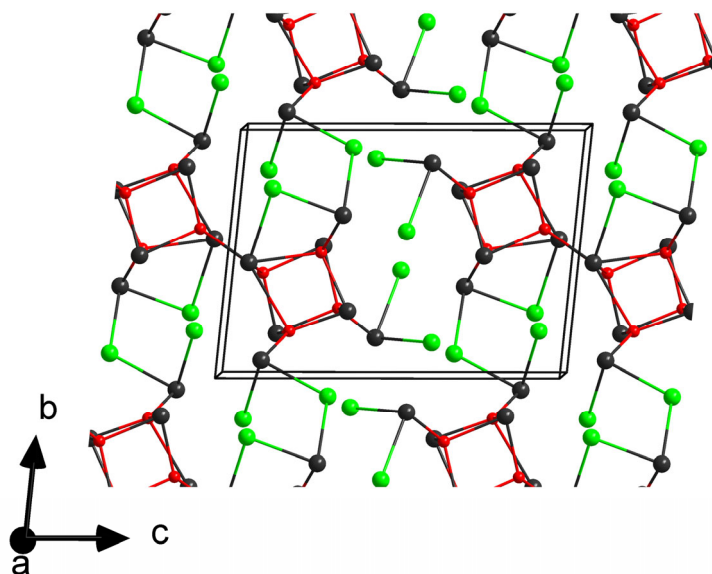


**Figure 14.** Perspective view on the crystal structure of Sn<sub>7</sub>O<sub>4</sub>Cl<sub>6</sub>, showing the location of the cubane-like dimer along the *bc* plane. Tin is shown in black, oxygen in red, and chlorine in green.

The overall crystal structure of Sn<sub>7</sub>O<sub>4</sub>Cl<sub>6</sub> is shown in Figure 14, where the cubane-like dimers can clearly be recognized. The apical tin atoms are surrounded by chlorine, which also bridges the dimers. The arrangement in tin oxide bromide is similar, but with two dimers per unit cell and a larger tilt of those dimers towards the *b*-axis.

As for some tin carbodiimide compounds, Sn<sub>7</sub>O<sub>4</sub>Cl<sub>6</sub> was used as a representative for the tin oxide halides for DFT calculations, which reveal Sn<sub>7</sub>O<sub>4</sub>Cl<sub>6</sub> to be a semiconductor with an indirect band gap of 2.8 eV, which is larger than for the related compound Sn<sub>9</sub>O<sub>5</sub>Cl<sub>4</sub>(CN<sub>2</sub>)<sub>2</sub> (2.3 eV),<sup>[67]</sup> likely due to more covalent Sn-O bonding of its structure. The ELF calculated for Sn<sub>7</sub>O<sub>4</sub>Cl<sub>6</sub> only showed a spheroidal distribution of electron pairs around chlorine and oxygen. The lone pair of tin is visible only as a small concave disk,

resulting in a tetrahedral coordination environment for tin when the lone pair is included with the three surrounding atoms. A closer look at the ELF reveals a weak but present ionic bond between Sn6 and O3/O4, as can be seen in Figure 15 by the lighter shades of blue between tin (Sn6) and the two oxygen atoms (O3 and O4) compared to the darker background. These bonds were indicated by dashed lines in Figure 13a.

The monoclinic crystal structure of the tin oxide iodide  $\text{Sn}_4\text{O}_6\text{I}_6$  differs from the triclinic structures of  $\text{Sn}_7\text{O}_4\text{Cl}_6$  and  $\text{Sn}_7\text{O}_4\text{Br}_6$ . Two features of its structure are displayed in Figure 16 (top). The oxygen of the  $[\text{Sn}_3\text{O}_6]$  fragment is coordinated trigonal planar by three tin atoms (Sn1, Sn2, Sn3), with a bond distance of around 2.1 Å, shorter than in  $\text{Sn}_7\text{O}_4\text{Cl}_6$  and  $\text{Sn}_7\text{O}_4\text{Br}_6$ . The three tin atoms are all in a distorted quadratic planar coordination, surrounded by four iodine and one oxygen atom. It seems that the additional space of the tin lone pair is pushing the four iodide atoms (which each coordinate one tin atom) out of the planar coordination towards oxygen, resulting in this distortion. The second interesting feature in the crystal structure of  $\text{Sn}_4\text{O}_6\text{I}_6$  is the  $[\text{Sn}_2\text{I}_8]$  dimer, displayed top right in Figure 16 and is bridging several of the  $[\text{Sn}_3\text{O}_6]$  units, as displayed in Figure 16 (bottom).

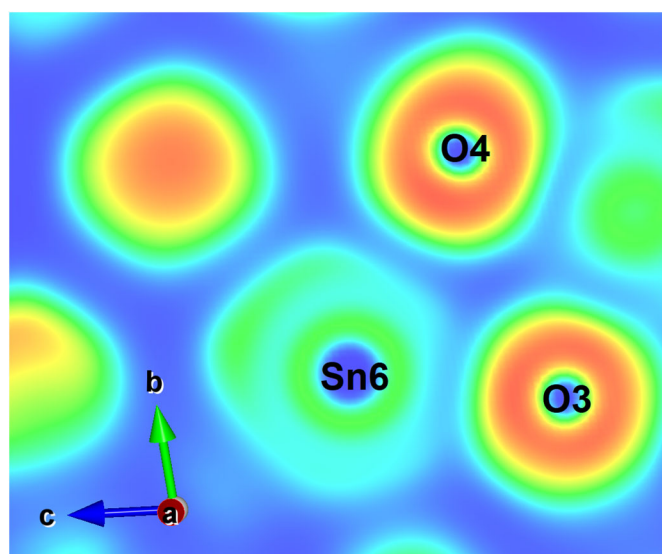


**Figure 15.** Section from the ELF of  $\text{Sn}_7\text{O}_4\text{Cl}_6$  to illustrate the interaction between a tin atom (Sn6) and two oxygen atoms (O3 and O4). Red indicates a high density of localized electrons, blue a low density of localized electrons.

Another tin oxide bromide,  $\text{Sn}_{14}\text{O}_{11}\text{Br}_6$ , was reported by another research group shortly after the publication of our work, describing the synthesis of  $\text{Sn}_{14}\text{O}_{11}\text{Br}_6$  as a promising birefringent material.<sup>[152]</sup>

### 3. Summary of the Main Results

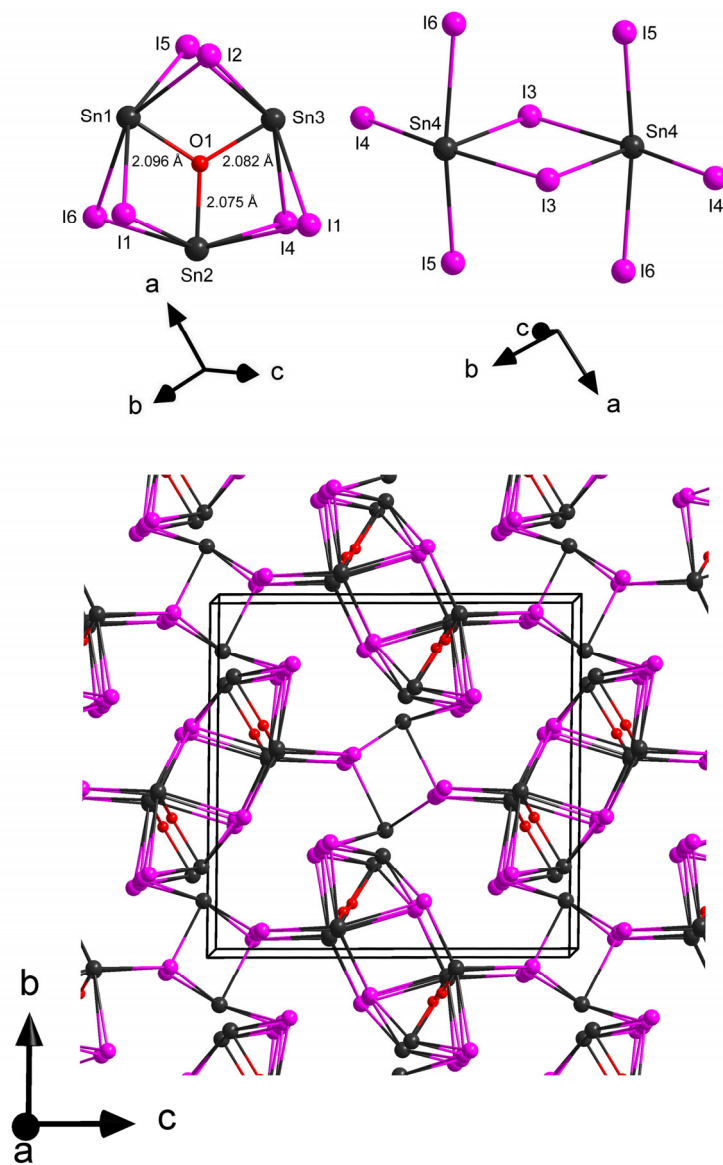


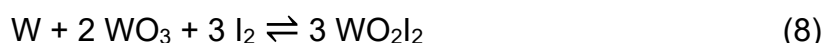
**Figure 16.** Sections of the crystal structure of  $\text{Sn}_4\text{O}_6$ . Top left:  $[\text{Sn}_3\text{O}]_6$  fragment and top right:  $[\text{Sn}_2]_6$  dimer. Bottom: perspective view of the crystal structure of  $\text{Sn}_4\text{O}_6$ .

### 3.5 Tungsten oxide iodides (Publ. 5)<sup>[153]</sup>

Tungsten oxide halides are known to exist for all four halogens, and some of them were tested in reactions with  $\text{Li}_2(\text{CN}_2)$  to synthesize a hypothetical tungsten oxide carbodiimide, such as  $\text{WO}_2(\text{CN}_2)$  or  $\text{WO}(\text{CN}_2)_2$ . Previous studies in which  $\text{WOCl}_4$ ,  $\text{WO}_2\text{Cl}_2$ , and  $\text{WOBr}_4$  were employed, failed. Hence, tungsten oxide iodides should be tested as a promising reactant.

In order to synthesize the oxide iodide  $\text{WO}_2\text{I}_2$ , which is often mentioned in the literature, a more than 50 years old synthetic procedure described by Tillack was used.<sup>[154]</sup>

Here, the author employed a 1:2:3 molar mixture of tungsten, tungsten(VI) oxide, and iodine. For higher yields, an excess of iodine was used (depending on the total mass of reactants). The reactions were carried out in fused silica ampules placed in a tube furnace, with mixtures of W,  $\text{WO}_3$ , and  $\text{I}_2$  in a 1:2:6 molar ratio. The ampule was placed in the tube furnace at a temperature gradient of 800/300 °C. After 5 h of reaction time, metallic lustrous platelet-shaped crystals appear at the colder part of the ampule. Some of these thin platelets could be measured with a single-crystal diffractometer, confirming that these platelets are the target compound  $\text{WO}_2\text{I}_2$ , presumably formed following reaction (8). After determining the crystal structure of these platelets, we found that there is no crystal structure data on  $\text{WO}_2\text{I}_2$  available (only some assumed lattice parameters in the work of Tillack). However, its synthesis and some of its properties were published more than half a century ago.



The crystal structure of  $\text{WO}_2\text{I}_2$  was solved and refined in the orthorhombic space group *Immm*. Tungsten is coordinated distorted octahedrally by four oxygen atoms situated in the octahedral plane and two iodine atoms, both situated on the tips.

Those octahedra are connected along the *a*- and *b*-axis via W-O bonds, which results in a layered arrangement. This layered arrangement is shown in Figure 17 (left); a top view of one of those layers is shown in Figure 17 (right). Unfortunately, attempts to synthesize a tungsten oxide carbodiimide using  $\text{WO}_2\text{I}_2$  failed as well.

Tillack further reported the appearance of a second compound, formed at higher temperatures than  $\text{WO}_2\text{I}_2$ . He supposed this unknown compound, with a blueish color, to have the composition  $\text{WO}_2\text{I}$ . According to the supposed formula, this compound might be formed by loss of iodine of  $\text{WO}_2\text{I}_2$ , a reaction mechanism known from several binary tungsten iodides.<sup>[155]</sup>

### 3. Summary of the Main Results

Our PXRD studies indeed indicated the formation of a second phase when heating  $\text{WO}_2\text{I}_2$  to 400 °C. We finally obtained some needle-shaped black crystals after many experiments at different temperatures with different dwell times and cooling rates.

The determination of the crystal structure of those crystals was really challenging but ultimately successful after many attempts, revealing a monoclinic lattice with the composition  $\text{W}_2\text{O}_3\text{I}_4$ . As reaction (9) indicates, this tungsten compound is formed from  $\text{WO}_2\text{I}_2$ , however, not by the loss of iodine but by the loss of oxygen.

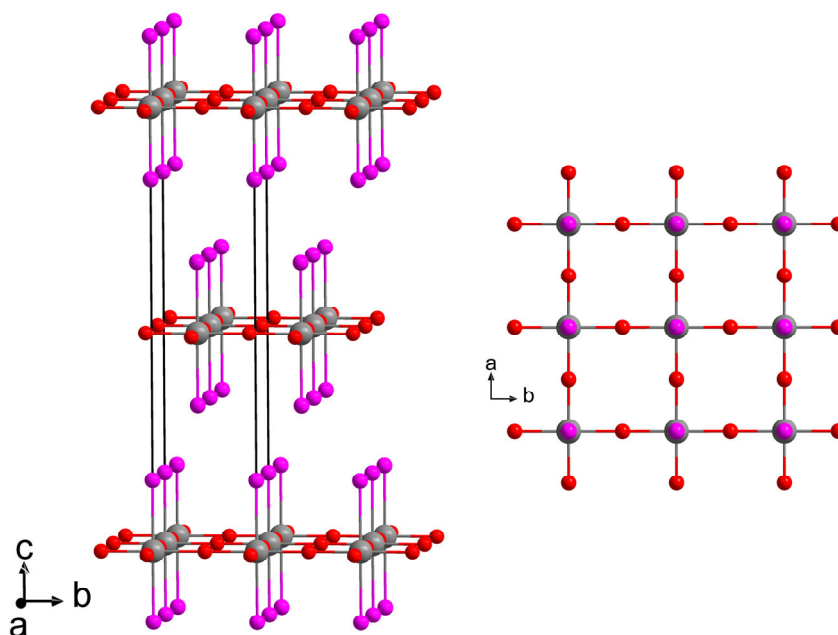


**Figure 17.** Two different projections of the crystal structure of  $\text{WO}_2\text{I}_2$ . Left: view along the  $cb$  plane, right: perspective view along the  $ab$  plane.

The crystal structure of  $\text{W}_2\text{O}_3\text{I}_4$  was solved and refined in the monoclinic space group  $I2/m$ . The crystal structure also adopts a layered arrangement, but unlike the crystal structure of  $\text{WO}_2\text{I}_2$ , two different coordination environments of tungsten are present, both shown as connected chains in Figure 18. Both are octahedrally coordinated and slightly distorted due to different bond distances. W1 is coordinated by four oxygen and two iodine atoms; W2 is surrounded by two oxygen and four iodine atoms. Those polyhedra are either connected by shared oxygen atoms (W1) or via iodine atoms (W2). This layered arrangement of the structure is shown in Figure 19 (left), furthermore, a top view of a layer is indicated in Figure 19 (right), emphasizing a Peierls distortion of the structure, resulting in alternating short and long W-W distances. The overall oxidation state of tungsten here is V, although, from a structural point of view, it is more plausible that two different oxidation states of tungsten, VI (W1) and IV (W2),

### 3. Summary of the Main Results

are present since alternating longer and shorter metal-metal distances, as present between W2 atoms, are known from tetravalent metal halides, such as  $\text{WBr}_4$ ,<sup>[156]</sup>  $\text{NbBr}_4$ ,<sup>[157]</sup> or  $\text{Nbl}_4$ .<sup>[158]</sup> In addition, the formal charges of the ligands match with +6 for W1 ( $\text{WO}_{4/2} \text{I}_2$ ) and +4 for W2 ( $\text{WO}_{2/2} \text{I}_{4/2}$ ).

When a sample of  $\text{WO}_2 \text{I}_2$  was heated beyond 400 °C, the formation of  $\text{WO}_2$  was observed, indicating a formal reduction of the oxidation state of tungsten from VI ( $\text{WO}_2 \text{I}_2$ ), to V ( $\text{W}_2\text{O}_3 \text{I}_4$ ) and finally to IV ( $\text{WO}_2$ ).

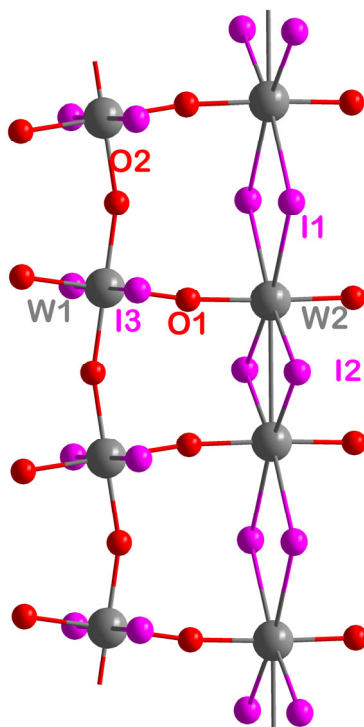


**Figure 18.** Two distinct chains in the crystal structure of  $\text{W}_2\text{O}_3\text{I}_4$ , emphasizing two different coordination environments of tungsten.

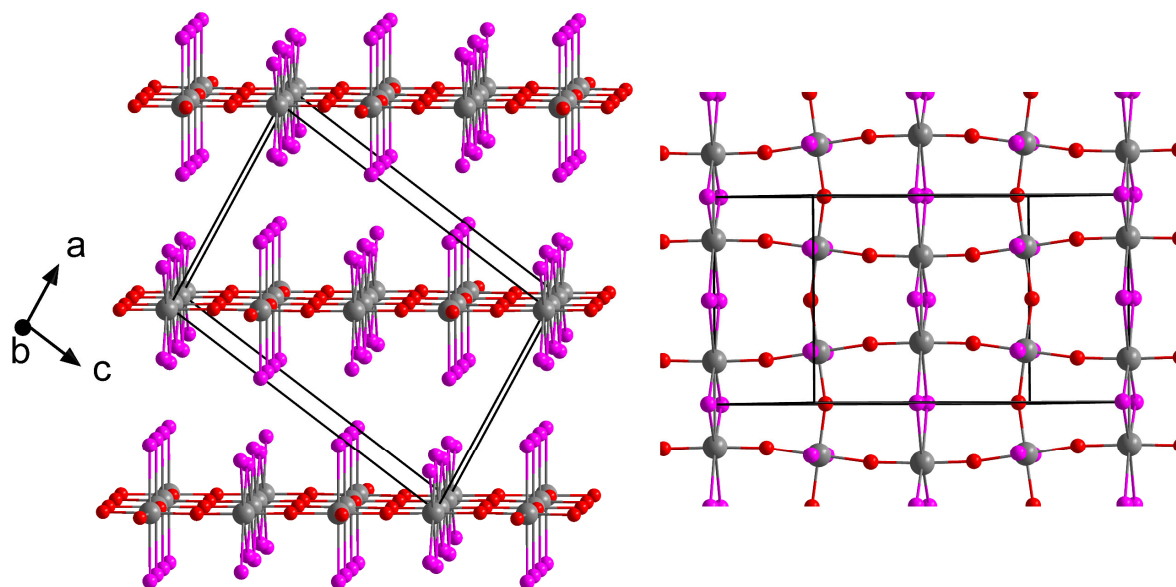


**Figure 19.** Two different projections of the crystal structure of  $W_2O_3I_4$ . Left: perspective view along the  $ac$  plane, right: perspective view, emphasizing the Peierls distortion, caused by alternating short/long  $W-W$  bonds.

The electronic structure of both compounds was investigated using DFT calculations. Surprisingly, those calculations reveal both  $WO_2I_2$  and  $W_2O_3I_4$  to be conductors with a behavior similar to a poor metal.

$WO_2I_2$  has long been associated with processes in halogen incandescent lamps. The most common theory today is that vaporized tungsten condenses on the bulb wall and reacts with iodine and minor oxygen or water impurities to form  $WO_2I_2$ . This  $WO_2I_2$  is now distributed in the bulb, where there is a large temperature gradient between the bulb wall and the filament. The idea is that  $WO_2I_2$  first decomposes into  $WO_2$  and iodine due to its thermal instability. This  $WO_2$  decomposes further into  $WO + O$  and finally into  $W + O$  at even higher temperatures near the filament. This gaseous tungsten now precipitates on the filament, but at the thicker, cooler areas, not on the thinner, hotter regions, where it would be needed to “repair” those weaker points.<sup>[159]</sup> The role of the new compound  $W_2O_3I_4$  in halogen incandescent lamps, however is not clear yet.



### 3.6 $\text{Pb}_{14.66}\text{Sn}_{7.34}\text{Br}_{26}(\text{CN}_2)_7\text{O}_2$ , a complex carbodiimide (Publ. 6)<sup>[15]</sup>

There are many carbodiimide compounds containing either tin, lead, or germanium that have been produced in our research group in recent years, for instance,  $\text{Sn}(\text{CN}_2)$ ,<sup>[24d]</sup>  $\text{APb}_2\text{Cl}_3(\text{CN}_2)$ , ( $A = \text{Li, Na, Ag}$ ),<sup>[101]</sup> or  $\text{ARE}[\text{Ge}(\text{CN}_2)_4]$ , ( $A = \text{K, Cs}$ , and  $RE = \text{La–Gd}$ , except  $\text{Pm}$ )<sup>[88]</sup>. Elements of group 14 seem to form NCN compounds in a particularly diverse way, combined with interesting physical properties, as reported for some of these compounds. Especially tin carbodiimide compounds, such as  $\text{Sn}(\text{CN}_2)$  or  $\text{Sn}_2\text{O}(\text{CN}_2)$ , are both semiconductors with band gaps on the order of 2 eV, respectively.<sup>[24d, 60]</sup> Furthermore,  $\text{Sn}(\text{CN}_2)$  was tested as anode material in Li-ion batteries,<sup>[160]</sup> whereas  $\text{Sn}_2\text{O}(\text{CN}_2)$  was shown to enhance the efficiency of  $\text{CuWO}_4$  photoanodes, used for PEC water splitting<sup>[148]</sup>.

In order to study reactions between lead and tin, we employed mixtures of  $\text{Pb}(\text{CN}_2)$  and different tin halides. Here reactions between  $\text{Pb}(\text{CN}_2)$  and  $\text{SnBr}_4$ , that were conducted to synthesize a tetravalent tin carbodiimide  $\text{Sn}(\text{CN}_2)_2$ , led to the formation of yellow single crystals, later identified as  $\text{Pb}_{14.66}\text{Sn}_{7.34}\text{Br}_{26}(\text{CN}_2)_7\text{O}_2$ .

The crystal structure refinement revealed one crystallographic site for the metal atoms, shared by tin and lead. EDX measurements determined an overall tin to lead ratio of 1:2, which is consistent with this crystal structure refinement.  $\text{Pb}_{14.66}\text{Sn}_{7.34}\text{Br}_{26}(\text{CN}_2)_7\text{O}_2$  can be synthesized phase-pure from appropriate reaction mixtures of  $\text{Pb}(\text{CN}_2)$ ,  $\text{PbBr}_2$ ,  $\text{SnBr}_2$ , and  $\text{SnO}$ , yielding a greenish to beige powder. As the molecular formula suggests, the crystal structure is quite complex and consists of nine different metal sites coordinated by bromine, NCN, or O. All nine different coordinations are shown in Figure 20. Some of these metal sites are arranged in two distinct motifs; a tetrahedron and a trigonal bipyramid. Both motifs are formed by tin and lead atoms and capped by NCN ions. These NCN units connect both arrangements and are linked to further polyhedra. A dimeric fragment of those two motifs and their arrangement in the crystal structure is depicted in Figure 21.

Although no pseudobinary tin(IV) carbodiimide was obtained in this reaction, it demonstrates the versatility of tin halides in solid-state reactions to form compounds of various kinds with NCN ions.

### 3. Summary of the Main Results

---

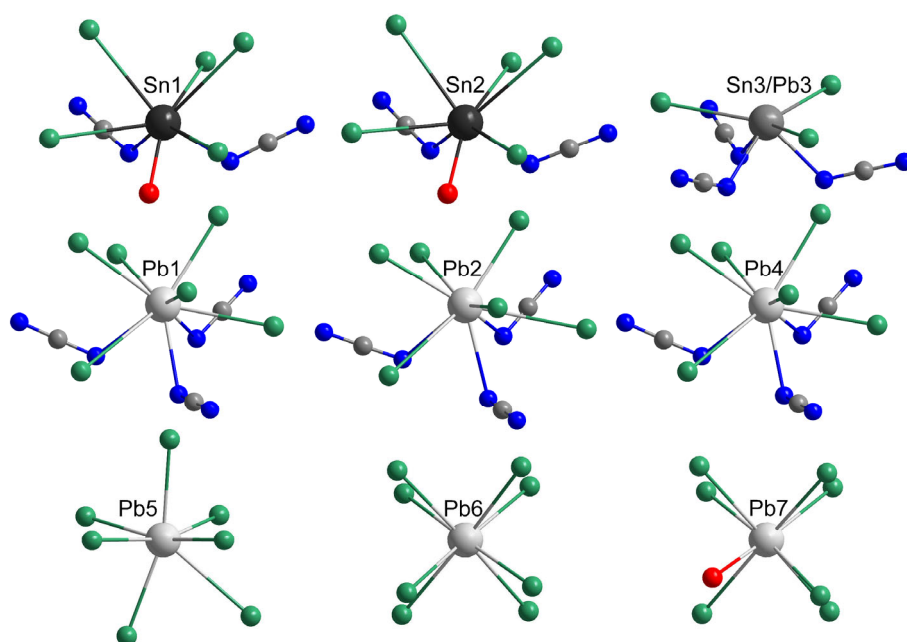


**Figure 20.** Nine distinct coordination environments in the crystal structure of  $\text{Pb}_{14.66}\text{Sn}_{7.34}\text{Br}_{26}(\text{CN}_2)_7\text{O}_2$ . Bromine is shown in green, oxygen in red, carbon in dark gray, and nitrogen in blue.

### 3. Summary of the Main Results

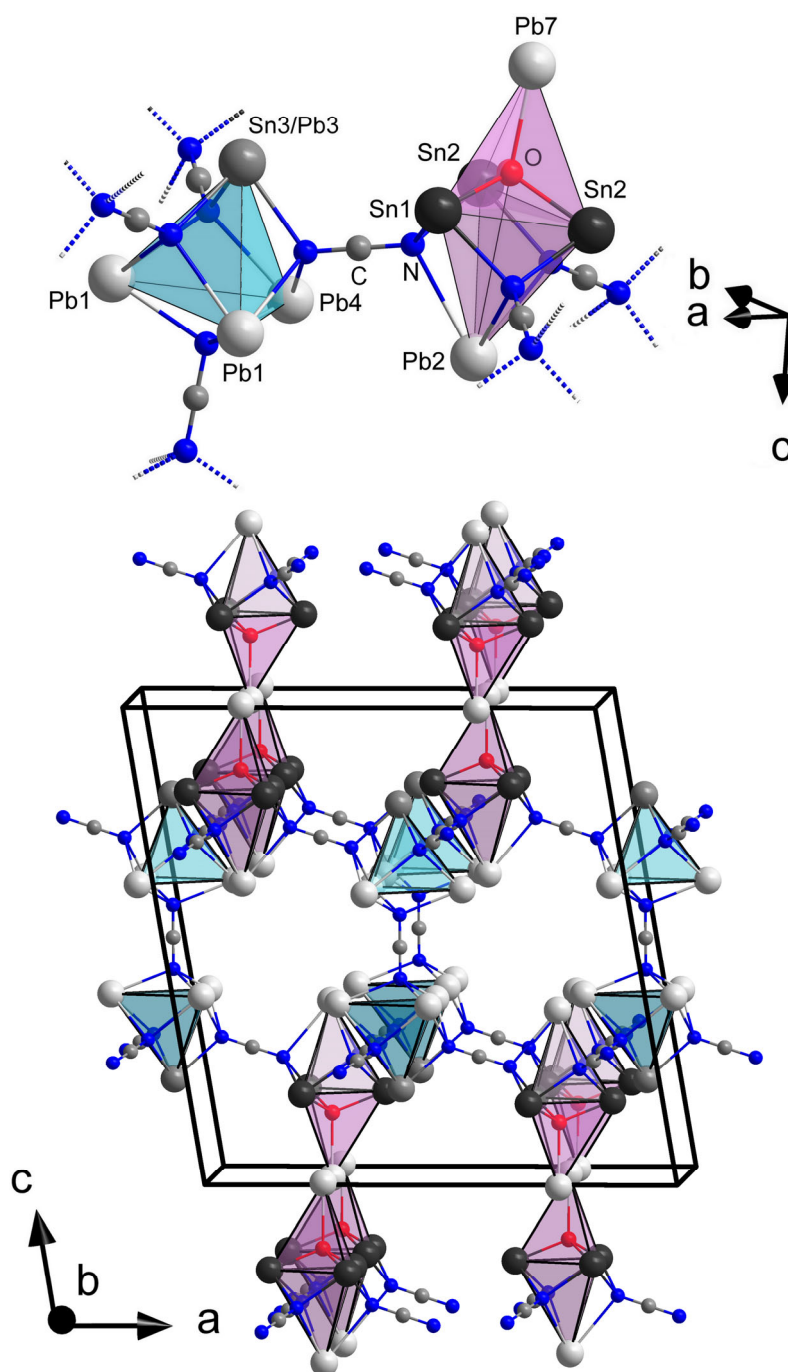


**Figure 21.** Top: dimeric fragment consisting of a tetrahedron (blue) and a trigonal bipyramid (red). Dashed lines emphasize the linkage to further polyhedra. Bottom: arrangement of the top motifs in the crystal structure of  $\text{Pb}_{14.66}\text{Sn}_{7.34}\text{Br}_{26}(\text{CN}_2)_7\text{O}_2$ .

### 3.7 $\text{LiSn}_2\text{Br}_3(\text{CN}_2)$ and $\text{Sn}_4\text{Br}_2(\text{CN}_2)_3$ (Publ.7)<sup>[61]</sup>

Divalent tin carbodiimide compounds have previously been obtained in our group from reactions of  $\text{Li}_2(\text{CN}_2)$  and  $\text{SnCl}_2$  ( $\text{Sn}(\text{CN}_2)$ ,  $\text{Sn}_4\text{Cl}_2(\text{CN}_2)_3$ ) and from reactions of  $\text{Li}_2(\text{CN}_2)$ ,  $\text{SnCl}_2$ , and  $\text{SnO}$  ( $\text{Sn}_2\text{O}(\text{CN}_2)$ ,  $\text{Sn}_9\text{O}_5\text{Cl}_4(\text{CN}_2)_2$ ). Since reactions with  $\text{Li}_2(\text{CN}_2)$  and  $\text{SnF}_2$  led only to the formation of  $\text{Sn}(\text{CN}_2)$ , we employed different mixtures of  $\text{Li}_2(\text{CN}_2)$  and  $\text{SnBr}_2$  to study the chemistry between them in contrast to the behavior of  $\text{SnCl}_2$  in the NCN system.

Different molar ratios of  $\text{Li}_2(\text{CN}_2)$  and  $\text{SnBr}_2$  led to the formation of two different compounds.  $\text{LiSn}_2\text{Br}_3(\text{CN}_2)$  and  $\text{Sn}_4\text{Br}_2(\text{CN}_2)_3$  were obtained from 1:2 and 3:4 molar mixtures of  $\text{Li}_2(\text{CN}_2)$  and  $\text{SnBr}_2$ , respectively. Both compounds could be obtained as transparent, colorless crystals at 350 °C and 400 °C, respectively. Both crystal structures are isotypic to some already known carbodiimide compounds.  $\text{Sn}_4\text{Br}_2(\text{CN}_2)_3$  is isotypic to  $\text{Sn}_4\text{Cl}_2(\text{CN}_2)_3$  that has been reported recently in our group.<sup>[24d]</sup>  $\text{LiSn}_2\text{Br}_3(\text{CN}_2)$  is isotypic to several known compounds that are  $\text{APb}_2\text{Cl}_3(\text{CN}_2)$ , ( $A = \text{Li}, \text{Na}, \text{Ag}$ ),  $\text{APb}_2\text{Br}_3(\text{CN}_2)$ , ( $A = \text{Li}, \text{Na}$ ) and  $\text{LiM}_2\text{X}_3(\text{CN}_2)$ , ( $M = \text{Eu}, \text{Sr}$ ), ( $X = \text{Br}, \text{I}$ ).<sup>[35, 94, 101]</sup> Both reactions can be monitored by thermal analysis.

A DTA of the 3:4 molar mixture, illustrated in Figure 22, was carried out with two heating/cooling cycles and indicates an exothermic effect between 150 and 205 °C in the first heating cycle. This effect is assigned to the formation of  $\text{LiSn}_2\text{Br}_3(\text{CN}_2)$ , which transforms later into  $\text{Sn}_4\text{Br}_2(\text{CN}_2)_3$  without noticeable effects. A small endothermic peak within the broad exothermic effect is assumed to be due to the formation of a eutectic melt, formed between  $\text{LiBr}$  and unreacted  $\text{SnBr}_2$ , which is confirmed by a DTA of  $\text{LiBr}$  and  $\text{SnBr}_2$ , where an endothermic effect occurs at a similar temperature (pure  $\text{SnBr}_2$  melts later). In the further course of the reaction, an endothermic effect is observed at 395 °C, as well as an exothermic effect upon cooling at 356 °C, which can be assigned to the melting and recrystallization of the product and the metathesis salt  $\text{LiBr}$ . Both effects occur again in a second heating/cooling cycle. A DTA of a 1:2 molar mixture of  $\text{Li}_2(\text{CN}_2)$  and  $\text{SnBr}_2$  showed similar results.

The crystal structure of  $\text{Sn}_4\text{Br}_2(\text{CN}_2)_3$  comprises a layered arrangement of tin atoms alternating with mixed layers of bromide and carbodiimide ions, as shown in Figure 23. Tin atoms are coordinated by three bromide and three NCN units.

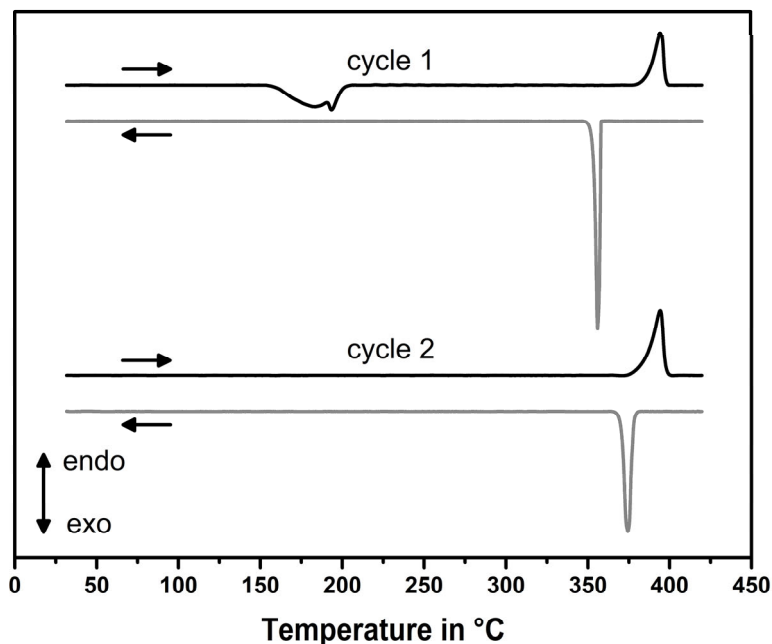


**Figure 22.** DTA of a 3:4 molar mixture of  $\text{Li}_2(\text{CN}_2)$  and  $\text{SnBr}_2$ , recorded with two heating/cooling cycles.

The crystal structure of  $\text{LiSn}_2\text{Br}_3(\text{CN}_2)$  is composed of two characteristic features; tin tetrahedra that are capped and connected by NCN units to a complex network (see Figure 24) and  $[\text{LiBr}_6]$  octahedra, that are linked at the corners by bromide ions (see Figure 25). Framework-like structures, such as in  $\text{LiSn}_2\text{Br}_3(\text{CN}_2)$ , are possible candidates for unusual thermoelastic properties like negative thermal expansion. Hence, the phonon band structure of  $\text{LiSn}_2\text{Br}_3(\text{CN}_2)$  was determined using DFPT calculations.

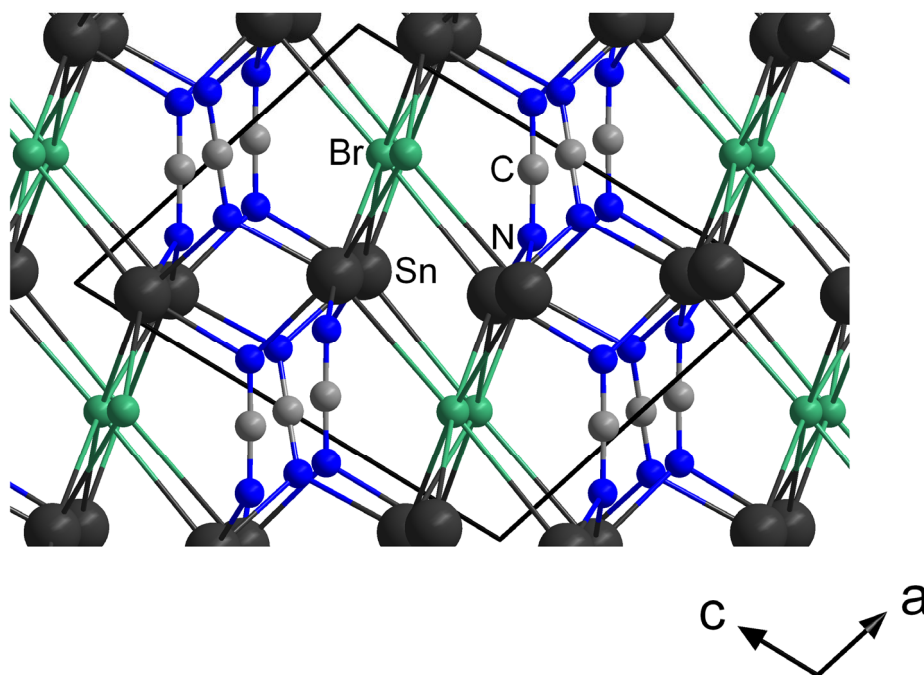


**Figure 23.** Perspective view of the crystal structure of  $\text{Sn}_4\text{Br}_2(\text{CN}_2)_3$ .

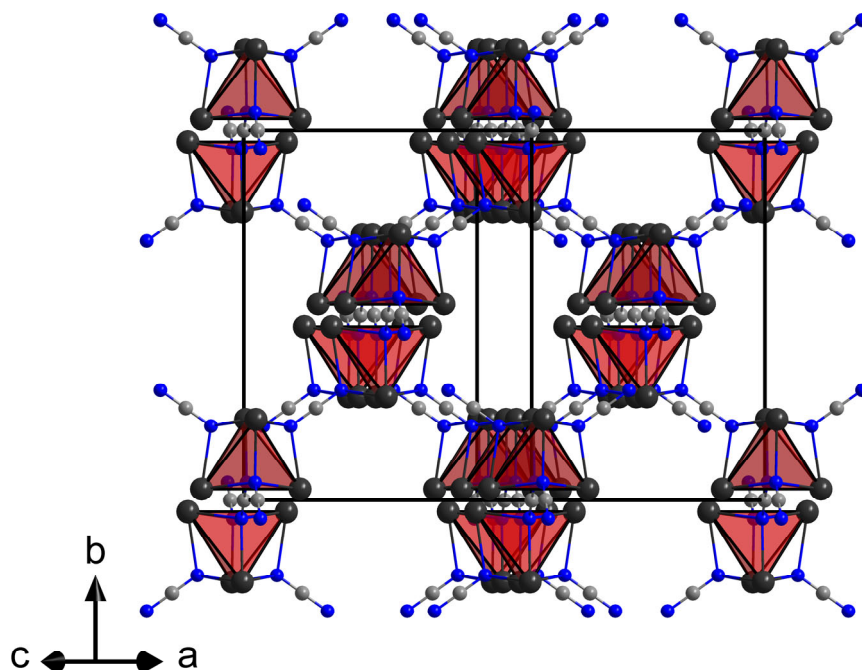


**Figure 24.** Section of the crystal structure of  $\text{LiSn}_2\text{Br}_3(\text{CN}_2)$ , indicating the arrangement of (red) tin tetrahedra and NCN ions. Tin is shown in black, carbon in dark gray, and nitrogen in blue.

This phonon band structure is shown in Figure 26 (top), along with a graph of the linear thermal expansion coefficient plotted vs. temperature (bottom). The phonon band structure of  $\text{LiSn}_2\text{Br}_3(\text{CN}_2)$  shows many low-energy phonons and below 25 K many modes with negative Grüneisen parameters, indicating negative thermal expansion below that temperature.

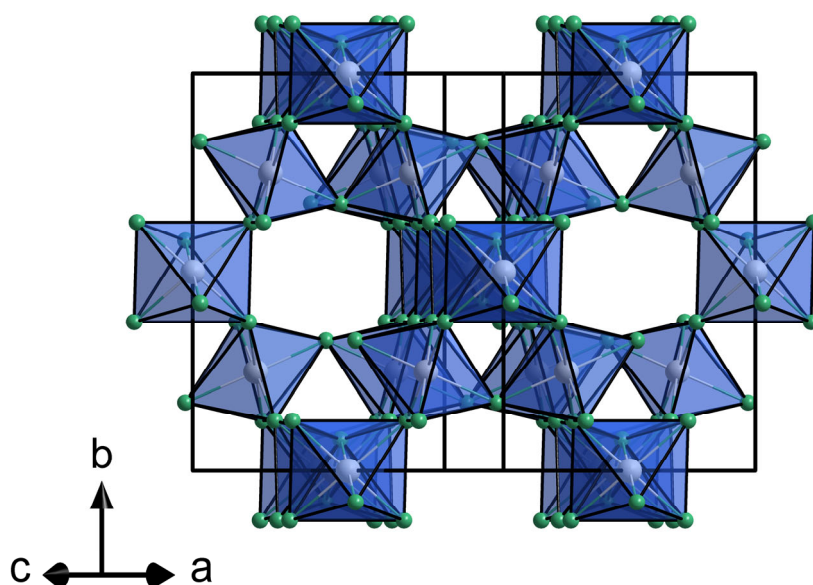


**Figure 25.** Section of the crystal structure of  $\text{LiSn}_2\text{Br}_3(\text{CN}_2)$ , showing the arrangement of  $[\text{LiBr}_6]$  octahedra. Li is shown in light gray, bromine in green.

### 3. Summary of the Main Results

As the temperature increases, the positive mode Grüneisen parameters also increasingly participate in the thermal expansion (see Figure 26 bottom), leading to a positive coefficient of thermal expansion, which is, however, still relatively small even at 300 K.

As with other tin compounds, the electronic band structure was calculated to make statements about the electronic properties. DFT calculations revealed an indirect band gap of 2.5 eV; thus,  $\text{LiSn}_2\text{Br}_3(\text{CN}_2)$ , like other tin carbodiimides, can be considered a semiconductor.

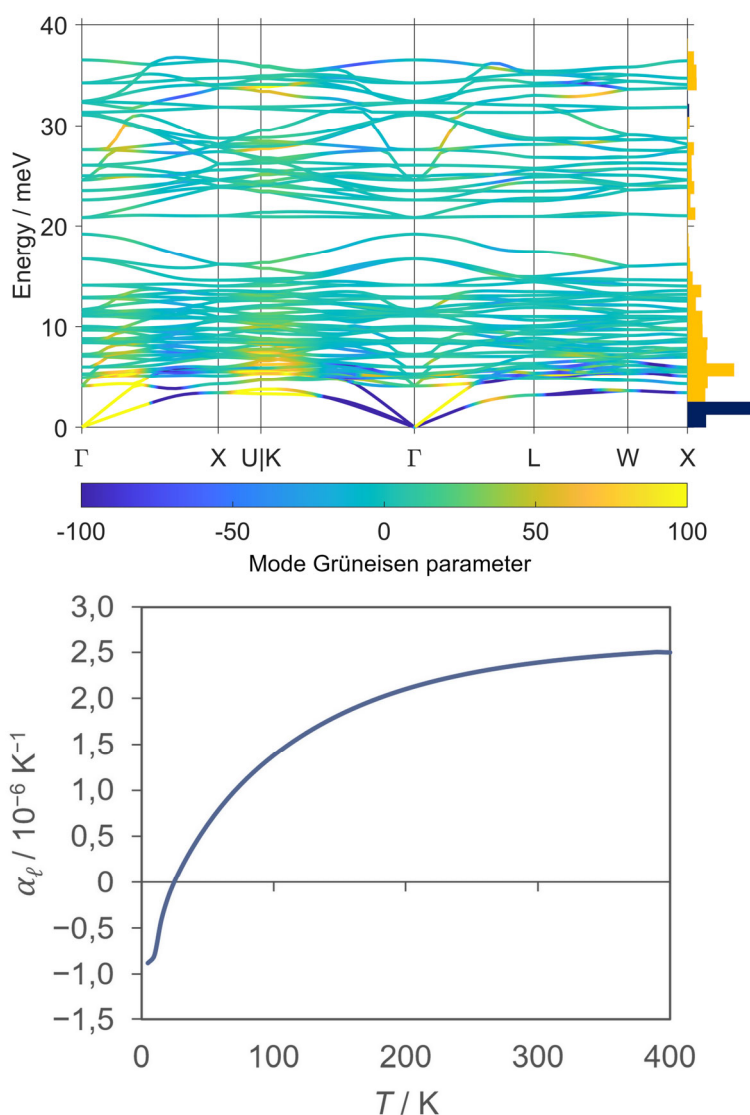


**Figure 26.** Top: calculated phonon band structure of  $\text{LiSn}_2\text{Br}_3(\text{CN}_2)$ . Bottom: calculated linear thermal expansion coefficient of  $\text{LiSn}_2\text{Br}_3(\text{CN}_2)$ , determined between 5 and 400 K.

### 3.8 The ternary lithium tin iodide $\text{LiSn}_3\text{I}_7$ (Publ. 8)<sup>[161]</sup>

During our explorative syntheses in the field of tin carbodiimide compounds, we employed different mixtures of  $\text{Li}_2(\text{CN}_2)$  and tin halides  $\text{SnX}_2$  ( $X = \text{F-I}$ ).

Experiments with  $\text{Li}_2(\text{CN}_2)$  and  $\text{SnI}_2$  yielded orange-red single crystals of a previously unknown compound. The parameters of the monoclinic unit cell were quite similar to those of  $\text{SnI}_2$ , but one axis in particular, as well as the monoclinic angle  $\beta$ , deviated strongly from this cell. Closer examination showed that one crystallographic site is occupied by both lithium and tin, resulting in the composition  $\text{LiSn}_3\text{I}_7$ .

Ternary tin halides such as  $\text{CsSnI}_3$  are particularly significant in the field of PSCs. They have become increasingly important in recent years as a potential candidate to replace the more common but toxic lead halides.<sup>[162]</sup> These lead halides, such as  $\text{MAPbI}_3$ ,  $\text{FAPbI}_3$ , or  $\text{CsPbI}_3$ , ( $\text{MA} = [\text{CH}_3\text{NH}_3]^+$ ,  $\text{FA} = [\text{CH}(\text{NH}_2)_2]^+$ ), were intensively studied and have become a possible alternative to conventional silicon-based solar cells.<sup>[163]</sup>

Perovskite tin-based halides like  $\text{CsSnI}_3$ , however, still lag behind lead compounds in terms of efficiency and stability, so much research remains to be done in this area.<sup>[162]</sup>

$\text{LiSn}_3\text{I}_7$  is synthesized straightforwardly by a 1:3 molar mixture of  $\text{LiI}$  and  $\text{SnI}_2$  at 300 °C. Its crystal structure is related to that of  $\text{SnI}_2$ . Hence, the lattice parameters of both  $\text{LiSn}_3\text{I}_7$  and  $\text{SnI}_2$  are given in Table 8.

**Table 8.** Unit cell parameters of  $\text{LiSn}_3\text{I}_7$  and the related compound  $\text{SnI}_2$ .

	$\text{LiSn}_3\text{I}_7$	$\text{SnI}_2$ <sup>[164]</sup>
Space group	$C2/m$	$C2/m$
Unit cell dimensions (Å)	$a = 14.2850(4)$	$a = 14.17(5)$
	$b = 4.4140(3)$	$b = 4.54(2)$
	$c = 13.2188(3)$	$c = 10.87(4)$
Angle (°)	$\beta = 105.445(3)$	$\beta = 92.0(2)$
Volume (Å <sup>3</sup> )	797.78(3)	698.09(433)
Z	2	6

The crystal structure of  $\text{LiSn}_3\text{I}_7$  is composed of two different coordination environments of the metal cations. One site, fully occupied by tin (Sn2) is coordinated capped trigonal prismatic by seven iodine atoms. The second site is shared by tin and lithium in a 1:1 ratio (Li1/Sn1). This site is coordinated octahedrally by six iodine atoms. Both sites are shown in Figure 27.



### 3. Summary of the Main Results

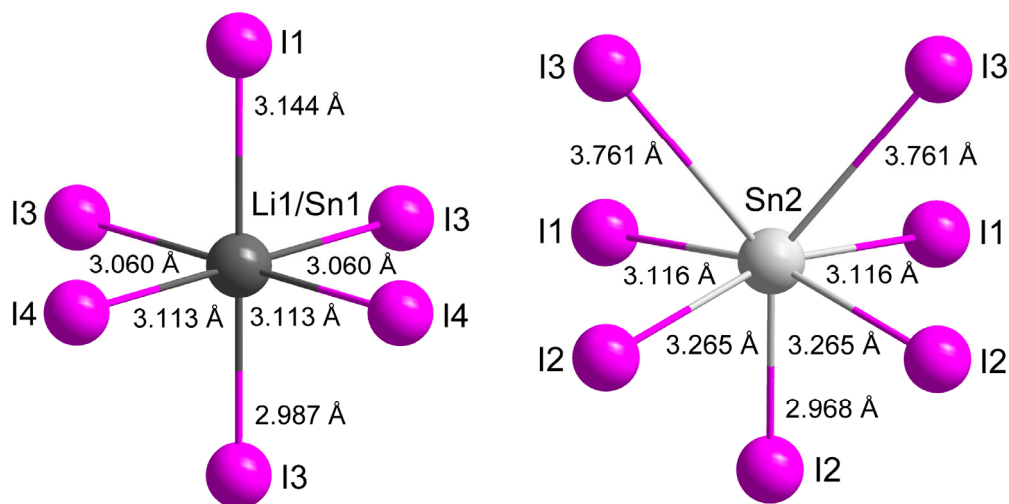


**Figure 27.** Two distinct coordination environments in the crystal structure of  $\text{LiSn}_3\text{I}_7$ .

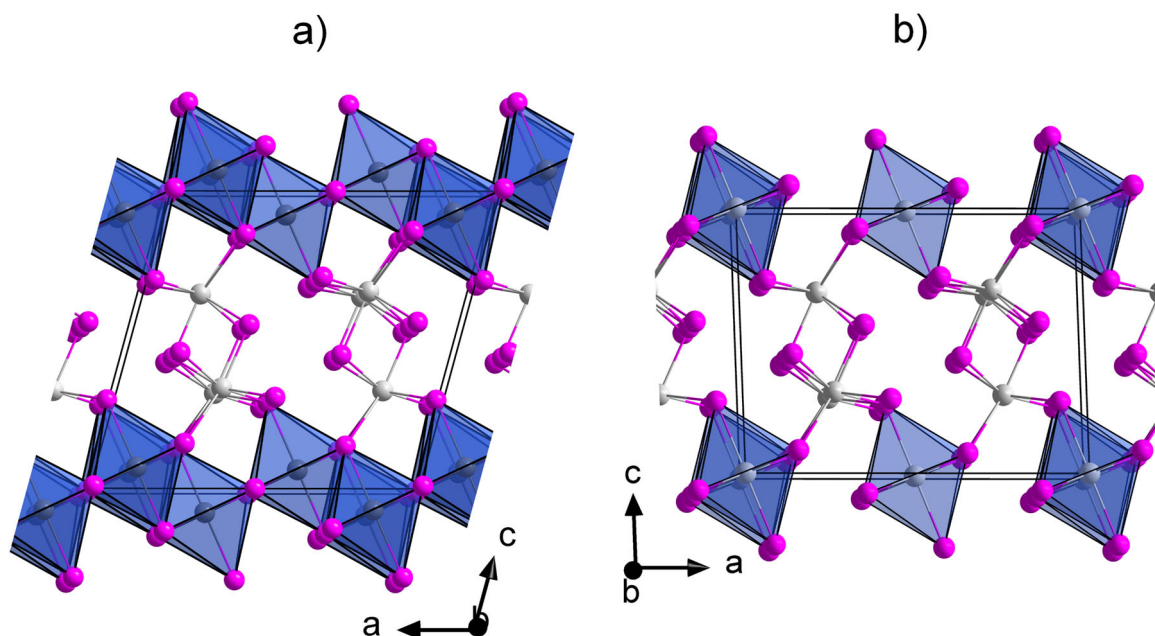


**Figure 28.** Comparison of the crystal structure of  $\text{LiSn}_3\text{I}_7$  (a) and  $\text{SnI}_2$ . Tin is shown in light gray, lithium/tin in dark gray, and iodine in purple.

The crystal structure of  $\text{LiSn}_3\text{I}_7$  consists of a layered network of edge-shared octahedra that alternates with two layers of the capped trigonal prismatic coordinated tin ( $\text{Sn}_2$ ) and linked by iodine atoms (Figure 28a). This arrangement can also be found in the crystal structure of  $\text{SnI}_2$  but with one empty octahedral gap, leading to a connection of the octahedra only along the  $b$ -axis (Figure 28b).

### 3. Summary of the Main Results

---

To study the incorporation of lithium into the structure, ssNMR spectra of  $\text{LiSn}_3\text{I}_7$ , as well as several other compounds, were recorded. The  $^7\text{Li}$  solid-state MAS NMR spectra of  $\text{LiSn}_3\text{I}_7$  showed a strong single peak, very similar to the spectra of  $\text{LiI}$ . To further prove that Li is incorporated into the crystal structure and is not just present as  $\text{LiI}$ ,  $^{127}\text{I}$  MAS ssNMR spectra of  $\text{LiSn}_3\text{I}_7$  and  $\text{LiI}$  were recorded, revealing a strong peak in  $\text{LiI}$  but only a weak, broad peak in  $\text{LiSn}_3\text{I}_7$ , presumably from residual  $\text{LiI}$ . However, the amount of  $\text{LiI}$  is too small to be considered as the origin of the  $^7\text{Li}$  peak of  $\text{LiSn}_3\text{I}_7$ , confirming the incorporation of Li into the crystal structure.

The  $^{119}\text{Sn}$  ssNMR spectra showed two broad peaks for both  $\text{SnI}_2$  and  $\text{LiSn}_3\text{I}_7$  that can be assigned to the two crystallographic tin sites, respectively.

In order to investigate the electronic structure of  $\text{LiSn}_3\text{I}_7$ , DFT calculations were performed. The calculated electronic band structure revealed an indirect band gap on the order of 2 eV, somewhat larger than the calculated band gap of  $\text{SnI}_2$  (1.5 eV)<sup>[165]</sup>.

Although the new compound  $\text{LiSn}_3\text{I}_7$  does not adopt the cubic perovskite structure, it is an important member of ternary tin halides, as it is the first ternary Li-Sn halide and since many tin compounds have interesting properties, such as semiconductivity, it may provide a perspective for further research.

#### 3.9 Appendix

All figures, except those cited, were taken from the publication referenced in the respective chapter heading (3.1–3.8). Adaptions for some figures are listed below.

**Figure 4:** A second projection is included in the original figure in Publication 1.

**Figure 5:** The red asterisk is not included in the original illustration in Publication 1. Figure 5b was not taken from Publication 1.

**Figure 13:** Figures a & b are two separate images in Publication 4.

**Figure 16:** The two motifs at the top and the structure at the bottom are two separate figures in Publication 4.

**Figure 17:** The figure does not include a detailed illustration of the coordination environment of W, as shown in Publication 5.

**Figure 24:** Combined with Figure 25 to form one illustration in Publication 7.

**Figure 25:** Combined with Figure 24 to form one illustration in Publication 7.

**Figure 26:** Both graphs are separate images in Publication 7.

**Figure 28:** Figures a & b are separate images in Publication 8.



## **4. References**

#### 4. References

---

- [1] C. Janiak, H.-J. Meyer, D. Gudat, P. Kurz, *Riedel Moderne Anorganische Chemie*, De Gruyter, Berlin, Boston, **2018**.
- [2] F. H. Spedding, K. Gschneidner Jr., A. H. Daane, *J. Am. Chem. Soc.* **1958**, *80*, 4499–4503.
- [3] M. Zayat, D. Levy, *Chem. Mater.* **2000**, *12*, 2763–2769.
- [4] H. Kohlmann, *Eur. J. Inorg. Chem.* **2019**, *2019*, 4174–4180.
- [5] A. J. Martinolich, PhD thesis, Colorado State University **2017**.
- [6] A. J. Martinolich, J. R. Neilson, *Chem. Mater.* **2017**, *29*, 479–489.
- [7] K. Gibson, M. Ströbele, B. Blaschkowski, J. Glaser, M. Weisser, R. Srinivasan, H.-J. Kolb, H.-J. Meyer, *Z. Anorg. Allg. Chem.* **2003**, *629*, 1863–1870.
- [8] H.-J. Meyer, *Dalton Trans.* **2010**, *39*, 5973–5982.
- [9] J. Ayres, PhD thesis, Cardiff University **2018**.
- [10] H.-D. Schädler, L. Jäger, I. Senf, *Z. Anorg. Allg. Chem.* **1993**, *619*, 1115–1120.
- [11] X. Qiao, D. Mroz, A. J. Corkett, T. Bisswanger, R. Dronskowski, *Z. Anorg. Allg. Chem.* **2021**, *647*, 496–499.
- [12] M. G. Down, M. J. Haley, P. Hubberstey, R. J. Pulham, A. E. Thunder, *J. Chem. Soc., Dalton Trans.* **1978**, 1407–1411.
- [13] M. Neukirch, S. Tragl, H.-J. Meyer, *Inorg. Chem.* **2006**, *45*, 8188–8193.
- [14] U. Berger, W. Schnick, *J. Alloys Compd.* **1994**, *206*, 179–184.
- [15] M. Löber, M. Ströbele, H.-J. Meyer, *Z. Anorg. Allg. Chem.* **2021**, *647*, 1973–1977.
- [16] M. L. Kastens, W. G. McBurney, *Ind. Eng. Chem.* **1951**, *43*, 1020–1033.
- [17] K. Suzuki, N. Kashiwa, K. Nomura, R. Asiloglu, N. Harada, *Biol. Fertil. Soils* **2021**, *57*, 269–279.
- [18] F. Di Gioia, M. Gonnella, V. Buono, O. Ayala, J. Cacchiarelli, P. Santamaria, *Agron. J.* **2017**, *109*, 354–362.
- [19] U. Dehlinger, *Z. Kristallogr. Cryst. Mater.* **1927**, *65*, 286–290.
- [20] a) M. A. Bredig, *J. Am. Chem. Soc.* **1942**, *64*, 1730–1731; b) Y. Yamamoto, K. Kinoshita, K. Tamaru, T. Yamanaka, *Bull. Chem. Soc. Jpn.* **1958**, *31*, 501–502; c) N.-G. Vannerberg, *Acta Chem. Scand.* **1962**, *16*, 2263–2266; d) O. Reckeweg, F. J. DiSalvo, *Z. Naturforsch. B* **2008**, *63*, 530–536.
- [21] M. Becker, J. Nuss, M. Jansen, *Z. Anorg. Allg. Chem.* **2000**, *626*, 2505–2508.
- [22] M. Becker, M. Jansen, *Solid State Sci.* **2000**, *2*, 711–715.
- [23] M. Krings, M. Wessel, W. Wilsmann, P. Müller, R. Dronskowski, *Inorg. Chem.* **2010**, *49*, 2267–2272.
- [24] a) R. Dronskowski, *Z. Naturforsch. B* **1995**, *50*, 1245–1251; b) R. Riedel, A. Greiner, G. Miehe, W. Dressler, H. Fuess, J. Bill, F. Aldinger, *Angew. Chem. Int. Ed.* **1997**, *36*, 603–606; c) X. Liu, A. Decker, D. Schmitz, R. Dronskowski, *Z. Anorg. Allg. Chem.* **2000**, *626*, 103–105; d) M. Löber, K. Dolabdjian, M. Ströbele, C. P. Romao, H.-J. Meyer, *Inorg. Chem.* **2019**, *58*, 7845–7851.
- [25] a) M. Becker, M. Jansen, *Acta Cryst.* **2001**, *C57*, 347–348; b) X. Liu, M. A. Wankeu, H. Lueken, R. Dronskowski, *Z. Naturforsch. B* **2005**, *60*, 593–596; c) X. Liu, M. Krott, P. Müller, C. Hu, H. Lueken, R. Dronskowski, *Inorg. Chem.* **2005**, *44*, 3001–3003; d) M. Krott, X. Liu, B. P. T. Fokwa, M. Speldrich, H. Lueken, R. Dronskowski, *Inorg. Chem.* **2007**, *46*, 2204–2207; e) X. Liu, L. Stork, M. Speldrich, H. Lueken, R. Dronskowski, *Chem. Eur. J.* **2009**, *15*, 1558–1561; f) K. B. Sterri, C. Besson, A. Houben, P. Jacobs, M. Hoelzel, R. Dronskowski, *New J. Chem.* **2016**, *40*, 10512–10519.
- [26] a) M. Becker, J. Nuss, M. Jansen, *Z. Naturforsch. B* **2000**, *55*, 383–385; b) M. Becker, M. Jansen, *Z. Anorg. Allg. Chem.* **2000**, *626*, 1639–1641; c) X. Liu, P. Müller, P. Kroll, R. Dronskowski, *Inorg. Chem.* **2002**, *41*, 4259–4265; d) G.

- Baldinozzi, B. Malinowska, M. Rakib, G. Durand, *J. Mater. Chem.* **2002**, *12*, 268–272; e) L. Stork, X. Liu, B. P. T. Fokwa, R. Dronskowski, *Z. Anorg. Allg. Chem.* **2007**, *633*, 1339–1342; f) K. Dolabdjian, A. Kobald, C. P. Romao, H.-J. Meyer, *Dalton Trans.* **2018**, *47*, 10249–10255.
- [27] a) O. Reckeweg, F. J. DiSalvo, *Z. Anorg. Allg. Chem.* **2003**, *629*, 177–179; b) O. Reckeweg, T. Schleid, F. J. DiSalvo, *Z. Naturforsch. B* **2007**, *62*, 658–662; c) J. Glaser, L. Unverfehrt, H. Bettentrup, G. Heymann, H. Huppertz, T. Jüstel, H.-J. Meyer, *Inorg. Chem.* **2008**, *47*, 10455–10460; d) D. Dutczak, M. Ströbele, D. Enseling, T. Jüstel, H.-J. Meyer, *Eur. J. Inorg. Chem.* **2016**, *2016*, 4011–4016; e) P. Kallenbach, M. Ströbele, H.-J. Meyer, *Z. Anorg. Allg. Chem.* **2020**, *646*, 1281–1284.
- [28] a) Y. Hashimoto, M. Takahashi, S. Kikkawa, F. Kanamaru, *J. Solid State Chem.* **1995**, *114*, 592–594; b) R. Srinivasan, J. Glaser, S. Tragl, H.-J. Meyer, *Z. Anorg. Allg. Chem.* **2005**, *631*, 479–483.
- [29] L. Unverfehrt, M. Ströbele, J. Glaser, H.-J. Meyer, *Z. Anorg. Allg. Chem.* **2009**, *635*, 1947–1952.
- [30] A. Harper, P. Hubberstey, *J. Chem. Res. (S)* **1989**, *7*, 194–195.
- [31] W. Schnick, H. Huppertz, *Z. Anorg. Allg. Chem.* **1995**, *621*, 1703–1707.
- [32] M. Becker, M. Jansen, *Z. Naturforsch. B* **1999**, *54*, 1375–1378.
- [33] R. Srinivasan, M. Ströbele, H.-J. Meyer, *Inorg. Chem.* **2003**, *42*, 3406–3411.
- [34] B. Wißmann, PhD thesis, Eberhard Karls Universität Tübingen **2001**.
- [35] W. Liao, R. Dronskowski, *Z. Anorg. Allg. Chem.* **2005**, *631*, 496–498.
- [36] R. Srinivasan, S. Tragl, H.-J. Meyer, *Z. Anorg. Allg. Chem.* **2005**, *631*, 719–722.
- [37] L. Unverfehrt, M. Ströbele, H.-J. Meyer, *Inorg. Chem.* **2012**, *51*, 12925–12928.
- [38] R. Okada, K. Kawanishi, K. Katagiri, K. Inumaru, *Ceram. Int.* **2019**, *45*, 9325–9329.
- [39] K. Dolabdjian, PhD thesis, Eberhard Karls Universität Tübingen **2018**.
- [40] E. Säilynoja, M. Lastusaari, J. Hölsä, P. Porcher, *J. Lumin.* **1997**, *72*, 201–203.
- [41] J. Hölsä, R.-J. Lamminmäki, M. Lastusaari, E. Säilynoja, P. Porcher, P. Dereń, W. Stręk, *Spectrochim. Acta A Mol. Biomol. Spectrosc.* **1998**, *54*, 2065–2069.
- [42] X. Guo, W. Yu, X. Dong, J. Wang, Q. Ma, G. Liu, M. Yang, *J. Am. Ceram. Soc.* **2015**, *98*, 1215–1222.
- [43] X. Guo, W. Yu, X. Dong, J. Wang, Q. Ma, G. Liu, M. Yang, *Eur. J. Inorg. Chem.* **2015**, *2015*, 389–396.
- [44] X. Tang, H. Xiang, X. Liu, M. Speldrich, R. Dronskowski, *Angew. Chem. Int. Ed.* **2010**, *49*, 4738–4742.
- [45] X. Qiao, K. Chen, A. J. Corkett, D. Mroz, X. Huang, R. Wang, R. Nelson, R. Dronskowski, *Inorg. Chem.* **2021**, *60*, 12664–12670.
- [46] M. J. Cooper, *Acta Cryst.* **1964**, *17*, 1452–1456.
- [47] U. Berger, W. Milius, W. Schnick, *Z. Anorg. Allg. Chem.* **1995**, *621*, 2075–2082.
- [48] Y. Hashimoto, M. Takahashi, S. Kikkawa, F. Kanamaru, *J. Solid State Chem.* **1996**, *125*, 37–42.
- [49] M. Li, W. Yuan, J. Wang, C. Gu, H. Zhao, *Powder Diffr.* **2007**, *22*, 59–63.
- [50] O. Reckeweg, F. J. DiSalvo, *Angew. Chem. Int. Ed.* **2000**, *39*, 412–414.
- [51] R. Niewa, P. Höhn, R. Kniep, A. Weiske, H. Jacobs, *Z. Kristallogr. NCS* **2001**, *216*, 335–336.
- [52] W. Liao, B. P. T. Fokwa, R. Dronskowski, *Chem. Commun.* **2005**, 3612–3614.
- [53] W. Liao, U. Englert, R. Dronskowski, *Eur. J. Inorg. Chem.* **2006**, *2006*, 4233–4236.
- [54] J. Sindlinger, J. Glaser, H. Bettentrup, T. Jüstel, H.-J. Meyer, *Z. Anorg. Allg. Chem.* **2007**, *633*, 1686–1690.

- [55] L. Unverfehrt, J. Glaser, M. Ströbele, S. Tragl, K. Gibson, H.-J. Meyer, *Z. Anorg. Allg. Chem.* **2009**, 635, 479–483.
- [56] L. Unverfehrt, PhD thesis, Eberhard Karls Universität Tübingen **2011**.
- [57] M. Kubus, J. Glaser, A. Klonkowski, H.-J. Meyer, *Z. Anorg. Allg. Chem.* **2010**, 636, 991–995.
- [58] L. Unverfehrt, M. Ströbele, J. Glaser, T. Langer, R.-D. Hoffmann, R. Pöttgen, H.-J. Meyer, *Inorg. Chem.* **2011**, 50, 6010–6018.
- [59] S. Zhang, D. A. Zharebtsov, F. J. DiSalvo, R. Niewa, *Z. Anorg. Allg. Chem.* **2012**, 638, 2111–2116.
- [60] K. Dolabdjian, A. L. Görne, R. Dronskowski, M. Ströbele, H.-J. Meyer, *Dalton Trans.* **2018**, 47, 13378–13383.
- [61] M. Löber, M. Ströbele, C. P. Romao, H.-J. Meyer, *Eur. J. Inorg. Chem.* **2021**, 2021, 4572–4578.
- [62] A. J. Corkett, Z. Chen, D. Bogdanovski, A. Slabon, R. Dronskowski, *Inorg. Chem.* **2019**, 58, 6467–6473.
- [63] D. Dutczak, A. Siai, M. Ströbele, D. Enseling, T. Jüstel, H.-J. Meyer, *Eur. J. Inorg. Chem.* **2020**, 2020, 3954–3958.
- [64] X. Qiao, X. Liu, L. Bayarjargal, A. J. Corkett, W. Wang, Z. Ma, Z. Lin, R. Dronskowski, *J. Mater. Chem. C* **2021**, 9, 967–974.
- [65] R. Srinivasan, PhD thesis, Eberhard Karls Universität Tübingen **2004**.
- [66] M. Kubus, D. Enseling, T. Jüstel, H.-J. Meyer, *Eur. J. Inorg. Chem.* **2013**, 2013, 3195–3199.
- [67] M. Löber, C. S. Geißenhöner, M. Ströbele, S. Indris, C. P. Romao, H.-J. Meyer, *Inorg. Chem.* **2019**, 58, 14560–14567.
- [68] F. Jach, P. Höhn, Y. Prots, M. Ruck, *Eur. J. Inorg. Chem.* **2019**, 2019, 1207–1211.
- [69] M. G. Barker, A. Harper, P. J. Hubberstey, *J. Chem. Res. (S)* **1978**, 432–433.
- [70] M. Becker, M. Jansen, *J. Chem. Res. (S)* **1998**, 86–87.
- [71] M. Becker, M. Jansen, A. Lieb, W. Milius, W. Schnick, *Z. Anorg. Allg. Chem.* **1998**, 624, 113–118.
- [72] T. Roßmeier, N. Korber, *Z. Anorg. Allg. Chem.* **2006**, 632, 228–230.
- [73] M. Krott, X. Liu, P. Müller, R. Dronskowski, *J. Solid State Chem.* **2007**, 180, 307–312.
- [74] X. Tang, A. Houben, X. Liu, L. Stork, R. Dronskowski, *Z. Anorg. Allg. Chem.* **2011**, 637, 1089–1091.
- [75] L. Unverfehrt, M. Ströbele, H.-J. Meyer, *Z. Anorg. Allg. Chem.* **2013**, 639, 22–24.
- [76] M. Kubus, R. Heinicke, M. Ströbele, D. Enseling, T. Jüstel, H.-J. Meyer, *Mater. Res. Bull.* **2015**, 62, 37–41.
- [77] A. J. Corkett, P. M. Konze, R. Dronskowski, *Z. Anorg. Allg. Chem.* **2017**, 643, 1456–1461.
- [78] A. J. Corkett, P. M. Konze, R. Dronskowski, *Inorganics* **2018**, 6, 1.
- [79] K. Dolabdjian, C. Castro, H.-J. Meyer, *Eur. J. Inorg. Chem.* **2018**, 2018, 1624–1630.
- [80] A. J. Corkett, K. Chen, R. Dronskowski, *Eur. J. Inorg. Chem.* **2020**, 2020, 2596–2602.
- [81] J. Glaser, H.-J. Meyer, *Angew. Chem. Int. Ed.* **2008**, 47, 7547–7550.
- [82] J. Glaser, H. Bettentrup, T. Jüstel, H.-J. Meyer, *Inorg. Chem.* **2010**, 49, 2954–2959.
- [83] L. Unverfehrt, M. Kalmutzki, M. Ströbele, H.-J. Meyer, *Dalton Trans.* **2011**, 40, 9921–9924.



#### 4. References

---

- [84] L. Unverfehrt, M. Ströbele, H.-J. Meyer, *Z. Anorg. Allg. Chem.* **2013**, *639*, 1722–1725.
- [85] L. Unverfehrt, M. Ströbele, H.-J. Meyer, *Z. Anorg. Allg. Chem.* **2013**, *639*, 84–88.
- [86] M. Kalmutzki, D. Enseling, J. E. C. Wren, S. Kroeker, V. V. Terskikh, T. Jüstel, H.-J. Meyer, *Inorg. Chem.* **2013**, *52*, 12372–12382.
- [87] M. Kalmutzki, M. Ströbele, S. Kroeker, J. E. C. Wren, H.-J. Meyer, *Eur. J. Inorg. Chem.* **2013**, *2013*, 6091–6096.
- [88] K. Dolabdjian, C. Schedel, D. Enseling, T. Jüstel, H.-J. Meyer, *Z. Anorg. Allg. Chem.* **2017**, *643*, 488–494.
- [89] A. J. Corkett, R. Dronskowski, *Dalton Trans.* **2019**, *48*, 15029–15035.
- [90] X. Qiao, A. J. Corkett, R. P. Stoffel, R. Dronskowski, *Z. Anorg. Allg. Chem.* **2021**, *647*, 2162–2166.
- [91] U. Berger, W. Schnick, *Z. Naturforsch. B* **1996**, *51*, 1–8.
- [92] W. Liao, C. Hu, R. K. Kremer, R. Dronskowski, *Inorg. Chem.* **2004**, *43*, 5884–5890.
- [93] W. Liao, J. von Appen, R. Dronskowski, *Chem. Commun.* **2004**, 2302–2303.
- [94] W. Liao, R. Dronskowski, *Z. Anorg. Allg. Chem.* **2005**, *631*, 1953–1956.
- [95] P. M. Mallinson, Z. A. Gál, S. J. Clarke, *Inorg. Chem.* **2006**, *45*, 419–423.
- [96] W. Liao, R. Dronskowski, *Inorg. Chem.* **2006**, *45*, 3828–3830.
- [97] J. K. Bendyna, P. Höhn, W. Schnelle, R. Kniep, *Sci. Technol. Adv. Mater.* **2007**, *8*, 393–398.
- [98] J. K. Bendyna, P. Höhn, R. Kniep, *Z. Kristallogr. - New Cryst. Struct.* **2009**, *224*, 5–6.
- [99] W. P. Clark, R. Niewa, *Z. Anorg. Allg. Chem.* **2020**, *646*, 114–119.
- [100] A. Olivé Corral, M. Kubus, M. Ströbele, H.-J. Meyer, *Z. Anorg. Allg. Chem.* **2014**, *640*, 902–904.
- [101] K. Dolabdjian, H.-J. Meyer, *Z. Anorg. Allg. Chem.* **2017**, *643*, 1898–1903.
- [102] X. Meng, F. Liang, W. Yin, Z. Lin, M. Xia, *New J. Chem.* **2019**, *43*, 9766–9770.
- [103] O. Reckeweg, A. Schulz, F. J. DiSalvo, *Z. Naturforsch. B* **2013**, *68*, 39–43.
- [104] a) A. Eguía-Barrio, E. Castillo-Martínez, X. Liu, R. Dronskowski, M. Armand, T. Rojo, *J. Mater. Chem. A* **2016**, *4*, 1608–1611; b) M. T. Sougrati, A. Darwiche, X. Liu, A. Mahmoud, R. P. Hermann, S. Jouen, L. Monconduit, R. Dronskowski, L. Stievano, *Angew. Chem. Int. Ed.* **2016**, *55*, 5090–5095; c) A. Eguía-Barrio, E. Castillo-Martínez, X. Liu, R. Dronskowski, L. Lezama, M. Armand, T. Rojo, *MRS Advances* **2017**, *2*, 1165–1176; d) A. Eguía-Barrio, E. Castillo-Martínez, F. Klein, R. Pinedo, L. Lezama, J. Janek, P. Adelhelm, T. Rojo, *J. Power Sources* **2017**, *367*, 130–137; e) M. T. Sougrati, J. J. Arayampambil, X. Liu, M. Mann, A. Slabon, L. Stievano, R. Dronskowski, *Dalton Trans.* **2018**, *47*, 10827–10832; f) J. J. Arayampambil, M. Mann, B. Fraisse, A. Iadecola, R. Dronskowski, L. Stievano, M. T. Sougrati, *ChemElectroChem* **2019**, *6*, 5101–5108.
- [105] a) M. Davi, A. Drichel, M. Mann, T. Scholz, F. Schrader, A. Rokicinska, P. Kustrowski, R. Dronskowski, A. Slabon, *J. Phys. Chem. C* **2017**, *121*, 26265–26274; b) M. Davi, M. Mann, Z. Ma, F. Schrader, A. Drichel, S. Budnyk, A. Rokicinska, P. Kustrowski, R. Dronskowski, A. Slabon, *Langmuir* **2018**, *34*, 3845–3852; c) Z. Chen, A. J. Corkett, C. de Bruin-Dickason, J. Chen, A. Rokicińska, P. Kuśtrowski, R. Dronskowski, A. Slabon, *Inorg. Chem.* **2020**, *59*, 13589–13597.
- [106] Z. Fu, Y. Wang, Z. Li, T. Song, B. Long, A. Ali, G.-J. Deng, *J. Colloid Interface Sci.* **2021**, *593*, 152–161.

#### 4. References

---

- [107] M. Grundmann, *The Physics of Semiconductors, Vol. 4*, Springer International Publishing, Basel, **2021**.
- [108] W. H. Baur, *Acta Cryst.* **1956**, *9*, 515–520.
- [109] E. Müller, *Acta Cryst.* **1984**, *B40*, 359–363.
- [110] M. N. Gitlitz, M. K. Moran, in *Kirk-Othmer Encyclopedia of Chemical Technology*, **2006**.
- [111] M. Karmaoui, A. B. Jorge, P. F. McMillan, A. E. Aliev, R. C. Pullar, J. A. Labrincha, D. M. Tobaldi, *ACS omega* **2018**, *3*, 13227–13238.
- [112] N. Bhardwaj, A. Pandey, B. Satpati, M. Tomar, V. Gupta, S. Mohapatra, *Phys. Chem. Chem. Phys.* **2016**, *18*, 18846–18854.
- [113] A. Kolmakov, Y. Zhang, G. Cheng, M. Moskovits, *Adv. Mater.* **2003**, *15*, 997–1000.
- [114] D. L. Kamble, N. S. Harale, V. L. Patil, P. S. Patil, L. D. Kadam, *J. Anal. Appl. Pyrolysis* **2017**, *127*, 38–46.
- [115] J. Shu, Z. Qiu, S. Lv, K. Zhang, D. Tang, *Anal. Chem.* **2017**, *89*, 11135–11142.
- [116] a) M.-S. Park, G.-X. Wang, Y.-M. Kang, D. Wexler, S.-X. Dou, H.-K. Liu, *Angew. Chem. Int. Ed.* **2007**, *46*, 750–753; b) D. McNulty, H. Geaney, Q. Ramasse, C. O'Dwyer, *Adv. Funct. Mater.* **2020**, *30*, 2005073.
- [117] L. Xiong, Y. Guo, J. Wen, H. Liu, G. Yang, P. Qin, G. Fang, *Adv. Funct. Mater.* **2018**, *28*, 1802757.
- [118] D. J. Sirbully, A. Tao, M. Law, R. Fan, P. Yang, *Adv. Mater.* **2007**, *19*, 61–66.
- [119] S. Mathur, S. Barth, H. Shen, J.-C. Pyun, U. Werner, *Small* **2005**, *1*, 713–717.
- [120] H. Zhang, C. Hu, *Catal. Commun.* **2011**, *14*, 32–36.
- [121] M. G. Helander, M. T. Greiner, Z. B. Wang, W. M. Tang, Z. H. Lu, *J. Vac. Sci. Technol. A* **2011**, *29*, 011019.
- [122] a) H. Kim, C. M. Gilmore, A. Piqué, J. S. Horwitz, H. Mattoussi, H. Murata, Z. H. Kafafi, D. B. Chrisey, *J. Appl. Phys.* **1999**, *86*, 6451–6461; b) T. Minami, *Thin Solid Films* **2008**, *516*, 5822–5828; c) S. Li, M. Tian, Q. Gao, M. Wang, T. Li, Q. Hu, X. Li, Y. Wu, *Nat. Mater.* **2019**, *18*, 1091–1097.
- [123] J. Pannetier, G. Denes, *Acta Cryst.* **1980**, *B36*, 2763–2765.
- [124] J. Köhler, J. Tong, R. Dinnebier, A. Simon, *Z. Anorg. Allg. Chem.* **2012**, *638*, 1970–1975.
- [125] Y. Ogo, H. Hiramatsu, K. Nomura, H. Yanagi, T. Kamiya, M. Hirano, H. Hosono, *Appl. Phys. Lett.* **2008**, *93*, 032113.
- [126] a) K. Nomura, in *SID Symposium Digest of Technical Papers, Vol. 46*, Wiley Online Library, San Jose, **2015**, pp. 591–594; b) K. J. Saji, K. Tian, M. Snure, A. Tiwari, *Adv. Electron. Mater.* **2016**, *2*, 1500453; c) K. J. Saji, Y. V. Subbaiah, K. Tian, A. Tiwari, *Thin Solid Films* **2016**, *605*, 193–201; d) X. Guan, Z. Wang, M. K. Hota, H. N. Alshareef, T. Wu, *Adv. Electron. Mater.* **2019**, *5*, 1800538.
- [127] X. An, S. Li, A. Yoshida, T. Yu, Z. Wang, X. Hao, A. Abudula, G. Guan, *ACS Appl. Mater. Interfaces* **2019**, *11*, 42114–42122.
- [128] a) J. Ning, T. Jiang, K. Men, Q. Dai, D. Li, Y. Wei, B. Liu, G. Chen, B. Zou, G. Zou, *J. Phys. Chem. C* **2009**, *113*, 14140–14144; b) S. Jaśkaniec, S. R. Kavanagh, J. Coelho, S. Ryan, C. Hobbs, A. Walsh, D. O. Scanlon, V. Nicolosi, *npj 2D Mater. Appl.* **2021**, *5*, 27.
- [129] Y. C. Lu, C. Ma, J. Alvarado, T. Kidera, N. Dimov, Y. S. Meng, S. Okada, *J. Power Sources* **2015**, *284*, 287–295.
- [130] a) P. H. Suman, A. A. Felix, H. L. Tuller, J. A. Varela, M. O. Orlandi, *Sens. Actuators B Chem.* **2013**, *186*, 103–108; b) P. H. Suman, A. A. Felix, H. L. Tuller, J. A. Varela, M. O. Orlandi, *Sens. Actuators B Chem.* **2015**, *208*, 122–127.
- [131] J. Wang, N. Umezawa, H. Hosono, *Adv. Energy Mater.* **2016**, *6*, 1501190.

#### 4. References

---

- [132] T. A. White, M. S. Moreno, P. A. Midgley, *Z. Kristallogr.* **2010**, *225*, 56–66.
- [133] a) B. F. Bilenkii, A. G. Mikolaichuk, D. M. Freik, *Phys. Status Solidi* **1968**, *28*, K5–K7; b) D. L. Greenaway, R. Nitsche, *J. Phys. Chem. Solids* **1965**, *26*, 1445–1458; c) D. Mootz, H. Puhl, *Acta Cryst.* **1967**, *23*, 471–476.
- [134] N. Koteeswara Reddy, M. Devika, E. S. R. Gopal, *Crit. Rev. Solid State Mater. Sci.* **2015**, *40*, 359–398.
- [135] a) J.-G. Kang, J.-G. Park, D.-W. Kim, *Electrochem. Commun.* **2010**, *12*, 307–310; b) J. Lu, C. Nan, L. Li, Q. Peng, Y. Li, *Nano Res.* **2013**, *6*, 55–64.
- [136] A. Voznyi, V. Kosyak, L. Grase, J. Vecstaudža, P. Onufrijevs, Y. Yeromenko, A. Medvid, A. Opanasyuk, *Mater. Sci. Semicond. Process.* **2018**, *79*, 32–39.
- [137] X. Huang, H. Woo, P. Wu, H. J. Hong, W. G. Jung, B.-J. Kim, J.-C. Vanel, J. W. Choi, *Sci. Rep.* **2017**, *7*, 16531.
- [138] a) T. Momma, N. Shiraishi, A. Yoshizawa, T. Osaka, A. Gedanken, J. Zhu, L. Sominski, *J. Power Sources* **2001**, *97–98*, 198–200; b) T.-J. Kim, C. Kim, D. Son, M. Choi, B. Park, *J. Power Sources* **2007**, *167*, 529–535.
- [139] Y. Zuo, Y. Liu, J. Li, R. Du, X. Yu, C. Xing, T. Zhang, L. Yao, J. Arbiol, J. Llorca, K. Sivula, N. Guijarro, A. Cabot, *ACS Appl. Mater. Interfaces* **2019**, *11*, 6918–6926.
- [140] a) Z.-G. Chen, X. Shi, L.-D. Zhao, J. Zou, *Prog. Mater. Sci.* **2018**, *97*, 283–346; b) R. Moshwan, L. Yang, J. Zou, Z.-G. Chen, *Adv. Funct. Mater.* **2017**, *27*, 1703278; c) R. Moshwan, W.-D. Liu, X.-L. Shi, Y.-P. Wang, J. Zou, Z.-G. Chen, *Nano Energy* **2019**, *65*, 104056; d) G. Li, G. Ding, G. Gao, *J. Phys.: Condens. Matter* **2016**, *29*, 015001.
- [141] J.-S. Liu, X.-H. Li, Y.-X. Guo, A. Qyyum, Z.-J. Shi, T.-C. Feng, Y. Zhang, C.-X. Jiang, X.-F. Liu, *Small* **2019**, *15*, 1902811.
- [142] N.-G. Park, *Mater. Today* **2015**, *18*, 65–72.
- [143] G. Kim, H. Min, K. S. Lee, S. M. Yoon, S. I. Seok, *Science* **2020**, *370*, 108–112.
- [144] A. Al-Ashouri, E. Köhnen, B. Li, A. Magomedov, H. Hempel, P. Caprioglio, J. A. Márquez, A. B. M. Vilches, E. Kasparavicius, J. A. Smith, N. Phung, D. Menzel, M. Grischek, L. Kegelmann, D. Skroblin, C. Gollwitzer, T. Malinauskas, M. Jošt, G. Matič, B. Rech, R. Schlatmann, M. Topič, L. Korte, A. Abate, B. Stannowski, D. Neher, M. Stolterfoht, T. Unold, V. Getautis, S. Albrecht, *Science* **2020**, *370*, 1300–1309.
- [145] U. Krishnan, M. Kaur, M. Kumar, A. Kumar, *J. Photonics Energy* **2019**, *9*, 021001.
- [146] Q. Tai, K.-C. Tang, F. Yan, *Energy Environ. Sci.* **2019**, *12*, 2375–2405.
- [147] J. Jiang, C. K. Onwudinanti, R. A. Hatton, P. A. Bobbert, S. Tao, *J. Phys. Chem. C* **2018**, *122*, 17660–17667.
- [148] Z. Chen, M. Löber, A. Rokicińska, Z. Ma, J. Chen, P. Kuśtrowski, H.-J. Meyer, R. Dronskowski, A. Slabon, *Dalton Trans.* **2020**, *49*, 3450–3456.
- [149] J. E. Yourey, B. M. Bartlett, *J. Mater. Chem.* **2011**, *21*, 7651–7660.
- [150] Z. Lv, W. Dong, B. Jia, S. Zhang, M. Xie, W. Zhao, F. Huang, *Chem. Eur. J.* **2021**, *27*, 2717–2723.
- [151] M. Löber, C. S. Geißenhöner, M. Ströbele, C. P. Romao, H. J. Meyer, *Eur. J. Inorg. Chem.* **2021**, *2021*, 283–288.
- [152] Z. Lu, F. Zhang, A. Tudi, Z. Yang, Z. Li, S. Pan, *J. Mater. Chem. C* **2021**, *9*, 7103–7109.
- [153] M. Löber, M. Ströbele, C. P. Romao, H.-J. Meyer, *Dalton Trans.* **2021**, *50*, 6789–6792.
- [154] J. Tillack, P. Eckerlin, J. H. Dettingmeijer, *Angew. Chem. Int. Ed.* **1966**, *5*, 421–421.

#### 4. References

---

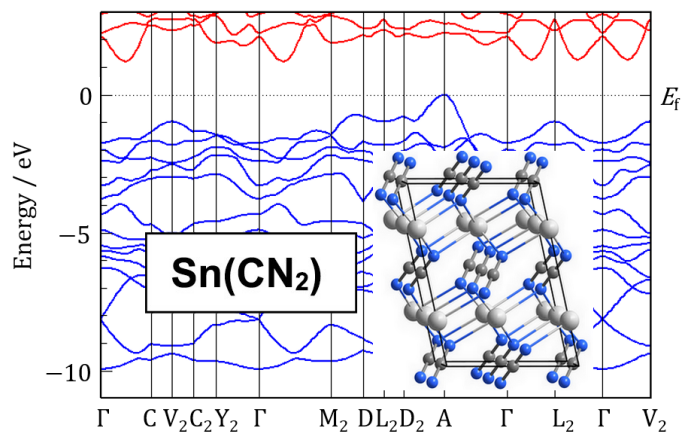
- [155] M. Ströbele, H.-J. Meyer, *Dalton Trans.* **2019**, 48, 1547–1561.
- [156] M. Ströbele, H.-J. Meyer, *Russ. J. Coord. Chem.* **2012**, 38, 178–182.
- [157] S. L. Benjamin, Y.-P. Chang, A. L. Hector, M. Jura, W. Levason, G. Reid, G. Stenning, *Dalton Trans.* **2016**, 45, 8192–8200.
- [158] L. F. Dahl, D. L. Wampler, *Acta Cryst.* **1962**, 15, 903–911.
- [159] M. Binnewies, *Chem. Unserer Zeit* **1986**, 20, 141–145.
- [160] C. Braun, L. Mereacre, W. Hua, T. Stuerzer, I. Ponomarev, P. Kroll, A. Slabon, Z. Chen, Y. Damour, X. Rocquefelte, J.-F. Halet, S. Indris, *ChemElectroChem* **2020**, 7, 4550–4561.
- [161] M. Löber, M. Ströbele, K. Eichele, C. P. Romao, H.-J. Meyer, *Eur. J. Inorg. Chem.* **2021**, 2021, 4929–4934.
- [162] W.-F. Yang, F. Igbari, Y.-H. Lou, Z.-K. Wang, L.-S. Liao, *Adv. Energy Mater.* **2020**, 10, 1902584.
- [163] M. L. Petrus, J. Schlipf, C. Li, T. P. Gujar, N. Giesbrecht, P. Müller-Buschbaum, M. Thelakkat, T. Bein, S. Hüttner, P. Docampo, *Adv. Energy Mater.* **2017**, 7, 1700264.
- [164] R. A. Howie, W. Moser, I. C. Trevena, *Acta Cryst.* **1972**, B28, 2965–2971.
- [165] P. Ravindran, A. Delin, R. Ahuja, B. Johansson, S. Auluck, J. M. Wills, O. Eriksson, *Phys. Rev. B* **1997**, 56, 6851–6861.

## **5. Publications**



# Publication 1

Synthesis, Structure, and Electronic Properties of  $\text{Sn}(\text{CN}_2)$  and  $\text{Sn}_4\text{Cl}_2(\text{CN}_2)_3$



<https://doi.org/10.1021/acs.inorgchem.9b00527>

Reprinted with permission from

*Inorg. Chem.* **2019**, *58*, 7845–7851

Copyright © 2019 American Chemical Society





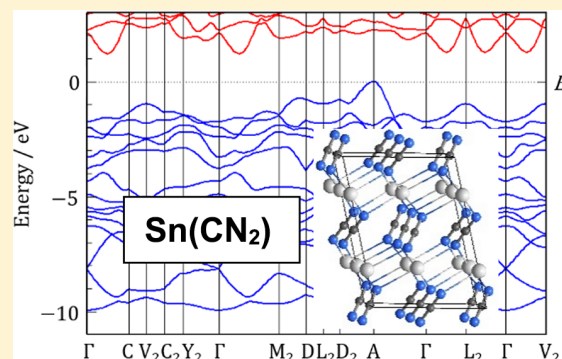
# Synthesis, Structure, and Electronic Properties of $\text{Sn}(\text{CN}_2)$ and $\text{Sn}_4\text{Cl}_2(\text{CN}_2)_3$

Manuel Löber, Konstantin Dolabdjian, Markus Ströbele,<sup>ib</sup> Carl P. Romao, and Hans-Jürgen Meyer\*<sup>ib</sup>

Section of Solid State and Theoretical Inorganic Chemistry, Institute of Inorganic Chemistry, University of Tübingen, Auf der Morgenstelle 18, D-72076 Tübingen, Germany

## S Supporting Information

**ABSTRACT:** A solid-state metathesis reaction between equimolar amounts of  $\text{Li}_2(\text{CN}_2)$  and  $\text{SnCl}_2$  revealed the formation of two new compounds,  $\text{Sn}_4\text{Cl}_2(\text{CN}_2)_3$  and  $\text{Sn}(\text{CN}_2)$ . Thermal analysis of this reaction indicated that  $\text{Sn}_4\text{Cl}_2(\text{CN}_2)_3$  forms exothermically near 200 °C and subsequently transforms into  $\text{Sn}(\text{CN}_2)$  at higher temperatures. The crystal structures of both compounds are presented. According to optical measurements and band structure calculations,  $\text{Sn}(\text{CN}_2)$  can be considered as a semiconductor with a band gap on the order of 2 eV. The presence of  $\text{Sn}^{2+}$  ions in the structure of  $\text{Sn}(\text{CN}_2)$  with a toroidally shaped lone pair is indicated by electron localization function calculations. The structure of  $\text{Sn}(\text{CN}_2)$  is shown to be related to the structures of  $\text{FeS}_2$  and  $\text{CaC}_2$ .



## INTRODUCTION

The development of metal dinitridocarbonates, which assume the carbodiimide ( $\text{N}=\text{C}=\text{N}$ )<sup>2-</sup> or cyanamide ( $\text{N}-\text{C}\equiv\text{N}$ )<sup>2-</sup> moiety, has progressed to include compounds with rare earth,<sup>1,2</sup> transition metal,<sup>3–7</sup> and main group elements.<sup>8–12</sup> These compounds are occasionally considered as pseudo-oxides with a spatially elongated  $(\text{NCN})^{2-}$  ion. Carbodiimides of the group IV elements are exemplified by  $\text{Si}(\text{CN}_2)_2$ ,<sup>13</sup>  $\text{Pb}(\text{CN}_2)_2$ ,<sup>14</sup> and the structurally related compounds  $\text{APb}_2\text{Cl}_3(\text{CN}_2)$  ( $\text{A} = \text{Li}, \text{Na}, \text{Ag}$ ).<sup>15</sup> The structures and optical properties of several tetracyanamido-metallates with a pseudotetrahedrally shaped  $[\text{T}(\text{CN}_2)_4]^{n-}$  ion ( $\text{T} = \text{Si}, \text{Ge}, \text{Ga}, \text{Al}$ ) have been reported.<sup>16–19</sup> However, this series of compounds is not continued for  $\text{T} = \text{Sn}$  and  $\text{Pb}$ .

Tin carbodiimides can appear in two different oxidation states.  $\text{Sn}(\text{IV})$  compounds have been reported as  $\text{A}_2\text{Sn}(\text{CN}_2)_3$  with  $\text{A} = \text{Li}$  or  $\text{Na}$ ,<sup>20</sup> and  $\text{Sn}(\text{II})$  is present in the carbodiimide-oxide  $\text{Sn}_2\text{O}(\text{CN}_2)$ .<sup>21</sup>  $\text{Sn}_2\text{O}(\text{CN}_2)$ , like  $\text{SnO}$ , is a semiconductor with a reported band gap on the order of 1–2 eV. Tin atoms in the  $\text{PbO}$ -type crystal structure of  $\alpha\text{-SnO}$  are surrounded with  $\text{O}^{2-}$  in a square fashion, yielding a  $[\text{SnO}_4]$  square pyramid; a similar  $\text{Sn}^{2+}$  environment is found in  $\text{Sn}_2\text{O}(\text{CN}_2)$ . This typical arrangement is consistent with  $\text{Sn}^{2+}$  possessing a stereochemically active lone pair.

The recently reported compound  $\text{Sn}_2\text{O}(\text{CN}_2)$  was originally obtained as a minority phase in the synthesis of  $\text{Li}_2\text{Sn}(\text{CN}_2)_3$ , demonstrating that reactions in this system can produce divalent or tetravalent tin. A thermoanalytical study of the synthesis of  $\text{Sn}_2\text{O}(\text{CN}_2)$  revealed the presence of intermediate compounds during the reaction; one of these was proposed to be  $\text{Sn}_4\text{Cl}_2(\text{CN}_2)_3$ . A closer study of reactivity in the  $\text{Li}_2(\text{CN}_2)/\text{SnCl}_2$  system now confirms the compound  $\text{Sn}_4\text{Cl}_2(\text{CN}_2)_3$  as an

intermediate phase which also appears in the formation of the new compound  $\text{Sn}(\text{CN}_2)$ . The structures and properties of both compounds are the subject of this work.

## EXPERIMENTAL AND CALCULATION DETAILS

**Synthesis of  $\text{Sn}(\text{CN}_2)$ .**  $\text{Li}_2(\text{CN}_2)$ <sup>1</sup> and  $\text{SnCl}_2$  (Sigma-Aldrich 99.999% ultradry) or  $\text{SnF}_2$  (Sigma-Aldrich 99%), respectively, were mixed in an agate mortar under a dry argon atmosphere (glovebox) in 1:1 molar ratio (total mass: 300 mg). The mixture with  $\text{SnCl}_2$  was sealed into a silica tube under vacuum, and the mixture with  $\text{SnF}_2$  was sealed into a niobium tube by arc-welding (and then fused into an evacuated silica ampule). Both reaction mixtures were heated in a crucible furnace up to 450 °C with a heating rate of 3 K  $\text{min}^{-1}$  and held at this temperature for 20 h before cooling to room temperature at 2 K  $\text{min}^{-1}$ . Reaction products were washed with ethanol and dried at 80 °C in a drying oven.

**Synthesis of  $\text{Sn}_4\text{Cl}_2(\text{CN}_2)_3$ .**  $\text{Li}_2(\text{CN}_2)$ <sup>1</sup> and  $\text{SnCl}_2$  (Sigma-Aldrich 99.999% ultradry) were mixed in a 3:4 molar ratio in an agate mortar and sealed into a silica tube under vacuum. The mixture was heated in a crucible furnace to 250 °C with a heating rate of 3 K/min and kept at this temperature for 5 h before being cooled to room temperature at 3 K/min. The crystalline powder was removed from the ampule, washed with ethanol, and dried at 80 °C in air.

**Thermoanalytical Studies.** Differential thermal analysis (DTA) was performed with a STA 449F3 Jupiter; Fa. Netzsch, Selb, Germany. Samples were fused into homemade silica containers and analyzed between room temperature and 500 °C with a heating and cooling rate of 2 K  $\text{min}^{-1}$ .

**X-ray Powder Diffraction.** X-ray powder diffraction (XRPD) was carried out with a powder diffractometer (STOE Darmstadt, STADI-P, Ge-monochromator) using  $\text{Cu K}\alpha_1$  ( $\lambda = 1.540598$  Å) radiation in

Received: February 22, 2019

Published: June 5, 2019

the range of  $5 < 2\theta < 120^\circ$ . The recorded X-ray powder diffraction patterns were indexed, and the crystal structure was subsequently solved with the program EXPO2009.<sup>22</sup> Structure refinement was performed using the Fullprof Suite.<sup>23</sup> The structure refinement based on the preparation with  $\text{SnCl}_2$  showed few weak unmatched reflections of unknown origin. The refinement based on the synthesis of  $\text{SnF}_2$  revealed  $\text{LiF}$  and elemental  $\text{Sn}$  (<10%) as a side phase.

**Single-Crystal X-ray Diffraction.** Data collection for single-crystal X-ray diffraction (XRD) was performed using a Bruker APEX DUO CCD diffractometer with  $\text{Mo-K}\alpha$  radiation ( $\lambda = 0.71073 \text{ \AA}$ ) and a graphite monochromator. Corrections for absorption effects were applied with SADABS.<sup>24</sup> The structure was solved by direct methods (SHELXS),<sup>25</sup> and full-matrix least-squares structure refinements were performed with SHELXL-2015.<sup>26</sup>

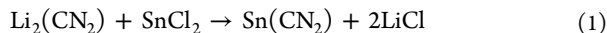
**Optical Measurements.** Reflection spectra of  $\text{Sn}(\text{CN}_2)$  and  $\text{Sn}_4\text{Cl}_2(\text{CN}_2)_3$  were recorded on an Edinburgh Instruments FS900 spectrometer equipped with a 450 W Xe arc lamp and a cooled single-photon counting photomultiplier (Hamamatsu R928).  $\text{BaSO}_4$  (99%, Sigma-Aldrich) was used as a reflectance standard.

**Infrared Spectra.** Vibrational spectra were recorded with a Bruker Vertex 70 spectrometer within the spectral range of  $400\text{--}4000 \text{ cm}^{-1}$ ; samples were prepared using KBr pellets.

**Density Functional Theory (DFT).** DFT calculations were performed using the ABINIT software package.<sup>27</sup> The Perdew–Burke–Ernzerhof exchange-correlation functional<sup>28,29</sup> was used with the vdW-DFT-D2 dispersion correction.<sup>30</sup> Optimized norm-conserving Vanderbilt pseudopotentials<sup>31</sup> from the ABINIT library were used as received. Electronic structures were determined following structural relaxation and convergence studies. Example input files are available as part of the [Supporting Information](#).

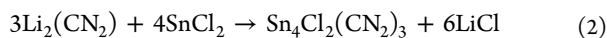
## RESULTS AND DISCUSSION

**Synthesis.** Reactions between  $\text{SnCl}_2$  and  $\text{Li}_2(\text{CN}_2)$  were explored in fused silica tubes at temperatures up to  $500^\circ\text{C}$ . Tin(II) carbodiimide was synthesized as a brown crystalline powder at  $450^\circ\text{C}$  from starting materials in equimolar proportions in accordance with [reaction 1](#).



The progression and course of the reaction was studied by DTA and differential scanning calorimetry (DSC) measurements. These studies revealed that the formation of  $\text{Sn}(\text{CN}_2)$  is not as straightforward as would be expected from [reaction 1](#). Thermal analysis clearly indicates that upon heating the reaction mixture (with a rate of  $2 \text{ K/min}$ ), the intermediate compound  $\text{Sn}_4\text{Cl}_2(\text{CN}_2)_3$  is formed close to  $200^\circ\text{C}$  (see below). However, no noticeable thermal effect could be assigned to the formation of  $\text{Sn}(\text{CN}_2)$ .

For the synthesis of pure  $\text{Sn}_4\text{Cl}_2(\text{CN}_2)_3$ , the proportion of starting materials was adjusted to a 3:4 molar ratio. Reactions in fused silica tubes at  $250^\circ\text{C}$  yielded a light brown crystalline powder of  $\text{Sn}_4\text{Cl}_2(\text{CN}_2)_3$  (see [reaction 2](#)).



Thermal analysis of [reaction 2](#) showed a strong exothermic reaction corresponding to the formation of  $\text{Sn}_4\text{Cl}_2(\text{CN}_2)_3$  at  $194^\circ\text{C}$  ([Figure 1](#)), with the melting and recrystallization shown in a second DTA cycle. The identity of the product was confirmed by PXRD. DTA studies also show that  $\text{Sn}_4\text{Cl}_2(\text{CN}_2)_3$  forms a melt with the coproduced  $\text{LiCl}$  at  $450^\circ\text{C}$  and remains stable up to  $550^\circ\text{C}$ .

Reaction between appropriate amounts of  $\text{Sn}_4\text{Cl}_2(\text{CN}_2)_3$  and  $\text{Li}_2(\text{CN}_2)$ , performed in fused silica tubes at  $400^\circ\text{C}$ , leads to the formation of  $\text{Sn}(\text{CN}_2)$  as given in [reaction 3](#).

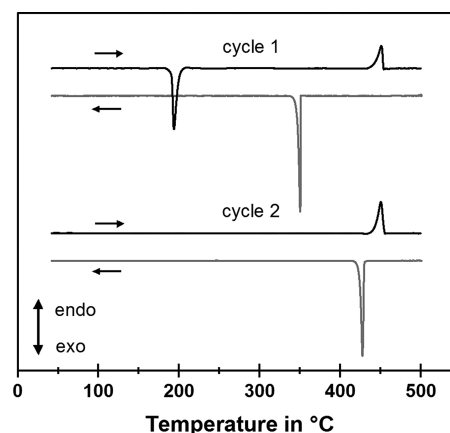
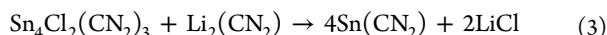


**Figure 1.** DTA of the reaction of  $\text{Li}_2(\text{CN}_2)$  and  $\text{SnCl}_2$  in 3:4 molar ratio according to [reaction 2](#).

The metathesis salt  $\text{LiCl}$  was removed from the reaction products with dry ethanol for [reactions 1–3](#).

DTA shows that the reaction of  $\text{Sn}_4\text{Cl}_2(\text{CN}_2)_3$  with  $\text{Li}_2(\text{CN}_2)$  into  $\text{Sn}(\text{CN}_2)$  occurs without a noticeable thermal effect near  $300^\circ\text{C}$ .

**Crystal Structure of  $\text{Sn}(\text{CN}_2)$ .** The crystal structure of  $\text{Sn}(\text{CN}_2)$  was solved and refined from a PXRD pattern with the monoclinic space group  $I2/a$  (no. 15). Due to the monoclinic angle of  $139.55^\circ$  in the standard setting  $C2/c$ , the use of the nonstandard setting  $I2/a$  is a common choice. The Rietveld refinement plot of  $\text{Sn}(\text{CN}_2)$  is displayed in [Figure 2](#), showing the presence of  $\text{LiF}$  as metathesis salt and elemental tin as a side phase. Crystallographic data are presented in [Table 1](#) and atomic positions in [Table 2](#).

The crystal structure of  $\text{Sn}(\text{CN}_2)$ , presented in [Figure 3](#), is comprised of an alternating sequence of layers of tin and carbodiimide ions stacked along the  $a$ -axis direction. Tin(II) is surrounded by four nitrogen atoms forming a distorted square  $[\text{Sn}(\text{N})_4]$  pyramid, and the  $(\text{N}=\text{C}=\text{N})^{2-}$  group is surrounded by four tin ions in an approximately rectangular formation ([Figure 4](#)). The unit cell plotted with dashed lines in [Figure 3](#) (below) highlights a smaller section of the unit cell that neglects to account for the alternating orientations of square  $[\text{Sn}(\text{N})_4]$  pyramids along  $\pm b$ .

The local environment of the  $\text{Sn}^{2+}$  ion in the structure of  $\text{Sn}(\text{CN}_2)$  is closely related to the environment of tin in the structure of  $\text{Sn}_2\text{O}(\text{CN}_2)$  and is similar to the square pyramidal  $[\text{Sn}(\text{O})_4]$  arrangement in  $\text{SnO}$ . The local  $C_{2v}$  symmetry of the environment of  $\text{Sn}^{2+}$  in  $\text{Sn}(\text{CN}_2)$  involves two short and two long  $\text{Sn-N}$  distances ( $2.185$  and  $2.529 \text{ \AA}$ ). The carbon atom of the  $(\text{N}=\text{C}=\text{N})^{2-}$  unit is situated at the inversion centers, resulting in a local  $D_{\infty h}$  symmetry, and has a  $\text{C-N}$  distance of  $1.210 \text{ \AA}$ . This observation is in line with the results of infrared measurements, which reveal a 2-fold degenerate bending vibration at  $673 \text{ cm}^{-1}$  and an asymmetric stretching vibration at  $1984 \text{ cm}^{-1}$  (see [Figure S3](#)).

To better understand the arrangement of atoms in the crystal structure of  $\text{Sn}(\text{CN}_2)$ , we refer to the well-known structure of tetragonal  $\text{CaC}_2$ . From this structure, shown in [Figure 5](#), the orthorhombic structure of  $\text{FeS}_2$  (marcasite) is constructed by tilting the  $\text{S-S}$  axis of the  $(\text{S}_2)^{2-}$  units within the plane of projection. This arrangement could be in fact a prototype for the structure of  $\text{Sn}(\text{CN}_2)$ . From the structural point of view, the stereochemically active asymmetric electron

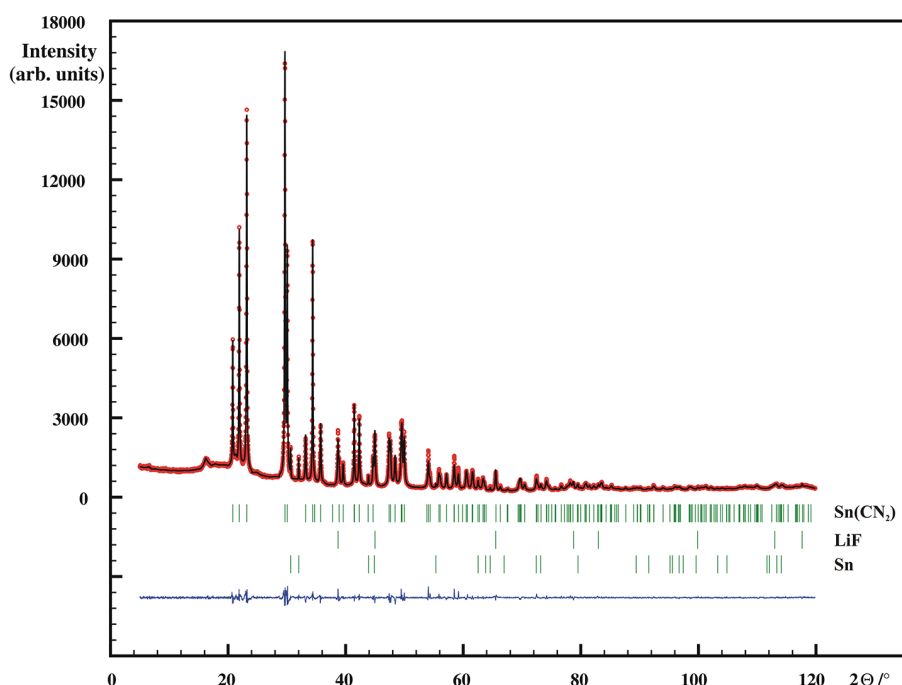


**Figure 2.** PXRD refinement pattern of  $\text{Sn}(\text{CN}_2)$  with the experimental (red) and calculated (black) patterns of the Rietveld refinement. Bragg positions (green) of  $\text{Sn}(\text{CN}_2)$  (top), LiF (middle row), Sn (bottom), and the difference curve (blue) are also shown.

**Table 1.** Crystal Data and Structure Refinement Parameters of  $\text{Sn}(\text{CN}_2)$

empirical formula	$\text{Sn}(\text{CN}_2)$	$\text{Sn}_4\text{Cl}_2(\text{CN}_2)_3$
CCDC no.	1898725	1898799
formula weight/ $\text{g}\cdot\text{mol}^{-1}$	158.74	665.75
temperature/K	298(2)	100(2)
wavelength/ $\text{Å}$	1.5406	0.7107
crystal system	monoclinic	monoclinic
space group	$I2/a$	$P2_1/n$
$a/\text{Å}$	8.3133(6)	6.8933(1)
$b/\text{Å}$	5.0196(4)	9.1740(2)
$c/\text{Å}$	6.0898(4)	8.9110(2)
$\beta/^\circ$	102.79(4)	106.05(2)
volume/ $\text{Å}^3$	247.82(3)	541.56(2)
$Z$	4	2
$\mu(\text{Cu } K\alpha)/\text{mm}^{-1}$	79.15	
$\mu(\text{Mo } K\alpha)/\text{mm}^{-1}$		9.58
density (calculated)/ $\text{g}\cdot\text{cm}^{-3}$	4.254	4.083
theta range for data collection/ $^\circ$	2.5–60	3–29
total number of reflections	191	1399
refined parameters	10	70
$R_p$	2.8914	
$R_{wp}$	3.9765	
$R_{Bragg}$	1.8661	
$R_1$		0.0176
$wR_2$		0.0423
goodness-of-fit on $F^2$	1.0610	1.061
$\chi^2$	1.1258	

density at the tin(II) atom and the packing effects in the structure result in an additional tilting of the  $(\text{NCN})$ -axes of carbodiimide ions out of the projection plane in Figure 5. This leads to the decrease of the coordination number of the metal atoms from six in the former structures to four in  $\text{Sn}(\text{CN}_2)$ . The alignment of carbodiimide units in the structure tends to

**Table 2.** Atomic Coordinates, Wyckoff Positions (Wyck), and Isotropic Displacement Parameters ( $U_{eq}$  in  $\text{Å}^2$ ) for  $\text{Sn}(\text{CN}_2)$

atom	Wyck	$x$	$y$	$z$	$U_{eq}^a$
Sn	4e	1/4	0.4638(1)	1/2	0.0425(2)
C	4b	1/2	0	1/2	0.054(3)
N	8f	0.4042(4)	0.1590(7)	0.3932(7)	0.036(2)

<sup>a</sup> $U_{eq}$  is defined as one-third of the trace of the orthogonalized  $U_{ij}$  tensor.

introduce an N–N repulsion that can be reduced by an angular distortion of the unit cell into its current shape. The shortest N–N distance between adjacent  $(\text{NCN})^{2-}$  ions is 2.88 Å.

**Crystal Structure of  $\text{Sn}_4\text{Cl}_2(\text{CN}_2)_3$ .** The crystal structure of  $\text{Sn}_4\text{Cl}_2(\text{CN}_2)_3$  was solved from single-crystal XRD in the monoclinic space group  $P2_1/n$ . The crystallographic data are given in Table 1, and the atomic positions are provided in the Supporting Information (Table S1). The crystal structure can be characterized by a layered arrangement in which one layer of tin ions alternates with one layer hosting chloride and carbodiimide anions (Figure 6).

The two crystallographically distinct  $\text{Sn}^{2+}$  ions in the structure are coordinated in a distorted octahedral fashion. Each tin atom is six-coordinated by three nitrogen atoms of the  $(\text{NCN})^{2-}$  units and three  $\text{Cl}^-$ . The Sn–Cl distance ranges between 2.9 and 3.7 Å (Figure 7). The two crystallographically independent carbodiimide ions are surrounded by four  $\text{Sn}^{2+}$  each, in two different ways. One environment of  $(\text{NCN})^{2-}$  is nearly planar, similar to that in  $\text{Sn}(\text{CN}_2)$ , and the other may be described as pseudotetrahedral (Figure 8). The carbodiimide ions show typical C–N distances of 1.22/1.23 Å as well as typical Sn–N distances of 2.22–2.35 Å.<sup>21</sup>

**Electronic Structure.** The electronic structures of  $\text{Sn}(\text{CN}_2)$  and  $\text{Sn}_4\text{Cl}_2(\text{CN}_2)_3$  were calculated using DFT to rationalize their structures and predict their properties. It is

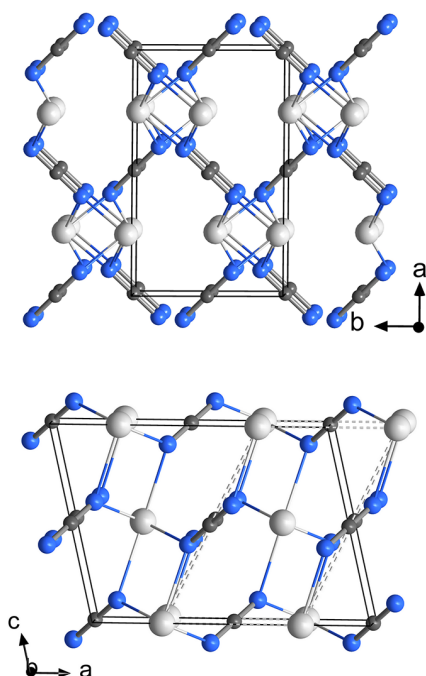


**Figure 3.** Two perspective views on the unit cell of the crystal structure of  $\text{Sn}(\text{CN}_2)$ . Dashed lines in the plot below emphasize an oversimplified pseudo unit cell that can be related to the  $\text{FeS}_2$  (marcasite) structure. Tin atoms are shown in light gray, nitrogen in blue, and carbon in dark gray.

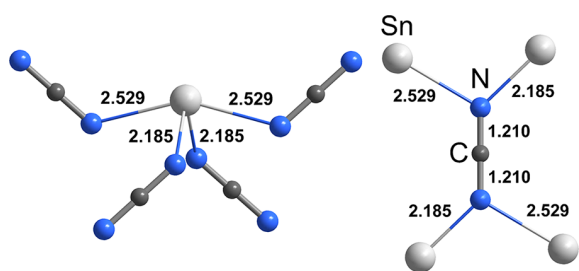


**Figure 4.** Coordination of  $\text{Sn}^{2+}$  by four N atoms of the  $(\text{NCN})^{2-}$  ions (left) and the environment of  $(\text{NCN})^{2-}$  ions in the structure of  $\text{Sn}(\text{CN}_2)$ .

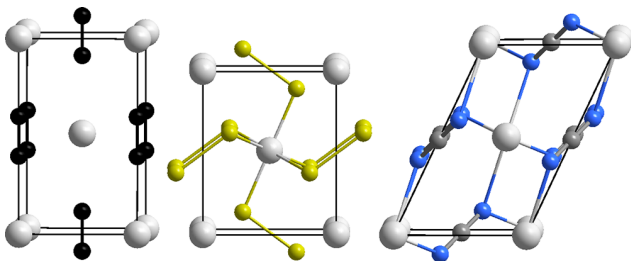


**Figure 5.** Projection of crystal structures of tetragonal  $\text{CaC}_2(\text{I})$ , orthorhombic  $\text{FeS}_2$  (marcasite), and a section of the  $\text{Sn}(\text{CN}_2)$  structure, shown from left to right. Metal atoms are shown in light gray, carbon in black, and sulfur in yellow.

important to note that DFT-calculated band gaps are consistently underestimated, as the energies of the calculated conduction band states do not account for the interaction energy between an excited electron and the valence

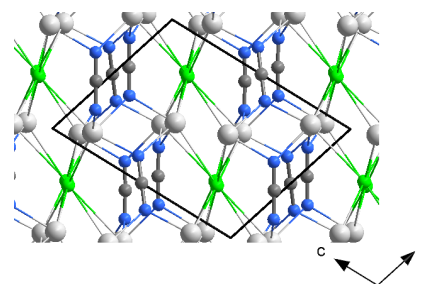


**Figure 6.** Perspective view featuring the arrangement of layers in the crystal structure of  $\text{Sn}_4\text{Cl}_2(\text{CN}_2)_3$ . Tin atoms are shown in light gray, nitrogen in blue, carbon in dark gray, and chlorine in green.

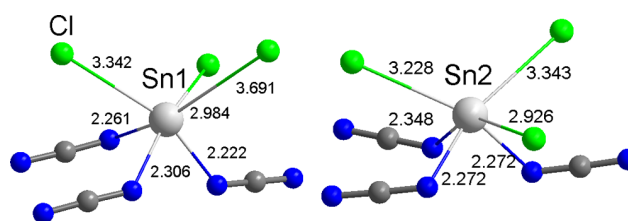


**Figure 7.** Coordination of  $\text{Sn}^{2+}$  by three N atoms of the  $(\text{NCN})^{2-}$  ions and three  $\text{Cl}^-$  ions in the crystal structure of  $\text{Sn}_4\text{Cl}_2(\text{CN}_2)_3$ .

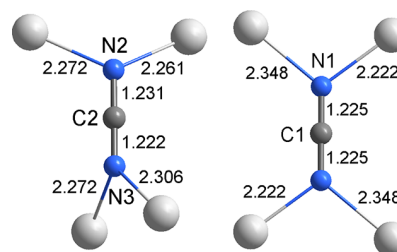


**Figure 8.** Coordination environments of two distinct  $(\text{NCN})^{2-}$  ions in the crystal structure of  $\text{Sn}_4\text{Cl}_2(\text{CN}_2)_3$ . The left one is coordinated pseudotetrahedrally, and the right one is almost planar.

electrons.<sup>32</sup> The calculated band structures are shown in [Figure 9](#) and [Figure 10](#) below.

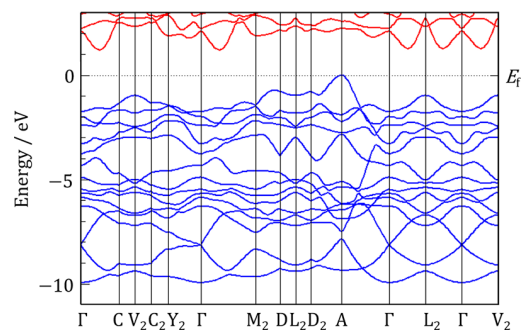


**Figure 9.** Calculated electronic band structure of  $\text{Sn}(\text{CN}_2)$ . Special points in the Brillouin zone were selected following Hinuma et al.<sup>33</sup>

$\text{Sn}(\text{CN}_2)$  is predicted to be a semiconductor with a small indirect band gap of 1.2 eV (the optical band gap was determined to be 2.0 eV, see [Figure S1](#)). The ca. 1 eV underestimation is typical for a DFT-calculated value.<sup>32</sup> The valence band maximum lies at the A (0 0 0.5) point of reciprocal space, at a point of relatively high curvature.

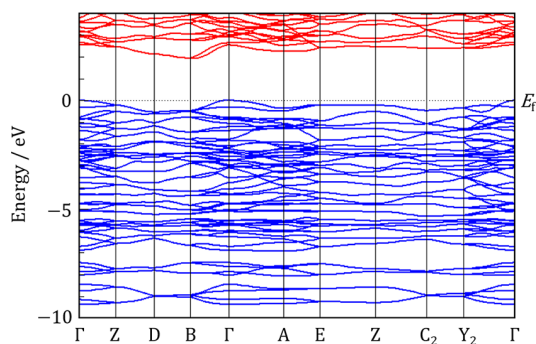


**Figure 10.** Calculated electronic band structure of  $\text{Sn}_4\text{Cl}_2(\text{CN}_2)_3$ . Special points in the Brillouin zone were selected following Hinuma et al.<sup>33</sup>

$\text{Sn}_4\text{Cl}_2(\text{CN}_2)_3$  is also predicted to be an indirect band gap semiconductor with a band gap of 1.9 eV. Its valence band maximum is located at  $\Gamma$  (0 0 0). From these results, we can estimate the experimental band gap of  $\text{Sn}_4\text{Cl}_2(\text{CN}_2)_3$  to be on the order of 3 eV (2.6 eV according to the reflectance measurement, see Figure S2).

To further understanding of the bonding within these structures and the role the  $\text{Sn}^{2+}$  lone pair plays in determining the structure, the electron localization function (ELF) was calculated.<sup>34,35</sup> The ELF is a measurement of the probability of finding an electron in the same region of space as a reference electron; higher values of the ELF are associated with electron pair probability and electron localization. The ELF can range from 0 to 1 with the homogeneous electron gas everywhere having the value 0.5. Isosurfaces of the ELF for  $\text{Sn}(\text{CN}_2)$  and  $\text{Sn}_4\text{Cl}_2(\text{CN}_2)_3$  are shown at the 0.7 level in Figure 11 and Figure 12 below. Note that, as the DFT calculations were performed with pseudopotentials, only valence and semicore electrons are included.

The ELF analysis shows significant differences between  $\text{Sn}(\text{CN}_2)$  and  $\text{Sn}_4\text{Cl}_2(\text{CN}_2)_3$ .  $\text{Sn}_4\text{Cl}_2(\text{CN}_2)_3$  shows significant electron localization around the N and Cl atoms and very little near the Sn atoms. The stereochemically active lone pairs of the  $\text{Sn}^{2+}$  atoms can be seen clearly in Figure 12; they lie near the [1 0–1] plane. The structure is therefore fairly close-packed if the lone pairs are considered to take up space

corresponding to an atom. The overall pattern of high localization near some atoms and little near others is consistent with an ionic structure.

In contrast, the ELF of  $\text{Sn}(\text{CN}_2)$  shows features indicating more electron delocalization and covalent bonding between the  $\text{CN}_2$  groups and the Sn atoms. Namely, there is a strong correlation between the peaks and nodes of the ELF and the bonding directions. The ELF does not show a classical  $\text{Sn}^{2+}$  lone pair; rather, the localized electrons are in a ring close to the core; the asymmetry of which makes it stereochemically active. This ring is coplanar with the short Sn–N bonds; there is a smaller pocket of electron localization directed along the long Sn–N bonds. Unlike in the  $\text{Sn}_4\text{Cl}_2(\text{CN}_2)_3$  structure, the empty space in the crystal structure appears to truly be void space, indicating that the  $\text{Sn}(\text{CN}_2)$  structure could be categorized as an open framework structure, like those of  $\text{Hf}(\text{CN}_2)_2$  and  $\text{Zr}(\text{CN}_2)_2$ .<sup>36</sup> The electron delocalization in  $\text{Sn}(\text{CN}_2)$  over both the Sn atoms and the  $\text{CN}_2$  units is consistent with its small bandgap.

## CONCLUSIONS

Two new tin carbodiimide compounds were introduced with their syntheses and crystal structures. The synthetic intermediate compound  $\text{Sn}_4\text{Cl}_2(\text{CN}_2)_3$  is formed from  $\text{SnCl}_2$  and  $\text{Li}_2(\text{CN}_2)$  at 200 °C, melts congruently at 450 °C, and remains stable up to 550 °C.  $\text{Sn}_4\text{Cl}_2(\text{CN}_2)_3$  acts as a versatile precursor because it can form  $\text{Sn}(\text{CN}_2)$  when reacted with  $\text{Li}_2(\text{CN}_2)$  and  $\text{Sn}_2\text{O}(\text{CN}_2)$  when reacted with  $\text{Li}_2(\text{CN}_2)$  and  $\text{Na}_2\text{O}$ .

The new compound  $\text{Sn}(\text{CN}_2)$  contains  $\text{Sn}^{2+}$  with a stereochemically active asymmetric electron density that is considered to have an impact on the crystal structure. Its structure is shown to be related to the  $\text{FeS}_2$  (marcasite) structure with a distortion that reduces the coordination number of the cation from six to four, as is typical for  $\text{Sn}^{2+}$  compounds.

The asymmetric lone pair of tin in the structure of  $\text{Sn}(\text{CN}_2)$  can be viewed as chemically active, showing overlap or covalent bonding with the carbodiimide, which gives rise to electron delocalization.  $\text{Sn}(\text{CN}_2)$  is a semiconductor with a band gap on the order of 2 eV according to band structure calculations and optical measurements.

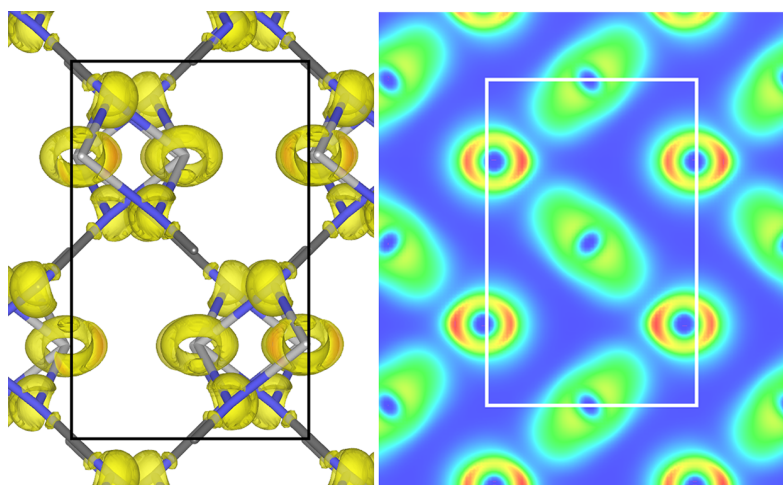


**Figure 11.** Calculated electron localization function of  $\text{Sn}(\text{CN}_2)$  shown as an isosurface at the 0.7 level (left) and as a section in the  $ab$  plane (right). The view along  $c$  corresponds to the projection of the structure in Figure 3 (top).

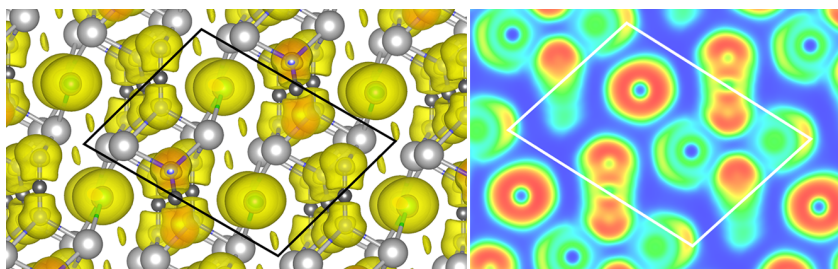


**Figure 12.** Calculated electron localization function of  $\text{Sn}_4\text{Cl}_2(\text{CN}_2)_3$ , shown as an isosurface at the 0.7 level (left) and as a section in the  $ac$  plane (right). The view along  $b$  corresponds to the projection of the structure in Figure 6.

## ■ ASSOCIATED CONTENT

### Supporting Information

The Supporting Information is available free of charge on the ACS Publications website at DOI: 10.1021/acs.inorgchem.9b00527.

DFT input files for band structure and ELF calculations (ZIP)

Table S1: atomic coordinates, Wyckoff positions, and isotropic displacement parameters of  $\text{Sn}_4\text{Cl}_2(\text{CN}_2)_3$ ; Figure S1: reflectance measurement of  $\text{Sn}(\text{CN}_2)$ ; Figure S2: reflectance measurement of  $\text{Sn}_4\text{Cl}_2(\text{CN}_2)_3$ ; Figure S3: infrared measurement of  $\text{Sn}(\text{CN}_2)$  (PDF)

### Accession Codes

CCDC 1898725 and 1898799 contain the supplementary crystallographic data for this paper. These data can be obtained free of charge via [www.ccdc.cam.ac.uk/data\\_request/cif](http://www.ccdc.cam.ac.uk/data_request/cif), by emailing [data\\_request@ccdc.cam.ac.uk](mailto:data_request@ccdc.cam.ac.uk), or by contacting The Cambridge Crystallographic Data Centre, 12 Union Road, Cambridge CB2 1EZ, UK; fax: +44 1223 336033.

## ■ AUTHOR INFORMATION

### Corresponding Author

\*E-mail: [juergen.meyer@uni-tuebingen.de](mailto:juergen.meyer@uni-tuebingen.de) (H.-J.M.).

### ORCID

Markus Ströbele: 0000-0002-5147-5677

Hans-Jürgen Meyer: 0000-0003-2450-4011

### Funding

Support of this project by the Deutsche Forschungsgemeinschaft (Bonn) via grant ME 914/25-2 is gratefully acknowledged.

### Notes

The authors declare no competing financial interest.

## ■ ACKNOWLEDGMENTS

We like to express our gratitude to Dr. David Enseling and Prof. Thomas Jüstel (FH Münster) for performing optical reflection spectroscopy. We also thank Elke Niquet and Dr. Cäcilia Maichle-Mössmer (Univ. Tübingen) for performing a single crystal X-ray measurement.

## ■ REFERENCES

- (1) Neukirch, M.; Tragl, S.; Meyer, H.-J. Syntheses and structural properties of rare earth carbodiimides. *Inorg. Chem.* **2006**, *45*, 8188–8193.
- (2) Meyer, H.-J. Solid state metathesis reactions as a conceptual tool in the synthesis of new materials. *Dalton Trans.* **2010**, *39*, 5973–5982.
- (3) Krott, M.; Liu, X.; Fokwa, B. P.; Speldrich, M.; Lueken, H.; Dronskowski, R. Synthesis, crystal-structure determination and

magnetic properties of two new transition-metal carbodiimides:  $\text{CoNCN}$  and  $\text{NiNCN}$ . *Inorg. Chem.* **2007**, *46*, 2204–2207.

(4) Liu, X.; Stork, L.; Speldrich, M.; Lueken, H.; Dronskowski, R.  $\text{FeNCN}$  and  $\text{Fe}(\text{NCNH})_2$ : Synthesis, Structure, and Magnetic Properties of a Nitrogen-Based Pseudo-oxide and-hydroxide of Divalent Iron. *Chem. - Eur. J.* **2009**, *15*, 1558–1561.

(5) Becker, M.; Jansen, M. Zinc cyanamide,  $\text{Zn}(\text{CN}_2)$ . *Acta Crystallogr., Sect. C: Cryst. Struct. Commun.* **2001**, *57*, 347–348.

(6) Becker, M.; Nuss, J.; Jansen, M. Kristallstruktur und schwingungsspektroskopische Daten von Silbercyanamid/Crystal Structure and Spectroscopic Data of Silver Cyanamide. *Z. Naturforsch., B: J. Chem. Sci.* **2000**, *55*, 383–385.

(7) Tang, X.; Xiang, H.; Liu, X.; Speldrich, M.; Dronskowski, R. A ferromagnetic carbodiimide:  $\text{Cr}_2(\text{NCN})_3$ . *Angew. Chem., Int. Ed.* **2010**, *49*, 4738–4742.

(8) Down, M. G.; Haley, M. J.; Hubberstey, P.; Pulham, R. J.; Thunder, A. E. Solutions of lithium salts in liquid lithium: preparation and X-ray crystal structure of the dilithium salt of carbodi-imide (cyanamide). *J. Chem. Soc., Dalton Trans.* **1978**, 1407–1411.

(9) Becker, M.; Jansen, M.; Lieb, A.; Milius, W.; Schnick, W. Synthese, Kristallstruktur und Festkörper-NMR-spektroskopische Untersuchungen von  $\text{K}_5\text{H}(\text{CN}_2)_3$ . *Z. Anorg. Allg. Chem.* **1998**, *624*, 113–118.

(10) Becker, M.; Nuss, J.; Jansen, M. Synthese und Charakterisierung von Natriumcyanamid. *Z. Anorg. Allg. Chem.* **2000**, *626*, 2505–2508.

(11) Berger, U.; Schnick, W. Syntheses, crystal structures, and vibrational spectroscopic properties of  $\text{MgCN}_2$ ,  $\text{SrCN}_2$ , and  $\text{BaCN}_2$ . *J. Alloys Compd.* **1994**, *206*, 179–184.

(12) Dronskowski, R.  $\text{In}_{2.24}(\text{NCN})_3$  and  $\text{NaIn}(\text{NCN})_2$ : Synthesis and Crystal Structures of New Main Group Metal Cyanamides. *Z. Naturforsch., B: J. Chem. Sci.* **1995**, *50*, 1245–1251.

(13) Riedel, R.; Greiner, A.; Mieke, G.; Dressler, W.; Fuess, H.; Bill, J.; Aldinger, F. The First Crystalline Solids in the Ternary Si-C-N System. *Angew. Chem., Int. Ed. Engl.* **1997**, *36*, 603–606.

(14) Liu, X.; Decker, A.; Schmitz, D.; Dronskowski, R. Crystal structure refinement of lead cyanamide and the stiffness of the cyanamide anion. *Z. Anorg. Allg. Chem.* **2000**, *626*, 103–105.

(15) Dolabdjian, K.; Meyer, H.-J. Lead Carbodiimides Related to the Mineral Bideauxite. *Z. Anorg. Allg. Chem.* **2017**, *643*, 1898–1903.

(16) Glaser, J.; Meyer, H.-J. Multilateral Solid-State Metathesis Reactions for the Preparation of Materials with Heteroanions: The  $[\text{Si}(\text{CN}_2)_4]^{4-}$  Ion. *Angew. Chem., Int. Ed.* **2008**, *47*, 7547–7550.

(17) Kalmutzki, M.; Enseling, D.; Wren, J. E.; Kroeker, S.; Tersikh, V. V.; Jüstel, T.; Meyer, H.-J. Solid State Complex Chemistry: Formation, Structure, and Properties of Homoleptic Tetracyanamidogermanates  $\text{RbRE}[\text{Ge}(\text{CN}_2)_4]$  (RE = La, Pr, Nd, Gd). *Inorg. Chem.* **2013**, *52*, 12372–12382.

(18) Kalmutzki, M.; Ströbele, M.; Kroeker, S.; Wren, J. E.; Meyer, H.-J. Synthesis and Characterization of the First Tetracyanamidogallate. *Eur. J. Inorg. Chem.* **2013**, *2013*, 6091–6096.

(19) Unverfehrt, L.; Kalmutzki, M.; Ströbele, M.; Meyer, H.-J. Solid state synthesis of homoleptic tetracyanamidaluminates. *Dalton Trans.* **2011**, *40*, 9921–9924.

- (20) Dolabdjian, K.; Castro, C.; Meyer, H.-J. Layered Carbodiimides  $A_2M(CN_2)_3$  with Tetravalent Cations  $M = Sn, Zr, \text{ and } Hf$ . *Eur. J. Inorg. Chem.* **2018**, *2018*, 1624–1630.
- (21) Dolabdjian, K.; Görne, A. L.; Dronskowski, R.; Ströbele, M.; Meyer, H.-J. Tin (II) oxide carbodiimide and its relationship to  $SnO$ . *Dalton Trans.* **2018**, *47*, 13378–13383.
- (22) Altomare, A.; Camalli, M.; Cuocci, C.; Giacovazzo, C.; Moliterni, A.; Rizzi, R. EXPO2009: structure solution by powder data in direct and reciprocal space. *J. Appl. Crystallogr.* **2009**, *42*, 1197–1202.
- (23) Roisnel, T.; Rodríguez-Carvajal, J. WinPLOTR: A windows tool for powder diffraction pattern analysis. *Mater. Sci. Forum* **2001**, *378*, 118–123.
- (24) (a) Sheldrick, G. SADABS, version 2008/1, University of Göttingen: Germany, 2008. (b) Sheldrick, G. *Bruker Analytical X-ray Division*; Bruker: Madison, WI, 1997.
- (25) (a) Sheldrick, G. SHELX-97, A Program for the Solution and Refinement of Crystal Structures; University of Göttingen: Germany, 1997. (b) Sheldrick, G. M. Phase annealing in SHELX-90: direct methods for larger structures. *Acta Crystallogr., Sect. A: Found. Crystallogr.* **1990**, *46*, 467–473.
- (26) Hübschle, C. B.; Sheldrick, G. M.; Dittrich, B. ShelXle: a graphical user interface for SHELXL. *J. Appl. Crystallogr.* **2011**, *44*, 1281–1284.
- (27) Gonze, X.; Jollet, F.; Araujo, F. A.; Adams, D.; Amadon, B.; Applencourt, T.; Audouze, C.; Beuken, J.-M.; Bieder, J.; Bokhanchuk, A. Recent developments in the ABINIT software package. *Comput. Phys. Commun.* **2016**, *205*, 106–131.
- (28) Perdew, J. P.; Burke, K.; Ernzerhof, M. Generalized gradient approximation made simple. *Phys. Rev. Lett.* **1996**, *77*, 3865.
- (29) Bottin, F.; Leroux, S.; Knyazev, A.; Zérah, G. Large-scale ab initio calculations based on three levels of parallelization. *Comput. Mater. Sci.* **2008**, *42*, 329–336.
- (30) Grimme, S. Semiempirical GGA-type density functional constructed with a long-range dispersion correction. *J. Comput. Chem.* **2006**, *27*, 1787–1799.
- (31) Hamann, D. Optimized norm-conserving Vanderbilt pseudopotentials. *Phys. Rev. B: Condens. Matter Mater. Phys.* **2013**, *88*, 085117.
- (32) Aryasetiawan, F.; Gunnarsson, O. The GW method. *Rep. Prog. Phys.* **1998**, *61*, 237.
- (33) Hinuma, Y.; Pizzi, G.; Kumagai, Y.; Oba, F.; Tanaka, I. Band structure diagram paths based on crystallography. *Comput. Mater. Sci.* **2017**, *128*, 140–184.
- (34) Becke, A. D.; Edgecombe, K. E. A simple measure of electron localization in atomic and molecular systems. *J. Chem. Phys.* **1990**, *92*, 5397–5403.
- (35) Savin, A.; Jepsen, O.; Flad, J.; Andersen, O. K.; Preuss, H.; von Schnering, H. G. Electron localization in solid-state structures of the elements: the diamond structure. *Angew. Chem., Int. Ed. Engl.* **1992**, *31*, 187–188.
- (36) Dolabdjian, K.; Kobald, A.; Romao, C. P.; Meyer, H.-J. Synthesis and thermoelastic properties of  $Zr(CN_2)_2$  and  $Hf(CN_2)_2$ . *Dalton Trans.* **2018**, *47*, 10249–10255.





# Supporting Information

## Synthesis, Structure and Electronic Properties of $\text{Sn}(\text{CN}_2)$ and $\text{Sn}_4\text{Cl}_2(\text{CN}_2)_3$

*Manuel Löber, Konstantin Dolabdjian, Markus Ströbele, Carl P. Romao, Hans-Jürgen Meyer*

Section for Solid State and Theoretical Inorganic Chemistry, Institute of Inorganic Chemistry,

University of Tübingen, Auf der Morgenstelle 18, D-72076 Tübingen, Germany

**Table S1.** Atomic coordinates, Wyckoff positions (Wyck) and isotropic displacement parameters ( $U_{eq}$  in  $\text{\AA}^2$ ) for  $\text{Sn}_4\text{Cl}_2(\text{CN}_2)_3$ .

Atom	Wyck	$x$	$y$	$z$	$U(eq)$
Sn(1)	4e	0.61208(3)	0.41849(2)	0.35117(2)	0.006(1)
Sn(2)	4e	0.55623(3)	0.84712(2)	0.38978(2)	0.007(1)
Cl(1)	4e	0.25896(10)	0.62000(7)	0.26083(8)	0.011(1)
N(1)	4e	0.6362(3)	0.4567(2)	0.1107(3)	0.008(1)
N(2)	4e	0.7460(3)	0.6409(2)	0.4247(3)	0.007(1)
N(3)	4e	1.0616(3)	0.6493(2)	0.6360(3)	0.008(1)
C(1)	2b	1/2	1/2	0	0.008(1)
C(2)	4e	0.9060(4)	0.6455(3)	0.5291(3)	0.007(1)

$U_{eq}$  is defined as one-third of the trace of the orthogonalized  $U_{ij}$  tensor.

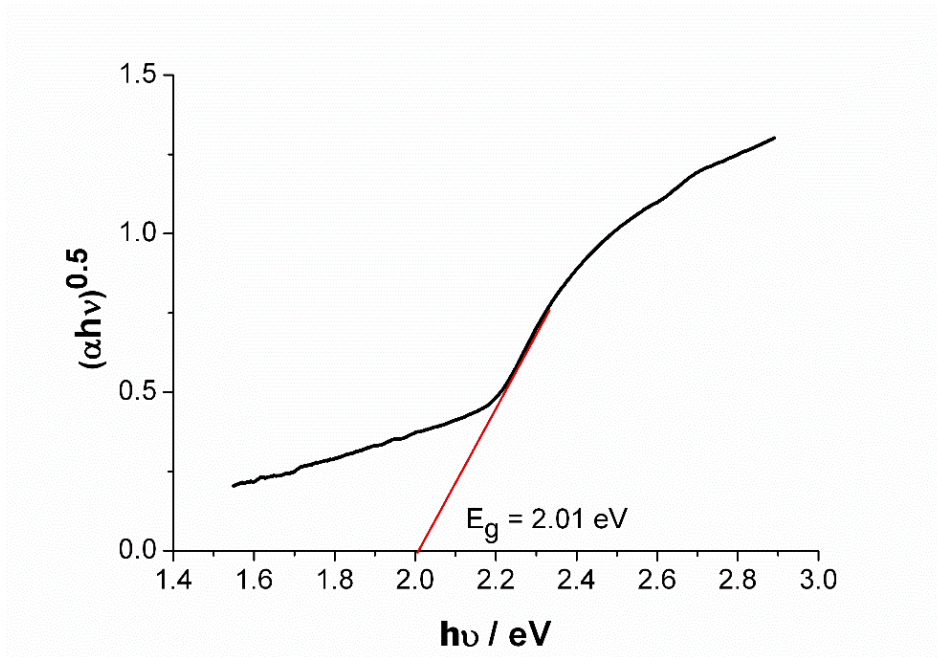


**Figure S1.** Reflectance measurement of  $\text{Sn}(\text{CN}_2)$ . Definition of the y-axis:  $\alpha$  is the absorption coefficient defined as  $\alpha = \frac{(1-R)^2}{2R}$ , where  $R$  is the reflectivity.  $h$  is Planck's constant and  $\nu$  the frequency. The exponent of 0.5 corresponds to an indirect bandgap.

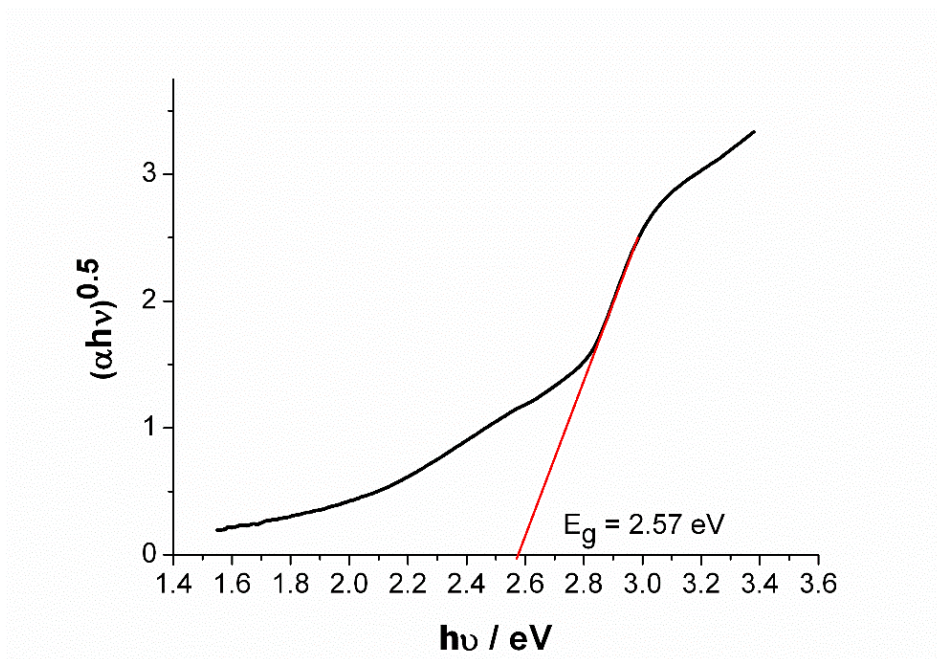


**Figure S2.** Reflectance measurement of  $\text{Sn}_4\text{Cl}_2(\text{CN}_2)_3$ .

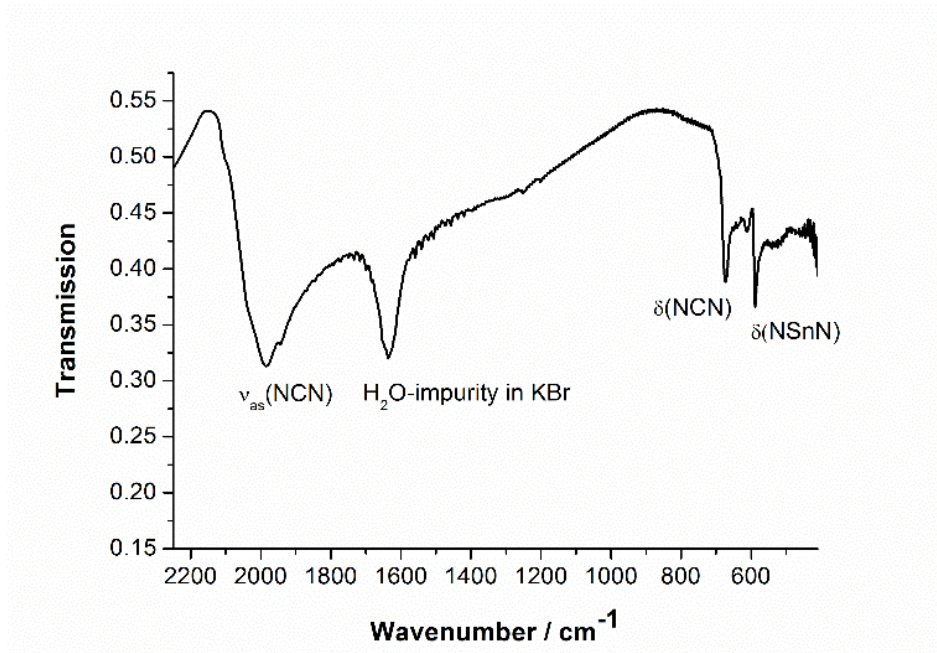
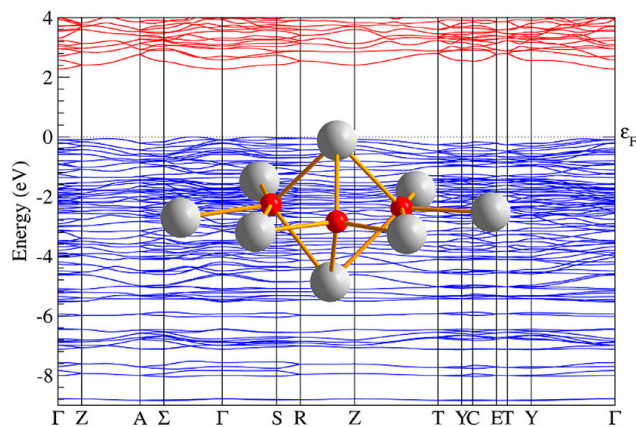


**Figure S3.** Infrared measurement of  $\text{Sn}(\text{CN}_2)$ .

# Publication 2

Synthesis, Structure, and Electronic Properties of  $\text{Sn}_9\text{O}_5\text{Cl}_4(\text{CN}_2)_2$



<https://doi.org/10.1021/acs.inorgchem.9b02229>

Reprinted with permission from

*Inorg. Chem.* **2019**, *58*, 14560–14567

Copyright © 2019 American Chemical Society



# Synthesis, Structure, and Electronic Properties of $\text{Sn}_9\text{O}_5\text{Cl}_4(\text{CN}_2)_2$

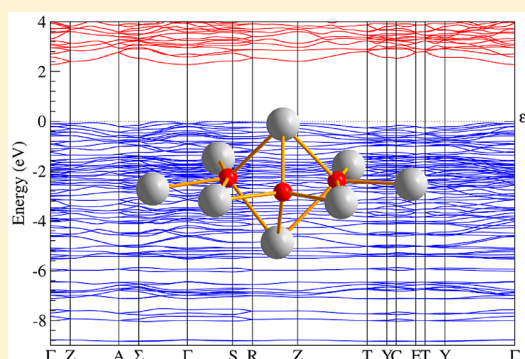
Manuel Löber,<sup>†</sup> Chris Steve Geißenhöner,<sup>†</sup> Markus Ströbele,<sup>†</sup> Sylvio Indris,<sup>‡</sup> Carl P. Romao,<sup>†</sup> and Hans-Jürgen Meyer<sup>\*,†</sup>

<sup>†</sup>Section for Solid State and Theoretical Inorganic Chemistry, Institute of Inorganic Chemistry, University of Tübingen, Auf der Morgenstelle 18, D-72076 Tübingen, Germany

<sup>‡</sup>Institute for Applied Materials (IAM), Karlsruhe Institute of Technology (KIT), Hermann-von-Helmholtz-Platz 1, 76344 Eggenstein-Leopoldshafen, Germany

## Supporting Information

**ABSTRACT:** The formation of the new compound  $\text{Sn}_9\text{O}_5\text{Cl}_4(\text{CN}_2)_2$  is reported and placed in the context of several other recently discovered tin carbodiimide compounds ( $\text{Sn}(\text{CN}_2)$ ,  $\text{Sn}_2\text{O}(\text{CN}_2)$ , and  $\text{Sn}_4\text{Cl}_2(\text{CN}_2)_3$ ), all of which contain divalent tin. The crystal structure of  $\text{Sn}_9\text{O}_5\text{Cl}_4(\text{CN}_2)_2$ , as determined by X-ray powder diffraction, includes an unusual  $[\text{Sn}_8\text{O}_3]$  cluster, in which tin atoms form the motif of a hexagonal bipyramid. An additional tin atom and two oxygen atoms connect these clusters into chains. Mössbauer spectroscopy shows tin to predominantly adopt the +2 oxidation state, and electronic structure calculations predict  $\text{Sn}_9\text{O}_5\text{Cl}_4(\text{CN}_2)_2$  to be a semiconductor.



## INTRODUCTION

Reactions between solids are often exothermic, but can also proceed endothermically. The release or consumption of heat during a reaction between two or more solids can be monitored by thermal analysis. The thermal scanning of chemical reactions can be a powerful method for the discovery of new compounds when compared to the classical explorative synthesis, where a mixture of solids is reacted at an intuitively selected temperature. The potential of the thermal scanning method has been demonstrated by the identification of more than 20 binary W–I compounds,<sup>1</sup> by solid-state metathesis (SSM) reactions<sup>2</sup> and by scanning a series of reduction reactions of  $\text{WCl}_6$  to detect numerous compounds, for example, in the Pb–W–Cl,<sup>3</sup> Co–W–Cl,<sup>4</sup> Fe–W–Cl,<sup>5</sup> and Cu–W–Cl<sup>6</sup> systems. SSM reactions have been successfully employed for the development of metal compounds of nitridoborates,<sup>7–10</sup> cyanurates,<sup>11</sup> and carbodiimides.

Carbodiimide compounds have been discovered with rare-earth,<sup>12</sup> transition metal,<sup>13–17</sup> and main group<sup>18–23</sup> elements. Such compounds, with variable band gaps, have shown potential interest for applications, for example, in photo-physics,<sup>24,25</sup> control of thermal expansion,<sup>26</sup> or as battery materials.<sup>27,28</sup>

Recently we have focused on the preparation of tin carbodiimides, wherein the carbodiimide anion can be considered chemically to act as a pseudochalcogenide.<sup>14</sup> Tin(II) chalcogenides were recently described as promising candidates for high performance thermoelectric materials.<sup>29</sup> The tin(II) sulfide  $\text{SnS}$  is a promising anode material for sodium ion batteries.<sup>30</sup> With its band gap of approximately 1.5

eV, it can be used for photodetector applications<sup>31</sup> and as an absorption layer for solar cell applications.<sup>32</sup> Recently, superconductivity was reported in  $\text{SnS}$  as well as in the homologous  $\text{SnSe}$ .<sup>33</sup> Stannous oxide ( $\text{SnO}$ ) is a p-type semiconductor that could be used in optoelectronics, such as thin film transistors.<sup>34,35</sup> The need for high performance photovoltaic materials motivates a wide field of research in which tin halides such as  $\text{CsSnI}_3$  or  $\text{CsSnBr}_3$  have been studied.<sup>36</sup>

Semiconducting tin oxide carbodiimide  $\text{Sn}_2\text{O}(\text{CN}_2)$  was recently synthesized from a mixture of solid  $\text{SnCl}_2$ ,  $\text{SnO}$ , and  $\text{Li}_2(\text{CN}_2)$ .<sup>37</sup> The formation of two intermediate phases was detected during heating in this reaction by differential thermal analysis (DTA). One intermediate phase was identified as  $\text{Sn}_4\text{Cl}_2(\text{CN}_2)_3$ , which also appears as an intermediate phase in the formation of  $\text{Sn}(\text{CN}_2)$ .<sup>38</sup>

## EXPERIMENTAL AND CALCULATION DETAILS

**Synthesis of  $\text{Sn}_9\text{O}_5\text{Cl}_4(\text{CN}_2)_2$ .** The starting materials  $\text{Li}_2(\text{CN}_2)$ ,<sup>12</sup>  $\text{SnCl}_2$  (Alfa Aesar, ultra dry, 99.9985%), and  $\text{SnO}$  (Sigma-Aldrich, 99.99%) were mixed in a 2:4:5 molar ratio under a dry argon atmosphere (glovebox), pestled in an agate mortar, and sealed into a silica tube under vacuum. The mixture was heated in a crucible furnace to 400 °C with a heating rate of 2 K/min and held at this temperature for 10 h before cooling the product down to room temperature at 2 K/min. The ampule was opened in air and kept in a drying oven for 30 min at 80 °C. This procedure is performed to make the compound more resistant against air and water as described

Received: July 24, 2019

Published: October 24, 2019

for  $\text{Sn}_2\text{O}(\text{CN}_2)$ .<sup>37</sup> The compound was then washed with water and ethanol in order to remove the metathesis salt  $\text{LiCl}$  and dried afterward at 80 °C for 30 min.

**Thermoanalytic Studies.** Differential thermal analysis (DTA) was performed with a STA 449F3 Jupiter; Fa. Netzsch, Selb, Germany. Samples were fused into homemade silica containers and analyzed between room temperature and 500 °C with a heating and cooling rate of 2 K/min.

**Powder X-ray Diffraction (PXRD).** PXRD patterns of products were collected with a Stadi-P (STOE, Darmstadt, Germany) powder diffractometer using germanium monochromated  $\text{Cu K}\alpha_1$  radiation ( $\lambda = 1.5406 \text{ \AA}$ ) and a Mythen 1K detector in the range of  $5 < 2\theta < 120^\circ$ . The recorded X-ray powder diffraction pattern was indexed, and the crystal structure was subsequently solved with the program EXPO2014.<sup>39</sup> Structure refinement was performed using the FullProf Suite.<sup>40</sup>

**Sn Mössbauer Spectroscopy.** Sn Mössbauer spectroscopy was performed at room temperature with a  $\text{CaSnO}_3$  source in the transmission mode. The velocity scale was calibrated with  $\beta$ -Sn metal foil. The powder samples were sealed in polyethylene/aluminum bags inside an argon-filled glovebox to avoid contact with air.

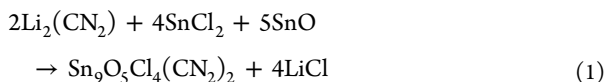
**Infrared Measurements.** The IR spectrum of  $\text{Sn}_9\text{O}_5\text{Cl}_4(\text{CN}_2)_2$  was recorded with a Bruker Vertex 70 spectrometer within the spectral range of 400–4000  $\text{cm}^{-1}$ . A KBr pellet was used for sample preparation.

**Optical Measurements.** For UV/vis spectroscopy, a commercial diffuse reflectance mirror optic (Harrick, Praying Mantis)<sup>41</sup> was used. The light source (Mikropack DH-2000-Bal halogen and deuterium lamp) and the FFT-CCD UV/vis spectrometer (Ocean Optics, Maya 2000) were connected to the mirror optic using optical fibers. By using a beam shutter, the sensors were only exposed to UV/vis radiation when recording a spectrum.  $\text{BaSO}_4$  was used as reflectance standard.

**Density Functional Theory.** Abinit 8.10.3 was used to perform electronic structure calculations.<sup>42–44</sup> The employed exchange-correlation functional was that of Perdew–Burke–Ernzerhof<sup>45</sup> together with the dispersion correction vdw-DFT-D2.<sup>46</sup> Both optimized norm-conserving Vanderbilt pseudopotentials<sup>47</sup> and projector augmented-wave data sets<sup>48</sup> were used as received from the Abinit Web site. Furthermore, convergence studies and structural relaxation were carried out prior to calculation of optimized electronic structures. Example input files can be found as part of the Supporting Information.

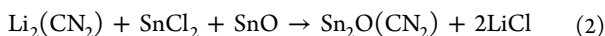
## RESULTS AND DISCUSSION

**Synthesis.**  $\text{Sn}_9\text{O}_5\text{Cl}_4(\text{CN}_2)_2$  was prepared from stoichiometric amounts of  $\text{SnCl}_2$ ,  $\text{SnO}$  and  $\text{Li}_2(\text{CN}_2)$  in fused silica tubing at 400 °C, following reaction 1.



$\text{Sn}_9\text{O}_5\text{Cl}_4(\text{CN}_2)_2$ , as obtained from this reaction, appears as a brown crystalline powder that remains stable in moist air and water, allowing its liberation from the coproduced  $\text{LiCl}$  by washing with water.

The same principal reaction was previously reported for the synthesis of  $\text{Sn}_2\text{O}(\text{CN}_2)$  at 450 °C, however, with different stoichiometric amounts of reactants, given in reaction 2.<sup>37</sup>



During this reaction two intermediate phases were detected by thermal analysis (DTA), of which one was identified as  $\text{Sn}_4\text{Cl}_2(\text{CN}_2)_3$  with a formation temperature below 200 °C.<sup>38</sup> The second intermediate was formed near 300 °C and is now identified as  $\text{Sn}_9\text{O}_5\text{Cl}_4(\text{CN}_2)_2$ . The successive formation of both phases did not occur in a quantitative way in reaction 2,

as a result of the chosen composition of starting materials for the synthesis of the target compound  $\text{Sn}_2\text{O}(\text{CN}_2)$ . Hence, explorative variations of the stoichiometry of starting materials were necessary to obtain pure  $\text{Sn}_9\text{O}_5\text{Cl}_4(\text{CN}_2)_2$ .

DTA of the formation of  $\text{Sn}_9\text{O}_5\text{Cl}_4(\text{CN}_2)_2$  (reaction 1) reveals two exothermic effects during heating, shown in Figure 1. The first thermal effect near 190 °C can be assigned to the

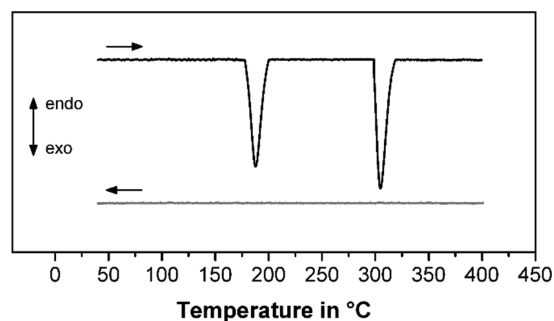


**Figure 1.** DTA of the reaction of  $\text{Li}_2(\text{CN}_2)$ ,  $\text{SnCl}_2$ , and  $\text{SnO}$  in a 2:4:5 molar ratio corresponding to reaction 1 showing one heating and cooling cycle.

formation of  $\text{Sn}_4\text{Cl}_2(\text{CN}_2)_3$ . The second, slightly stronger, thermal effect near 310 °C is assigned to the formation of  $\text{Sn}_9\text{O}_5\text{Cl}_4(\text{CN}_2)_2$ , as evidenced by PXRD measurements of both compounds. The cooling process did not show any thermal effects, and a second heating/cooling cycle was also featureless.  $\text{Sn}_9\text{O}_5\text{Cl}_4(\text{CN}_2)_2$  is stable up to 450 °C, where it decomposes into tin oxides, elemental tin, and some X-ray amorphous phases.

**Crystal Structure of  $\text{Sn}_9\text{O}_5\text{Cl}_4(\text{CN}_2)_2$ .** The crystal structure of  $\text{Sn}_9\text{O}_5\text{Cl}_4(\text{CN}_2)_2$  was solved in the space group  $C222_1$  with EXPO2014.<sup>39</sup> The Rietveld refinement was carried out on a phase-pure sample of  $\text{Sn}_9\text{O}_5\text{Cl}_4(\text{CN}_2)_2$  using the FullProf-WinPLOTR software;<sup>40</sup> the final refinement plot is displayed in Figure 2. Crystallographic data for  $\text{Sn}_9\text{O}_5\text{Cl}_4(\text{CN}_2)_2$  are summarized in Table 1 and atomic coordinates in Table 2.

Crystal structures of metal carbodiimides are usually layered, with layers of carbodiimide ions alternating with connecting layers of metal atoms. This pattern is somewhat preserved in the structure of  $\text{Sn}_9\text{O}_5\text{Cl}_4(\text{CN}_2)_2$ ; however, a more complex arrangement of tin atoms is found. The remarkable pattern of tin oxide clusters can be used to explain the collective arrangement in the structure. Tin atoms are arranged to form  $[\text{Sn}_4\text{O}]$  tetrahedra, with three tetrahedra sharing a common edge, thereby generating the motif of a hexagonal bipyramid of tin atoms. These  $[\text{Sn}_8\text{O}_3]$  moieties are connected by another tin atom ( $\text{Sn5}$ ) and additional oxygen ( $\text{O1}$ ) to form chains. A section of this arrangement is displayed in Figure 3.

The interatomic distances between tin atoms in the structure of  $\text{Sn}_9\text{O}_5\text{Cl}_4(\text{CN}_2)_2$ , highlighted by connecting lines in Figure 3, range between 3.36 and 3.89 Å and can be considered as nonbonding contacts. However, the  $\text{Sn1}–\text{Sn1}$  contact between the tips of the hexagonal  $[\text{Sn}_8\text{O}_3]$  bipyramid is only 3.17 Å. Bonding interactions between tin atoms are generally shorter, for example, between 2.92 and 3.02 Å in the “naked” tin cluster of  $\text{K}_4\text{Sn}_9$ ,<sup>49</sup> or even shorter in the Zintl phases  $\text{BaSnD}_{3/4-x}$  (2.89 Å)<sup>50</sup> and  $\text{Ca}_5\text{Sn}_3\text{H}$  (2.88 Å).<sup>51</sup> Oxide ions occupy tetrahedral interstices between tin atoms with  $\text{Sn}–\text{O}$  distances ranging from 2.17 to 2.38 Å.



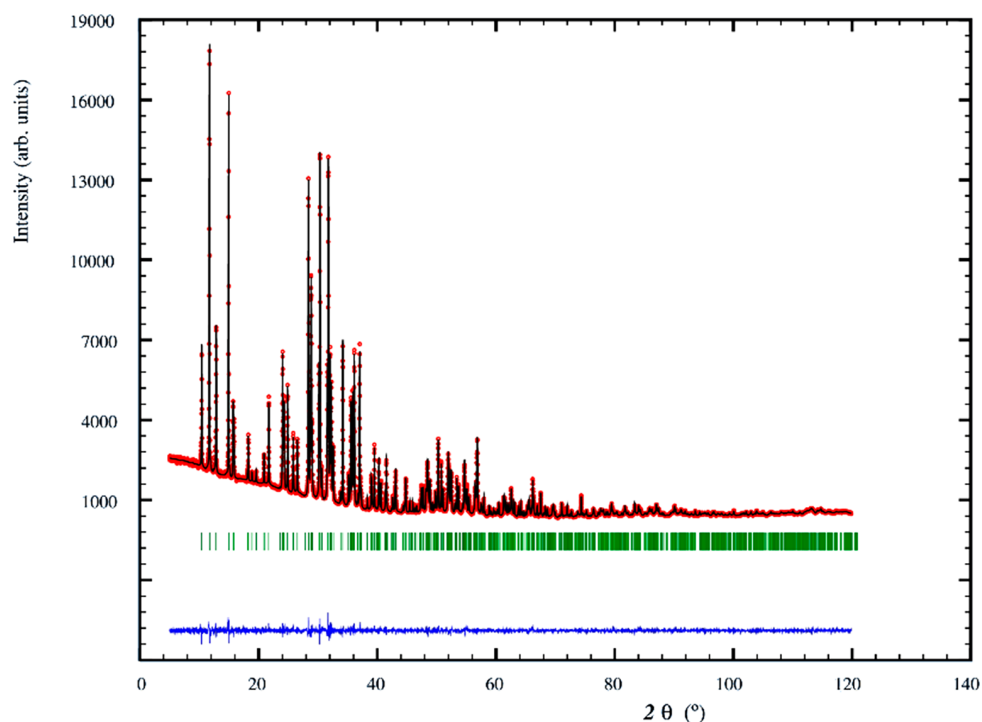


**Figure 2.** PXRD refinement pattern of  $\text{Sn}_9\text{O}_5\text{Cl}_4(\text{CN}_2)_2$ . Experimental PXRD pattern (red) and calculated pattern (black). Bragg positions (green) and difference curve (blue) after Rietveld refinement.

**Table 1.** Crystal Structure Data of  $\text{Sn}_9\text{O}_5\text{Cl}_4(\text{CN}_2)_2$

empirical formula	$\text{Sn}_9\text{O}_5\text{Cl}_4(\text{CN}_2)_2$
CSD No.	1939861
formula weight ( $\text{g}\cdot\text{mol}^{-1}$ )	1370.25
temp (K)	298(2)
wavelength (Å)	1.5406
crystal system	orthorhombic
space group	$C22_1$
<i>a</i> (Å)	11.8306(4)
<i>b</i> (Å)	9.7690(3)
<i>c</i> (Å)	19.9713(6)
volume (Å <sup>3</sup> )	1961.42(1)
<i>Z</i>	4
$\mu$ ( $\text{Cu K}\alpha$ ; $\text{mm}^{-1}$ )	94.779
density (calcd; $\text{g}\cdot\text{cm}^{-3}$ )	4.64
theta range for data collection (°)	2.5–60.0
total number of reflections	856
refined parameters	64
$R_p$ , $R_{wp}$	2.3581, 3.0568
$R_{Bragg}$	2.1200
$\chi^2$	1.0069

Tin atoms in  $\text{Sn}_9\text{O}_5\text{Cl}_4(\text{CN}_2)_2$  occupy five different sites as can be seen in Table 2. A detailed view on the coordination environments of tin ions is displayed in Figure 4, revealing four 3-fold and one 4-fold coordination with different ions.

The complete crystal structure of  $\text{Sn}_9\text{O}_5\text{Cl}_4(\text{CN}_2)_2$  can be described as chains of tin oxide clusters running parallel to each other along the crystallographic *c*-direction. These chains are interconnected by  $(\text{N}=\text{C}=\text{N})^{2-}$  ions along *a*- and by chloride ions along the *b*-axis direction, as can be seen in the two projections of the structure in Figure 5.

Atoms of the  $(\text{NCN})^{2-}$  ion occupy general position in the structure of  $\text{Sn}_9\text{O}_5\text{Cl}_4(\text{CN}_2)_2$ , shown in Figure 6, with C1–N1

**Table 2.** Atomic Coordinates, Wyckoff Positions (Wyck), and Isotropic Displacement Parameters ( $U_{eq}$  in  $\text{pm}^2$ ) for  $\text{Sn}_9\text{O}_5\text{Cl}_4(\text{CN}_2)_2$

atom	Wyck	<i>x</i>	<i>y</i>	<i>z</i>	$U_{eq}^a$
Sn1	8c	0.3863(5)	0.85588(9)	0.29960(4)	0.0418(2)
Sn2	8c	0.3668(6)	0.8509(1)	0.07080(4)	0.0396(2)
Sn3	8c	0.4486(6)	0.1576(1)	0.15694(4)	0.0407(3)
Sn4	8c	0.0692(7)	0.05009(9)	0.34376(5)	0.0377(3)
Sn5	4a	0.6321(1)	0	0	0.0490(4)
Cl1	8c	0.9215(2)	0.2091(3)	0.4829(2)	0.058(1)
Cl2	8c	0.3060(2)	0.1831(3)	0.3316(2)	0.0389(9)
O1	8c	0.5104(1)	0.9942(2)	0.08044(7)	0.039(2)
O2	4b	0	0.5224(2)	1/4	0.031(3)
O3	8c	0.0576(1)	0.2611(1)	0.32168(9)	0.045(2)
C1	8c	0.1928(2)	0.0241(2)	0.1851(1)	0.032(4)
N1	8c	0.0945(1)	0.0309(2)	0.21219(9)	0.035(3)
N2	8c	0.2872(1)	1.0168(2)	0.1470(1)	0.069(4)

<sup>a</sup> $U_{eq}$  is defined as one-third of the trace of the orthogonalized  $U_{ij}$  tensor.

and C1–N2 distances of 1.25 and 1.29 Å. In view of the small deviations of these values the  $(\text{NCN})^{2-}$  ion can still be considered as a carbodiimide ion (rather than cyanamide). This was also confirmed by IR measurements, as no symmetric stretching vibrations of the NCN unit could be detected (expected in the range of  $1200\text{ cm}^{-1}$  for a cyanamide). IR measurements furthermore revealed an asymmetric stretching vibration at  $1985\text{ cm}^{-1}$  and a bending vibration at  $669\text{ cm}^{-1}$ , clearly confirming the presence of the carbodiimide ion. The symmetric stretching vibration of the Sn–O bond<sup>52</sup> was identified at  $618\text{ cm}^{-1}$ , as was the bending vibration of the N–Sn–N body at  $551\text{ cm}^{-1}$  (see Figure S1). The  $(\text{NCN})^{2-}$  ion is surrounded by four tin atoms with Sn–N distances ranging between 2.17 and 2.36 Å.

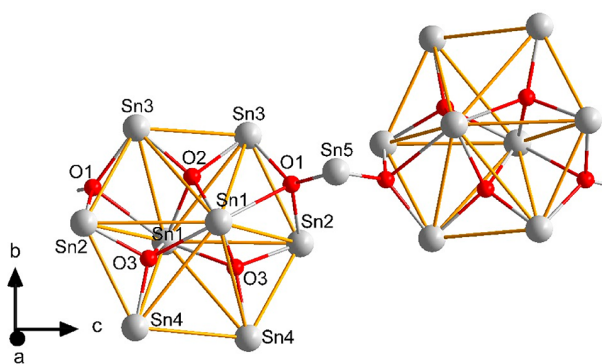


**Figure 3.** Section of the structure of  $\text{Sn}_9\text{O}_5\text{Cl}_4(\text{CN}_2)_2$  emphasizing two  $[\text{Sn}_8\text{O}_3]$  clusters, interconnected by oxygen (O1) and tin (Sn5) into chains. Oxide ions (shown red) occupy approximately tetrahedral sites.

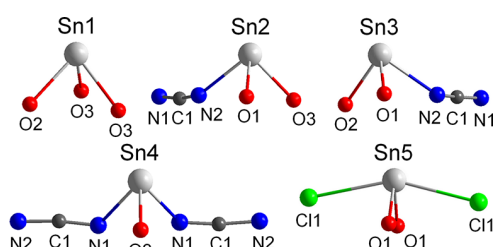


**Figure 4.** Five different  $\text{Sn}^{2+}$  ions in the structure of  $\text{Sn}_9\text{O}_5\text{Cl}_4(\text{CN}_2)_2$  with their coordination environments.

**Mössbauer Spectroscopy.** Sn Mössbauer spectra of  $\text{SnO}$ ,  $\text{Sn}_4\text{Cl}_2(\text{CN}_2)_3$ , and  $\text{Sn}_9\text{O}_5\text{Cl}_4(\text{CN}_2)_2$  are shown in Figure 7. The spectrum of  $\text{SnO}$  shows predominantly a doublet with isomer shift  $\text{IS} = 2.63$  mm/s and quadrupole splitting  $\text{QS} = 1.35$  mm/s. This isomer shift is characteristic for  $\text{Sn}^{2+}$  ions in an oxide environment and the large quadrupole splitting reflects the local asymmetry around the Sn ions with direct Sn–Sn bonds. A second minor contribution is visible with  $\text{IS} = 0.0$  mm/s and  $\text{QS} = 0.5$  mm/s. These values are close to those reported for  $\text{SnO}_2$ .<sup>53</sup>

The spectrum of  $\text{Sn}_4\text{Cl}_2(\text{CN}_2)_3$  shows exclusively a broad doublet with  $\text{IS} = 3.35$  mm/s and a large splitting of  $\text{QS} = 1.28$  mm/s revealing that only  $\text{Sn}^{2+}$  is present in this sample. The even larger isomer shift in comparison to  $\text{SnO}$  is caused by the presence of direct nitrogen neighbors with low electronegativity.<sup>54</sup>

The spectrum of  $\text{Sn}_9\text{O}_5\text{Cl}_4(\text{CN}_2)_2$  is again dominated by a broad doublet with isomer shift  $\text{IS} = 3.15$  mm/s and quadrupole splitting  $\text{QS} = 1.82$  mm/s. The large positive value of the isomer shift reveals again that Sn is present in the 2+ oxidation state and has nitrogen neighbors. The very large quadrupole splitting corresponds to a strong local asymmetry around the Sn ions, as expected from the crystal structure described above. A second minor contribution (area fraction of about 7%) is visible with  $\text{IS} = 0.0$  mm/s and  $\text{QS} = 0.5$  mm/s. This might hint at some minor impurity or passivation layer, possibly amorphous, containing  $\text{Sn}^{4+}$  in an oxidizing environment, and could be explained by the presence of a small amount of  $\text{Sn}^{4+}$  in the precursor  $\text{SnO}$ . This is evident since it could be detected in  $\text{SnO}$  samples obtained from both Sigma-Aldrich and Alfa Aesar. The results of fitting the Mössbauer spectra are summarized in Table 3.

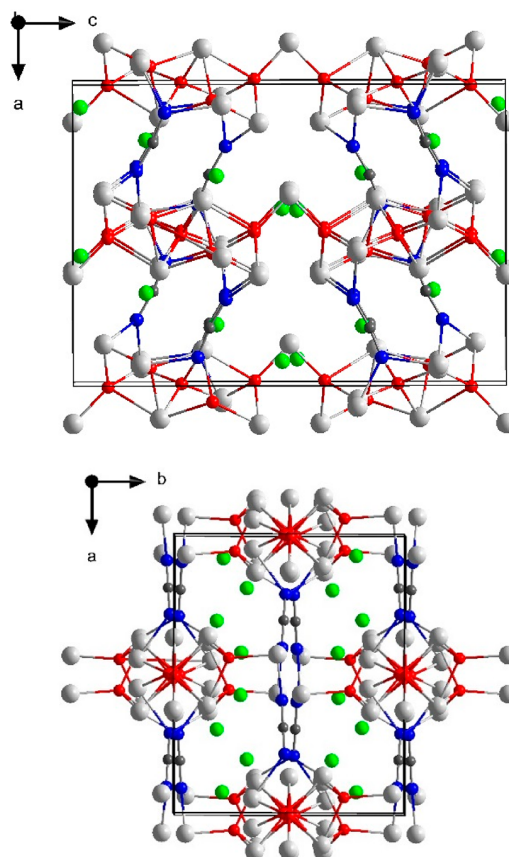


**Figure 5.** Two projections of the structure of  $\text{Sn}_9\text{O}_5\text{Cl}_4(\text{CN}_2)_2$  showing chains of  $[\text{Sn}_8\text{O}_3]$  clusters running along  $[001]$ . Tin is shown in light gray, oxygen is shown in red, chlorine is shown in green, nitrogen is shown in blue, and carbon is shown in dark gray.

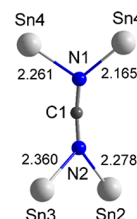


**Figure 6.** Environment of the  $(\text{N}=\text{C}=\text{N})^{2-}$  ion in the structure of  $\text{Sn}_9\text{O}_5\text{Cl}_4(\text{CN}_2)_2$ , surrounded by four tin atoms.

**Electronic Structure.** In order to determine the electronic structure and properties of  $\text{Sn}_9\text{O}_5\text{Cl}_4(\text{CN}_2)_2$ , density functional theory (DFT) was used. Because the energies of the calculated conduction bands do not account for the interaction energy between an excited electron and hole and the valence electrons, band gaps calculated with DFT are systematically underestimated.<sup>55</sup> The calculated band structure is shown in Figure 8.

When comparing  $\text{Sn}_9\text{O}_5\text{Cl}_4(\text{CN}_2)_2$  to the two previously synthesized tin carbodiimide compounds  $\text{Sn}(\text{CN}_2)$  and  $\text{Sn}_4\text{Cl}_2(\text{CN}_2)_3$ ,<sup>38</sup> some similarities are found. All three compounds are indirect band gap semiconductors, with  $\text{Sn}_9\text{O}_5\text{Cl}_4(\text{CN}_2)_2$  exhibiting the largest band gap (2.3 eV, the optical band gap was determined to be 3.1, see Figure 9). This underestimation is typical for a DFT calculation and coincides with the results obtained from  $\text{Sn}(\text{CN}_2)$  (calculated, 1.2 eV;

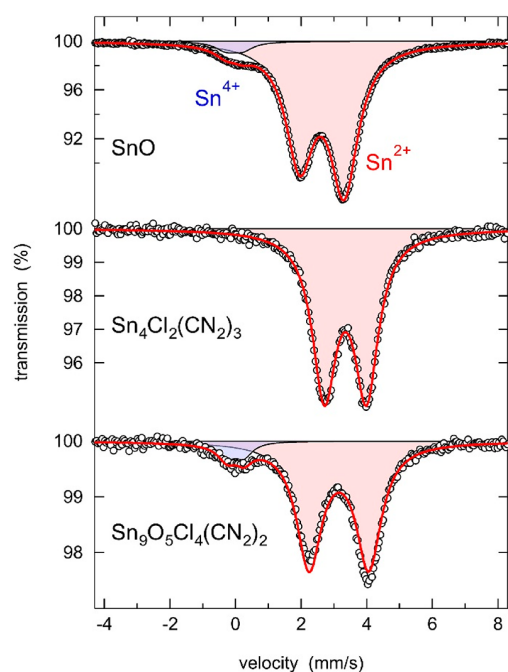


**Figure 7.** Sn Mössbauer spectra of SnO,  $\text{Sn}_4\text{Cl}_2(\text{CN}_2)_3$ , and  $\text{Sn}_9\text{O}_5\text{Cl}_4(\text{CN}_2)_2$ . The experimental data points are shown as white spheres, the overall fit as a red line, and the subspectra are shown as red and blue doublets.

measured, 2.0 eV) and  $\text{Sn}_4\text{Cl}_2(\text{CN}_2)_3$  (calculated, 1.9 eV; measured, 2.6 eV). The indirect band gap indicated in Figure 8 is only slightly smaller than the direct gap at  $\Gamma$  (2.4 eV). The energy of the valence band maximum between  $\Gamma$  and S is also only marginally higher than the maximum between  $\Gamma$  and  $\Sigma$ , with the calculated difference being less than 0.01 eV. The band structure of  $\text{Sn}_9\text{O}_5\text{Cl}_4(\text{CN}_2)_2$  has small band curvature, indicating a large electron effective mass. This increased effective mass is consistent with a structure with reduced delocalization due to a smaller number of tin–carbodiimide interactions in comparison to other tin carbodiimide compounds. The maximum energy of the valence band lies along the  $\Gamma(0\ 0\ 0)$ – $S(0\ 0.5\ 0.0)$  direction; a second local maximum close to the Fermi level ( $\epsilon_F$ ) is located along the  $\Sigma(0.42\ 0.42\ 0)$ – $\Gamma(0\ 0\ 0)$  direction. In addition to the band structure calculation, the electron localization function (ELF) was determined.<sup>57,58</sup> The ELF is a measure of the probability of finding an electron at the same position as a reference electron with the same spin; it thereby provides information about the localization of electrons. From this definition, it is obvious that electron pairs have a high ELF value and are readily visible. The maximum value of the ELF is defined as 1,

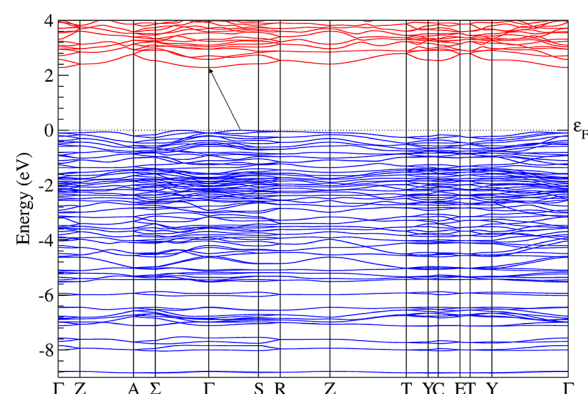


**Figure 8.** Calculated electronic band structure of  $\text{Sn}_9\text{O}_5\text{Cl}_4(\text{CN}_2)_2$ . An arrow marks the indirect band gap. Special points in the Brillouin zone were selected following Hinuma et al.<sup>56</sup>

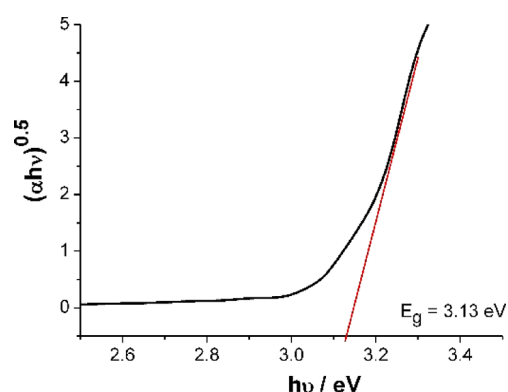


**Figure 9.** Reflectance measurement of  $\text{Sn}_9\text{O}_5\text{Cl}_4(\text{CN}_2)_2$ . Definition of the y-axis:  $\alpha$  is the absorption coefficient defined as  $\alpha = \frac{(1-R)^2}{2R}$ , where  $R$  is the reflectivity,  $h$  is Planck's constant, and  $\nu$  is the frequency. The exponent of 0.5 corresponds to an indirect bandgap. The determination of the band gap (Tauc plot) was done as described in Tauc<sup>59</sup> and Davis.<sup>60</sup>

the minimum 0, and the value 0.5 corresponds to the homogeneous electron gas. Information from the ELF enables us to further compare the electronic structure of  $\text{Sn}_9\text{O}_5\text{Cl}_4(\text{CN}_2)_2$ , especially the structural influence of the tin lone pair, with that of  $\text{Sn}(\text{CN}_2)$  and  $\text{Sn}_4\text{Cl}_2(\text{CN}_2)_3$ .

At variance with band structure calculation, where projector augmented-wave data sets were used, norm-conserving Vanderbilt pseudopotentials were employed to calculate the ELF. The change of the atomic data sets was necessary as the Abinit code does not presently support the projector augmented-wave method when calculating the ELF.<sup>47</sup> The

**Table 3. Parameters Obtained from Fitting the Mössbauer Spectra: Isomer Shift IS, quadrupole Splitting QS, and Line Width  $\Gamma$  are Given in mm/s**

		IS	QS	$\Gamma$	area frac. (%)
SnO (Sigma-Aldrich)	$\text{Sn}^{2+}$	2.629(1)	1.352(1)	1.032(2)	95.4
	$\text{Sn}^{4+}$	−0.047(11)	0.507(25)	0.795(42)	4.6
SnO (Alfa Aesar)	$\text{Sn}^{2+}$	2.633(2)	1.390(2)	1.195(4)	95.2
	$\text{Sn}^{4+}$	0.014(14)	0.583(25)	0.757(48)	4.8
$\text{Sn}_4\text{Cl}_2(\text{CN}_2)_3$	$\text{Sn}^{2+}$	3.346(2)	1.283(3)	0.887(5)	100.0
$\text{Sn}_9\text{O}_5\text{Cl}_4(\text{CN}_2)_2$	$\text{Sn}^{2+}$	3.149(3)	1.818(4)	0.933(7)	92.6
	$\text{Sn}^{4+}$	−0.008(20)	0.513(37)	0.644(65)	7.4

fact that pseudopotentials were used for this calculation influences the depictions below, as only valence and semicore electrons are visualized.

The ELF analysis of  $\text{Sn}_9\text{O}_5\text{Cl}_4(\text{CN}_2)_2$  shows characteristics similar to those found in both  $\text{Sn}(\text{CN}_2)$  and  $\text{Sn}_4\text{Cl}_2(\text{CN}_2)_3$ . With the latter compound, it shares the electron localization around the carbodiimide units; there is significant localization around the nitrogen and almost none around the carbon atoms. Electron localization around the chlorine atoms is present, but is more diffuse and does not reach the 0.55 level. Different to  $\text{Sn}_4\text{Cl}_2(\text{CN}_2)_3$ , but similar to  $\text{Sn}(\text{CN}_2)$ ,  $\text{Sn}_9\text{O}_5\text{Cl}_4(\text{CN}_2)_2$  features void space in the crystal structure in between the hexagonal bipyramids formed by the tin atoms (Figure 3). This property could justify classifying it as an open framework structure, like  $\text{Sn}(\text{CN}_2)$ . A quite interesting feature, one that also distinguishes all three compounds, is the localization of the tin lone pairs. Showing neither the toroidal lone pair of  $\text{Sn}(\text{CN}_2)$ , nor the classic lobe of  $\text{Sn}_4\text{Cl}_2(\text{CN}_2)_3$ , those in  $\text{Sn}_9\text{O}_5\text{Cl}_4(\text{CN}_2)_2$  are spread more homogeneously around each tin atom (Figure 10).

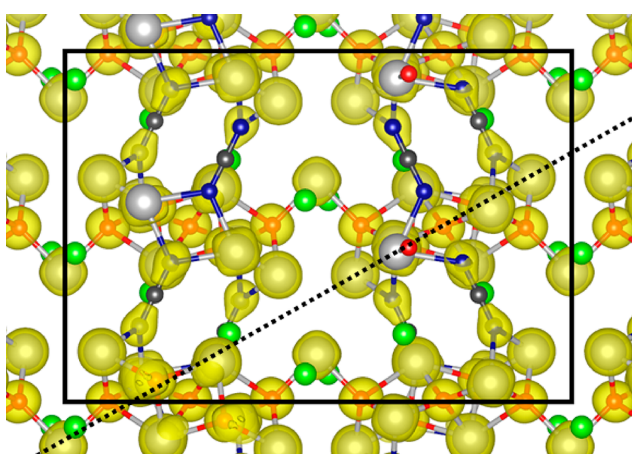


**Figure 10.** Calculated electron localization function of  $\text{Sn}_9\text{O}_5\text{Cl}_4(\text{CN}_2)_2$  shown as an isosurface at the 0.55 level in the  $ac$  plane. The view along  $b$  corresponds to the projection of the structure in Figure 5 (top). The dashed line was added to indicate the plane of the section shown in Figure 11.

Figure 10 shows the properties of the ELF near the tin atoms more clearly and reveals that the tin atoms possess differences in their electronic structures. The section shown in Figure 10 is inclined relative to the  $bc$  plane to show a more precise view of the tin atoms in the hexagonal bipyramid shown in Figure 3 (right). Those tin atoms are the ones arranged in a hexagon in the top right corner of Figure 11 encircling three oxygen atoms. While the two tin atoms at the bottom of the hexagon exhibit more homogeneous electron localization and ionic character, the ones at the middle and top show strong inhomogeneous electron localization and a significant correlation between the peaks and nodes and the bonding direction of a specific tin atom. It is also important to note that their electron localization around the atoms is significantly distorted from a sphere. In particular, the geometry of the ones at the top resemble rounded cubes. The strong distortion of the electron localization is an indicator of covalent bonding between the tin and oxygen atoms.

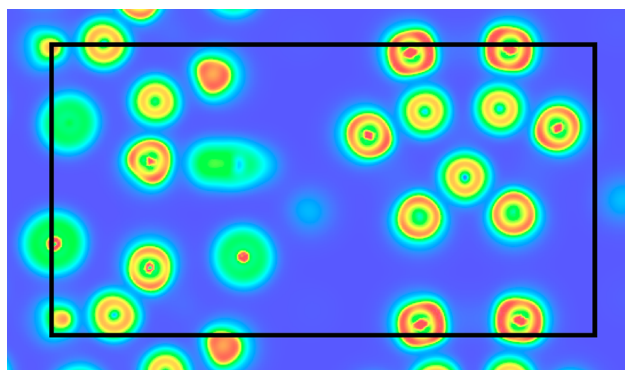


**Figure 11.** ELF as an inclined section through the  $bc$  plane. The view corresponds to the projection of the structure in Figure 3. The plane of the section is plotted in Figure 10 as dashed line. The six atoms encircling the three oxygen atoms in the top right corner correspond to the base of the right hexagonal bipyramid in Figure 3.

## CONCLUSION

The new compound  $\text{Sn}_9\text{O}_5\text{Cl}_4(\text{CN}_2)_2$  is presented with its synthesis and crystal structure.  $\text{Sn}_9\text{O}_5\text{Cl}_4(\text{CN}_2)_2$  is generated around 300 °C from  $\text{SnO}$ ,  $\text{SnCl}_2$ , and  $\text{Li}_2(\text{CN}_2)$  via the precursor compound  $\text{Sn}_4\text{Cl}_2(\text{CN}_2)_3$  formed near 190 °C. The intermediate formation of  $\text{Sn}_4\text{Cl}_2(\text{CN}_2)_3$  has already been observed in previous syntheses of  $\text{Sn}_2\text{O}(\text{CN}_2)$  and  $\text{Sn}(\text{CN}_2)$ , where it is formed near 150 and 200 °C, respectively.

Crystalline  $\text{Sn}_9\text{O}_5\text{Cl}_4(\text{CN}_2)_2$  resists air and water and is stable up to 450 °C where decomposition starts. The arrangement of tin atoms in the structure follows the motif of a hexagonal bipyramid, thereby forming  $[\text{Sn}_6\text{O}_3]$  clusters that are connected into chains by an additional tin atom. Tin Mössbauer measurements revealed the presence of Sn(II) with small amounts of Sn(IV) in  $\text{Sn}_9\text{O}_5\text{Cl}_4(\text{CN}_2)_2$ , but not in  $\text{Sn}_4\text{Cl}_2(\text{CN}_2)_3$ . The origin of the  $\text{Sn}^{4+}$  can be traced back to the  $\text{SnO}$  source, which was used in the synthesis, as shown by Mössbauer spectroscopy of  $\text{SnO}$ . DFT calculations predict that  $\text{Sn}_9\text{O}_5\text{Cl}_4(\text{CN}_2)_2$  is a wide-bandgap semiconductor with an indirect band gap. The calculated ELF indicates that the lone pairs of the tin atoms participate in bonding, with a mixture of ionic and covalent character within each hexagonal bipyramidal cluster.

Recently prepared tin(II) carbodiimides  $\text{Sn}(\text{CN}_2)$ ,  $\text{Sn}_2\text{O}(\text{CN}_2)$ ,  $\text{Sn}_4\text{Cl}_2(\text{CN}_2)_3$ , and  $\text{Sn}_9\text{O}_5\text{Cl}_4(\text{CN}_2)_2$  represent semiconductors with band gaps in the order of 2–3 eV. Although these compounds are mostly stable in air, a potential application is not yet clear. An investigation on the photochemical properties of  $\text{Sn}_2\text{O}(\text{CN}_2)$ <sup>37</sup> is currently underway.

## ASSOCIATED CONTENT

### Supporting Information

The Supporting Information is available free of charge on the ACS Publications website at DOI: 10.1021/acs.inorgchem.9b02229.

DFT input files for band structure and ELF calculations (ZIP)

Figure S1: Infrared measurement of  $\text{Sn}_9\text{O}_5\text{Cl}_4(\text{CN}_2)_2$  (PDF)

### Accession Codes

CCDC 1939861 contains the supplementary crystallographic data for this paper. These data can be obtained free of charge

via [www.ccdc.cam.ac.uk/data\\_request/cif](http://www.ccdc.cam.ac.uk/data_request/cif), or by emailing [data\\_request@ccdc.cam.ac.uk](mailto:data_request@ccdc.cam.ac.uk), or by contacting The Cambridge Crystallographic Data Centre, 12 Union Road, Cambridge CB2 1EZ, U.K.; Fax: +44 1223 336033.

## AUTHOR INFORMATION

### Corresponding Author

\*E-mail: [juergen.meyer@uni-tuebingen.de](mailto:juergen.meyer@uni-tuebingen.de).

### ORCID

Manuel Löber: 0000-0002-4492-952X

Markus Ströbele: 0000-0002-5147-5677

Sylvio Indris: 0000-0002-5100-113X

Hans-Jürgen Meyer: 0000-0003-2450-4011

### Funding

Support of this project by the Deutsche Forschungsgemeinschaft (Bonn) via Grant ME 914/25-2 is gratefully acknowledged. The authors acknowledge support by the state of Baden-Württemberg through bwHPC and the German Research Foundation (DFG) through Grant No. INST 40/467-1 FUGG (JUSTUS cluster).

### Notes

The authors declare no competing financial interest.

## ACKNOWLEDGMENTS

The authors would like to express their gratitude to Andreas Früh (Univ. Tübingen) for performing the optical reflection measurements.

## REFERENCES

- (1) Ströbele, M.; Meyer, H.-J. Pandora's box of binary tungsten iodides. *Dalton Trans* **2019**, *48*, 1547–1561.
- (2) Meyer, H.-J. Solid state metathesis reactions as a conceptual tool in the synthesis of new materials. *Dalton Trans* **2010**, *39*, 5973–5982.
- (3) Mos-Hummel, A.; Ströbele, M.; Meyer, H.-J. A journey through ternary lead chlorido tungstates by thermal scanning. *Dalton Trans* **2017**, *46*, 7743–7749.
- (4) Mos, A.; Ströbele, M.; Meyer, H.-J. Thermal Detection, Synthesis, and Structural Characterization of Compounds in the Co–W–Cl System. *J. Cluster Sci.* **2015**, *26*, 187–198.
- (5) Mos, A.; Castro, C.; Indris, S.; Ströbele, M.; Fink, R. F.; Meyer, H.-J. From  $WCl_6$  to  $WCl_2$ : Properties of Intermediate Fe–W–Cl Phases. *Inorg. Chem.* **2015**, *54*, 9826–9832.
- (6) Mos-Hummel, A.; Ströbele, M.; Meyer, H.-J. Snap-Shots of a Reduction Pathway: The Reaction of  $WCl_6$  with Copper Powder. *Eur. J. Inorg. Chem.* **2016**, *2016*, 4234–4240.
- (7) Yamane, H.; Kikkawa, S.; Horiuchi, H.; Koizumi, M. Structure of a new polymorph of lithium boron nitride,  $Li_3BN_2$ . *J. Solid State Chem.* **1986**, *65*, 6–12.
- (8) Womelsdorf, H.; Meyer, H. J. Zur Kenntnis der Struktur von  $Sr_3(BN_2)_2$ . *Z. Anorg. Allg. Chem.* **1994**, *620*, 262–265.
- (9) Reckeweg, O.; Meyer, H. J. Lanthanide Nitrido Borates with Six-Membered  $B_3N_6$  Rings:  $Ln_3B_3N_6$ . *Angew. Chem., Int. Ed.* **1999**, *38*, 1607–1609.
- (10) Rohrer, F. E.; Nesper, R.  $M_2BN_2X$  (M = Ca, Sr; X = F, Cl): New Halogenide Compounds with Isolated  $BN_3^-$  Units. *J. Solid State Chem.* **1998**, *135*, 194–200.
- (11) Kalmutzki, M.; Ströbele, M.; Meyer, H.-J. From cyanate to cyanurate: cyclotrimerization reactions towards the novel family of metal cyanurates. *Dalton Trans* **2013**, *42*, 12934–12939.
- (12) Neukirch, M.; Tragl, S.; Meyer, H.-J. Syntheses and structural properties of rare earth carbodiimides. *Inorg. Chem.* **2006**, *45*, 8188–8193.
- (13) Krott, M.; Liu, X.; Fokwa, B. P.; Speldrich, M.; Lueken, H.; Dronskowski, R. Synthesis, crystal-structure determination and magnetic properties of two new transition-metal carbodiimides:  $CoNCN$  and  $NiNCN$ . *Inorg. Chem.* **2007**, *46*, 2204–2207.
- (14) Liu, X.; Stork, L.; Speldrich, M.; Lueken, H.; Dronskowski, R.  $FeNCN$  and  $Fe(NCNH)_2$ : Synthesis, Structure, and Magnetic Properties of a Nitrogen-Based Pseudo-oxide and-hydroxide of Divalent Iron. *Chem. - Eur. J.* **2009**, *15*, 1558–1561.
- (15) Becker, M.; Jansen, M. Zinc cyanamide,  $Zn(CN_2)$ . *Acta Crystallogr., Sect. C: Cryst. Struct. Commun.* **2001**, *57*, 347–348.
- (16) Becker, M.; Nuss, J.; Jansen, M. Kristallstruktur und schwingungsspektroskopische Daten von Silbercyanamid/Crystal Structure and Spectroscopic Data of Silver Cyanamide. *Z. Naturforsch., B: J. Chem. Sci.* **2000**, *55*, 383–385.
- (17) Tang, X.; Xiang, H.; Liu, X.; Speldrich, M.; Dronskowski, R. A ferromagnetic carbodiimide:  $Cr_2(NCN)_3$ . *Angew. Chem., Int. Ed.* **2010**, *49*, 4738–4742.
- (18) Down, M. G.; Haley, M. J.; Hubberstey, P.; Pulham, R. J.; Thunder, A. E. Solutions of lithium salts in liquid lithium: preparation and X-ray crystal structure of the dilithium salt of carbodi-imide (cyanamide). *J. Chem. Soc., Dalton Trans.* **1978**, 1407–1411.
- (19) Becker, M.; Nuss, J.; Jansen, M. Synthese und Charakterisierung von Natriumcyanamid. *Z. Anorg. Allg. Chem.* **2000**, *626*, 2505–2508.
- (20) Becker, M.; Jansen, M.; Lieb, A.; Milius, W.; Schnick, W. Synthese, Kristallstruktur und Festkörper-NMR-spektroskopische Untersuchungen von  $K_5H(CN_2)_3$ . *Z. Anorg. Allg. Chem.* **1998**, *624*, 113–118.
- (21) Berger, U.; Schnick, W. Syntheses, crystal structures, and vibrational spectroscopic properties of  $MgCN_2$ ,  $SrCN_2$ , and  $BaCN_2$ . *J. Alloys Compd.* **1994**, *206*, 179–184.
- (22) Dronskowski, R.  $In_{2.24}(NCN)_3$  and  $NaIn(NCN)_2$ : Synthesis and Crystal Structures of New Main Group Metal Cyanamides. *Z. Naturforsch., B: J. Chem. Sci.* **1995**, *50*, 1245–1251.
- (23) Corkett, A. J.; Chen, Z.; Bogdanovski, D.; Slabon, A.; Dronskowski, R. Band Gap Tuning in Bismuth Oxide Carbodiimide  $Bi_2O_2NCN$ . *Inorg. Chem.* **2019**, *58*, 6467–6473.
- (24) Zhao, W.; Liu, Y.; Liu, J.; Chen, P.; Chen, I.-W.; Huang, F.; Lin, J. Controllable synthesis of silver cyanamide as a new semiconductor photocatalyst under visible-light irradiation. *J. Mater. Chem. A* **2013**, *1*, 7942–7948.
- (25) Dutczak, D.; Ströbele, M.; Ensling, D.; Juestel, T.; Meyer, H.-J.  $Eu_2(CN_2)_3$  and  $KEu[Si(CN_2)_4]$ : Missing Members of the Rare Earth Metal Carbodiimide and Tetracyanamidosilicate Series. *Eur. J. Inorg. Chem.* **2016**, *2016*, 4011–4016.
- (26) Dolabdjian, K.; Kobald, A.; Romao, C. P.; Meyer, H.-J. Synthesis and thermoelastic properties of  $Zr(CN_2)_2$  and  $Hf(CN_2)_2$ . *Dalton Trans* **2018**, *47*, 10249–10255.
- (27) Eguía-Barrio, A.; Castillo-Martínez, E.; Liu, X.; Dronskowski, R.; Armand, M.; Rojo, T. Carbodiimides: new materials applied as anode electrodes for sodium and lithium ion batteries. *J. Mater. Chem. A* **2016**, *4*, 1608–1611.
- (28) Sougrati, M. T.; Darwiche, A.; Liu, X.; Mahmoud, A.; Hermann, R. P.; Jouen, S.; Monconduit, L.; Dronskowski, R.; Stievano, L. Transition-Metal Carbodiimides as Molecular Negative Electrode Materials for Lithium- and Sodium-Ion Batteries with Excellent Cycling Properties. *Angew. Chem., Int. Ed.* **2016**, *55*, 5090–5095.
- (29) Dong, B.; Wang, Z.; Hung, N. T.; Oganov, A. R.; Yang, T.; Saito, R.; Zhang, Z. New two-dimensional phase of tin chalcogenides: candidates for high-performance thermoelectric materials. *Phys. Rev. Mater.* **2019**, *3*, 013405.
- (30) Yu, S.; Kim, S.-O.; Kim, H.-S.; Choi, W. Computational Screening of Anode Materials for Sodium-Ion Batteries. *J. Electrochem. Soc.* **2019**, *166*, A1915–A1919.
- (31) Barman, B.; Bangerla, K. V.; Shivakumar, G. Evaluation of semiconducting p-type tin sulfide thin films for photodetector applications. *Superlattices Microstruct.* **2019**, *133*, 106215.
- (32) Gunasekaran, M.; Ichimura, M. Photovoltaic cells based on pulsed electrochemically deposited SnS and photochemically

deposited CdS and Cd<sub>1-x</sub>Zn<sub>x</sub>S. *Sol. Energy Mater. Sol. Cells* **2007**, *91*, 774–778.

(33) Matsumoto, R.; Song, P.; Adachi, S.; Saito, Y.; Hara, H.; Yamashita, A.; Nakamura, K.; Yamamoto, S.; Tanaka, H.; Irifune, T.; Takeya, H.; Takano, Y. Pressure-induced superconductivity in tin sulfide. *Phys. Rev. B: Condens. Matter Mater. Phys.* **2019**, *99*, 184502.

(34) Ogo, Y.; Hiramatsu, H.; Nomura, K.; Yanagi, H.; Kamiya, T.; Hirano, M.; Hosono, H. p-channel thin-film transistor using p-type oxide semiconductor, SnO. *Appl. Phys. Lett.* **2008**, *93*, 032113.

(35) Eqbal, E.; Anila, E. Properties of transparent conducting tin monoxide (SnO) thin films prepared by chemical spray pyrolysis method. *Phys. B* **2018**, *528*, 60–65.

(36) Toshniwal, A.; Kheraj, V. Development of organic-inorganic tin halide perovskites: a review. *Sol. Energy* **2017**, *149*, 54–59.

(37) Dolabdjian, K.; Görne, A. L.; Dronskowski, R.; Ströbele, M.; Meyer, H.-J. Tin (II) oxide carbodiimide and its relationship to SnO. *Dalton Trans* **2018**, *47*, 13378–13383.

(38) Löber, M.; Dolabdjian, K.; Ströbele, M.; Romao, C. P.; Meyer, H.-J. Synthesis, Structure, and Electronic Properties of Sn(CN)<sub>2</sub> and Sn<sub>4</sub>Cl<sub>2</sub>(CN)<sub>3</sub>. *Inorg. Chem.* **2019**, *58*, 7845–7851.

(39) Altomare, A.; Cuocci, C.; Giacobozzo, C.; Moliterni, A.; Rizzi, R.; Corriero, N.; Falcicchio, A. EXPO2013: a kit of tools for phasing crystal structures from powder data. *J. Appl. Crystallogr.* **2013**, *46*, 1231–1235.

(40) Rodríguez-Carvajal, J.; Roisnel, T. Line broadening analysis using FullProf\*: determination of microstructural properties. *Mater. Sci. Forum* **2004**, *443*, 123–126.

(41) Harbeck, S.; Szatvanyi, A.; Barsan, N.; Weimar, U.; Hoffmann, V. DRIFT studies of thick film un-doped and Pd-doped SnO<sub>2</sub> sensors: temperature changes effect and CO detection mechanism in the presence of water vapour. *Thin Solid Films* **2003**, *436*, 76–83.

(42) Gonze, X.; Jollet, F.; Araujo, F. A.; Adams, D.; Amadon, B.; Applencourt, T.; Audouze, C.; Beuken, J.-M.; Bieder, J.; Bokhanchuk, A.; et al. Recent developments in the ABINIT software package. *Comput. Phys. Commun.* **2016**, *205*, 106–131.

(43) Torrent, M.; Jollet, F.; Bottin, F.; Zérah, G.; Gonze, X. Implementation of the projector augmented-wave method in the ABINIT code: Application to the study of iron under pressure. *Comput. Mater. Sci.* **2008**, *42*, 337–351.

(44) Bottin, F.; Leroux, S.; Knyazev, A.; Zérah, G. Large-scale ab initio calculations based on three levels of parallelization. *Comput. Mater. Sci.* **2008**, *42*, 329–336.

(45) Perdew, J. P.; Burke, K.; Ernzerhof, M. Generalized gradient approximation made simple. *Phys. Rev. Lett.* **1996**, *77*, 3865.

(46) Grimme, S. Semiempirical GGA-type density functional constructed with a long-range dispersion correction. *J. Comput. Chem.* **2006**, *27*, 1787–1799.

(47) Hamann, D. Optimized norm-conserving Vanderbilt pseudopotentials. *Phys. Rev. B: Condens. Matter Mater. Phys.* **2013**, *88*, 085117.

(48) Jollet, F.; Torrent, M.; Holzwarth, N. Generation of Projector Augmented-Wave atomic data: A 71 element validated table in the XML format. *Comput. Phys. Commun.* **2014**, *185*, 1246–1254.

(49) Hoch, C.; Wendorff, M.; Roehr, C. Tetrapotassium non-astannide, K<sub>4</sub>Sn<sub>9</sub>. *Acta Crystallogr., Sect. C: Cryst. Struct. Commun.* **2002**, *58*, i45–i46.

(50) Auer, H.; Guehne, R.; Bertmer, M.; Weber, S.; Wenderoth, P.; Hansen, T. C.; Haase, J.; Kohlmann, H. Hydrides of Alkaline Earth–Tetrel (AeTt) Zintl Phases: Covalent Tt–H Bonds from Silicon to Tin. *Inorg. Chem.* **2017**, *56*, 1061–1071.

(51) Leon-Escamilla, E. A.; Corbett, J. D. Hydrogen impurity effects. A<sub>3</sub>Tt<sub>3</sub> intermetallic compounds between A= Ca, Sr, Ba, Eu and Tt= Si, Ge, Sn with Cr<sub>3</sub>B<sub>3</sub>-like structures that are stable both as binary and as ternary hydride and fluoride phases. *J. Solid State Chem.* **2001**, *159*, 149–162.

(52) Amalric-Popescu, D.; Bozon-Verduraz, F. Infrared studies on SnO<sub>2</sub> and Pd/SnO<sub>2</sub>. *Catal. Today* **2001**, *70*, 139–154.

(53) Indris, S.; Scheuermann, M.; Becker, S. M.; Sepelák, V.; Kruk, R.; Suffner, J.; Gyger, F.; Feldmann, C.; Ulrich, A. S.; Hahn, H. Local

Structural Disorder and Relaxation in SnO<sub>2</sub> Nanostructures Studied by <sup>119</sup>Sn MAS NMR and <sup>119</sup>Sn Mössbauer Spectroscopy. *J. Phys. Chem. C* **2011**, *115*, 6433–6437.

(54) Harrison, P. Inorganic tin (II) derivatives. *J. Chem. Soc., Chem. Commun.* **1972**, 544–544.

(55) Aryasetiawan, F.; Gunnarsson, O. The GW method. *Rep. Prog. Phys.* **1998**, *61*, 237.

(56) Hinuma, Y.; Pizzi, G.; Kumagai, Y.; Oba, F.; Tanaka, I. Band structure diagram paths based on crystallography. *Comput. Mater. Sci.* **2017**, *128*, 140–184.

(57) Becke, A. D.; Edgecombe, K. E. A simple measure of electron localization in atomic and molecular systems. *J. Chem. Phys.* **1990**, *92*, 5397–5403.

(58) Savin, A.; Jepsen, O.; Flad, J.; Andersen, O. K.; Preuss, H.; von Schnering, H. G. Electron localization in solid-state structures of the elements: the diamond structure. *Angew. Chem., Int. Ed. Engl.* **1992**, *31*, 187–188.

(59) Tauc, J.; Grigorovici, R.; Vancu, A. Optical properties and electronic structure of amorphous germanium. *Phys. Status Solidi B* **1966**, *15*, 627–637.

(60) Davis, E.; Mott, N. Conduction in non-crystalline systems V. Conductivity, optical absorption and photoconductivity in amorphous semiconductors. *Philos. Mag.* **1970**, *22*, 0903–0922.

# Supporting Information

## Synthesis, Structure and Electronic Properties of



*Manuel Löber,<sup>†</sup> Chris Steve Geißenhöner,<sup>†</sup> Markus Ströbele,<sup>†</sup> Sylvio Indris,<sup>‡</sup> Carl P. Romao,<sup>†</sup>  
and Hans-Jürgen Meyer<sup>†\*</sup>*

<sup>†</sup>Section for Solid State and Theoretical Inorganic Chemistry, Institute of Inorganic Chemistry,  
University of Tübingen, Auf der Morgenstelle 18, D-72076 Tübingen, Germany

<sup>‡</sup>Institute for Applied Materials (IAM), Karlsruhe Institute of Technology (KIT), Hermann-von-  
Helmholtz-Platz 1, 76344 Eggenstein-Leopoldshafen, Germany

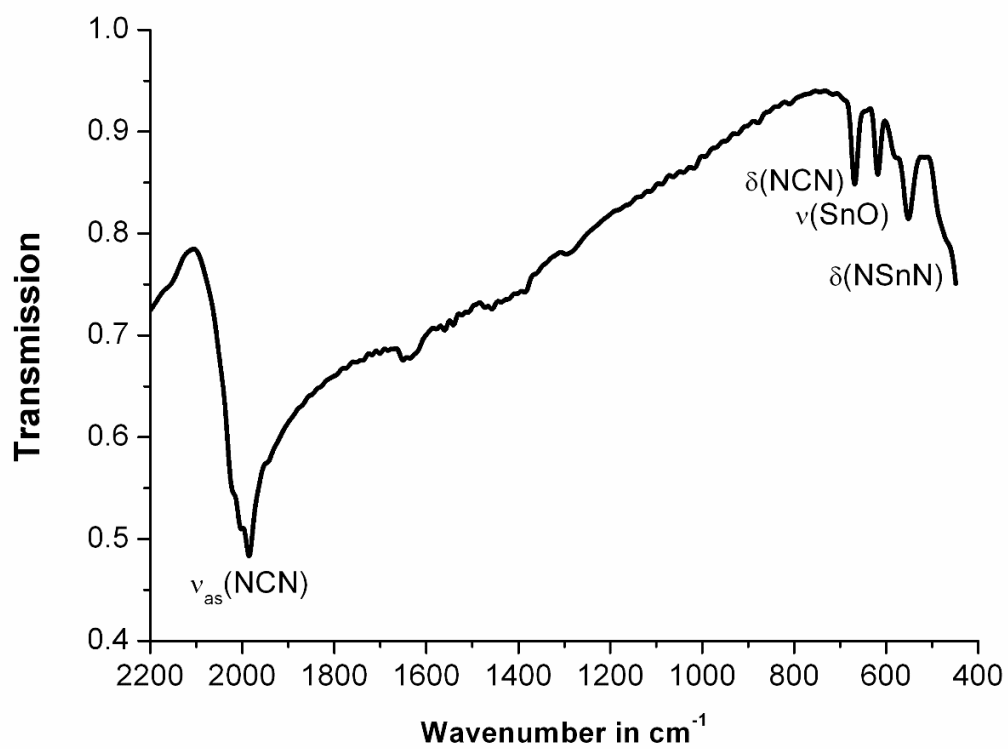
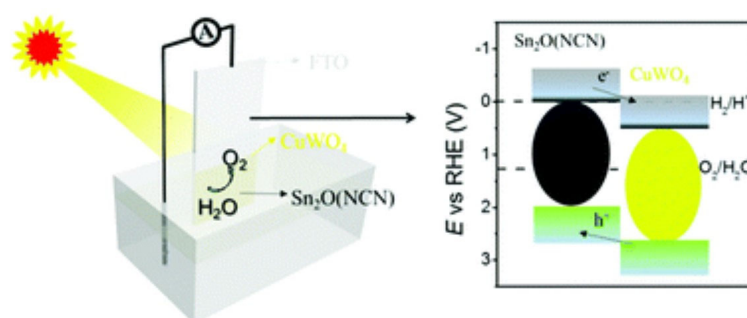


Figure S1. Infrared measurement of  $\text{Sn}_9\text{O}_5\text{Cl}_4(\text{CN}_2)_2$



# Publication 3

Increased photocurrent of  $\text{CuWO}_4$  photoanodes by modification with the oxide carbodiimide  $\text{Sn}_2\text{O}(\text{NCN})$



<https://doi.org/10.1039/C9DT04752B>

Reprinted with permission from

*Dalton Trans.* **2020**, 49, 3450–3456

Copyright © 2020 The Royal Society of Chemistry



Cite this: *Dalton Trans.*, 2020, **49**,  
3450

## Increased photocurrent of CuWO<sub>4</sub> photoanodes by modification with the oxide carbodiimide Sn<sub>2</sub>O(NCN)<sup>†</sup>

Zheng Chen,<sup>a</sup> Manuel Löber,<sup>b</sup> Anna Rokicińska,<sup>c</sup> Zili Ma,<sup>a</sup> Jianhong Chen,<sup>d</sup> Piotr Kuśtrowski,<sup>c</sup> Hans-Jürgen Meyer,<sup>b</sup> Richard Dronskowski<sup>a,e</sup> and Adam Slabon<sup>d</sup>\*

Tin(II) oxide carbodiimide is a novel prospective semiconductor material with a band gap of 2.1 eV and lies chemically between metal oxides and metal carbodiimides. We report on the photochemical properties of this oxide carbodiimide and apply the material to form a heterojunction with CuWO<sub>4</sub> thin films for photoelectrochemical (PEC) water oxidation. Mott–Schottky experiments reveal that the title compound is an n-type semiconductor with a flat-band potential of −0.03 V and, as such, the position of the valence band edge would be suitable for photochemical water oxidation. Sn<sub>2</sub>O(NCN) increases the photocurrent of CuWO<sub>4</sub> thin films from 32 μA cm<sup>−2</sup> to 59 μA cm<sup>−2</sup> at 1.23 V vs. reversible hydrogen electrode (RHE) in 0.1 M phosphate buffer (pH 7.0) under backlight AM 1.5G illumination. This upsurge in photocurrent originates in a synergistic effect between the oxide and oxide carbodiimide, because the heterojunction photoanode displays a higher current density than the sum of its individual components. Structural analysis by powder X-ray diffraction (XRD) and X-ray photoelectron spectroscopy (XPS) reveals that Sn<sub>2</sub>O(NCN) forms a core–shell structure Sn<sub>2</sub>O(NCN)@SnPO<sub>x</sub> during the PEC water oxidation in phosphate buffer. The electrochemical activation is similar to the behavior of Mn(NCN) but different from Co(NCN).

Received 14th December 2019,  
Accepted 17th February 2020

DOI: 10.1039/c9dt04752b

rsc.li/dalton

## Introduction

One of the critical technical problems facing humanity is the development of a long-term sustainable energy economy.<sup>1</sup> This especially includes clean and renewable energy generation; a task that can be theoretically fulfilled by photoelectrochemical (PEC) water-splitting to yield hydrogen.<sup>2</sup> Water-splitting consists of two half reactions: the transfer of two electrons for the hydrogen evolution reaction (HER) and four electrons for the oxygen evolution reaction (OER).<sup>3</sup> The photo-generated charge and holes separate and migrate through the semiconductor in opposite directions to generate a photocurrent. Since the initial report on solar-driven water-splitting on a TiO<sub>2</sub> photo-

electrode in 1972,<sup>4</sup> metal oxide semiconductors have been intensively investigated, and BiVO<sub>4</sub> has emerged as the benchmark oxide photoanode.<sup>5</sup> There are only few known oxidic photoanode candidates that display a smaller band gap than BiVO<sub>4</sub>, such as CuWO<sub>4</sub> with an electronic band gap in the range of 2.2–2.4 eV.<sup>6</sup>

There are several critical characteristics for a semiconductor material in terms of realistic application as a water-splitting photoelectrode: (i) suitable conduction and/or valence band edge positions; (ii) stability under operating conditions; (iii) efficient charge carrier separation and transport along and across the thin-film electrode; (iv) low-cost and earth-abundant elements; and (v) sufficient light absorption.<sup>5–7</sup> Additionally, the surface of the light absorber has to be modified in most cases with a suitable catalyst to overcome poor reaction kinetics, *i.e.* to drive the HER and/or OER.<sup>8</sup>

Copper tungstate is one of the few promising photoanode materials with a suitable band gap, a valence band edge (VBE) more positive than 1.23 V vs. RHE to permit water oxidation, stability under neutral conditions and composed of abundant elements.<sup>9</sup> It can be manufactured on differential electrically conductive substrates by electrochemical deposition,<sup>10</sup> atomic layer deposition (ALD),<sup>11</sup> spray pyrolysis,<sup>12</sup> and spin-casting.<sup>13</sup> Several strategies have been reported to improve the perform-

<sup>a</sup>Chair of Solid-State and Quantum Chemistry, Institute of Inorganic Chemistry, RWTH Aachen University, 52056 Aachen, Germany<sup>b</sup>Section of Solid State and Theoretical Inorganic Chemistry, Institute of Inorganic Chemistry, University of Tübingen, 72076 Tübingen, Germany<sup>c</sup>Faculty of Chemistry, Jagiellonian University, 30-387 Krakow, Poland<sup>d</sup>Department of Materials and Environmental Chemistry, Stockholm University, 10691 Stockholm, Sweden. E-mail: adam.slabon@mmk.su.se<sup>e</sup>Hoffmann Institute of Advanced Materials, Shenzhen Polytechnic, 7098 Liuxian Blvd, Shenzhen, China<sup>†</sup>Electronic supplementary information (ESI) available. See DOI: 10.1039/c9dt04752b

ance of  $\text{CuWO}_4$  by doping with zinc,<sup>14</sup> molybdenum<sup>15</sup> or iron,<sup>12</sup> incorporating with silver nanowires,<sup>16</sup> functionalizing with gold nanoparticles.<sup>17</sup> Charge transport is also facilitated by post-synthetic hydrogen or nitrogen treatment of  $\text{CuWO}_4$  due to the formation of oxygen vacancies.<sup>10,18</sup> Recently, we have reported that surface modification of  $\text{CuWO}_4$  with  $\text{Ag}_2(\text{NCN})^{8a}$  or  $\text{Mn}(\text{NCN})^{8b}$  displays synergetic effects between its constituents, which improve PEC water oxidation efficiency.

Carbodiimides have received attention as novel materials for photochemical energy conversion in addition to their application as electrode materials for Li-ion batteries.<sup>19</sup> This has been mainly motivated by their suitable band gap values for solar light harvesting and a beneficial VBE position for PEC water oxidation.<sup>20</sup> They are related to oxides but are characterized by a higher degree of covalency.<sup>21</sup> The carbodiimide anion ( $\text{N}=\text{C}=\text{N}^-$ ) is considered as a pseudo-chalcogenide anion and lies between oxide and sulfide anions in view of the HSAB concept.<sup>22</sup> The oxide carbodiimides are as such mixed-anion compounds. The oxide carbodiimide representative  $\text{Sn}_2\text{O}(\text{NCN})$  was obtained recently by Meyer *et al.* as crystalline powder with an optical band gap of approximately 2.0 eV.<sup>23</sup> The title compound is closely related to tin(II) oxide ( $\text{SnO}$ ); a semiconductor with a band gap of 2.8 eV as calculated on the basis of electronic band structure calculations.<sup>24</sup>

In this work, we report on the photochemical properties of  $\text{Sn}_2\text{O}(\text{NCN})$  and the fabrication of heterojunction  $\text{CuWO}_4/\text{Sn}_2\text{O}(\text{NCN})$  thin film photoanodes. We show that  $\text{Sn}_2\text{O}(\text{NCN})$  undergoes structural changes during PEC water oxidation and can augment the photocurrent of  $\text{CuWO}_4$  photoanodes.

## Experimental

### Synthesis of $\text{Sn}_2\text{O}(\text{NCN})$

$\text{Li}_2(\text{NCN})$  was prepared as previously reported by Meyer.<sup>23,25</sup> Equimolar amounts of  $\text{Li}_2(\text{NCN})$ ,  $\text{Na}_2\text{O}$  and  $\text{SnCl}_2$  (Sigma Aldrich 99.999%, ultra dry) were mixed and ground in an agate mortar under argon. Samples of 250 mg were sealed into silica tubes under vacuum and each mixture was heated in a furnace to temperatures ranging from 450 to 500 °C. The samples were kept for 12 h before cooling to room temperature. The ampoules were opened in air, the product was washed with deionized water and dried in oven at 80 °C for 4 h.  $\text{Sn}_2\text{O}(\text{NCN})$  was obtained as a red powder.

### Synthesis of $\text{CuWO}_4$ thin films

$\text{CuWO}_4$  thin films were produced on conductive fluorine-doped tin oxide (FTO) glass (2.0 mm thick, Sigma-Aldrich), based on a synthesis by Bartlett.<sup>9a</sup> Before the electrochemical synthesis, the FTO glass was cleaned in diluted nitric acid (Sigma), acetone and ethanol, respectively. 1.26 g (3.8 mmol) sodium tungstate dihydrate ( $\text{Na}_2\text{WO}_4 \cdot 2\text{H}_2\text{O}$ , 99.9%, Acros Organics) was dissolved in 15 mL deionized water by stirring, and 1 mL hydrogen peroxide (30%, Geyer Chemsolute) was added to the tungstate precursor solution. The solution was

stirred for 20 min at room temperature. 25 mL deionized water and 25 mL isopropanol (>99.7%, Fisher Scientific) were added to the solution. A solution of 0.73 g (2.7 mmol) copper(II) nitrate trihydrate ( $\text{Cu}(\text{NO}_3)_2 \cdot 3\text{H}_2\text{O}$ , >99%, Sigma) in 10 mL deionized water was added to the tungsten precursor solution. The pH value was adjusted to 1.2 by adding nitric acid and the solution was used for electrochemical deposition on FTO glass. The electrochemical deposition was performed in a three-electrode setup with platinum wire and 1 M  $\text{Ag}/\text{AgCl}$  (WAT Venture) as a counter electrode and a reference electrode, respectively. The electrochemical deposition was carried out by a Gamry potentiostat and the Gamry framework software package. The potential was swept in the range from -0.9 to +0.2 V vs. 1 M  $\text{Ag}/\text{AgCl}$  for 12 cycles at the scan rate of 50  $\text{mV s}^{-1}$ . The working electrode was disconnected in the electrical circuit, washed with deionized water and dried at room temperature under vacuum. The working electrode was heated at 450 °C for 2 h under ambient atmosphere. The excess of copper oxides was etched by immersing the working electrode into 0.5 M HCl for acidic treatment. The electrode was subsequently annealed one more time at 450 °C for 30 min under ambient atmosphere.

### Preparation of $\text{Sn}_2\text{O}(\text{NCN})$ and $\text{CuWO}_4/\text{Sn}_2\text{O}(\text{NCN})$ photoanodes

$\text{Sn}_2\text{O}(\text{NCN})$  powder was dispersed in ethanol ( $120 \mu\text{g mL}^{-1}$ ) by ultrasounds. FTO, a bare graphite (for XPS) and  $\text{CuWO}_4$  thin film electrode were placed on a heating plate at 50 °C. The  $\text{Sn}_2\text{O}(\text{NCN})$  dispersion was drop-casted on the surfaces of the corresponding thin film electrodes.

### Structural characterization

Powder XRD patterns were recorded in transmission mode on a STOE STADI-P diffractometer ( $\text{Cu K}\alpha_1$  radiation) operating with a DECTRIS Mythen 1K detector. For the analysis of the photoanodes by XRD, the samples were mechanically removed from the photoanodes in advance. SEM images of  $\text{Sn}_2\text{O}(\text{NCN})$  powder were recorded by a Leo Supra 35VP SMT (Zeiss).

A Themis Z TEM (Thermo Fisher) equipped with a SuperX energy dispersive X-ray (EDX) detector operated at 300 kV in the scanning TEM mode was used for determination of the chemical composition of  $\text{Sn}_2\text{O}(\text{NCN})$  particles, which were subject to chronoamperometry at 1.23 V vs. RHE. Prior to the analysis, the particles were mechanically removed from the pure  $\text{Sn}_2\text{O}(\text{NCN})$  electrode.

XPS spectra were collected by a hemispherical VG SCIENTA R3000 analyzer using a monochromatized aluminum source  $\text{Al K}\alpha$  ( $E = 1486.6 \text{ eV}$ ) at constant pass energy of 100 eV. The binding energies were referenced to the Au 4f core level ( $E_b = 84.0 \text{ eV}$ ). The composition and chemical surrounding of the sample surface were determined on the basis of the areas and binding energies of Na 1s, K 2p, P 2p, O 1s, N 1s, C 1s and Sn 3d photoelectron peaks. The fitting of high resolution spectra was obtained by using the Casa XPS software. UV-Vis spectra were recorded on a Shimadzu UV-2600 spectrophotometer. Measurements were recorded in absorbance and reflectance



mode. The Tauc plots were calculated by Kubelka–Munk function  $F(R) = (1 - R)^2/2R$  to determine the electronic band gap.

### Photoelectrochemistry

The experiments were carried out in an electrochemical cell operating in a three-electrode setup. The photoanode was used as a working electrode. Platinum wire and a 1 M Ag/AgCl electrode were used as a counter electrode and a reference electrode, respectively. All current values of the electrodes were recorded vs. 1 M Ag/AgCl reference electrode and converted vs. RHE according to  $E_{\text{RHE}} (\text{V}) = E_{1 \text{ M Ag/AgCl}} (\text{V}) + 0.236 (\text{V}) + [0.059 \times \text{pH}] (\text{V})$  at 25 °C. The electrochemical data were recorded by a potentiostat (Gamry instruments). A solar light simulator (class-AAA 94023A, Newport) with an ozone-free 450 W xenon short-arc lamp was used to illuminate the photoanode with  $100 \text{ mW cm}^{-2}$  (AM 1.5G) simulated visible light. The power output of the solar simulator was calibrated with a Si reference cell (LOT-Quantum Design, Germany). 0.1 M potassium/sodium phosphate (K/NaPi) buffer (or with 0.05 M  $\text{Na}_2\text{SO}_3$  as hole scavenger) at pH 7.0 was used as the electrolyte for PEC experiments and prepared with Milli-Q water ( $18.3 \Omega \text{ cm}$ ) at 25 °C. The linear square voltammetry (LSV) and cyclic voltammetry (CV) were swept at a scan rate of  $10 \text{ mV s}^{-1}$  from 0.64 to 1.44 V vs. RHE. Mott–Schottky (MS) measurements were carried out under dark in an electromagnetically shielded box. A sinusoidal modulation of 10 mV was applied at frequencies of 10 Hz, 100 Hz and 1000 Hz in the potential range from 0.05 V to 1.23 V vs. RHE with an equilibration time of 10 s.

## Results and discussion

### Structure characterization of the bulk

Fig. 1a shows SEM images of the obtained microcrystalline  $\text{Sn}_2\text{O}(\text{NCN})$  and the thin film  $\text{CuWO}_4/\text{Sn}_2\text{O}(\text{NCN})$  photoanode.  $\text{Sn}_2\text{O}(\text{NCN})$  crystallizes in an orthorhombic crystal structure (space group *Pccn*) and has  $\text{Sn}^{2+}$  ions situated in a fourfold, mixed  $\text{O}^{2-}/\text{NCN}^{2-}$  coordination environment.<sup>23</sup> The carbodiimide anion is closely related to the oxide anion and can be regarded as an N-based pseudo-oxide.<sup>26</sup> For structural characterization, we tested the photoanodes for PEC water oxidation (*vide infra*) and removed subsequently a part of the thin film for XRD and XPS characterization. The powder XRD patterns of a pure  $\text{Sn}_2\text{O}(\text{NCN})$  photoanode indicate that the compound maintains its structural bulk stability after PEC water oxidation in phosphate electrolyte at pH 7.0 (Fig. 2).

The corresponding powder XRD patterns of the composite  $\text{CuWO}_4/\text{Sn}_2\text{O}(\text{NCN})$  photoanodes do not exhibit reflection peaks of the oxide carbodiimide due to the low amount of the latter (Fig. 3). The XRD patterns before and after PEC operation remain unchanged and match the simulated patterns of the copper tungstate.

### Electronic structure

The electronic band gaps of  $\text{CuWO}_4$  and  $\text{Sn}_2\text{O}(\text{NCN})$  were determined by the Kubelka–Munk function. The results show

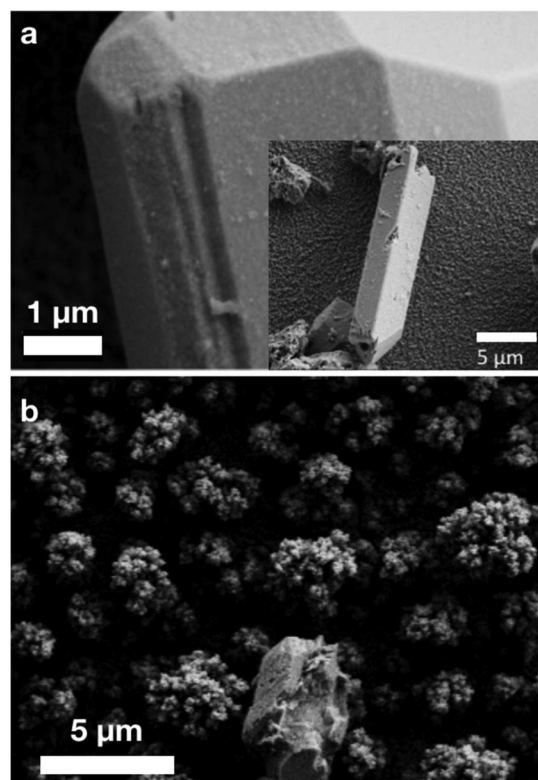


Fig. 1 SEM micrographs of (a)  $\text{Sn}_2\text{O}(\text{NCN})$  and (b) thin film photoanode  $\text{CuWO}_4/\text{Sn}_2\text{O}(\text{NCN})$ . The latter contains the continuous  $\text{CuWO}_4$  thin film on which the rectangular-shaped  $\text{Sn}_2\text{O}(\text{NCN})$  particle is deposited (bottom).

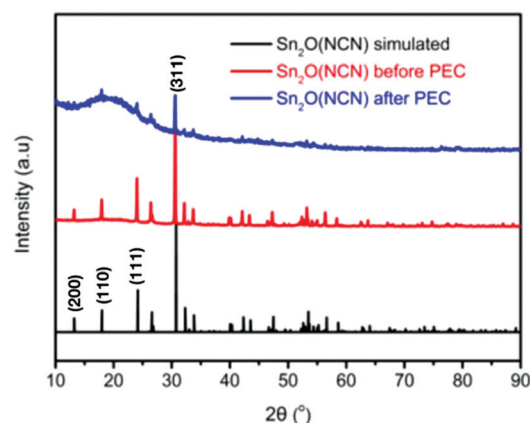


Fig. 2 Experimental and simulated powder XRD patterns of  $\text{Sn}_2\text{O}(\text{NCN})$  before and after PEC water oxidation. The reflection peaks (310), (400) and (211) overlap between (111) and (311) and are not marked in the patterns.

that the band gap of  $\text{CuWO}_4$  and  $\text{Sn}_2\text{O}(\text{NCN})$  are 2.31 and 2.10 eV, respectively (Fig. 4). Both determined values are close to the previously reported values of 2.2–2.4 eV for  $\text{CuWO}_4$ <sup>14</sup> and 2.0 eV for  $\text{Sn}_2\text{O}(\text{NCN})$ .<sup>23</sup> This would render both compounds as potential photoanode candidates for water oxidation.



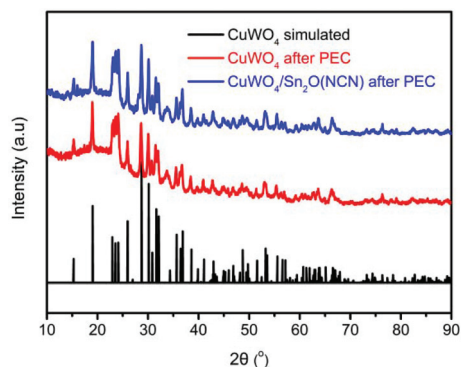


Fig. 3 Experimental and simulated powder XRD patterns of  $\text{CuWO}_4$  and  $\text{CuWO}_4/\text{Sn}_2\text{O}(\text{NCN})$  after PEC water oxidation.

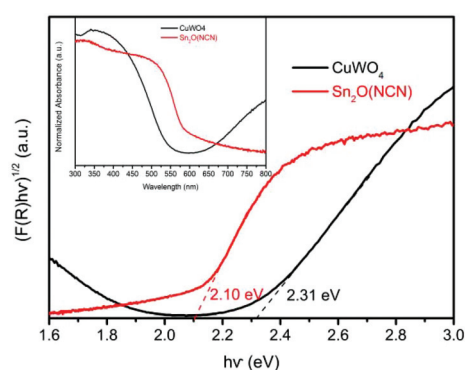


Fig. 4 Tauc plots for  $\text{Sn}_2\text{O}(\text{NCN})$  and  $\text{CuWO}_4$ . The inset shows the normalized absorbance spectra.

The semiconducting type and band edge positions of  $\text{Sn}_2\text{O}(\text{NCN})$  were determined by MS measurements. Fig. 5 illustrates the MS plots of  $\text{Sn}_2\text{O}(\text{NCN})$  photoanodes for applied different frequencies of 10, 100 and 1000 Hz. All curves exhibit a positive slope, indicating that the oxide carbodiimide  $\text{Sn}_2\text{O}(\text{NCN})$  is an n-type semiconductor; similar to  $\text{CuWO}_4$ . For all three different frequencies, extrapolation of the measured data yields a flat-band potential of  $-0.03$  V vs. RHE. For an n-type

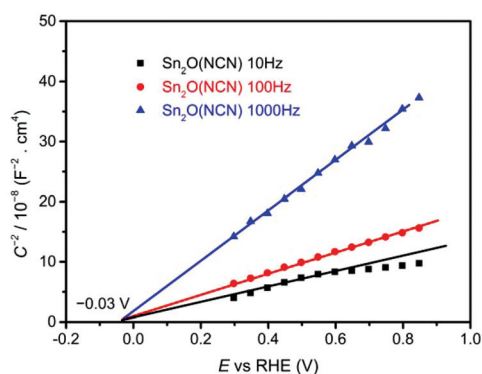


Fig. 5 MS analysis of EIS measurements of  $\text{Sn}_2\text{O}(\text{NCN})$  electrodes applied frequencies of 10, 100 and 1000 Hz.

semiconductor, the value of the flat-band potential is close to the conduction band edge (CBE) position. Taking into account the determined band gap, the VBE and CBE positions are 2.07 V and  $-0.03$  V vs. RHE, respectively. A comparison of the CBE and VBE positions for the binary tin oxides is shown in Fig. S1.† Similar to  $\text{SnO}_2$ , the oxide carbodiimide would be theoretically suited for overall water-splitting.<sup>24,27</sup>

### Photoelectrochemistry

For the investigation of heterojunction photoanodes  $\text{CuWO}_4/\text{Sn}_2\text{O}(\text{NCN})$ , two additional electrodes of the individual components were produced. All measurements were performed in phosphate electrolyte at pH 7.0. The summarized LSV curves for all three electrodes, recorded with a scan rate at  $10$   $\text{mV s}^{-1}$  under backlight AM 1.5G illumination ( $100$   $\text{mW cm}^{-2}$ ), are depicted in Fig. 6. The  $\text{CuWO}_4$  photoanode developed an anodic current that reached  $32$   $\mu\text{A cm}^{-2}$  at  $1.23$  V vs. RHE.

Upon functionalizing the surface with  $\text{Sn}_2\text{O}(\text{NCN})$  particles by drop-casting, the photocurrent showed an upsurge which was reached when adding  $36$   $\mu\text{g}$  (Fig. S2†). A bare  $\text{Sn}_2\text{O}(\text{NCN})$  electrode with the same amount of material as for the composite photoanode  $\text{CuWO}_4/\text{Sn}_2\text{O}(\text{NCN})$  developed only a small photocurrent. The photocurrent produced by the heterojunction electrode, being equal  $59$   $\mu\text{A cm}^{-2}$  at  $1.23$  V vs. RHE, exceeds the sum of its individual components and exhibits as such a synergistic effect. This trend is more visible during chronoamperometry (CA) with interrupted illumination (Fig. 7). The photocurrent remains relatively stable for a tested period of 2 hours (Fig. S3†).

Since the photocurrent of the oxide carbodiimide was very small, we created another  $\text{Sn}_2\text{O}(\text{NCN})$  photoanode by electrophoretic deposition with a higher amount of material. Fig. 8 illustrates the results of CA for this  $\text{Sn}_2\text{O}(\text{NCN})$  photoanode and FTO glass, as a reference measurement, at  $1.23$  V vs. RHE in the same electrolyte under illumination. It can be clearly seen that the photocurrent of  $\text{Sn}_2\text{O}(\text{NCN})$  outperforms the substrate. As such one can rule out that the photoactivity of  $\text{Sn}_2\text{O}(\text{NCN})$  may be due to surface oxidation toward a tin oxide phase.

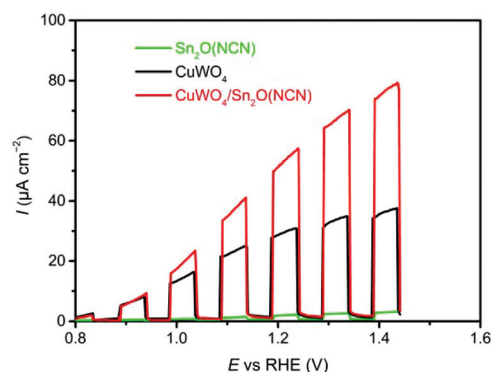
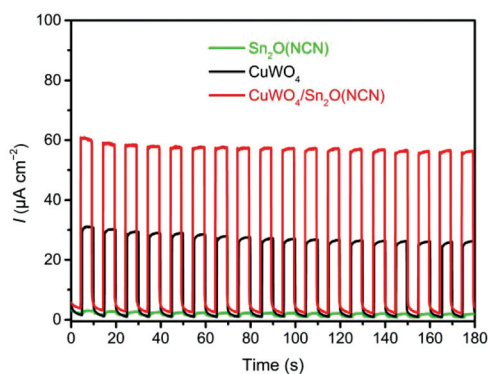
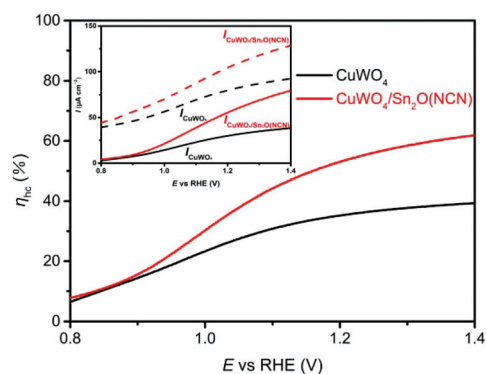


Fig. 6 LSV of  $\text{Sn}_2\text{O}(\text{NCN})$ ,  $\text{CuWO}_4$  and  $\text{CuWO}_4/\text{Sn}_2\text{O}(\text{NCN})$  photoanodes. Measurements were performed in  $0.1$  M phosphate electrolyte (pH 7.0) with scan at rate of  $10$   $\text{mV s}^{-1}$  under sequentially interrupted backlight AM 1.5G illumination ( $100$   $\text{mW cm}^{-2}$ ).





**Fig. 7** CA of  $\text{Sn}_2\text{O}(\text{NCN})$ ,  $\text{CuWO}_4$  and  $\text{CuWO}_4/\text{Sn}_2\text{O}(\text{NCN})$  photoanodes at 1.23 V vs. RHE. Measurements were performed in 0.1 M K phosphate electrolyte (pH 7.0) under sequentially interrupted backlight AM 1.5G illumination ( $100 \text{ mW cm}^{-2}$ ).



**Fig. 9** Hole collection efficiencies  $\eta_{\text{hc}}$  of  $\text{CuWO}_4$  and  $\text{CuWO}_4/\text{Sn}_2\text{O}(\text{NCN})$  photoanodes. The inset shows the photocurrent densities during water (solid line) and sulfite oxidation (dashed line) for  $\text{CuWO}_4$  (black) and  $\text{CuWO}_4/\text{Sn}_2\text{O}(\text{NCN})$  photoanodes.

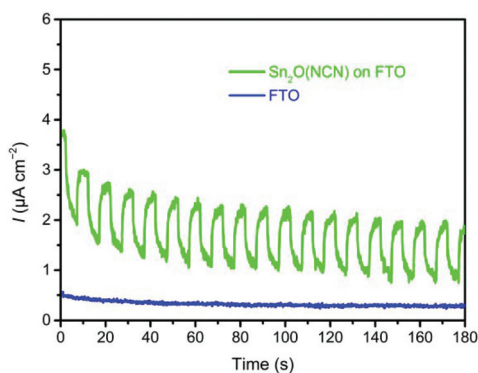


**Fig. 8** CA of bare  $\text{Sn}_2\text{O}(\text{NCN})$  and the FTO substrate at 1.23 V vs. RHE. Measurements were performed in 0.1 M phosphate electrolyte (pH 7.0) under sequentially interrupted backlight AM 1.5G illumination ( $100 \text{ mW cm}^{-2}$ ).

In order to elucidate the origin of increased photocurrents after  $\text{Sn}_2\text{O}(\text{NCN})$  functionalization, we determined the hole collection efficiency  $\eta_{\text{hc}}$ . The oxidation of a hole scavenger, such as the sulfite anion, allows to determine the number of surface-reaching holes because this oxidation reaction is much faster than the sluggish oxidation of water. This allows to estimate that each hole reaching the semiconductor–electrolyte interface will be used for an oxidative reaction. The comparison of the photocurrents for sulfite oxidation ( $J_{\text{Na}_2\text{SO}_3}$ ) and water oxidation ( $J_{\text{H}_2\text{O}}$ ) allows to calculate  $\eta_{\text{hc}} = (J_{\text{H}_2\text{O}}/J_{\text{Na}_2\text{SO}_3})$ . For the  $\text{CuWO}_4$  thin films, the  $\eta_{\text{hc}}$  value significantly increases upon functionalization with  $\text{Sn}_2\text{O}(\text{NCN})$  at higher potentials (Fig. 9). This indicates that the reactivity of the surface increases upon functionalization with the oxide carbodiimide.

To investigate the key factors of improved PEC performance, we analyzed the surface of bare  $\text{Sn}_2\text{O}(\text{NCN})$  photoanodes after the PEC experiment by XPS. The electrode was prepared on graphite instead of FTO substrate to avoid interference with Sn stemming from FTO. Except the presence of O, C, N and Sn, XPS reveals the presence of Na, K and P which originate

from the K/NaP<sub>i</sub> electrolyte. In Fig. 10, the high-resolution XPS Sn 3d spectrum, with the Sn 3d<sub>5/2</sub> and Sn 3d<sub>3/2</sub> peaks distanced at the splitting energy of 8.4 eV, is shown. The latter one is partially overlapped with the Na KLL Auger signal. The relative high values of binding energies found for both components (487.5 eV for Sn 3d<sub>5/2</sub> and 495.9 eV for Sn 3d<sub>3/2</sub>) obviously suggest that  $\text{Sn}_2\text{O}(\text{NCN})$  formed a phosphate-type shell on the surface being exposed to the phosphate electrolyte, *i.e.* a core–shell structure  $\text{Sn}_2\text{O}(\text{NCN})@\text{SnPO}_x$ . This indicates that the catalytically active form is a tin phosphate shell while the core contains the semiconducting  $\text{Sn}_2\text{O}(\text{NCN})$ . Similar positions of the Sn 3d signals have been observed recently for tin phosphate ( $\text{SnPO}_x$ ) in relation to  $\text{SnO}_2$ , which exhibited the Sn 3d<sub>5/2</sub> and Sn 3d<sub>3/2</sub> components at 486.0 eV and 494.4 eV, respectively.<sup>28</sup> Different from the behavior of Co (NCN) electrocatalysts,<sup>29</sup> the electrochemical activation is similar to the behavior of Mn(NCN) electrocatalysts<sup>8b</sup> as previously reported. Tin phosphate is known as a heterogeneous catalyst for efficient dehydration of glucose into 5-hydroxymethylfurfural in ionic liquid according to the literature

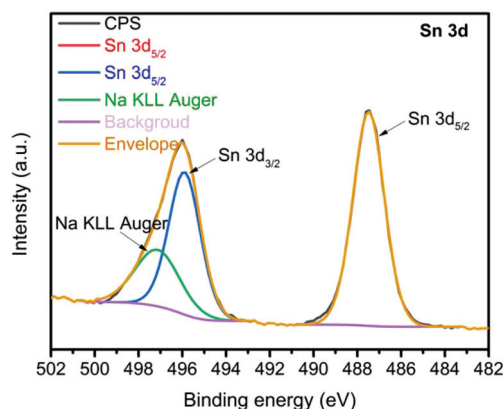


**Fig. 10** XPS Sn 3d spectrum of bare  $\text{Sn}_2\text{O}(\text{NCN})$  on graphite after PEC water oxidation.



report. The fourfold coordinated  $\text{Sn}^{4+}$  sites from tin phosphate are identified as the active species.<sup>28</sup>

The presence of phosphorous was also confirmed by complementary TEM EDX analysis, which was performed on  $\text{Sn}_2\text{O}(\text{NCN})$  particles that were mechanically removed from a FTO/ $\text{Sn}_2\text{O}(\text{NCN})$  thin film electrode after 30 min of CA at 1.23 V vs. RHE. The high-angle annular dark field (HAADF) images in Fig. 11 shows agglomerated particles that were scanned by means of EDX. Besides phosphorous, the presence of tin, oxygen, carbon and nitrogen could be confirmed, too.

The augmented charge carrier separation for the heterojunction can be understood by analyzing the energy band diagram of both semiconductors (Fig. 12).<sup>8a</sup> The energetically higher position of the CBE for  $\text{Sn}_2\text{O}(\text{NCN})$  in comparison to  $\text{CuWO}_4$  enables injection of electrons into the conduction band of the latter. At the same time, the photogenerated holes can diffuse from the VBE of  $\text{CuWO}_4$  to  $\text{Sn}_2\text{O}(\text{NCN})$ . This results in decreased recombination of photogenerated electrons and holes. In addition to the improved hole collection efficiency, being the consequence of the tin phosphate shell,

the PEC water oxidation efficiency could be further increased by 10% when depositing cobalt phosphate as co-catalyst on the surface of the heterojunction photoanode (Fig. S4†).

## Conclusions

We have investigated the photochemical properties of  $\text{Sn}_2\text{O}(\text{NCN})$  and showed that this n-type semiconductor can be successfully coupled to  $\text{CuWO}_4$  thin film photoanodes.  $\text{Sn}_2\text{O}(\text{NCN})$  exhibits a flat-band potential of approx.  $-0.03$  V and as such, the position of the valence band edge would be suitable for photochemical water oxidation. During PEC water oxidation in phosphate buffer electrolyte  $\text{Sn}_2\text{O}(\text{NCN})$  undergoes an *in situ* transformation to a core-shell structure; maintaining a semiconducting core while forming an electrocatalytically-active  $\text{SnPO}_x$  shell. The obtained composite  $\text{CuWO}_4/\text{Sn}_2\text{O}(\text{NCN})@ \text{SnPO}_x$  photoanodes display a synergetic effect between its constituents during the PEC water oxidation, which shows up in an upsurge of photocurrent from  $32 \mu\text{A cm}^{-2}$  to  $59 \mu\text{A cm}^{-2}$  at 1.23 V vs. RHE at pH 7.0 under simulated AM 1.5G illumination. This is due to improved charge carrier separation and augmented hole collection efficiency. Our study demonstrates that mixed-anion compounds containing an oxidic and carbodiimide anion are potential materials for photochemical oxidation reactions, while at the same time, the surface can be electrochemically activated into a catalytically-active form.

## Conflicts of interest

There are no conflicts to declare.

## Acknowledgements

Zh. C. would like to thank the China Scholarship Council for a PhD scholarship. We thank Ulrich Simon for access to electron microscopy facilities, Birgit Hahn for SEM analysis, and Marek Drozdek for performing XPS, and Istvan-Zoltan Jenei for fruitful discussion. A. S. thank the Fonds der Chemischen Industrie (FCI) and Stockholm University for financial support. The XPS measurements were carried out with the equipment purchased with the financial support of the European Regional Development Fund in the framework of the Polish Innovation Operational Program (contract no. POIG.02.01.00-12-023/08).

## References

- 1 J. P. Holdren, *Science*, 2007, **315**, 737.
- 2 (a) N. S. Lewis, *Nat. Nanotechnol.*, 2016, **11**, 1010–1019; (b) M. Grätzel, *Nature*, 2001, **414**, 338–344; (c) Z. Ma, T. Thersleff, A. L. Görne, N. Cordes, Y. Liu, S. Jakobi, A. Rokicinska, Z. G. Schichtl, R. H. Coridan, P. Kuśrowski,

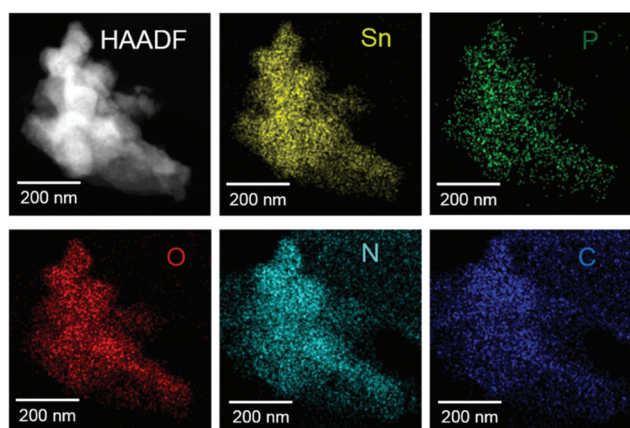


Fig. 11 HAADF image and corresponding elemental maps of  $\text{Sn}_2\text{O}(\text{NCN})$  particles that were subject to CA at 1.23 V vs. RHE.

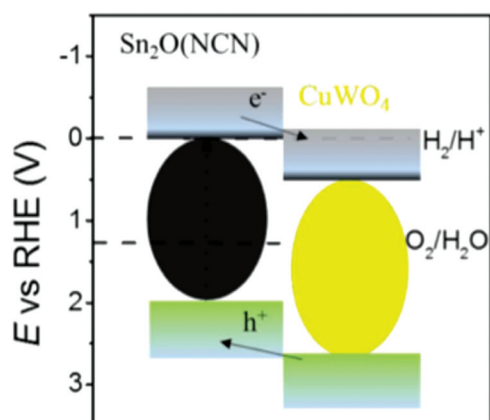


Fig. 12 Energy band diagram of the heterojunction  $\text{CuWO}_4/\text{Sn}_2\text{O}(\text{NCN})$ .





- W. Schnick, R. Dronskowski and A. Slabon, *ACS Appl. Mater. Interfaces*, 2019, **11**, 19077–19086.
- 3 K. Sivula and R. van de Krol, *Nat. Rev. Mater.*, 2016, **1**, 15010.
- 4 A. Fujishima and K. Honda, *Nature*, 1972, **238**, 37–38.
- 5 (a) Z. Wang, C. Li and K. Domen, *Chem. Soc. Rev.*, 2019, **48**, 2109–2125; (b) C. Jiang, S. J. A. Moniz, A. Wang, T. Zhang and J. Tang, *Chem. Soc. Rev.*, 2017, **46**, 4645–4660; (c) H. S. Han, S. Shin, D. H. Kim, I. J. Park, J. S. Kim, P. S. Huang, J. K. Lee, I. S. Cho and X. Zheng, *Energy Environ. Sci.*, 2018, **11**, 1299–1306; (d) T. R. Kuo, H. J. Liao, Y. T. Chen, C. Y. Wei, C. C. Chang, Y. C. Chen, Y. H. Chang, J. C. Lin, Y. C. Lee, C. Y. Wenand and S. S. Li, *Green Chem.*, 2018, **20**, 1640–1647.
- 6 (a) D. K. Lee, D. Lee, M. A. Lumley and K. S. Choi, *Chem. Soc. Rev.*, 2019, **48**, 2126–2157; (b) J. H. Kim and J. S. Lee, *Adv. Mater.*, 2019, **31**, 1806938.
- 7 (a) K. Maeda, K. Teramura, D. Lu, T. Takata, N. Saito, Y. Inoue and K. Domen, *Nature*, 2006, **440**, 295; (b) N. S. Lewis, *Science*, 2007, **315**, 798; (c) M. Ertl, Z. Ma, T. Thersleff, P. Lyu, S. Huettner, P. Nachtigall, J. Breu and A. Slabon, *Inorg. Chem.*, 2019, **58**, 9655–9662.
- 8 (a) M. Davi, A. Drichel, M. Mann, T. Scholz, F. Schrader, A. Rokicinska, P. Kuśtrowski, R. Dronskowski and A. Slabon, *J. Phys. Chem. C*, 2017, **121**, 26265–26274; (b) M. Davi, M. Mann, Z. Ma, F. Schrader, A. Drichel, S. Budnyk, A. Rokicinska, P. Kuśtrowski, R. Dronskowski and A. Slabon, *Langmuir*, 2018, **34**, 3845–3852; (c) M. Davi, F. Schrader, T. Scholz, Z. Ma, A. Rokicinska, R. Dronskowski, P. Kuśtrowski and A. Slabon, *ACS Appl. Nano Mater.*, 2018, **1**, 869–876; (d) M. Davi, G. Ogutu, F. Schrader, A. Rokicinska, P. Kuśtrowski and A. Slabon, *Eur. J. Inorg. Chem.*, 2017, **37**, 4267–4274.
- 9 (a) J. E. Yourey and B. M. Bartlett, *J. Mater. Chem.*, 2011, **21**, 7651–7660; (b) V. Leute, *Z. Phys. Chem.*, 1966, **48**, 319–339.
- 10 Z. Ma, O. Linnenberg, A. Rokicinska, P. Kuśtrowski and A. Slabon, *J. Phys. Chem. C*, 2018, **122**, 19281–19288.
- 11 (a) X. Zhou, R. Liu, K. Sun, K. M. Papadantonakis, B. S. Brunshwig and N. S. Lewis, *Energy Environ. Sci.*, 2016, **9**, 892–897; (b) Y. Gao, O. Zandi and T. W. Hamann, *J. Mater. Chem. A*, 2016, **4**, 2826–2830; (c) X. Zhou, R. Liu, K. Sun, D. Friedrich, M. T. McDowell, F. Yang, S. T. Omelchenko, F. H. Saadi, A. C. Nielander, S. Yalamanchili, K. M. Papadantonakis, B. S. Brunshwig and N. S. Lewis, *Energy Environ. Sci.*, 2015, **8**, 2644–2649.
- 12 D. Bohra and W. A. Smith, *Phys. Chem. Chem. Phys.*, 2015, **17**, 9857–9866.
- 13 (a) J. E. Yourey, K. J. Pyper, J. B. Kurtz and B. M. Bartlett, *J. Phys. Chem. C*, 2013, **117**, 8708–8718; (b) C. R. Lhermitte and B. M. Bartlett, *Acc. Chem. Res.*, 2016, **49**, 1121–1129.
- 14 J. E. Yourey, J. B. Kurtz and B. M. Bartlett, *Inorg. Chem.*, 2012, **51**, 10394–10401.
- 15 J. C. Hill, Y. Ping, G. A. Galli and K. S. Choi, *Energy Environ. Sci.*, 2013, **6**, 2440–2446.
- 16 H. Zhang, P. Yilmaz, J. O. Ansari, F. F. Khan, R. Binions, S. Krause and S. Dunn, *J. Mater. Chem. A*, 2015, **3**, 9638–9644.
- 17 M. Valenti, D. Dolat, G. Biskos, A. Schmidt-Ott and W. A. Smith, *J. Phys. Chem. C*, 2015, **119**, 2096–2104.
- 18 Y. Tang, N. Rong, F. Liu, M. Chu, H. Dong, Y. Zhang and P. Xiao, *Appl. Surf. Sci.*, 2016, **361**, 133–140.
- 19 J. Chouvin, C. Branci, J. Sarradin, J. Olivier-Fourcade, J. C. Jumas, B. Simon and P. Biensan, *J. Power Sources*, 1999, **81**, 277–281.
- 20 M. T. Sougrati, J. J. Arayampambil, X. Liu, M. Mann, A. Slabon, L. Stievano and R. Dronskowski, *Dalton Trans.*, 2018, **47**, 10827.
- 21 A. Eguia-Barrio, E. Castillo-Martinez, X. Liu, R. Dronskowski, M. Armand and T. Rojo, *J. Mater. Chem. A*, 2016, **4**, 1608–1611.
- 22 H. D. Schädler, L. Jäger and I. Senf, *Z. Anorg. Allg. Chem.*, 1993, **619**, 1115–1120.
- 23 K. Dolabdjian, A. L. Görne, R. Dronskowski, M. Ströbele and H. J. Meyer, *Dalton Trans.*, 2018, **47**, 13378–13383.
- 24 J. P. Allen, D. O. Scanlon, L. F. J. Piper and G. W. Watson, *J. Mater. Chem. C*, 2013, **1**, 8194–8208.
- 25 M. Neukirch, S. Tragl and H. J. Meyer, *Inorg. Chem.*, 2006, **45**, 8188–8193.
- 26 X. Liu, R. Dronskowski, R. Glaum and A. L. Tchougréeff, *Z. Anorg. Allg. Chem.*, 2010, **636**, 343–348.
- 27 (a) J. P. Allen, D. O. Scanlon, L. F. J. Piper and G. W. Watson, *J. Mater. Chem. C*, 2013, **1**, 8194–8208; (b) M. Manikandan, T. Tanabe, P. Li, S. Ueda, G. V. Ramesh, R. Kodiyath, J. Wang, T. Hara, A. Dakshanamoorthy, S. Ishihara, K. Ariga, J. Ye, N. Umezawa and H. Abe, *ACS Appl. Mater. Interfaces*, 2014, **6**, 3790–3793; (c) S. Kaizra, B. Bellal, Y. Louafi and M. Trari, *J. Saudi Chem. Soc.*, 2018, **22**, 76–83; (d) W. Xia, H. Wang, X. Zeng, J. Han, J. Zhu, M. Zhou and S. Wu, *CrystEngComm*, 2014, **16**, 6841–6847; (e) M. Aslam, M. T. Qamar, S. Ali, A. U. Rehman, M. T. Soomro, I. Ahmed, I. M. I. Ismail and A. Hameed, *J. Environ. Manage.*, 2018, **217**, 805–814; (f) L. Yang, J. Huang, L. Shi, L. Cao, W. Zhou, K. Chang, X. Meng, G. Liu, Y. Jie and J. Ye, *Nano Energy*, 2017, **36**, 331–340; (g) Y. Ogo, H. Hiramatsu, K. Nomura, H. Yanagi, T. Kamiya, M. Hirano and H. Hosono, *Appl. Phys. Lett.*, 2008, **93**, 032113.
- 28 Q. Hou, M. Zhen, L. Liu, Y. Chen, F. Huang, S. Zhang, W. Li and M. Ju, *Appl. Catal., B*, 2018, **224**, 183–193.
- 29 R. J. Müller, I. Kuznetsov, Y. Arbelo, M. Trottmann, C. S. Menoni, J. J. Rocca, G. R. Patzke and D. Bleiner, *Anal. Chem.*, 2018, **90**, 9234–9240.





## Electronic Supplementary Information (ESI) for

### Increased Photocurrent of CuWO<sub>4</sub> Photoanodes by Modification with the Oxide Carbodiimide Sn<sub>2</sub>O(NCN)

Zheng Chen,<sup>a</sup> Manuel Löber,<sup>b</sup> Anna Rokicińska,<sup>c</sup> Zili Ma,<sup>a</sup> Jianhong Chen,<sup>d</sup> Piotr Kuśtrowski,<sup>c</sup> Hans-Jürgen Meyer,<sup>b</sup> Richard Dronskowski<sup>a,e</sup> and Adam Slabon<sup>\*d</sup>

<sup>a</sup>Chair of Solid-State and Quantum Chemistry, Institute of Inorganic Chemistry, RWTH Aachen University, 52056 Aachen, Germany

<sup>b</sup>Section of Solid State and Theoretical Inorganic Chemistry, Institute of Inorganic Chemistry, University of Tübingen, 72076 Tübingen, Germany

<sup>c</sup>Faculty of Chemistry, Jagiellonian University, 30-387 Krakow, Poland

<sup>d</sup>Department of Materials and Environmental Chemistry, Stockholm University, 10691 Stockholm, Sweden

<sup>e</sup>Hoffmann Institute of Advanced Materials, Shenzhen Polytechnic, 7098 Liuxian Blvd, Shenzhen, China

\*Corresponding author. E-mail: adam.slabon@mmk.su.se

#### Supplement:

**Fig. S1** Electronic structures of Sn<sub>2</sub>O(NCN), SnO, SnO<sub>2</sub> and Sn<sub>3</sub>O<sub>4</sub>. Band edge potentials are referenced to RHE.

**Fig. S2** LSV of several CuWO<sub>4</sub>/ Sn<sub>2</sub>O(NCN) photoanodes with different amounts of added Sn<sub>2</sub>O(NCN). Measurements were performed in 0.1 M K/NaP<sub>i</sub> electrolyte (pH 7.0) with scan at rate of 10 mV s<sup>-1</sup> under AM 1.5G illumination.

**Fig. S3** CA of CuWO<sub>4</sub>/ Sn<sub>2</sub>O(NCN) photoanodes at 1.23 V vs. RHE for stability test. Measurements were performed in 0.1 M K/NaP<sub>i</sub> electrolyte (pH 7.0) under interrupted illumination.

**Fig. S4** CA of CuWO<sub>4</sub>/Sn<sub>2</sub>O(NCN)/cobalt phosphate (CoP<sub>i</sub>) photoanodes at 1.23 V vs. RHE. Measurements were performed in 0.1 M K/NaP<sub>i</sub> electrolyte (pH 7.0) under interrupted AM 1.5G illumination.

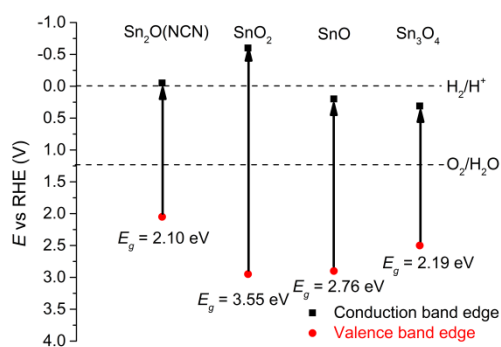


**Fig. S1** Electronic structures of  $\text{Sn}_2\text{O}(\text{NCN})$ ,  $\text{SnO}$ ,  $\text{SnO}_2$  and  $\text{Sn}_3\text{O}_4$ . Band edge potentials are referenced to RHE.

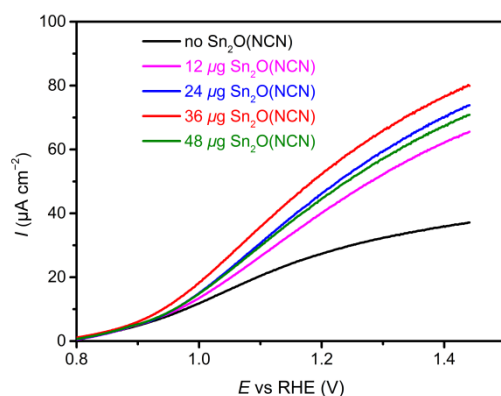


**Fig. S2** LSV of several  $\text{CuWO}_4/\text{Sn}_2\text{O}(\text{NCN})$  photoanodes with different amounts of added  $\text{Sn}_2\text{O}(\text{NCN})$ . Measurements were performed in 0.1 M  $\text{K}/\text{NaP}_i$  electrolyte (pH 7.0) with scan at rate of  $10 \text{ mV s}^{-1}$  under AM 1.5G illumination.

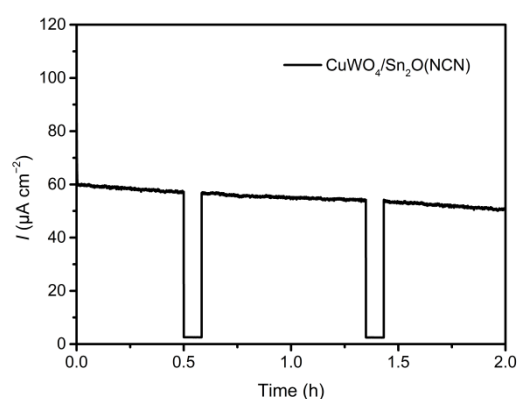


**Fig. S3** CA of  $\text{CuWO}_4/\text{Sn}_2\text{O}(\text{NCN})$  photoanodes at 1.23 V vs. RHE for stability test. Measurements were performed in 0.1 M  $\text{K}/\text{NaP}_i$  electrolyte (pH 7.0) under interrupted illumination.

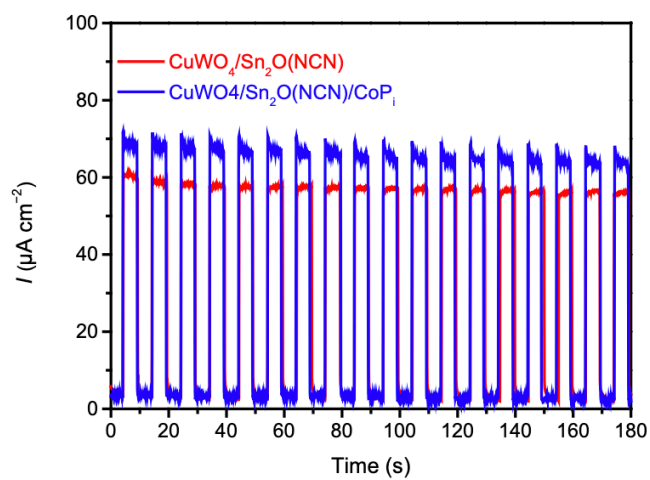
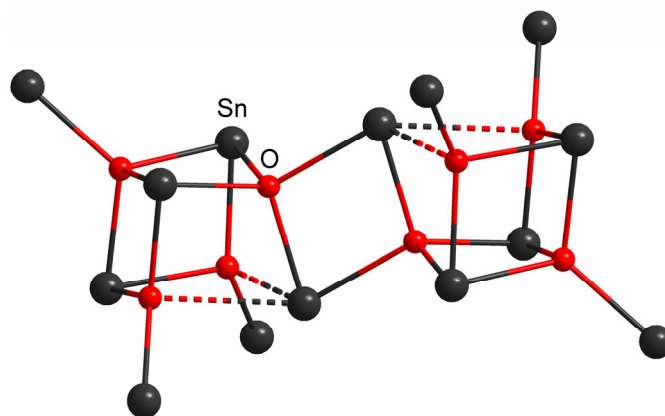


**Fig. S4** CA of  $\text{CuWO}_4/\text{Sn}_2\text{O}(\text{NCN})/\text{cobalt phosphate (CoP}_i)$  photoanodes at 1.23 V vs. RHE. Measurements were performed in 0.1 M  $\text{K}/\text{NaP}_i$  electrolyte (pH 7.0) under interrupted AM 1.5G illumination.  $\text{CoP}_i$  was deposited as in our previous work (*ACS Appl. Mater. Interfaces* 2019, 11, 21, 19077-19086).



# Publication 4

Synthesis, Structure and Electronic Properties of Three Tin Oxide Halides



<https://doi.org/10.1002/ejic.202000874>

Reprinted with permission from  
*Eur. J. Inorg. Chem.* **2021**, 2021, 283–288

Copyright © 2020 Wiley-VCH GmbH





# Synthesis, Structure and Electronic Properties of Three Tin Oxide Halides

Manuel Löber,<sup>[a]</sup> Chris Steve Geißenhöner,<sup>[a]</sup> Markus Ströbele,<sup>[a]</sup> Carl P. Romao,<sup>[a]</sup> and Hans-Jürgen Meyer<sup>\*[a]</sup>

Three tin oxide halides, Sn<sub>7</sub>O<sub>4</sub>Cl<sub>6</sub>, Sn<sub>7</sub>O<sub>4</sub>Br<sub>6</sub>, and Sn<sub>4</sub>OI<sub>6</sub>, were synthesized by solid-state reactions of SnO and SnX<sub>2</sub> (X=Cl, Br, I) at 300 °C. Crystal structures were solved and refined from single crystal X-ray diffraction data, revealing the presence of cubane-

like [Sn<sub>4</sub>O<sub>4</sub>] units in the structures of Sn<sub>7</sub>O<sub>4</sub>Cl<sub>6</sub> and Sn<sub>7</sub>O<sub>4</sub>Br<sub>6</sub>. The electronic structure of Sn<sub>7</sub>O<sub>4</sub>Cl<sub>6</sub> was analyzed by DFT band structure calculations and the electron localization function (ELF).

## Introduction

Oxide halides are known to exist for alkaline metals,<sup>[1]</sup> alkaline earth metals,<sup>[2]</sup> transition metals,<sup>[3]</sup> rare-earth elements<sup>[4]</sup> and for some main group elements, including bismuth,<sup>[5]</sup> lead<sup>[6]</sup> and tin. Crystal structures of three tin oxide fluorides have been reported: Sn<sub>4</sub>O<sub>2</sub>F<sub>4</sub>,<sup>[7]</sup> Sn<sub>4</sub>O<sub>6</sub>F<sub>8</sub><sup>[8]</sup> with divalent tin and Sn<sub>4</sub>O<sub>2</sub>F<sub>10</sub><sup>[9]</sup> with mixed-valence tin. Two tin (II) oxide chlorides, Sn<sub>2</sub>OCl<sub>2</sub> and Sn<sub>4</sub>O<sub>3</sub>Cl<sub>2</sub>, have been reported in the literature but no crystal structure data are available. Sn<sub>2</sub>OCl<sub>2</sub> was described as a light grey powder, obtained from a 1:1 molar mixture of SnO and SnCl<sub>2</sub> heated to 300 °C,<sup>[10]</sup> and Sn<sub>4</sub>O<sub>3</sub>Cl<sub>2</sub> was described as a brown material, synthesized by heating Sn<sub>4</sub>(OH)<sub>6</sub>Cl<sub>2</sub> to 212 °C.<sup>[11]</sup> Our attempts to reproduce these compounds failed. Furthermore, von Schnering et al. reported the crystal structure of a so called "basic tin chloride", structurally characterized as Sn<sub>21</sub>Cl<sub>16</sub>(OH)<sub>14</sub>O<sub>6</sub>.<sup>[12]</sup> When heating this compound, several decomposition products were obtained, assigned as Sn<sub>21</sub>Cl<sub>16</sub>O<sub>13</sub> and Sn<sub>9</sub>Cl<sub>4</sub>O<sub>7</sub>, however, without crystal structure data.<sup>[13]</sup>

Generally, metal oxide halides are candidates for applications, often related to their electronic properties. Bismuth oxide halides e.g. BiOCl and Bi<sub>24</sub>O<sub>31</sub>Br<sub>10</sub> are investigated for their photocatalytic activity, for example for water splitting (BiOBr)<sup>[14]</sup> and the removal of pharmaceutical compounds from water.<sup>[15]</sup> TiOF<sub>2</sub> and FeOCl were recently investigated as electrode materials in Li-ion batteries.<sup>[16]</sup> The photoluminescence properties of Eu- and Pb-doped alkaline earth oxide halides M<sub>4</sub>OX<sub>6</sub> were investigated for M=Ca, Sr, Ba; X=Cl, Br<sup>[17]</sup> as well as for some Eu-doped rare-earth oxide halides.<sup>[18]</sup> The compound

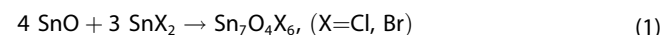
Sn<sub>21</sub>Cl<sub>16</sub>(OH)<sub>14</sub>O<sub>6</sub> was recently investigated in view of its efficient photocatalytic degradation of methyl orange.<sup>[19]</sup>

Recent studies of the tin oxide carbodiimide compounds Sn<sub>2</sub>O(CN<sub>2</sub>)<sup>[20]</sup> and Sn<sub>9</sub>O<sub>5</sub>Cl<sub>4</sub>(CN<sub>2</sub>)<sub>2</sub><sup>[21]</sup> suggested the existence of some yet unknown tin oxide halides, which are reported in this work. Building upon band structures and photochemical properties previously reported for tin oxide carbodiimide compounds<sup>[20–22]</sup> we herein present the electronic band structure and electron localization function of Sn<sub>7</sub>O<sub>4</sub>Cl<sub>6</sub>, as calculated by density functional theory.

## Results and Discussion

### Syntheses of Sn<sub>7</sub>O<sub>4</sub>Cl<sub>6</sub>, Sn<sub>7</sub>O<sub>4</sub>Br<sub>6</sub>, Sn<sub>4</sub>OI<sub>6</sub>

In the course of our explorative studies on the synthesis of tin oxide carbodiimide (Sn<sub>2</sub>O(CN<sub>2</sub>)<sup>[20]</sup>) and tin oxide chloride carbodiimide (Sn<sub>9</sub>O<sub>5</sub>Cl<sub>4</sub>(CN<sub>2</sub>)<sub>2</sub><sup>[21]</sup>) compounds some unknown side phases were detected when departing from SnX<sub>2</sub> (X=Cl, Br, I). Some of these side phases were investigated and identified as tin oxide halides. The tin oxide halides reported herein were prepared straightforwardly by reacting appropriate proportions of SnO and SnX<sub>2</sub> (X=Cl, Br, I) in fused silica ampoules at 300 °C. Sn<sub>7</sub>O<sub>4</sub>Cl<sub>6</sub> and Sn<sub>7</sub>O<sub>4</sub>Br<sub>6</sub> were obtained as beige crystalline powders following reaction (1).



The oxide-poorer tin oxide iodide Sn<sub>4</sub>OI<sub>6</sub> was obtained according to reaction (2) as a crystalline powder having a yellow to orange color.



All three compounds remain stable under atmospheric conditions for several days, but decompose when in direct contact with water.

The discovery of these compounds allows their use in the synthesis of mixed carbodiimide compounds such as

[a] M. Löber, C. S. Geißenhöner, M. Ströbele, C. P. Romao, H.-J. Meyer  
Section for Solid State and Theoretical Inorganic Chemistry  
Institute of Inorganic Chemistry  
Eberhard Karls University Tübingen  
Auf der Morgenstelle 18, 72076 Tübingen, Germany  
E-mail: juergen.meyer@uni-tuebingen.de

© 2020 The Authors. European Journal of Inorganic Chemistry published by Wiley-VCH GmbH. This is an open access article under the terms of the Creative Commons Attribution Non-Commercial NoDerivs License, which permits use and distribution in any medium, provided the original work is properly cited, the use is non-commercial and no modifications or adaptations are made.

Empirical formula	Sn <sub>7</sub> O <sub>4</sub> Cl <sub>6</sub>	Sn <sub>7</sub> O <sub>4</sub> Br <sub>6</sub>	Sn <sub>4</sub> O <sub>6</sub>
CCDC code	1909538	1946137	1942516
Formula weight (g/mol)	1107.67	2748.58	1252.16
Wavelength (Mo–K <sub>α</sub> ) (Å)	0.71073	0.71073	0.71073
Crystal system	triclinic	triclinic	monoclinic
Space group	<i>P</i> $\bar{1}$ (No. 2)	<i>P</i> $\bar{1}$ (No. 2)	<i>P</i> 2 <sub>1</sub> / <i>c</i> (No. 14)
Unit cell dimensions (Å, °)	<i>a</i> = 7.7275(4) <i>b</i> = 8.8129(4) <i>c</i> = 12.0430(6) $\alpha$ = 81.489(4) $\beta$ = 79.362(4) $\gamma$ = 78.096(4)	<i>a</i> = 8.2207(2) <i>b</i> = 12.8530(4) <i>c</i> = 17.5452(5) $\alpha$ = 95.200(2) $\beta$ = 97.687(2) $\gamma$ = 104.552(2)	<i>a</i> = 9.1331(3) <i>b</i> = 12.9398(4) <i>c</i> = 13.7863(4) $\beta$ = 109.049(2)
Volume (Å <sup>3</sup> )	783.55(7)	1763.26(9)	1540.05(8)
Z	2	4	4
Density (calculated) (g/cm <sup>3</sup> )	4.694	5.177	5.400
Theta range for data collection (°)	2.38 to 26.02	2.36 to 25.03	2.22 to 25.35
Total number of reflections	10697	22464	18977
Refined parameters	155	308	101
R1, wR2	0.018, 0.038	0.022, 0.045	0.032, 0.068
GOOF	1.207	1.166	1.450

Sn<sub>9</sub>O<sub>5</sub>Cl<sub>4</sub>(CN<sub>2</sub>)<sub>2</sub><sup>[21]</sup> as successfully prepared from an appropriate mixture of Li<sub>2</sub>(CN<sub>2</sub>) and Sn<sub>7</sub>O<sub>4</sub>Cl<sub>6</sub> at 400 °C.

The crystal structures of compounds obtained from reactions 1 and 2 were determined by single crystal X-ray diffraction.

### Crystal Structure of Sn<sub>7</sub>O<sub>4</sub>Cl<sub>6</sub>

The crystal structure of Sn<sub>7</sub>O<sub>4</sub>Cl<sub>6</sub> was refined within a triclinic lattice (*P* $\bar{1}$ ) containing two formula units per unit cell (Table 1). The most remarkable feature in the crystal structure of Sn<sub>7</sub>O<sub>4</sub>Cl<sub>6</sub> is the presence of [Sn<sub>4</sub>O<sub>4</sub>] units with a structure following the motif of carbon atoms in the cubane structure (C<sub>8</sub>H<sub>8</sub>), surrounded by additional tin atoms. Pairs of such heterocubane units are linked via Sn–O bonds to form a dimeric arrangement in the structure of Sn<sub>7</sub>O<sub>4</sub>Cl<sub>6</sub>. The two [Sn<sub>4</sub>O<sub>4</sub>] units of the dimer are related by a center of symmetry as shown in Figure 1. Each oxygen atom of a [Sn<sub>4</sub>O<sub>4</sub>] unit is connected to an apical tin atom (Sn2, Sn5, Sn7) or with the linking tin atom (Sn6) of an

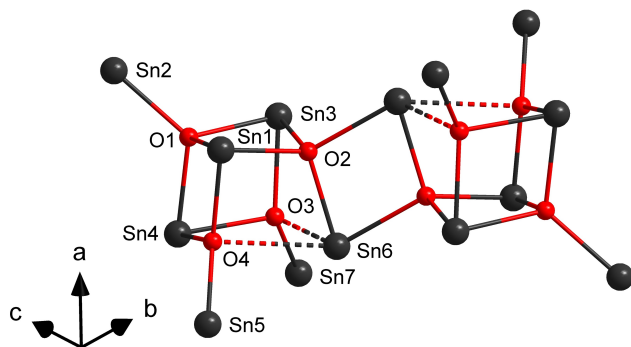


Figure 1. The [Sn<sub>4</sub>O<sub>4</sub>] dimer with surrounding tin atoms in the structure of Sn<sub>7</sub>O<sub>4</sub>Cl<sub>6</sub>.

adjacent [Sn<sub>4</sub>O<sub>4</sub>] unit resulting in tetrahedral (OSn<sub>4</sub>) environments for the oxygen atoms. The four tin atoms in [Sn<sub>4</sub>O<sub>4</sub>] have three oxygen neighbors, except for the bridging atom (Sn6) that is surrounded by four oxygen atoms. Apical tin atoms have one oxygen and two chloride neighbors. The coordination environment of tin atoms having a pyramidal [SnO<sub>3</sub>] arrangement, visualized in Figure 1, suggests a localization of the 5s<sup>2</sup> lone pair of Sn<sup>2+</sup> that is analyzed in more detail on basis of ELF calculations as follows.

The bond lengths between Sn and O vary between 2.10 and 2.74 Å. The markedly longer distances between Sn6 and O3, O4 of 2.51 and 2.74 Å are shown as dashed lines in Figure 1, and they will be discussed with the electronic structure below.

Each of the apical tin atoms (Sn2, Sn7 and Sn5) is surrounded by two chloride ions as can be seen in Figure 2.

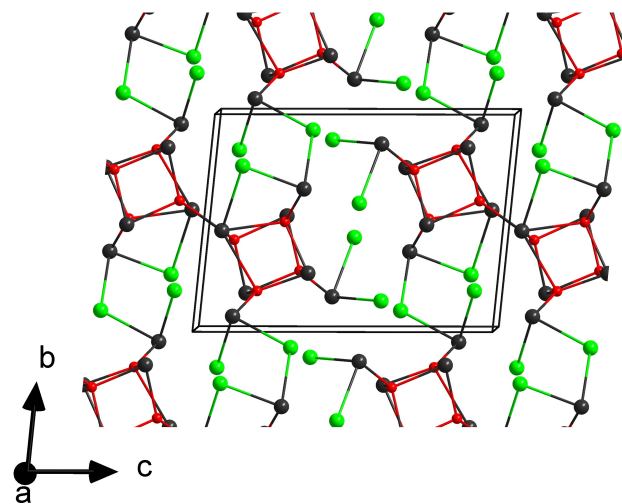
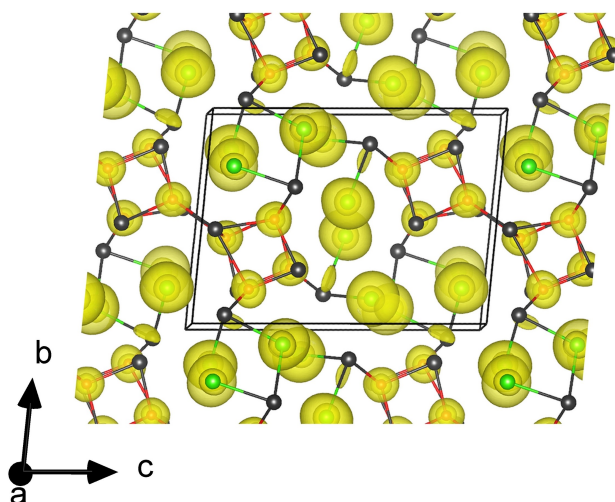


Figure 2. Perspective view of the unit cell of Sn<sub>7</sub>O<sub>4</sub>Cl<sub>6</sub>, with one [Sn<sub>4</sub>O<sub>4</sub>] dimer per unit cell. Tin atoms are shown in black, oxygen in red and chlorine in green.

## Electronic Structure of $\text{Sn}_7\text{O}_4\text{Cl}_6$

The electronic band structure and electron localization function (ELF) of  $\text{Sn}_7\text{O}_4\text{Cl}_6$  were calculated using DFT in order to further understand the structure and properties of this phase, especially the localization of the lone pair of the  $\text{Sn}^{2+}$  and its effect on the structure. The ELF measures the probability of finding an electron at the same point in space as a reference electron with the same spin; therefore areas with high ELF values have high electron localization and are associated with electron pairs.<sup>[23]</sup> The ELF is particularly useful for understanding the behavior of the  $\text{Sn}^{2+}$  lone pair.<sup>[21,24]</sup>

The calculated ELF is shown in the *bc* plane in Figure 3 (in a similar projection as in Figure 2). The isosurfaces clearly show the spheroidal distributions of electron pairs around the chloride and oxide anions. The lone pairs of the tin cations are more disperse, and consequently they appear as small concave discs occupying the apical positions above the tin coordination polyhedra. This result indicates a tetrahedral coordination of the tin atoms including the lone pair, and that the tin atoms are ionically bonded.<sup>[25]</sup> Additionally, the structure can be seen to



**Figure 3.** Perspective view of the calculated electron localization function of  $\text{Sn}_7\text{O}_4\text{Cl}_6$  shown as a yellow isosurface at the 0.8 level.

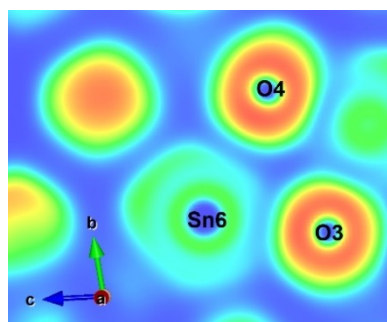


**Figure 4.** A section of the ELF of  $\text{Sn}_7\text{O}_4\text{Cl}_6$  (shown in the rainbow color scale with red indicating high electron localization) emphasizing the interactions between tin and two crystallographically distinct oxygen atoms.

be approximately close-packed, with the empty space between layers filled with lone pair electron density. For further understanding of the interaction between the larger Sn–O bonds a more detailed view is shown in Figure 4, where the nodal planes of the ELF between Sn6 and O3, O4 can be seen when looking at the lighter blue color in the space between Sn and O in contrast to the darker background color. These nodal planes indicate ionic bonding between Sn and O.<sup>[25]</sup>

The calculated electronic band structure of  $\text{Sn}_7\text{O}_4\text{Cl}_6$  is shown in Figure 5.  $\text{Sn}_7\text{O}_4\text{Cl}_6$  is demonstrated to be a semiconductor, with an indirect band gap of 2.8 eV between the Z ( $0\ 0\ \frac{1}{2}$ ) and T ( $0\ \frac{1}{2}\ \frac{1}{2}$ ) points in the Brillouin zone. This bandgap is significantly larger than that calculated for the related material  $\text{Sn}_9\text{O}_3\text{Cl}_4(\text{CN})_2$  (2.3 eV),<sup>[21]</sup> which can be explained by the more covalent nature of the Sn–O bonding in that material, perhaps aided by the covalently bonded  $\text{CN}_2$  ligands. Previous comparisons of the calculated band gaps of tin compounds to experimentally measured values indicate a systematic underestimation of approximately 1 eV.<sup>[21]</sup>

## Crystal structure of $\text{Sn}_7\text{O}_4\text{Br}_6$

The crystal structure of  $\text{Sn}_7\text{O}_4\text{Br}_6$  was refined in a triclinic lattice (*P* $\bar{1}$ ) with four formula units per unit cell, twice that of  $\text{Sn}_7\text{O}_4\text{Cl}_6$  (Table 1). Both structures feature dimeric heterocubane-like  $[\text{Sn}_4\text{O}_4]$  units surrounded by additional tin atoms, but with different arrangements in the structure.

The two  $[\text{Sn}_4\text{O}_4]$  units forming the dimer in the structure of  $\text{Sn}_7\text{O}_4\text{Br}_6$  are no longer related by a center of inversion (Figure 6) as was the case in the structure of  $\text{Sn}_7\text{O}_4\text{Cl}_6$ . Moreover, the two  $[\text{Sn}_4\text{O}_4]$  dimers in the structure of  $\text{Sn}_7\text{O}_4\text{Br}_6$  have different locations within the unit cell (Figure 7).

Tin atoms within  $[\text{Sn}_4\text{O}_4]$  units are coordinated by three oxygen atoms to form a pyramidal  $[\text{SnO}_3]$  arrangement, suggesting a localization of the  $5s^2$  lone pair of  $\text{Sn}^{2+}$  as was found in the structure of the homologous chloride, except for the bridging tin atom (Sn7). Sn–O bond lengths vary from 2.1 to 2.4 Å. Connectivities between Sn3 and O5 (2.81 Å) and

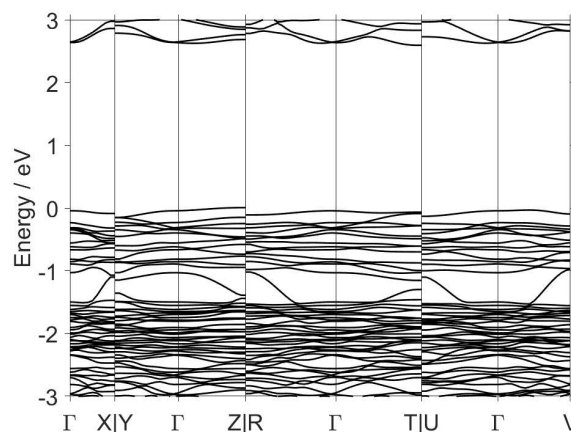


**Figure 5.** Calculated electronic band structure of  $\text{Sn}_7\text{O}_4\text{Cl}_6$ . Special points in and paths through the Brillouin zone were chosen following Ref. [26].

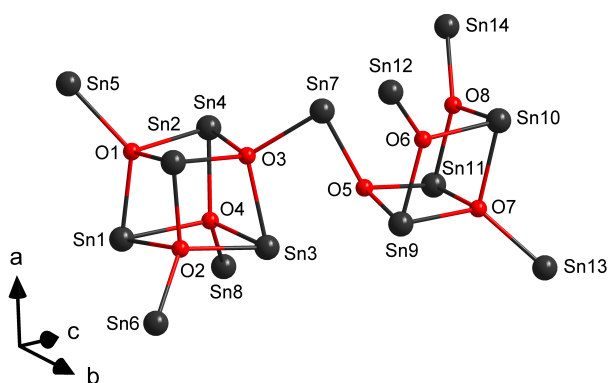


Figure 6. The  $[Sn_4O_4]$  dimer with surrounding tin atoms in the structure of  $Sn_7O_4Br_6$ .

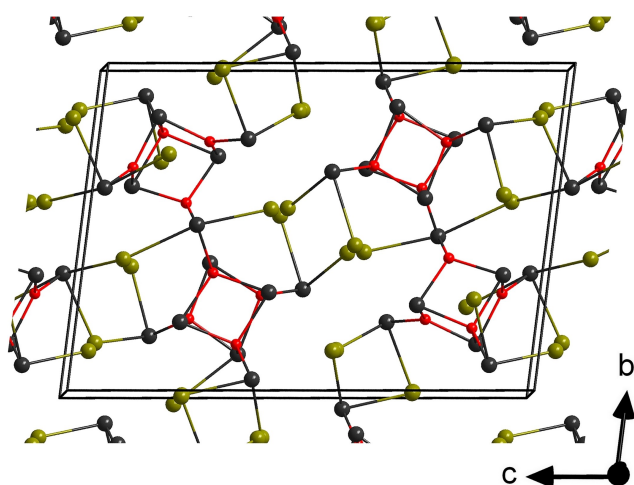


Figure 7. Crystal structure of  $Sn_7O_4Br_6$ , containing two  $[Sn_4O_4]$  dimers in the unit cell. Tin is shown in black, oxygen in red and bromine in olive.

between Sn7 and O6, O8 (3.16 Å and 3.21 Å) are not considered in Figure 6. Apical tin atoms (Sn5, Sn6, Sn8, Sn12, Sn13, Sn14) have coordination numbers of three with one oxygen and two bromine neighbors.

Heterocubane-type assemblies with tin can be found in some already known compounds. Examples involve the basic tin chloride  $Sn_{21}Cl_{16}(OH)_{14}O_6$ , where one  $[Sn_4O_4]$  cubane-type unit is linked to the O atoms of the corners of another unit via Sn and  $OH^-$  interactions, in which Sn–O distances vary between 2.16 and 2.33 Å.<sup>[12]</sup> Another Sn–O cubane-type motif was reported in  $Sn_8O_{28}C_{12}[Fe(C_{10}H_8)_2]_6$  where one  $[Sn_4O_4]$  unit is surrounded by six ferrocene units with Sn–O distances from 2.05 to 2.19 Å.<sup>[27]</sup>

In tin oxide sulfate  $Sn_2O(SO_4)$  a cubane-like  $Sn_4O_4$  motif is surrounded by sulfate anions with Sn–O bond length between 2.15 to 2.35 Å.<sup>[28]</sup> An example with a  $[Sn_4As_4]$  unit is the compound  $[TerSnAs]_4$  in which Ter=2,6-bis(2,4,6-trimethylphenyl)phenyl.<sup>[29]</sup>

Like in the compounds  $Sn_7O_4Cl_6$  and  $Sn_7O_4Br_6$ , anion-centered metal tetrahedra containing oxide ions are a common

feature in many inorganic compounds and minerals. Numerous metal cations like  $Cu^{2+}$ ,  $Zn^{2+}$ ,  $Pb^{2+}$ ,  $Sn^{2+}$ ,  $Bi^{3+}$  are reported as ligands.<sup>[30]</sup> Those anion centered metal tetrahedra can arrange as chains, frameworks or finite units.<sup>[31]</sup>

### Crystal structure of $Sn_4OI_6$

$Sn_4OI_6$  crystallizes in the monoclinic space group  $P2_1/c$  (Table 1) with four crystallographically distinct tin atoms in the structure. The crystal structure may be described as containing two fragments, displayed in Figure 8, that are interconnected with each other in a three-dimensional network as displayed in Figure 9.

Three crystallographically distinct tin atoms (Sn1, Sn2, Sn3) form a  $[Sn_3O]$  fragment surrounded by six iodine ligands. The Sn–O bond lengths are approximately 2.1 Å; Sn–I bond lengths range from 2.98 to 3.23 Å. The  $[Sn_3OI_6]$  fragment displayed in

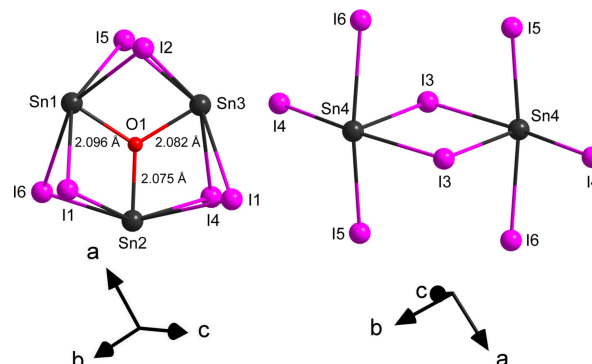


Figure 8. Coordination environments of tin atoms in the structure of  $Sn_4OI_6$ , showing the  $[Sn_3OI_6]$  fragment (left) and the  $[Sn_4I_6]$  dimer (right).

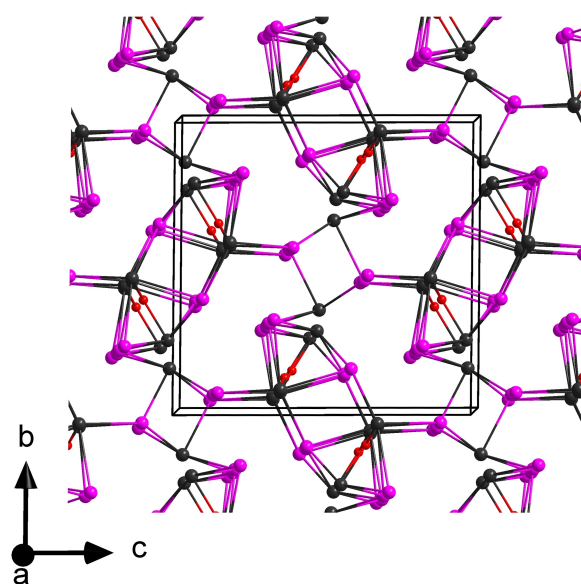


Figure 9. Perspective view of the structure of  $Sn_4OI_6$ . Tin is shown in black, oxygen in red, and iodine in light purple.

Figure 8 (left) is coupled by inversion symmetry via shared I1 atoms to form a dimer. Some remaining iodine atoms (I4, I5, I6) are shared with the second motif, the  $[\text{SnI}_4]$  dimer.

Tin atoms show an interesting coordination pattern, which differs from those in the previous  $\text{Sn}_7\text{O}_4\text{X}_6$  structures, but still gives reason to envision that a localized  $5s^2$  lone pair of  $\text{Sn}^{2+}$  is present in the structure.

## Conclusions

Three tin oxide halides with divalent tin were synthesized from solid-state reactions of  $\text{SnO}$  and  $\text{SnX}_2$  ( $\text{X}=\text{Cl}, \text{Br}, \text{I}$ ) and their crystal structures determined by single-crystal X-ray diffraction. The crystal structures of  $\text{Sn}_7\text{O}_4\text{Cl}_6$  and  $\text{Sn}_7\text{O}_4\text{Br}_6$  contain centrosymmetric and non-centrosymmetric heterocubane-like  $[\text{Sn}_4\text{O}_4]$  dimers with surrounding (apical) tin atoms. Both crystal structures can be visualized as dimeric  $[\text{Sn}_4\text{O}_4\text{Sn}_3]_2$  heterocubanes, displayed in Figure 1 and Figure 6, being embedded in a matrix of chloride respectively bromide. The characteristic threefold coordination of tin atoms, following the motif of a trigonal  $[\text{SnO}_3]$  pyramid, gives reason to assume a localized  $5s^2$  electron pair of  $\text{Sn}^{2+}$ .

In order to understand the bonding and the electronic structure the electron localization function of  $\text{Sn}_7\text{O}_4\text{Cl}_6$  was calculated. It could be shown that some weak  $\text{Sn}-\text{O}$  bonds with above-average lengths of up to 2.7 Å exist, furthermore the location of the tin lone pair could be identified to be on the corners of the cubane-like units. A band structure calculation revealed  $\text{Sn}_7\text{O}_4\text{Cl}_6$  to be a semiconductor with a calculated bandgap of 2.8 eV, which is in accord with the light color of the compound. As some oxide halides have potential applications, e.g. as photocatalysts or as battery materials, more research in this field is recommended although many compounds are somewhat unstable in air.

The crystal structure of  $\text{Sn}_4\text{OI}_6$  is also reported with four- and five-coordinate tin atoms, and indications of a localized  $5s^2$  lone pair of  $\text{Sn}^{2+}$ .

## Experimental Section

**Synthesis of  $\text{Sn}_7\text{O}_4\text{Cl}_6$ .** The starting materials  $\text{SnCl}_2$  (Alfa Aesar, ultra-dry, 99.9985%) and  $\text{SnO}$  (Sigma-Aldrich, 99.99%) were mixed and pestled in a 3:4 molar ratio (total mass: 100 mg) under dry argon atmosphere in a glove-box and sealed into a silica tube under vacuum. The mixture was heated to 300 °C in a crucible furnace at 2 K/min and remained there for 10 h. The reaction product then was cooled to room temperature at 2 K/min. The yield of  $\text{Sn}_7\text{O}_4\text{Cl}_6$  was estimated >90%, according to XRD powder patterns. Single-crystals were obtained from a corresponding mixture that was heated at 300 °C for 300 h and cooled to room temperature at 6 K/day. Crystal powder and single crystals could be treated in air.

**Synthesis of  $\text{Sn}_7\text{O}_4\text{Br}_6$ .** The starting materials  $\text{SnBr}_2$  (Sigma-Aldrich, p.A.) and  $\text{SnO}$  (Sigma-Aldrich, 99.99%) were mixed and pestled in a 3:4 molar ratio (total mass: 100 mg) under dry argon atmosphere in a glove-box and sealed into silica tube under vacuum. The mixture was heated to 300 °C in a crucible furnace at 2 K/min and

remained there for 10 h and cooled to room temperature at 2 K/min. The yield of  $\text{Sn}_7\text{O}_4\text{Br}_6$  was estimated >90%, according to XRD powder patterns. Crystals were obtained by heating a 2:1 molar mixture ratio up to 300 °C for 100 h and cooling to room temperature at 0.1 K/min. Crystal powder and single crystals could be treated in air.

**Synthesis of  $\text{Sn}_4\text{OI}_6$ .** The starting materials  $\text{SnI}_2$  (Sigma-Aldrich 99.99%) and  $\text{SnO}$  (Sigma-Aldrich, 99.99%) were mixed and pestled in a 3:1 molar ratio (total mass: 100 mg) under dry argon atmosphere in a glove-box and sealed into silica tube under vacuum. The mixture was heated to 300 °C in a crucible furnace at 2 K/min and remained there for 10 h before being cooled to room temperature at 2 K/min. The yield of  $\text{Sn}_4\text{OI}_6$  was estimated >95%, according to XRD powder patterns. Crystals were obtained by heating a 3:4 molar mixture ratio to 300 °C for 100 h before cooling to room temperature at 0.1 K/min. Crystal powder and single crystals could be treated in air.

**X-ray Diffraction.** Powder X-ray diffraction studies were performed using a StadiP diffractometer (Stoe, Darmstadt) with Ge-monochromated  $\text{Cu}-\text{K}\alpha_1$  radiation and a Mythen1 Detector.

Single crystals of  $\text{Sn}_7\text{O}_4\text{Cl}_6$ ,  $\text{Sn}_7\text{O}_4\text{Br}_6$  and  $\text{Sn}_4\text{OI}_6$  were selected and placed on the tip of a glass fiber. Data were collected using a single-crystal X-ray diffractometer (IPDS 2T, Stoe, Darmstadt), equipped with graphite-monochromated  $\text{Mo}-\text{K}\alpha$  radiation ( $\lambda=0.71073$  Å). The intensity data were corrected for Lorentz factors and polarization effects by the IPDS software. Absorption effects were corrected by the X-Red/X-Shape program of the Stoe software. Crystal structure solutions were obtained by direct methods (SHELXS), followed by full-matrix least-squares structure refinements with SHELXL-2017.<sup>[32]</sup>

Deposition Numbers 1909538 (for  $\text{Sn}_7\text{O}_4\text{Cl}_6$ ), 1946137 (for  $\text{Sn}_7\text{O}_4\text{Br}_6$ ), and 1942516 (for  $\text{Sn}_4\text{OI}_6$ ) contain the supplementary crystallographic data for this paper. These data are provided free of charge by the joint Cambridge Crystallographic Data Centre and Fachinformationszentrum Karlsruhe Access Structures service [www.ccdc.cam.ac.uk/structures](http://www.ccdc.cam.ac.uk/structures).

**Density Functional Theory.** Density functional theory (DFT) was used to calculate the electronic structure of  $\text{Sn}_7\text{O}_4\text{Cl}_6$  using the Abinit software package.<sup>[33]</sup> Convergence studies were used to choose a 40 Ha plane-wave basis set energy cutoff and a  $2\times 2\times 1$  Monkhorst–Pack grid<sup>[34]</sup> of k points. Norm-conserving pseudopotentials were used as received from the Abinit library. Example input files are available as part of the Supplementary Information.

## Acknowledgements

Funding by the Deutsche Forschungsgemeinschaft (DFG) through grant ME 914/25-2 is gratefully acknowledged. Computational resources were provided by the state of Baden-Württemberg through bwHPC and the DFG through grant no. INST 40/467-1 FUGG (JUSTUS cluster). Open access funding enabled and organized by Projekt DEAL.

## Conflict of Interest

The authors declare no conflict of interest.

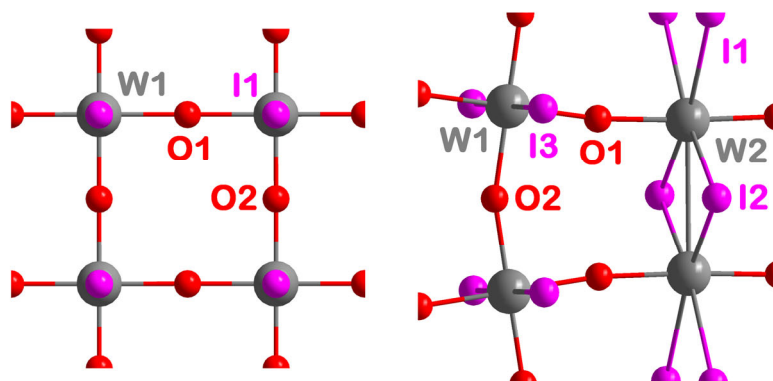
**Keywords:** Oxide halides · Tin · Solid state reactions · Density functional calculations · Electron localization function

- [1] a) O. Reckeweg, B. Blaschkowski, T. Schleid, *Z. Anorg. Allg. Chem.* **2012**, 638, 2081–2086; b) K. Hippler, S. Sitta, P. Vogt, H. Sabrowsky, *Acta Crystallogr.* **1990**, C46, 736–738; c) A.-V. Mudring, M. Jansen, *Z. Naturforsch. B* **2001**, 56, 209–212; d) C. Feldmann, M. Jansen, *Z. Naturforsch. B* **1996**, 51, 1352–1354.
- [2] a) H.-J. Meyer, G. Meyer, M. Simon, *Z. Anorg. Allg. Chem.* **1991**, 596, 89–92; b) H.-R. Hagemann, F. Kubel, H. Bill, *Eur. J. Solid State Inorg. Chem.* **1996**, 33, 1101–1109; c) B. Frit, B. Holmberg, J. Galy, *Acta Crystallogr.* **1970**, B26, 16–19.
- [3] a) H. Schäfer, F. Wartenpfuhl, E. Weise, *Z. Anorg. Allg. Chem.* **1958**, 295, 268–280; b) M. Lind, *Acta Crystallogr.* **1970**, B26, 1058–1062; c) B. Araújo, A. Arévalo-López, J. P. Atfield, C. Paschoal, A. Ayala, *Appl. Phys. Lett.* **2018**, 113, 222901; d) K. Dehnicke, K. U. Meyer, *Z. Anorg. Allg. Chem.* **1964**, 331, 121–128; e) G. Ferguson, M. Mercer, D. Sharp, *J. Chem. Soc. A* **1969**, 2415–2418; f) H. Hess, H. Hartung, *Z. Anorg. Allg. Chem.* **1966**, 344, 157–166; g) P. G. Jones, H. Rumpel, E. Schwarzmann, G. M. Sheldrick, *Acta Crystallogr.* **1979**, B35, 2380–2381.
- [4] a) G. Meyer, T. Staffel, *Z. Anorg. Allg. Chem.* **1986**, 532, 31–36; b) L. Brixner, E. Moore, *Acta Crystallogr.* **1983**, C39, 1316–1316; c) T. Aitasalo, J. Hölsä, M. Lastusaari, J. Legendziewicz, L. Lehto, J. Lindén, M. Maryško, *J. Alloys Compd.* **2004**, 380, 296–302; d) G. Brandt, R. Diehl, *Mater. Res. Bull.* **1974**, 9, 411–419.
- [5] K. Keramidias, G. Voutsas, P. Rentzeperis, *Z. Kristallogr. Cryst. Mater.* **1993**, 205, 35–40.
- [6] H. Vincent, G. Perrault, *Bull. Soc. Fr. Mineral. Cristallogr.* **1971**, 94, 323–331.
- [7] B. Darriet, J. Galy, *Acta Crystallogr.* **1977**, B33, 1489–1492.
- [8] I. Abrahams, S. J. Clark, J. D. Donaldson, Z. I. Khan, J. T. Southern, *J. Chem. Soc. Dalton Trans.* **1994**, 17, 2581–2583.
- [9] J.-H. Chang, J. Köhler, *Z. Kristallogr. New Cryst. Struct.* **1999**, 214, 147–148.
- [10] L. D. Polyachenok, K. Nazarov, N. V. Galitskii, *Khim. Khim. Tekhnol.* **1975**, 9, 9–13.
- [11] J. Donaldson, W. Moser, W. Simpson, *J. Chem. Soc.* **1963**, 1727–1731.
- [12] H. G. von Schnering, R. Nesper, H. Pelshenke, *Z. Naturforsch. B* **1981**, 36, 1551–1560.
- [13] H. von Schnering, H. Pelshenke, *Angew. Chem. Int. Ed.* **1965**, 77, 1038–1039.
- [14] M. Shi, G. Li, J. Li, X. Jin, X. Tao, B. Zeng, E. A. Pidko, R. Li, C. Li, *Angew. Chem. Int. Ed.* **2020**, 59, 6590–6595.
- [15] a) S. Heidari, M. Haghighi, M. Shabani, *J. Cleaner Prod.* **2020**, 120679; b) X. Zhong, K.-X. Zhang, D. Wu, X.-Y. Ye, W. Huang, B.-X. Zhou, *Chem. Eng. J.* **2020**, 383, 123148.
- [16] J. M. Powell, PhD diss. thesis, University of Tennessee **2017**.
- [17] W. Schipper, Z. Vroon, G. Blasse, T. Schleid, G. Meyer, *Chem. Mater.* **1992**, 4, 688–692.
- [18] B. Es-Sakhi, F. Guillen, A. Garcia, C. Fouassier, P. Hagenmuller, *J. Electrochem. Soc.* **1988**, 135, 2099.
- [19] B. Liang, W. Zhang, *Mater. Res. Express* **2019**, 6, 115066.
- [20] K. Dolabdjian, A. L. Görne, R. Dronskowski, M. Ströbele, H.-J. Meyer, *Dalton Trans.* **2018**, 47, 13378–13383.
- [21] M. Löber, C. S. Geißenhöner, M. Ströbele, S. Indris, C. P. Romao, H.-J. Meyer, *Inorg. Chem.* **2019**, 58, 14560–14567.
- [22] Z. Chen, M. Löber, A. Rokicińska, Z. Ma, J. Chen, P. Kuśrowski, H.-J. Meyer, R. Dronskowski, A. Slabon, *Dalton Trans.* **2020**, 49, 3450–3456.
- [23] A. D. Becke, K. E. Edgecombe, *J. Chem. Phys.* **1990**, 92, 5397–5403.
- [24] M. Löber, K. Dolabdjian, M. Ströbele, C. P. Romao, H.-J. Meyer, *Inorg. Chem.* **2019**, 58, 7845–7851.
- [25] A. Savin, O. Jepsen, J. Flad, O. K. Andersen, H. Preuss, H. G. von Schnering, *Angew. Chem. Int. Ed.* **1992**, 31, 187–188; *Angew. Chem.* **1992**, 104, 186–188.
- [26] Y. Hinuma, G. Pizzi, Y. Kumagai, F. Oba, I. Tanaka, *Comput. Mater. Sci.* **2017**, 128, 140–184.
- [27] A. L. Zheng, J. F. Ma, Z. M. Su, L. K. Yan, J. Yang, Y. Y. Li, J. F. Liu, *Angew. Chem. Int. Ed.* **2004**, 43, 2409–2411; *Angew. Chem.* **2004**, 116, 2463–2465.
- [28] G. Lundren, G. Wernfors, T. Yamaguchi, *Acta Crystallogr.* **1982**, B38, 2357–2361.
- [29] A. Hinz, J. M. Goicoechea, *Dalton Trans.* **2018**, 47, 8879–8883.
- [30] S. V. Krivovichev, S. K. Filatov, *Am. Mineral.* **1999**, 84, 1099–1106.
- [31] S. V. Krivovichev, S. K. Filatov, *Acta Crystallogr.* **1999**, B55, 664–676.
- [32] G. M. Sheldrick, *Acta Crystallogr.* **2015**, C71, 3–8.
- [33] X. Gonze, B. Amadon, G. Antonius, F. Arnardi, L. Baguet, J.-M. Beuken, J. Bieder, F. Bottin, J. Bouchet, E. Bousquet, N. Brouwer, F. Bruneval, G. Brunin, T. Gavignac, J.-B. Charraud, W. Chen, M. Göte, S. Gottenier, J. Denier, G. Geneste, P. Ghosez, M. Giantomassi, Y. Gillet, O. Gingras, D. R. Hamann, G. Hautier, X. He, N. Helbig, N. Holzwarth, Y. Jia, F. Jollet, W. Lafargue-Dit-Hauret, K. Lejaeghere, M. A. L. Marques, A. Martin, C. Martins, H. P. C. Miranda, F. Naccarato, K. Persson, G. Petretto, V. Planes, Y. Puillon, S. Prokhorenko, F. Ricci, G.-M. Rignanese, A. H. Romero, M. M. Schmitt, M. Torrent, M. J. Van Setten, B. Van Troeye, M. J. Verstraete, G. Zerah, J. W. Zwanziger, *Comput. Phys. Commun.* **2020**, 248, 107042.
- [34] H. J. Monkhorst, J. D. Pack, *Phys. Rev. B* **1976**, 13, 5188.

Manuscript received: September 16, 2020  
Revised manuscript received: November 3, 2020

# Publication 5

$W_2O_3I_4$  and  $WO_2I_2$ : metallic phases in the chemical transport reaction of tungsten



<https://doi.org/10.1039/D1DT01212F>

Reprinted with permission from

*Dalton Trans.* **2021**, 50, 6789–6792

Copyright © 2021 The Royal Society of Chemistry





Cite this: *Dalton Trans.*, 2021, **50**, 6789Received 13th April 2021,  
Accepted 29th April 2021

DOI: 10.1039/d1dt01212f

rsc.li/dalton

## W<sub>2</sub>O<sub>3</sub>I<sub>4</sub> and WO<sub>2</sub>I<sub>2</sub>: metallic phases in the chemical transport reaction of tungsten†

Manuel Löber, Markus Ströbele, Carl P. Romao and Hans-Jürgen Meyer \*

The crystal structures of the hitherto unknown phase W<sub>2</sub>O<sub>3</sub>I<sub>4</sub> and of WO<sub>2</sub>I<sub>2</sub>, a compound that is known to play an important role in the chemical vapor transport of elemental tungsten are reported. We demonstrate that WO<sub>2</sub>I<sub>2</sub> transforms into W<sub>2</sub>O<sub>3</sub>I<sub>4</sub>, and then into WO<sub>2</sub> with increasing temperature. Crystals of WO<sub>2</sub>I<sub>2</sub> appear as thin platelets, showing metallic luster; crystals of W<sub>2</sub>O<sub>3</sub>I<sub>4</sub> appear as black colored needle-shaped platelets. Both compounds adopt layered structures; electronic band structure calculations reveal metallic conductivity for W<sub>2</sub>O<sub>3</sub>I<sub>4</sub> and surprisingly also for WO<sub>2</sub>I<sub>2</sub>.

Elemental tungsten has been used as a filament in incandescent light bulbs for over one century due to its exceptional properties, including the highest melting point of all metals ( $T > 3400$  °C) and the highest enthalpy of vaporization ( $\Delta H_v \approx 860$  kJ mol<sup>-1</sup>).<sup>1</sup> The stability and inertness of tungsten metal requires careful choice of synthetic routes and precursors for the discovery of tungsten compounds.<sup>2</sup> Tungsten diiodide (WO<sub>2</sub>I<sub>2</sub>) is a highly prominent tungsten compound which appears in textbooks due to its importance in the chemical vapor transport (CVT) reaction of tungsten in halogen lamps.<sup>3</sup> The formation of WO<sub>2</sub>I<sub>2</sub> has been described by Tillack equation (1)<sup>4</sup> and has often been reproduced by other researchers:<sup>5,6</sup>

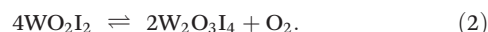


Experimental studies and thermodynamic calculations regarding WO<sub>2</sub>I<sub>2</sub> have reached slightly varying conclusions (*e.g.* formation enthalpies  $\Delta H^\circ = -146$  to  $-152$  kcal mol<sup>-1</sup>)<sup>7,8</sup> but its crystal structure has remained unknown until now (the only structurally characterized tungsten oxide iodide was WOI<sub>3</sub>).<sup>9</sup> The treatment of this (exothermic) compound at elevated

temperatures reverses the formation reaction (1) and produces tungsten metal *via* CVT.

A descriptive mechanism of the chemistry inside the halogen lamp has been established in which WO<sub>2</sub>I<sub>2</sub> is believed to be the essential compound. The mechanism (which has frequently been revised) explains the transport reaction of tungsten, as it is initially deposited on the glass tube of the bulb by an aging process, and then recycled to the tungsten filament.<sup>3</sup> The first step of the recovery of tungsten is the exothermic formation of WO<sub>2</sub>I<sub>2</sub>, followed by its transformation into gaseous WO<sub>2</sub> and WO within the temperature gradient inside the bulb, leading to the deposition of tungsten atoms onto the tungsten filament.

WO<sub>2</sub>I<sub>2</sub> can be formed from tungsten metal in the presence of iodine and water in the halogen lamp at elevated temperatures.<sup>8</sup> Its preparation is performed in a temperature gradient (900 °C–300 °C) according to reaction (1) in a fused (silica) vessel. This was confirmed in our reactions, (using a temperature gradient 800 °C–300 °C) where WO<sub>2</sub>I<sub>2</sub> deposited in the cooler region of the reaction vessel, crystallizing as very thin crystal platelets, often several mm in length, which showed metallic luster. When WO<sub>2</sub>I<sub>2</sub> was treated at 380 °C in a vacuum sealed ampoule it transforms into the hitherto unknown compound W<sub>2</sub>O<sub>3</sub>I<sub>4</sub>, as described in eqn (2):



Crystals of W<sub>2</sub>O<sub>3</sub>I<sub>4</sub> have a slightly different appearance to those of the parent compound WO<sub>2</sub>I<sub>2</sub>, with needle-like morphology and a black color. The thermal transformation of WO<sub>2</sub>I<sub>2</sub> into W<sub>2</sub>O<sub>3</sub>I<sub>4</sub> involves a reduction of the formal oxidation state of tungsten from W<sup>6+</sup> to W<sup>5+</sup>.

When W<sub>2</sub>O<sub>3</sub>I<sub>4</sub> was heated to about 400 °C (vacuum sealed ampoule) the formation of WO<sub>2</sub> was observed eqn (3), as confirmed by the powder X-ray diffraction.



The selection of appropriate crystals for single-crystal X-ray diffraction experiments was challenging, but ultimately suc-

Section for Solid State and Theoretical Inorganic Chemistry, Institute of Inorganic Chemistry, Eberhard Karls Universität Tübingen, Auf der Morgenstelle 18, 72076 Tübingen, Germany. E-mail: juergen.meyer@uni-tuebingen.de

† Electronic supplementary information (ESI) available: Experimental details and supplementary tables, DFT files. CCDC 2004434 and 2054404. For ESI and crystallographic data in CIF or other electronic format see DOI: 10.1039/d1dt01212f

successful for both  $\text{WO}_2\text{I}_2$  and  $\text{W}_2\text{O}_3\text{I}_4$ . Although the crystal structure of  $\text{WO}_2\text{I}_2$  was previously unreported, lattice parameters belonging to a monoclinic crystal system are given in the literature.<sup>4</sup>

The structure of  $\text{WO}_2\text{I}_2$  was refined on basis of single-crystal X-ray diffraction (XRD) data in the orthorhombic space group *Immm*, revealing a layered arrangement (Fig. 1). Further crystallographic and structure refinement data can be found in the ESI in Table S1.† Additionally, atomic coordinates, Wyckoff positions and equivalent isotropic displacement parameters are displayed in Table S2.† The structure is composed of regular two-dimensional  $[\text{WO}_{4/2}\text{I}_2]$  layers, in which tungsten atoms are interconnected by shared oxygen atoms. We note two distinct W–O distances (187.42(2) pm and 195.25(2) pm) in the structure of  $\text{WO}_2\text{I}_2$ , causing the absence of tetragonal symmetry. Alternating layers are stacked along the *c* axis so that the iodine atoms belonging to one layer point to the centers of rectangular  $[\text{WO}_{4/2}]$  faces of two adjacent layers (Fig. 1).

A similar structure has been reported for orthorhombic and monoclinic phases of  $\text{WO}_2\text{Cl}_2$ . A structure refinement of  $\text{WO}_2\text{Cl}_2$  from powder neutron diffraction data yielded a disordered *Immm* structure with fractional occupations for all atom positions.<sup>10</sup>

The structure of the hitherto unknown compound  $\text{W}_2\text{O}_3\text{I}_4$  was refined on the basis of single-crystal XRD data in the monoclinic space group *I2/m*.  $\text{W}_2\text{O}_3\text{I}_4$  also adopts a layered structure, as displayed in Fig. 2. Individual layers in the structure are strongly distorted when compared to the nearly square planar  $[\text{WO}_{4/2}]$  layers in the structure or  $\text{WO}_2\text{I}_2$ .

Atomic coordinates, Wyckoff positions and equivalent isotropic displacement parameters of  $\text{W}_2\text{O}_3\text{I}_4$  are displayed in Table S3.†

The crystal structure of  $\text{W}_2\text{O}_3\text{I}_4$  is based on two crystallographically distinct tungsten atoms, W1 and W2, which have

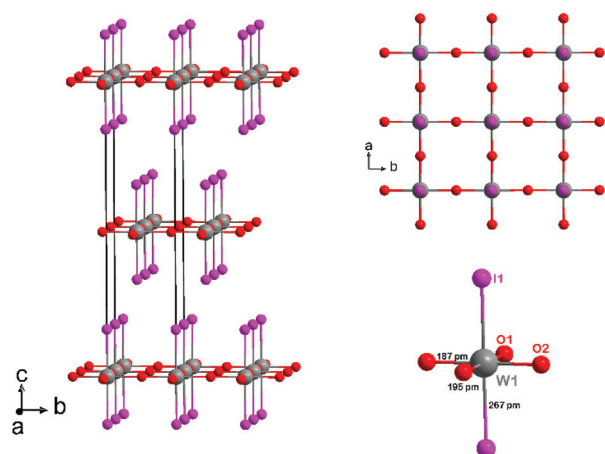


Fig. 1 Section of the crystal structure of  $\text{WO}_2\text{I}_2$  with an outlined unit cell, showing tungsten (grey), oxygen (red), and iodine (violet) atoms and the cell edges (black). A section of one isolated *ab* layer, and the  $\text{WO}_{4/2}\text{I}_2$  building block are shown at right.

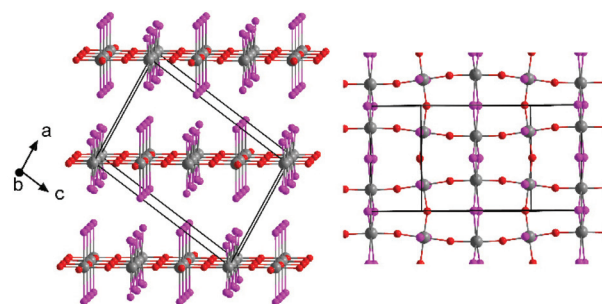


Fig. 2 Crystal structure of  $\text{W}_2\text{O}_3\text{I}_4$ , with the arrangement of tungsten (grey), oxygen (red), and iodine (violet) atoms in the unit cell (left), and a section of one isolated layer (right).

different network connectivities. A section of one layer is displayed in Fig. 3. It emphasizes the two-dimensional edge-bridging connectivity of  $[\text{WO}_{4/2}\text{I}_2]$  octahedra by shared oxygen atoms (W–O distances 189.2(1) pm, 190.7(6) pm for W1 and 187.4(6) for W2); a pattern that is essentially the same as in the structure of  $\text{WO}_2\text{I}_2$ . The second tungsten atom, W2, is situated within edge-sharing  $[\text{WI}_{4/2}\text{O}_{2/2}]$  octahedra connected *via* iodine atoms, introducing alternating short (310.45(9) pm) and long (438.37(7) pm) W–W distances parallel to the *b* axis direction. This structural pattern is well-known in structures of transition metal tetrahalides, whose electronic  $d^1$  or  $d^2$  configurations introduce a Peierls distortion, as exemplified in the structures of  $\text{NbCl}_4$ <sup>11</sup> and  $\text{WCl}_4$ <sup>12</sup> ( $\text{WI}_4$  is unknown).<sup>13</sup> From a structural point of view, the alternating long and short metal-to-metal distances along the edge-sharing octahedral chain indicate semi-localized electron density, and thus metal–metal interactions corresponding to the shorter distances (drawn in gray in Fig. 3).

Hence, it could be assumed that the overall formal oxidation state of five for tungsten in  $\text{W}_2\text{O}_3\text{I}_4$  is represented by mixed states of 6+ for W1, and 4+ for W2. A closer inspection of this question and the origin of the metallic lustre in  $\text{W}_2\text{O}_3\text{I}_4$  and  $\text{WO}_2\text{I}_2$  was performed using density functional theory (DFT) calculations.

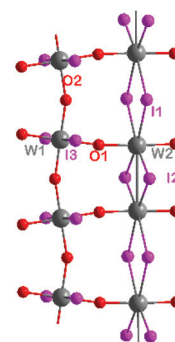


Fig. 3 A section of one isolated layer (cutout from Fig. 2, right) in the crystal structure of  $\text{W}_2\text{O}_3\text{I}_4$ , containing two distinct tungsten atoms, W1 and W2, lined up within the layer.

The calculated electronic band structures of  $\text{WO}_2\text{I}_2$  and  $\text{W}_2\text{O}_3\text{I}_4$  are shown in Fig. 4 and 5, respectively.  $\text{WO}_2\text{I}_2$  was found to be a poor metal, with bands crossing the Fermi level between the  $\Gamma$  [0 0 0], R [ $0 \frac{1}{2}$  0], S [ $\frac{1}{2}$  0 0], and T [ $0 \ 0 \ \frac{1}{2}$ ] points in reciprocal space, indicating delocalization of electrons and metallic bonding both within and between layers.  $\text{W}_2\text{O}_3\text{I}_4$  was found to have higher metallicity, as indicated by a higher density of states at the Fermi level. In both materials, the bands crossing the Fermi level were found to have primarily W d orbital character, mixed with some O p and I p orbital character, indicating covalency. In  $\text{W}_2\text{O}_3\text{I}_4$ , both the W1 and W2 sites contribute to the density of states at the Fermi level.

These calculated electronic properties allow an analogy to be drawn between  $\text{WO}_2\text{I}_2$  and  $\text{W}_2\text{O}_3\text{I}_4$  and the sodium tungsten bronzes ( $\text{Na}_x\text{WO}_3$ ), which also display metallicity at high sodium loadings, with bands crossing the Fermi level near the corners of the Brillouin zone (as in  $\text{WO}_2\text{I}_2$ ).<sup>15</sup> These features can also be seen in the band structure of  $\text{W}_2\text{O}_3\text{I}_4$ ; however the

structural and chemical changes have shifted the Fermi level upwards relatively by about 0.4 eV.

The oxidation states of the tungsten atoms were investigated by Voronoi integration of the electron density.<sup>16</sup> This method assigned a formal charge of +3.6 to the tungsten atoms in  $\text{WO}_2\text{I}_2$  and of +3.6 and +3.3 to the W1 and W2 sites, respectively, in  $\text{W}_2\text{O}_3\text{I}_4$ . These values are lower than would be assumed from the stoichiometry of these compounds but can be explained by the small formal charges on the oxygen atoms (−0.1 to −0.2), further demonstrating that the bonding between W and O, and the W2–W2 interactions in  $\text{W}_2\text{O}_3\text{I}_4$  are covalent and not ionic.

$\text{W}_2\text{O}_3\text{I}_4$  appears as a new phase in the W–O–I system, formed by chemical transformation from  $\text{WO}_2\text{I}_2$  at 380 °C. Both  $\text{W}_2\text{O}_3\text{I}_4$  and  $\text{WO}_2\text{I}_2$  were found to adopt layered structures composed of W-centered octahedra with corner sharing through oxygen atoms, and, in the case of  $\text{W}_2\text{O}_3\text{I}_4$ , edge sharing through iodine atoms. Crystals of both compounds are hardly distinguishable by visual inspection, and their coexistence can cause confusion in the assignment of X-ray powder diffraction patterns. The refined crystal structure of  $\text{WO}_2\text{I}_2$  is a parent structure of  $\text{WO}_2\text{Cl}_2$ , earlier reported with a related, but heavily disordered structure. The intercalation compounds  $\text{A}_x\text{WO}_2\text{Cl}_2$  (A = Li–Cs),<sup>17,18</sup> can also be considered to be derivatives of the  $\text{WO}_2\text{I}_2$  structure.

The full role of the new compound  $\text{W}_2\text{O}_3\text{I}_4$  in the chemical transport reaction of tungsten is outside the scope of this work. According to our studies it is clear that thermal treatment of  $\text{WO}_2\text{I}_2$  (formally  $\text{W}^{6+}$ ) leads to  $\text{W}_2\text{O}_3\text{I}_4$  ( $\text{W}^{5+}$ ) first, and then to  $\text{WO}_2$  ( $\text{W}^{4+}$ ). There is some evidence that  $\text{W}_2\text{O}_3\text{I}_4$  may have been erroneously assigned as “ $\text{WO}_2\text{I}$ ” in earlier studies which did not report analytical or structural data.<sup>8,19,20</sup> DFT calculations were used to determine the electronic structures of  $\text{WO}_2\text{I}_2$  and  $\text{W}_2\text{O}_3\text{I}_4$ . Both were found to be metals due to the covalent nature of the W–O bonds. The addition of iodine to  $\text{WO}_2\text{I}_2$ , forming  $\text{W}_2\text{O}_3\text{I}_4$ , does not lead to a large change in the formal charge of the tungsten atoms but shifts the Fermi level downwards and leads to increased metallicity.

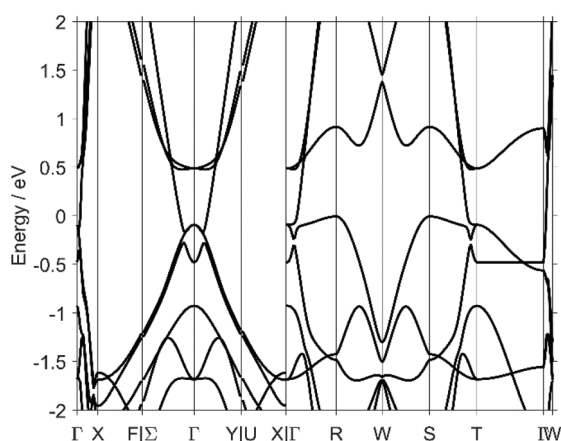


Fig. 4 The electronic band structure of  $\text{WO}_2\text{I}_2$ . Special points in and paths through the Brillouin zone were chosen following ref. 14.

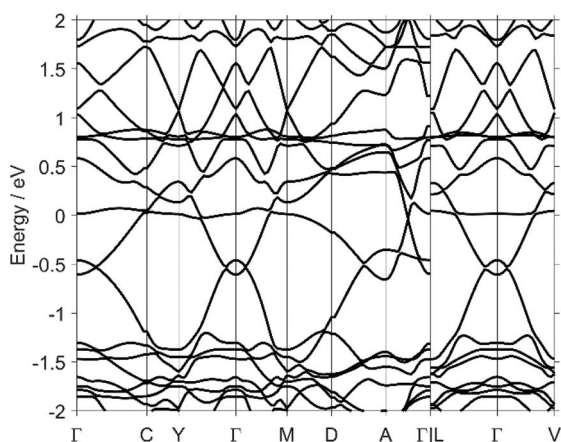


Fig. 5 The electronic band structure of  $\text{W}_2\text{O}_3\text{I}_4$ . Special points in and paths through the Brillouin zone were chosen following ref. 14.

## Conflicts of interest

There are no conflicts to declare.

## Acknowledgements

Support by the state of Baden-Württemberg through bwHPC and the German Research Foundation (DFG) through grant no. INST 40/575-1 FUGG (JUSTUS 2 cluster), and through the DFG grant ME 914/32-1 is gratefully acknowledged.

## Notes and references

- 1 E. Lassner and W.-D. Schubert, *Tungsten*, Springer New York, 1999.

- 2 M. Ströbele, C. Castro, R. F. Fink and H.-J. Meyer, *Angew. Chem., Int. Ed. Engl.*, 2016, **55**, 4814–4817.
- 3 M. Binnewies, *Chem. Unserer Zeit*, 1986, **20**, 141–145.
- 4 J. Tillack, P. Eckerlin and J. H. Dettingmeijer, *Angew. Chem., Int. Ed. Engl.*, 1966, **5**, 421–421.
- 5 J. H. Dettingmeijer and B. Meinders, *Z. Anorg. Allg. Chem.*, 1968, **357**, 1–10.
- 6 L. O. Atovmyan, Z. G. Aliev and B. M. Tarakanov, *J. Struct. Chem.*, 1969, **9**, 985–986.
- 7 H. Oppermann, G. Kunze and G. A. Kokovin, *Z. Anorg. Allg. Chem.*, 1982, **490**, 153–158.
- 8 J. Tillack, *Z. Anorg. Allg. Chem.*, 1968, **357**, 11–24.
- 9 B. Krebs, C. Brendel and H. Schäfer, *Z. Anorg. Allg. Chem.*, 1987, **553**, 127–135.
- 10 I. Abrahams, J. L. Nowinski, P. G. Bruce and V. C. Gibson, *J. Solid State Chem.*, 1993, **102**, 140–145.
- 11 D. R. Taylor, J. C. Calabrese and E. M. Larsen, *Inorg. Chem.*, 1977, **16**, 721–722.
- 12 V. Kolesnichenko, D. C. Swenson and L. Messerle, *Inorg. Chem.*, 1998, **37**, 3257–3262.
- 13 P. Schneiderhan, P. Schmidt, M. Ströbele, C. P. Romao and H.-J. Meyer, *Cryst. Growth Des.*, 2020, **20**, 3780–3784.
- 14 Y. Hinuma, G. Pizzi, Y. Kumagai, F. Oba and I. Tanaka, *Comput. Mater. Sci.*, 2017, **128**, 140–184.
- 15 S. Raj, H. Matsui, S. Souma, T. Sato, T. Takahashi, A. Chakraborty, D. D. Sarma, P. Mahadevan, S. Oishi and W. H. McCarroll, *Phys. Rev. B: Condens. Matter Mater. Phys.*, 2007, **75**, 155116.
- 16 M. Thomas, M. Brehm and B. Kirchner, *Phys. Chem. Chem. Phys.*, 2015, **17**, 3207–3213.
- 17 J. F. Ackerman, *Mater. Res. Bull.*, 1988, **23**, 165–169.
- 18 A. I. Smith, H. V. Wladkowski, Z. H. Hecht, Y. She, S. Kattel, P. I. Samarawickrama, S. R. Rich, J. R. Murphy, J. Tian, J. F. Ackerman, W. D. Rice, E. B. Hulley and B. M. Leonard, *Chem. Mater.*, 2020, **32**, 10482–10488.
- 19 H. Schäfer, D. Giegling and K. Rinke, *Z. Anorg. Allg. Chem.*, 1968, **357**, 25–29.
- 20 S. K. Gupta, *J. Phys. Chem.*, 1969, **73**, 4086–4094.

# **Supporting Information**

*for*

## **W<sub>2</sub>O<sub>3</sub>I<sub>4</sub> and WO<sub>2</sub>I<sub>2</sub>: Metallic Phases in the Chemical Transport Reaction of Tungsten**

Manuel Löber, Markus Ströbele, Carl P. Romao, and Hans-Jürgen Meyer\*

Section for Solid State and Theoretical Inorganic Chemistry, Institute of Inorganic Chemistry, University of Tübingen, Auf der Morgenstelle 18, 72076 Tübingen, Germany.

## Experimental Section

**Synthesis of  $\text{WO}_2\text{I}_2$ :**<sup>1</sup> W,  $\text{WO}_3$  and  $\text{I}_2$  were mixed and pestled in an agate mortar under dry argon atmosphere in a 1 : 2 : 6 molar ratio (100 mg total mass). The reaction mixture was transferred to a silica ampoule (length approx. 15 cm) and fused under vacuum. The silica ampoule was placed in a tube furnace with the reaction mixture in the middle of the tube. The ampoule was heated in a temperature gradient of 800 °C (middle of the tube) to 300 °C at 2 °C/min for 5 h, until cooling to room temperature at 2 °C/min. The crystalline product ( $\text{WO}_2\text{I}_2$ ) was obtained as metallic lustrous needle-shaped plates at the cooler section of the ampoule.

**Synthesis of  $\text{W}_2\text{O}_3\text{I}_4$ :** Ground powder of (50 mg)  $\text{WO}_2\text{I}_2$  was placed in a silica ampoule (length approx. 7 cm) under dry argon atmosphere. The silica ampoule was fused under vacuum and placed into a crucible furnace. The ampoule was heated at 2 °C/min to 380 °C and remained there for 48 h, until cooling to room temperature at 2 °C/min. The compound ( $\text{W}_2\text{O}_3\text{I}_4$ ) was obtained as black needles with metallic luster.

**Computational methods:** Density functional theory calculations were performed with the DFT software package Abinit (v. 9.2.2).<sup>2</sup> The projector-augmented wave (PAW) method<sup>3</sup> was used with the Perdew–Burke–Erzenhof exchange correlation functional<sup>4</sup> and the vdW-DFT-D3 dispersion correction.<sup>5</sup> PAW datasets were used as received from the Abinit repository. Methfessel–Paxton smearing was used to determine the occupation of metallic bands.<sup>6</sup> Plane-wave basis set cutoffs and  $\mathbf{k}$ -point grid spacings were chosen following convergence studies (to 1% in pressure). Structural relaxation was performed prior to calculations of electronic band structures. Example input files are available as Supporting Information.

### **Powder X-ray Diffraction:**

PXRD patterns of well ground powders were recorded using a StadiP diffractometer (Stoe, Darmstadt) with Ge-monochromated  $\text{Cu-K}\alpha_1$  radiation and a Mythen1 Detector.

### **Single-Crystal X-ray Diffraction:**

Single crystals of  $\text{WO}_2\text{I}_2$  and  $\text{W}_2\text{O}_3\text{I}_4$  were collected and placed on the tip of a cryoloop. Data were recorded using a Rigaku XtaLAB Synergy-S single-crystal X-ray diffractometer equipped with HyPix-6000HE detector and monochromated  $\text{Mo-K}\alpha$  radiation ( $\lambda = 0.7107 \text{ \AA}$ ) at 100 K. The X-ray intensities were corrected for absorption with numerical method using CrysAlisPro 1.171.41.80a (Rigaku Oxford Diffraction, 2021). The structure was solved by direct methods (SHELXS),<sup>7</sup> and full-matrix least-squares structure refinements, performed with SHELXL-2014<sup>8</sup> implemented in Olex2 1.3-ac4.<sup>9</sup>

## Results

**Table S1.** selected Crystal and structure refinement data of  $\text{WO}_2\text{I}_2$  and  $\text{W}_2\text{O}_3\text{I}_4$ , recorded at 100 K.

Empirical formula	$\text{WO}_2\text{I}_2$	$\text{W}_2\text{O}_3\text{I}_4$
CSD No.	2004434	2054404
Formula weight / $\text{g}\cdot\text{mol}^{-1}$	469.65	923.30
Temperature / K	100	100
Wavelength/ pm	71.073	71.073
Crystal system	Orthorhombic	Monoclinic
Space group	<i>Immm</i>	<i>I2/m</i>
<i>a</i> / pm	374.84(3)	924.84(6)
<i>b</i> / pm	390.49(3)	748.82(4)
<i>c</i> / pm	1662.8(1)	1336.48(8)
$\beta/^\circ$		98.810(6)
Volume / $\text{nm}^3$	0.24339(4)	0.91464(10)
Z	2	4
$\mu$ (Mo-K $\alpha$ ) / $\text{mm}^{-1}$	36.26	38.58
Density (calculated) / $\text{g}\cdot\text{cm}^{-3}$	6.41	6.71
Theta range for data collection / $^\circ$	4.90 to 25.93	3.52 to 26.02
Total number of reflections	873	9630
Refined parameters	14	48
$R_1$	0.0181	0.0297
$wR_2$	0.0403	0.0672
Goodness-of-fit on $F^2$	1.071	1.048

**Table S2.** Atomic coordinates, Wyckoff positions (Wyck) and equivalent isotropic displacement parameters (in  $\text{pm}^2 \times 10^{-1}$ ) for  $\text{WO}_2\text{I}_2$ .

atom	Wyck	x	y	z	$U(\text{eq})^a$
W1	2a	1/2	1/2	1/2	39(1)
I1	4i	1/2	1/2	0.66072(4)	12(1)
O1	2d	1/2	0	1/2	6(2)
O2	2b	0	1/2	1/2	18(2)

<sup>a)</sup>  $U(\text{eq})$  is defined as one-third of the trace of the orthogonalized  $U^{ij}$  tensor.

**Table S3.** Atomic coordinates, Wyckoff positions (Wyck) and equivalent isotropic displacement parameters (in  $\text{pm}^2 \times 10^{-1}$ ) for  $\text{W}_2\text{O}_3\text{I}_4$ .

atom	Wyck	x	y	z	$U(\text{eq})^a$
W1	4e	1/4	1/4	1/4	4(1)
W2	4g	1/2	0.2927(1)	1/2	5(1)
I1	4i	0.3420(1)	0	0.5661(1)	7(1)
I2	4i	0.6923(1)	1/2	0.4190(1)	8(1)
I3	8j	0.0142(1)	0.2482(1)	0.3483(1)	9(1)
O1	8j	0.3741(6)	0.2866(7)	0.3761(4)	8(1)
O2	4i	0.2261(10)	1/2	0.2351(7)	18(2)

<sup>a)</sup>  $U(\text{eq})$  is defined as one-third of the trace of the orthogonalized  $U^{ij}$  tensor.

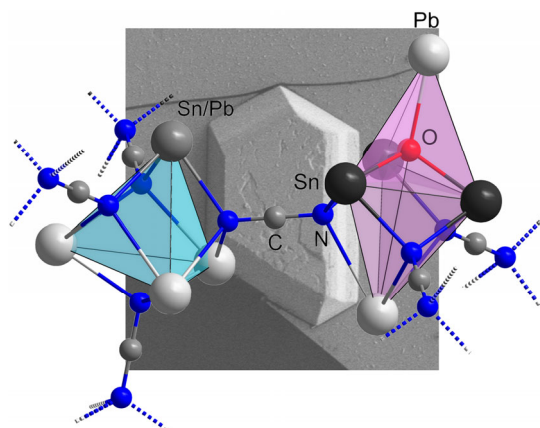
## References

- 1 J. Tillack, P. Eckerlin and J. H. Dettingmeijer, *Angew. Chem. Int. Ed.*, 1966, **5**, 421-421.
- 2 A. H. Romero, D. C. Allan, B. Amadon, G. Antonius, T. Applencourt, L. Baguet, J. Bieder, F. Bottin, J. Bouchet, E. Bousquet, F. Bruneval, G. Brunin, D. Caliste, M. Côté, J. Denier, C. Dreyer, P. Ghosez, M. Giantomassi, Y. Gillet, O. Gingras, D. R. Hamann, G. Hautier, F. Jollet, G. Jomard, A. Martin, H. P. C. Miranda, F. Naccarato, G. Petretto, N. A. Pike, V. Planes, S. Prokhorenko, T. Rangel, F. Ricci, G.-M. Rignanese, M. Royo, M. Stengel, M. Torrent, M. J. van Setten, B. Van Troeye, M. J. Verstraete, J. Wiktor, J. W. Zwanziger and X. Gonze, *J. Chem. Phys.*, 2020, **152**, 124102.
- 3 M. Torrent, F. Jollet, F. Bottin, G. Zérah and X. Gonze, *Comput. Mater. Sci.*, 2008, **42**, 337-351.
- 4 J. P. Perdew, K. Burke and M. Ernzerhof, *Phys. Rev. Lett.*, 1996, **77**, 3865.
- 5 S. Grimme, J. Antony, S. Ehrlich and H. Krieg, *J. Chem. Phys.*, 2010, **132**, 154104.
- 6 M. Methfessel and A. T. Paxton, *Phys. Rev. B*, 1989, **40**, 3616.
- 7 M. Sheldrick, University of Göttingen, 1997.
- 8 G. M. Sheldrick, *Acta Cryst.*, 2015, **C71**, 3-8.
- 9 O. V. Dolomanov, L. J. Bourhis, R. J. Gildea, J. A. K. Howard and H. Puschmann, *J. Appl. Crystallogr.*, 2009, **42**, 339-341.



# Publication 6

Synthesis and crystal structure of  $\text{Pb}_{14.66}\text{Sn}_{7.34}\text{Br}_{26}(\text{CN}_2)_7\text{O}_2$ , a complex member of group 14 carbodiimides



<https://doi.org/10.1002/zaac.202100273>

Reprinted with permission from

*Z. Anorg. Allg. Chem.* **2021**, 647, 1973–1977

Copyright © 2021 Wiley-VCH GmbH



# Synthesis and crystal structure of $\text{Pb}_{14.66}\text{Sn}_{7.34}\text{Br}_{26}(\text{CN}_2)_7\text{O}_2$ , a complex member of group 14 carbodiimides

Manuel Löber,<sup>[a]</sup> Markus Ströbele,<sup>[a]</sup> and Hans-Jürgen Meyer\*<sup>[a]</sup>

A mixed lead/tin bromide carbodiimide oxide was synthesized by solid-state reaction between  $\text{Pb}(\text{CN}_2)$ ,  $\text{PbBr}_2$ ,  $\text{SnBr}_2$  and  $\text{SnO}$  at 400 °C. Its monoclinic crystal structure was solved and refined in the space group  $C2/m$  by single-crystal X-ray diffraction from a yellow single crystal. One crystallographic site was found to be occupied by both tin and lead, in agreement with the results

of energy-dispersive X-ray spectroscopy (EDX). The crystal structure comprises a complex network of tin/lead tetrahedra and tin/lead trigonal bipyramids linked by NCN units. In contrast to  $\text{Pb}(\text{CN}_2)$ , where the NCN ion is present as a cyanamide moiety, IR-spectroscopy of the title compound revealed the carbodiimide character of the NCN ion.

## Introduction

Metal dinitridocarbonates have been established with many different elements. The large number of new compounds obtained in recent decades is due to the fact that compounds with the  $[\text{NCN}]^{2-}$  ion have previously gained less attention compared to *simple* ions, but nevertheless they offer a variety of interesting properties, such as luminescence,<sup>[1]</sup> magnetism,<sup>[2]</sup> negative thermal expansion,<sup>[3]</sup> semiconductivity<sup>[4]</sup> or electrochemical properties.<sup>[5]</sup>

A characteristic feature of this group of compounds is the appearance of the  $[\text{NCN}]^{2-}$  ion as cyanamide moiety  $[\text{N}=\text{C}-\text{N}]^{2-}$  or as carbodiimide moiety  $[\text{N}=\text{C}=\text{N}]^{2-}$ . Its preferred shape depends on the hardness of the counter cation and the individual coordination numbers of terminal nitrogen atoms of the  $[\text{NCN}]^{2-}$  ions. For hard cations, such as  $\text{Li}^+$ ,  $\text{Na}^+$ ,  $\text{Mg}^{2+}$ ,  $\text{Ca}^{2+}$ , the carbodiimide form is preferred,<sup>[6]</sup> while for soft cations, such as  $\text{Hg}^{2+}$ ,  $\text{Pb}^{2+}$ ,  $\text{Ag}^+$ , the cyanamide form is favored.<sup>[7]</sup>

So far, the largest number of compounds has been described as rare earth dinitridocarbonates,<sup>[8]</sup> followed by a significant number of transition metal<sup>[2a,b, 9]</sup> and main group<sup>[6a,c,d,10]</sup> compounds, appearing as binary, ternary, quaternary, or even more complex compounds, with varying numbers of cations and anions.<sup>[8b,11]</sup> Furthermore some polyatomic anions, such as  $(\text{CN})^-$ ,<sup>[12]</sup>  $(\text{C}_2\text{N})^{3-}$ <sup>[13]</sup> or  $(\text{SiO}_4)^{4-}$ <sup>[14]</sup> can also be combined with the  $(\text{CN}_2)^{2-}$  ion.

During the past years a remarkable number of tin dinitridocarbonates has been reported. Among them are divalent tin compounds such as  $\text{Sn}(\text{CN}_2)$ ,  $\text{Sn}_4\text{Cl}_2(\text{CN}_2)_3$ ,<sup>[4b]</sup>  $\text{Sn}_2\text{O}(\text{CN}_2)$ ,<sup>[4a]</sup>  $\text{Sn}_9\text{O}_5\text{Cl}_4(\text{CN}_2)_2$ <sup>[15]</sup> and tetravalent tin compounds as  $\text{A}_2\text{Sn}(\text{CN}_2)_3$ ,<sup>[16]</sup> and  $\text{A}_2\text{MnSn}_2(\text{CN}_2)_6$ <sup>[17]</sup> ( $\text{A} = \text{Li}, \text{Na}$ ), all obtained by solid-state metathesis (SSM)<sup>[18]</sup> reactions. Some lead compounds were obtained already earlier, which are  $\text{Pb}(\text{CN}_2)$ ,<sup>[10b]</sup>  $\text{APb}_2\text{Cl}_3(\text{CN}_2)$  ( $\text{A} = \text{Li}, \text{Na}, \text{Ag}$ ),  $\text{LiPb}_2\text{Br}_3(\text{CN}_2)$  and  $\text{LiPbCl}(\text{CN}_2)$ <sup>[19]</sup> and  $\text{K}_{12}\text{Pb}_{51}\text{Cl}_{54}(\text{CN}_2)_{30}$ ,<sup>[20]</sup>  $\text{Pb}(\text{CN}_2)$ , at first crystallized from aqueous solution, was recently also synthesized metathetically.<sup>[21]</sup>

Motivated by the variety of these group 14 compounds, we performed studies in tin and lead dinitridocarbonate systems and report the hitherto unknown mixed lead/tin compound  $\text{Pb}_{14.66}\text{Sn}_{7.34}\text{Br}_{26}(\text{CN}_2)_7\text{O}_2$ , which is subject of this work.

## Results and Discussion

**Synthesis of  $\text{Pb}_{14.66}\text{Sn}_{7.34}\text{Br}_{26}(\text{CN}_2)_7\text{O}_2$ .** After the binary tin carbodiimide is known as  $\text{Sn}(\text{CN}_2)$  with divalent tin, a corresponding tin (IV) carbodiimide is likely to exist as  $\text{Sn}(\text{CN}_2)_2$ . This compound, if existent, would parallel the tin oxide chemistry ( $\text{SnO}$ ,  $\text{SnO}_2$ ) and could be an interesting material for reversible (lithium ion) intercalation, once an appropriate structure would be given. After  $\text{Li}_2\text{Sn}(\text{CN}_2)_3$  has been established with tetravalent tin by reacting tin halide with lithium carbodiimide, we attempted reactions with tin halide and  $\text{Pb}(\text{CN}_2)$ , revealing the title compound.

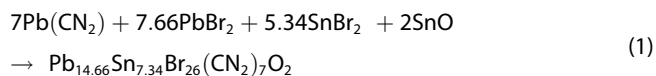
Reactions of mixtures of  $\text{SnBr}_4$  and  $\text{Pb}(\text{CN}_2)$  were heated in fused silica tubing at 500 °C. Cooled samples revealed yellow platelet-shaped single crystals, which could be identified as  $\text{Pb}_{14.66}\text{Sn}_{7.34}\text{Br}_{26}(\text{CN}_2)_7\text{O}_2$ . Tin was obviously reduced from +4 to +2 as a result of the reducing nature of the  $[\text{NCN}]^{2-}$  ion. The initial observation of  $\text{Pb}_{14.66}\text{Sn}_{7.34}\text{Br}_{26}(\text{CN}_2)_7\text{O}_2$  as a minority phase is believed to originate from an oxide impurity, presumably contained in the starting mixture, although not detected by PXRD. The title compound was finally obtained as phase pure sample (according to PXRD patterns), when reacting appropri-

[a] M. Löber, Dr. M. Ströbele, Prof. Dr. H.-J. Meyer  
Section for Solid State and Theoretical Inorganic Chemistry  
Institute of Inorganic Chemistry, Eberhard Karls University Tübingen  
Auf der Morgenstelle 18, D-72076 Tübingen, Germany  
E-mail: juergen.meyer@uni-tuebingen.de

Supporting information for this article is available on the WWW under <https://doi.org/10.1002/zaac.202100273>

© 2021 The Authors. *Zeitschrift für anorganische und allgemeine Chemie* published by Wiley-VCH GmbH. This is an open access article under the terms of the Creative Commons Attribution Non-Commercial NoDerivs License, which permits use and distribution in any medium, provided the original work is properly cited, the use is non-commercial and no modifications or adaptations are made.

ate amounts of  $\text{Pb}(\text{CN}_2)$  with  $\text{PbBr}_2$ ,  $\text{SnBr}_2$  and  $\text{SnO}$ , at  $400^\circ\text{C}$ , in accordance with reaction (1).



### Crystal structure of $\text{Pb}_{14.66}\text{Sn}_{7.34}\text{Br}_{26}(\text{CN}_2)_7\text{O}_2$

The crystal structure of  $\text{Pb}_{14.66}\text{Sn}_{7.34}\text{Br}_{26}(\text{CN}_2)_7\text{O}_2$  was solved and refined in the monoclinic space group  $C2/m$ , based on single-crystal X-ray diffraction data. An electron micrograph of a single crystal of  $\text{Pb}_{14.66}\text{Sn}_{7.34}\text{Br}_{26}(\text{CN}_2)_7\text{O}_2$  is shown in Figure 1. Selected details of the single-crystal measurement and the refinement are displayed in Table 1. During the structure refinement process, it was noticed that tin and lead share one crystallographic site ( $\text{Sn3}/\text{Pb3}$ ) at a 0.67/0.33 ratio. This ratio is

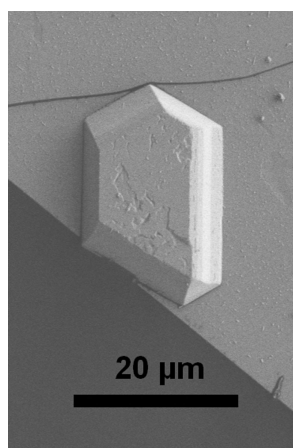


**Figure 1.** Electron micrograph of a single crystal of  $\text{Pb}_{14.66}\text{Sn}_{7.34}\text{Br}_{26}(\text{CN}_2)_7\text{O}_2$ .

**Table 1.** Selected crystallographic and structure refinement data of  $\text{Pb}_{14.66}\text{Sn}_{7.34}\text{Br}_{26}(\text{CN}_2)_7\text{O}_2$ , recorded at room temperature.

Empirical formula	$\text{Pb}_{14.66}\text{Sn}_{7.34}\text{Br}_{26}(\text{CN}_2)_7\text{O}_2$
CSD code	2059414
Formula weight (g/mol)	6298.90
Wavelength (Mo–K $\alpha$ ) (Å)	0.71073
Crystal system	Monoclinic
Space group	$C2/m$
Unit cell dimensions (Å)	$a = 17.8924(5)$ $b = 10.3062(2)$ $c = 18.4034(5)$
(°)	$\beta = 99.518(2)$
Volume (Å <sup>3</sup> )	3346.9(2)
Z	2
Density (calculated) (g/cm <sup>3</sup> )	6.25
2 Theta range for data collection (°)	4.48 to 51.36
Total number of reflections	22967
Refined parameters	188
R1, wR2	0.028, 0.056
GOOF	1.143

consistent with results of EDX analyses of the compound, which revealed an overall tin to lead ratio of 2 (Pb) to 1 (Sn) for the compound and a metal (Pb+Sn) to Br ratio of 1 to 1.2 (see SI).

In the crystal structure of  $\text{Pb}_{14.66}\text{Sn}_{7.34}\text{Br}_{26}(\text{CN}_2)_7\text{O}_2$  two distinct tin and six distinct lead sites are present (in addition to one shared tin/lead site). Wyckoff positions, site occupation factors, atomic coordinates and isotropic displacement parameters of  $\text{Pb}_{14.66}\text{Sn}_{7.34}\text{Br}_{26}(\text{CN}_2)_7\text{O}_2$  are given in the SI.

The two tin sites are very similar and are both coordinated by five bromine, two  $\text{CN}_2$  units and one oxygen atom, with only minor differences in bond distances and angles. Both coordination environments can be considered as bicapped prismatic and are, due to different ligands and bond distances of Sn–Br (3.35–3.52 Å), Sn–N (2.34–2.36 Å) and Sn–O (2.18–2.20 Å), heavily distorted.

Among the six distinct lead sites, Pb1, Pb2 and Pb4 are all coordinated by six bromine and three  $\text{CN}_2$  units. Their coordination environment can be considered from a tricapped trigonal antiprism. Pb5 is coordinated by seven bromine atoms in a distorted capped octahedral fashion. Pb6 and Pb7 can be well derived from a cubic coordination geometry, with either 8 bromine (Pb6) or seven bromine and one oxygen atoms leading to a heavier distortion of the coordination of Pb7. The mixed tin/lead site is coordinated by three bromine atoms and three  $\text{CN}_2$  units. All nine distinct coordination environments of tin and lead are depicted in Figure 2.

The three crystallographically distinct NCN units are all coordinated pseudo-octahedrally by six metal atoms, as shown in Figure 3. This coordination environment of the NCN ion differs from those in  $\text{Sn}(\text{CN}_2)$ ,<sup>[4b]</sup>  $\text{Sn}_2\text{O}(\text{CN}_2)$ ,<sup>[4a]</sup>  $\text{Sn}_4\text{Cl}_2(\text{CN}_2)_3$ <sup>[4b]</sup> and  $\text{Sn}_5\text{O}_5\text{Cl}_4(\text{CN}_2)_2$ ,<sup>[15]</sup> where a fourfold coordination of the  $\text{NCN}_2$  units is present. The bond distances of Pb–N are between 2.54 and 2.82 Å, being somewhat longer than in the related lead compounds  $\text{Pb}(\text{CN}_2)$  (2.31–2.62 Å),<sup>[10b]</sup>  $\text{LiPb}_2\text{Cl}_3(\text{CN}_2)$  (2.54 Å) and  $\text{LiPbCl}(\text{CN}_2)$  (2.39–2.70 Å).<sup>[19]</sup> The distances between Sn and N are 2.34–2.36 Å and comparable to those in related tin compounds. The shared tin/lead site has a metal to N distance

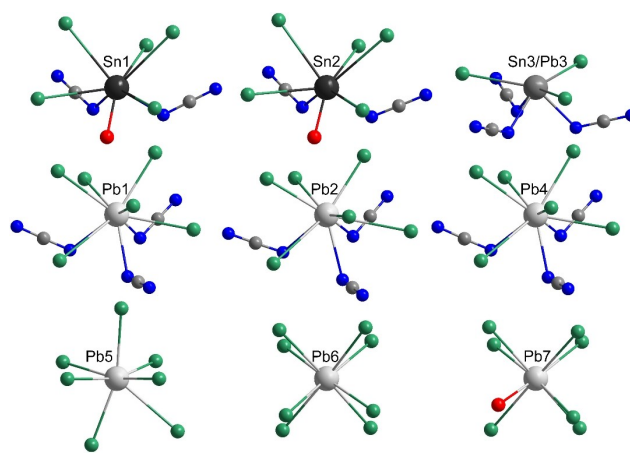


**Figure 2.** Different coordination environments of tin and lead in  $\text{Pb}_{14.66}\text{Sn}_{7.34}\text{Br}_{26}(\text{CN}_2)_7\text{O}_2$ . Bromine is shown in green, oxygen in red, carbon in dark grey and nitrogen in blue.

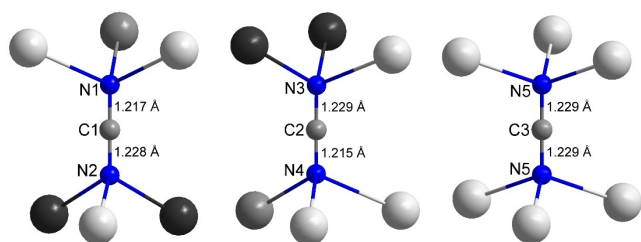


**Figure 3.** Three crystallographically different  $\text{CN}_2$  units, coordinated all pseudo octahedrally by either tin (black), lead (light grey) or a shared tin/lead site (dark grey).

of 2.42 Å, which can be considered as an average bond distance of both lead and tin, concerning the unequal occupation of this site (0.67 to 0.33).

The C–N bond distances of the three crystallographically distinct NCN units vary between 1.22 Å and 1.23 Å. Despite this minor difference in length of the two CN bonds, all three  $\text{CN}_2$  units can be mainly considered as carbodiimide moieties, as confirmed by IR-measurements of the title compound, which showed the asymmetric stretching vibration of the NCN unit at  $1927\text{ cm}^{-1}$  and the CN bending vibration at  $643\text{ cm}^{-1}$ . Both similar to vibrational spectra of other tin carbodiimide compounds.<sup>[4,15]</sup> Furthermore, the IR spectra revealed a bending vibration at  $421\text{ cm}^{-1}$ , that can be assigned to the N–Sn–N body. The symmetric stretching vibrations, which are IR forbidden for the symmetric carbodiimide ion, are hardly visible in the IR-spectrum (at  $1228\text{ cm}^{-1}$  and  $1322\text{ cm}^{-1}$ ), confirming the predominant carbodiimide character of the NCN ion. However, these symmetric stretching vibrations are strongly pronounced in the spectra of  $\text{Pb}(\text{CN}_2)$  (at  $1215\text{ cm}^{-1}$  and  $1305\text{ cm}^{-1}$ ), which was recorded for comparison (see SI).

The overall crystal structure can be described by two distinct motifs, as shown in Figure 4 (top). One is a tetrahedron (blue) consisting of three lead atoms (Pb1, Pb4) and the shared lead/tin atom (Pb3/Sn3), that are face-capped by four  $\text{CN}_2$  units in  $[(\text{Pb}/\text{Sn})_4(\text{CN}_2)_4]$ . The second motif is a distorted trigonal bipyramid (pink), with three tin atoms in the plane (Sn1, Sn2) and two lead atoms (Pb2, Pb7) at each of the two tips. The lower tetrahedron in Figure 4 (top) of this trigonal bipyramid is face-capped by three  $\text{CN}_2$  units, while the upper tetrahedron is oxide-centered, coordinated by tin and lead. The connectivity pattern of the individual polyhedra in the structure can be envisioned from Figure 4 (bottom).

These polyhedra form a layered arrangement, as indicated in Figure 5, in which one tetrahedron is connected to two trigonal bipyramids and, along the *c*-axis, to a second-layer tetrahedron.

This double layered arrangement alternates with two layers of trigonal bipyramids, connected not by NCN units but by bromide ions.

As already shown in Figure 2, bromine is coordinating all nine different metal sites and is either coordinated by four, five or six metal atoms. The arrangement of bromide and the additional lead atoms (Pb5 and Pb6) are not considered in

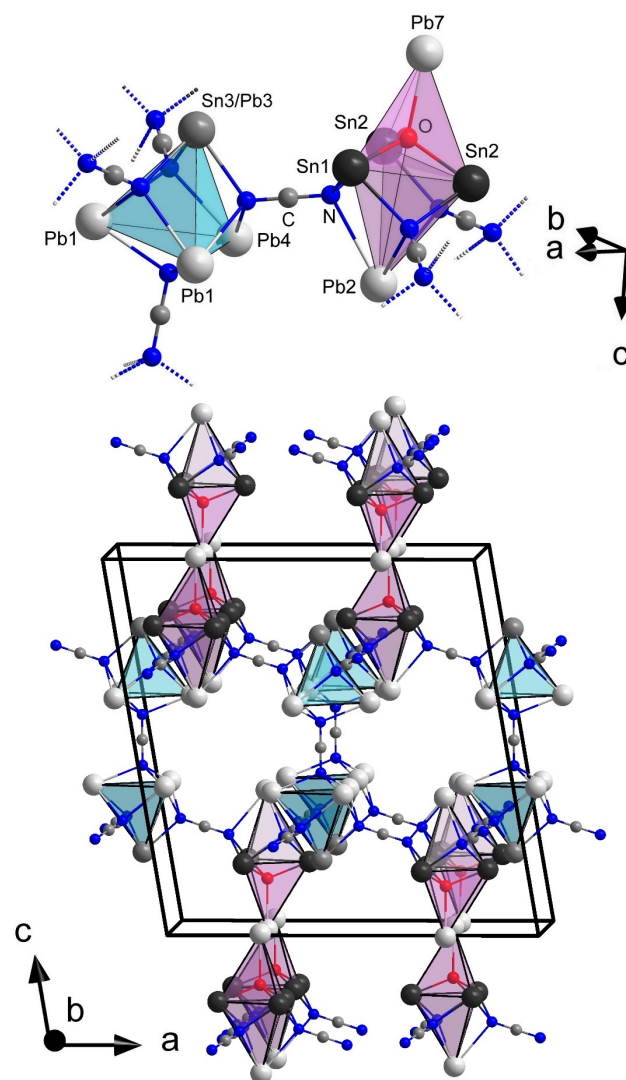


**Figure 4.** Top: dimeric fragment consisting of a tin/lead tetrahedron (blue) and a tin/lead trigonal bipyramid (pink) linked by a  $\text{CN}_2$  unit. Dashed lines indicate further linkage to equivalent units. Bottom: Perspective view on the *ac* plane of the crystal structure of  $\text{Pb}_{1.466}\text{Sn}_{7.34}\text{Br}_{26}(\text{CN}_2)_7\text{O}_2$ , emphasizing the arrangement of the upper motif. Bromine atoms are not considered here.

Figures 4 and 5, to emphasize the two motifs and their bonding situation. However, a section of the structure, including the bromine atoms, is available in the SI.

## Conclusion

Reactions between lead carbodiimide and tin(IV) bromide led to the formation of a hitherto unknown lead-tin bromide carbodiimide oxide that could later synthesized phase pure by using appropriate amounts of  $\text{Pb}(\text{CN}_2)$ ,  $\text{PbBr}_2$ ,  $\text{SnBr}_2$  and  $\text{SnO}$ .

The crystal structure was determined by single-crystal X-ray diffraction, revealing two specific features. A tetrahedron and a

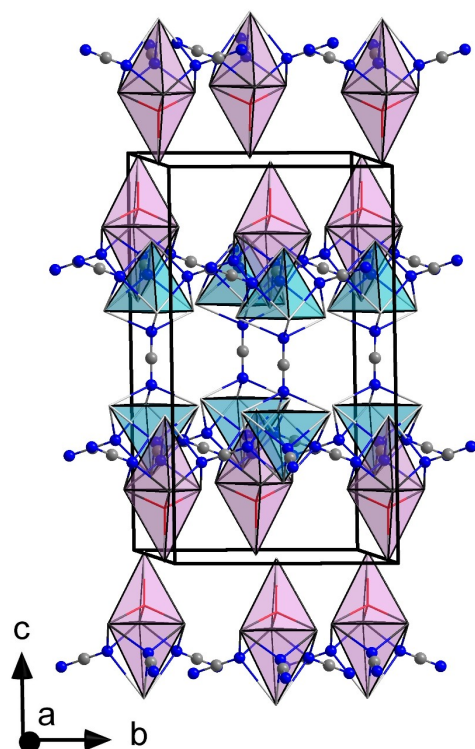


**Figure 5.** Perspective view along the *cb* plane. Polyhedra are displayed without atoms, to highlight the layered arrangement and to point out the linkage via NCN units.

trigonal bipyramid consisting of tin and lead, both face-capped and linked by carbodiimide ions. Among the nine crystallographically distinct metal sites, one position is shared by both lead and tin. EDX measurements confirmed the formula  $\text{Pb}_{14.66}\text{Sn}_{7.34}\text{Br}_{26}(\text{CN}_2)_7\text{O}_2$ , in accordance with the structure refinement. IR measurements showed only asymmetric stretching vibrations of the  $\text{CN}_2$  ion, verifying the carbodiimide character of the title compound. This work shows once again the diversity of the NCN ion and of the group 14 carbodiimide compounds, which could be synthesized and characterized especially in the last years.

The existence of Sn(IV) in binary tin carbodiimide as  $\text{Sn}(\text{CN}_2)_2$  is not yet established. The compound may be labile without the presence of an electropositive counter cation as present in  $\text{Li}_2\text{Sn}(\text{CN}_2)_3$  or  $\text{Li}_2\text{MnSn}_2(\text{CN}_2)_6$ .

## Experimental Section

**Synthesis of  $\text{Pb}_{14.66}\text{Sn}_{7.34}\text{Br}_{26}(\text{CN}_2)_7\text{O}_2$ .** The starting materials  $\text{Pb}(\text{CN}_2)$ , (synthesized as described in<sup>[10b]</sup>),  $\text{PbBr}_2$  (Sigma-Aldrich, 99.999%),  $\text{SnBr}_2$  (Sigma-Aldrich, p.a.) and  $\text{SnO}$  (Sigma-Aldrich, 99.99%) were mixed and ground in an agate mortar under dry argon atmosphere in a 7:7.66:5.34:2 molar ratio. The reaction mixture was transferred into a silica ampoule and sealed under vacuum. The mixture was heated to 400 °C at 2 K/min, kept there for 20 h and cooled to room temperature at 2 K/min. Yellow single

crystals of  $\text{Pb}_{14.66}\text{Sn}_{7.34}\text{Br}_{26}(\text{CN}_2)_7\text{O}_2$  could be obtained when heating a 2:1 molar mixture of  $\text{Pb}(\text{CN}_2)$  and  $\text{SnBr}_4$  (Sigma-Aldrich, 99%) to 500 °C, at 2 K/min, remained there for 20 h until cooling to room temperature at 0.1 K/min.  $\text{Pb}_{14.66}\text{Sn}_{7.34}\text{Br}_{26}(\text{CN}_2)_7\text{O}_2$  could be synthesized phase pure in accordance with a recorded PXRD pattern, given in the SI. The crystals and the powder could be treated in air.

## X-ray Diffraction

Powder X-ray diffraction (PXRD) pattern were recorded on a Stoe StadiP diffractometer (Stoe, Darmstadt) with Ge-monochromated  $\text{Cu-K}\alpha_1$  radiation and a Mythen1 Detector.

A single crystal of  $\text{Pb}_{14.66}\text{Sn}_{7.34}\text{Br}_{26}(\text{CN}_2)_7\text{O}_2$  was measured using a Stoe IPDS 2T single-crystal diffractometer (Stoe, Darmstadt) equipped with graphite-monochromated  $\text{Mo-K}\alpha$  radiation ( $\lambda = 0.71073 \text{ \AA}$ ). Intensities were corrected for Lorentz factors and polarization effects using IPDS software. Absorption correction was performed using the X-Red/X-Shape program of the Stoe software. The crystal structure was solved by direct methods (SHELXS) followed by full-matrix least-squares structure refinements using SHELXL-2014.<sup>[22]</sup>

**EDX measurements.** Energy dispersive X-ray spectroscopy (EDX) data were collected with a Hitachi SU8030 with a Bruker Quantax 70 EDX-System. The data were collected on eight different spots on several single-crystals.

## Acknowledgements

Funding of this work by the Deutsche Forschungsgemeinschaft (DFG) through grant ME 914/25-2 is gratefully acknowledged. We would like to thank Mrs. Elke Nadler (Uni Tübingen) for performing the EDX measurements and recording the electron micrographs. Open Access funding enabled and organized by Projekt DEAL.

## Conflict of Interest

The authors declare no conflict of interest.

**Keywords:** Carbodiimide · Tin · Lead · Crystal structure · EDX

- [1] J. Glaser, L. Unverfehrt, H. Bettentrup, G. Heymann, H. Huppertz, T. Jüstel, H.-J. Meyer, *Inorg. Chem.* **2008**, *47*, 10455–10460.
- [2] a) X. Liu, L. Stork, M. Speldrich, H. Lueken, R. Dronskowski, *Chem. Eur. J.* **2009**, *15*, 1558–1561; b) X. Tang, H. Xiang, X. Liu, M. Speldrich, R. Dronskowski, *Angew. Chem. Int. Ed.* **2010**, *49*, 4738–4742; *Angew. Chem.* **2010**, *122*, 4846–4850; c) K. B. Sterri, C. Besson, A. Houben, P. Jacobs, M. Hoelzel, R. Dronskowski, *New J. Chem.* **2016**, *40*, 10512–10519.
- [3] K. Dolabdjian, A. Kobald, C. P. Romao, H.-J. Meyer, *Dalton Trans.* **2018**, *47*, 10249–10255.
- [4] a) K. Dolabdjian, A. L. Görne, R. Dronskowski, M. Ströbele, H.-J. Meyer, *Dalton Trans.* **2018**, *47*, 13378–13383; b) M. Löber, K. Dolabdjian, M. Ströbele, C. P. Romao, H.-J. Meyer, *Inorg. Chem.* **2019**, *58*, 7845–7851.

- [5] M. T. Sougrati, J. J. Arayamparambil, X. Liu, M. Mann, A. Slabon, L. Stievano, R. Dronskowski, *Dalton Trans.* **2018**, 47, 10827–10832.
- [6] a) M. G. Down, M. J. Haley, P. Hubberstey, R. J. Pulham, A. E. Thunder, *J. Chem. Soc. Dalton Trans.* **1978**, 1407–1411; b) M. Becker, J. Nuss, M. Jansen, *Z. Anorg. Allg. Chem.* **2000**, 626, 2505–2508; c) U. Berger, W. Schnick, *J. Alloys Compd.* **1994**, 206, 179–184; d) M. A. Bredig, *J. Am. Chem. Soc.* **1942**, 64, 1730–1731.
- [7] X. Qiao, D. Mroz, A. J. Corkett, T. Bisswanger, R. Dronskowski, *Z. Anorg. Allg. Chem.* **2021**, 647, 496–499.
- [8] a) M. Neukirch, S. Tragl, H.-J. Meyer, *Inorg. Chem.* **2006**, 45, 8188–8193; b) L. Unverfehrt, M. Ströbele, J. Glaser, H.-J. Meyer, *Z. Anorg. Allg. Chem.* **2009**, 635, 1947–1952.
- [9] a) X. Liu, M. Krott, P. Müller, C. Hu, H. Lueken, R. Dronskowski, *Inorg. Chem.* **2005**, 44, 3001–3003; b) X. Liu, M. A. Wankeu, H. Lueken, R. Dronskowski, *Z. Naturforsch. B* **2005**, 60, 593–596; c) M. Krott, X. Liu, B. P. Fokwa, M. Speldrich, H. Lueken, R. Dronskowski, *Inorg. Chem.* **2007**, 46, 2204–2207.
- [10] a) R. Riedel, A. Greiner, G. Miehe, W. Dressler, H. Fuess, J. Bill, F. Aldinger, *Angew. Chem. Int. Ed.* **1997**, 36, 603–606; *Angew. Chem.* **1997**, 109, 657–660; b) X. Liu, A. Decker, D. Schmitz, R. Dronskowski, *Z. Anorg. Allg. Chem.* **2000**, 626, 103–105.
- [11] a) Y. Hashimoto, M. Takahashi, S. Kikkawa, F. Kanamaru, *J. Solid State Chem.* **1995**, 114, 592–594; b) O. Reckeweg, F. J. DiSalvo, *Angew. Chem. Int. Ed.* **2000**, 39, 412–414; *Angew. Chem.* **2000**, 112, 397–399; c) R. Srinivasan, M. Ströbele, H.-J. Meyer, *Inorg. Chem.* **2003**, 42, 3406–3411; d) R. Srinivasan, J. Glaser, S. Tragl, H. J. Meyer, *Z. Anorg. Allg. Chem.* **2005**, 631, 479–483; e) L. Unverfehrt, J. Glaser, M. Ströbele, S. Tragl, K. Gibson, H.-J. Meyer, *Z. Anorg. Allg. Chem.* **2009**, 635, 479–483; f) M. Kubus, D. Enseling, T. Jüstel, H. J. Meyer, *Eur. J. Inorg. Chem.* **2013**, 2013, 3195–3199.
- [12] U. Berger, W. Milius, W. Schnick, *Z. Anorg. Allg. Chem.* **1995**, 621, 2075–2082.
- [13] F. Jach, P. Höhn, Y. Prots, M. Ruck, *Eur. J. Inorg. Chem.* **2019**, 2019, 1207–1211.
- [14] M. Kubus, J. Glaser, A. Klonkowski, H.-J. Meyer, *Z. Anorg. Allg. Chem.* **2010**, 636, 991–995.
- [15] M. Löber, C. S. Geißenhöner, M. Ströbele, S. Indris, C. P. Romao, H.-J. Meyer, *Inorg. Chem.* **2019**, 58, 14560–14567.
- [16] K. Dolabdjian, C. Castro, H.-J. Meyer, *Eur. J. Inorg. Chem.* **2018**, 2018, 1624–1630.
- [17] A. J. Corkett, R. Dronskowski, *Dalton Trans.* **2019**, 48, 15029–15035.
- [18] H.-J. Meyer, *Dalton Trans.* **2010**, 39, 5973–5982.
- [19] K. Dolabdjian, H.-J. Meyer, *Z. Anorg. Allg. Chem.* **2017**, 643, 1898–1903.
- [20] X. Meng, F. Liang, W. Yin, Z. Lin, M. Xia, *New J. Chem.* **2019**.
- [21] X. Qiao, Z. Ma, D. Luo, A. J. Corkett, A. Slabon, A. Rokicinska, P. Kuśtrowski, R. Dronskowski, *Dalton Trans.* **2020**, 49, 14061–14067.
- [22] G. M. Sheldrick, *Acta Crystallogr.* **2015**, C71, 3–8.

Manuscript received: August 27, 2021

Revised manuscript received: September 14, 2021





# Zeitschrift für anorganische und allgemeine Chemie

Supporting Information

**Synthesis and crystal structure of  $\text{Pb}_{14.66}\text{Sn}_{7.34}\text{Br}_{26}(\text{CN}_2)_7\text{O}_2$ , a complex member of group 14 carbodiimides**

Manuel Löber, Markus Ströbele, and Hans-Jürgen Meyer\*

# Supporting Information for:

## Synthesis and crystal structure of $\text{Pb}_{14.66}\text{Sn}_{7.34}\text{Br}_{26}(\text{CN}_2)_7\text{O}_2$ , a complex member of group 14 carbodiimides

Manuel Löber, Markus Ströbele and Hans-Jürgen Meyer\*

Section for Solid State and Theoretical Inorganic Chemistry, Institute of Inorganic Chemistry,  
University of Tübingen, Auf der Morgenstelle 18, 72076 Tübingen, Germany

Corresponding Author

\*Prof. Dr. H.-Jürgen Meyer

Section for Solid State and Theoretical Inorganic Chemistry

Institute of Inorganic Chemistry

University of Tübingen

Auf der Morgenstelle 18

72076 Tübingen

E-mail: [juergen.meyer@uni-tuebingen.de](mailto:juergen.meyer@uni-tuebingen.de)

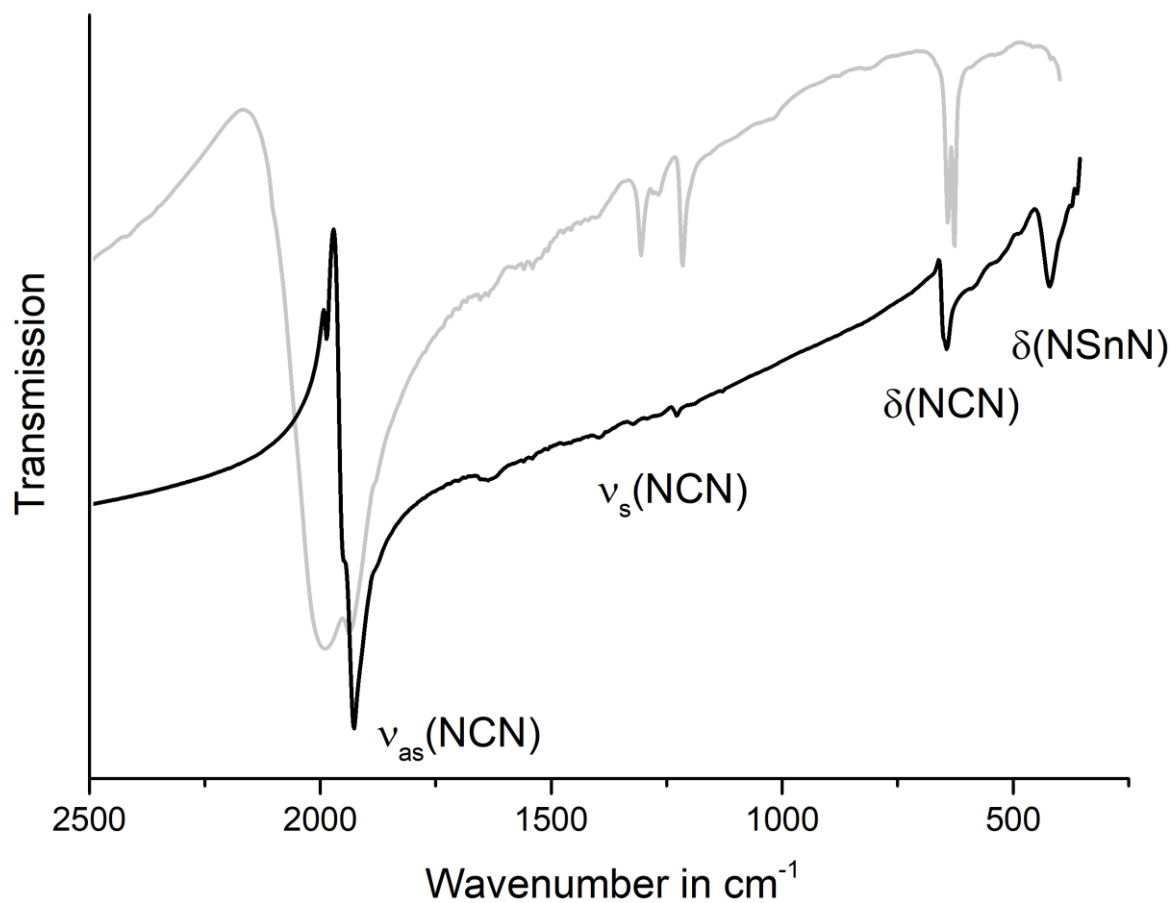


**Figure S1.** IR spectra of  $\text{Pb}_{14.66}\text{Sn}_{7.34}\text{Br}_{26}(\text{CN}_2)_7\text{O}_2$  (black) and  $\text{Pb}(\text{CN}_2)$  (grey).

**Table S1.** Ratio (At-%) of tin, lead and bromine determined by EDX on different single crystals.

	Tin to lead ratio	Metal (Pb+Sn) to Br ratio
Sample 1	2.26	1.26
Sample 2	2.16	1.22
Sample 3	1.95	1.11
Sample 4	1.87	1.21
Sample 5	1.91	1.16
Sample 6	2.12	1.22
Sample 7	1.90	1.24
Sample 8	2.33	1.21
Average	2.06	1.20

**Table S2.** Wyckoff positions, site occupation factors (s.o.f.), atomic coordinates and isotropic displacement parameters ( $U_{eq}$  in  $\text{\AA}^2$ ) of  $\text{Pb}_{14.66}\text{Sn}_{7.34}\text{Br}_{26}(\text{CN}_2)_7\text{O}_2$ .

Atom	Wyck.	s.o.f.	x	y	z	$U_{eq}^a$
Pb1	8i		0.04708(2)	0.30110(4)	0.38229(2)	0.02741(11)
Pb2	4i		-0.18932(3)	0	0.36682(3)	0.02771(13)
Pb3	4i	0.333	-0.04912(4)	$\frac{1}{2}$	0.20208(4)	0.01785(15)
Pb4	4i		-0.15205(3)	$\frac{1}{2}$	0.38027(3)	0.02791(13)
Pb5	4i		0.12297(3)	0	0.23734(3)	0.02338(12)
Pb6	4g		0	0.24814(6)0	0	0.03067(13)
Pb7	4i		0.25146(3)	0	0.00406(3)	0.02590(13)
Sn1	4i		-0.10664(4)	0	0.17675(4)	0.01420(17)
Sn2	8j		-0.27730(3)	0.17091(5)0	0.17686(3)	0.01455(13)
Sn3	4i	0.667	-0.04912(4)	$\frac{1}{2}$	0.20208(4)	0.01785(15)
Br1	8i		0.03339(5)	0.23633(9)0	0.17646(5)	0.0258(2)
Br2	8j		0.20555(5)	-0.19877(9)0	0.34003(5)	0.0249(2)
Br3	4i		0.27258(7)	0	0.18440(7)	0.0227(3)
Br4	4i		0.00820(8)	0	0.33959(7)	0.0251(3)
Br5	4i		0.09423(8)	0	0.04875(8)	0.0297(3)
Br6	4i		0.40977(8)	0	-0.06259(7)	0.0274(3)
Br7	8j		-0.10246(6)	0.21407(10)	0.45576(5)	0.0254(2)
Br8	8j		-0.15549(6)	0.25786(10)	0.06125(6)	0.0310(2)
Br9	4i		0.31652(8)	0	-0.45680(7)	0.0254(3)
N1	4i		0.0665(6)	$\frac{1}{2}$	0.2911(5)	0.016(2)
N2	4i		0.1892(6)	$\frac{1}{2}$	0.2490(5)	0.016(2)
N3	8j		-0.1572(4)	0.1548(7)0	0.2493(4)	0.0178(15)
N4	8j		-0.0838(4)	0.3487(7)	0.2910(4)	0.0164(15)
N5	4i		0.4888(6)	0	0.4323(5)	0.016(2)
C1	4i		0.1275(7)	$\frac{1}{2}$	0.2700(6)	0.014(2)
C2	8j		-0.1200(5)	0.2521(8)	0.2700(4)	0.0132(16)
C3	2d		$\frac{1}{2}$	0	$\frac{1}{2}$	0.015(3)
O1	4i		-0.2272(5)	0	0.1317(4)	0.0141(16)

<sup>a</sup> $U_{eq}$  is defined as one-third of the trace of the orthogonalized  $U_{ij}$  tensor.

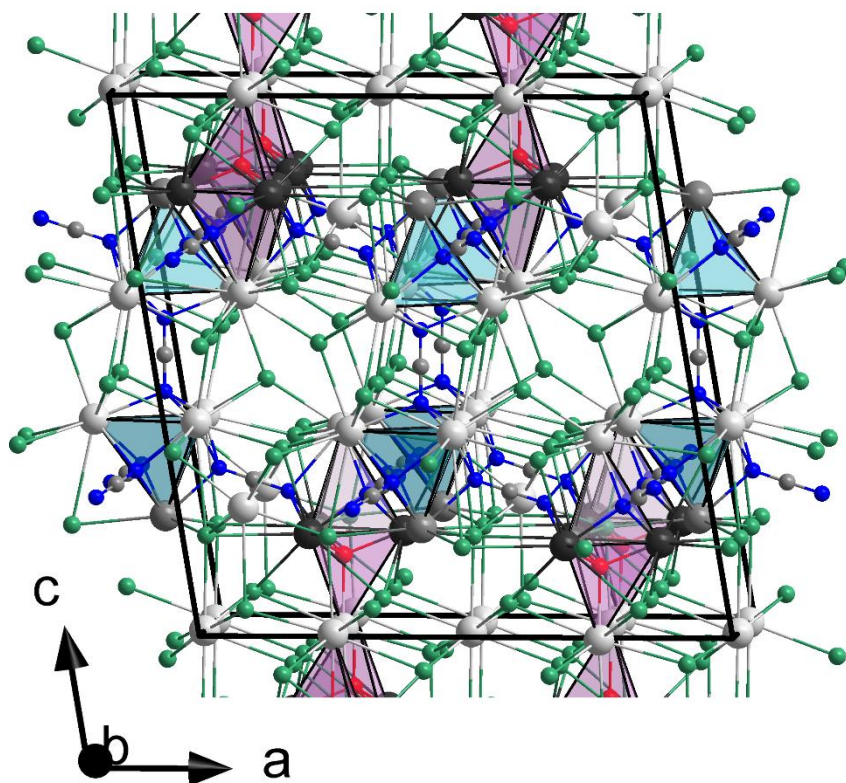


**Figure S2.** Perspective view along the  $ac$  plane in the crystal structure of  $\text{Pb}_{14.66}\text{Sn}_{7.34}\text{Br}_{26}(\text{CN}_2)_7\text{O}_2$ . Tin is shown in black, lead in light grey, the shared tin/lead site is shown in dark grey, oxygen in red, bromine in green nitrogen in blue and carbon in dark grey (small spheres).

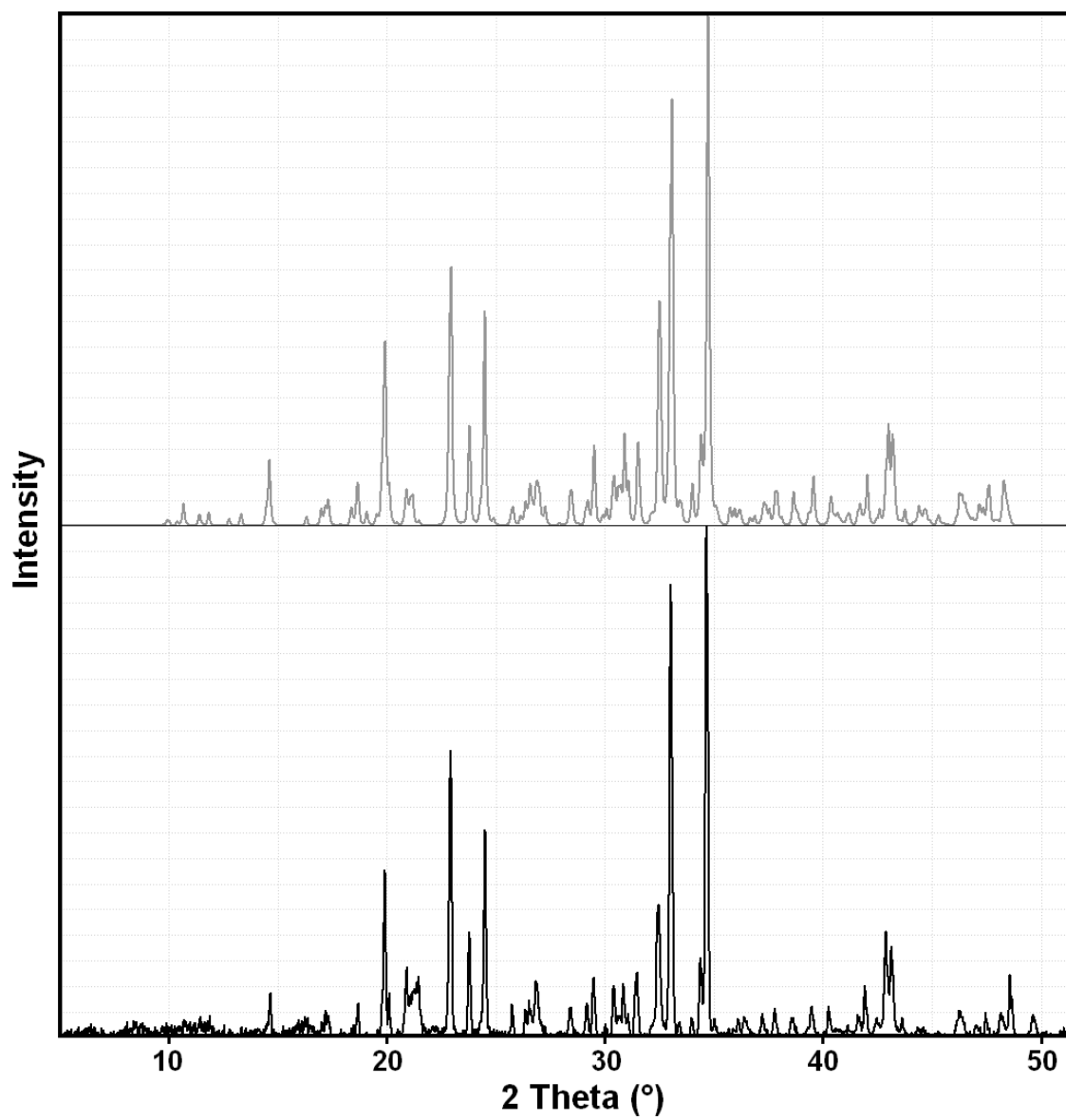
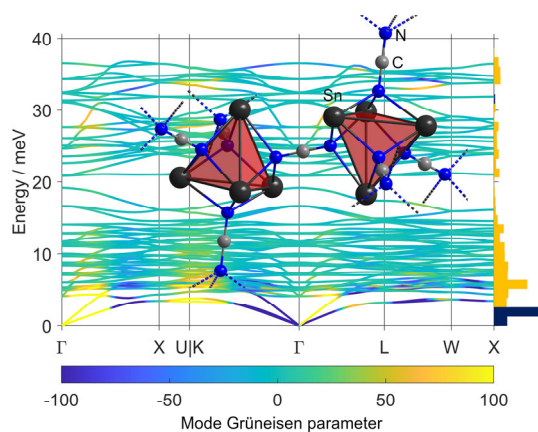


**Figure S3.** Recorded (black) and calculated (grey) X-ray diffraction powder pattern of  $\text{Pb}_{14.66}\text{Sn}_{7.34}\text{Br}_{26}(\text{CN}_2)_7\text{O}_2$ .



# Publication 7

Synthesis, Structure, and Thermoelastic Properties of  $\text{LiSn}_2\text{Br}_3(\text{CN}_2)$  and  $\text{Sn}_4\text{Br}_2(\text{CN}_2)_3$



<https://doi.org/10.1002/ejic.202100660>

Reprinted with permission from  
*Eur. J. Inorg. Chem.* **2021**, 2021, 4572–4578

Copyright © 2020 Wiley-VCH GmbH





# Synthesis, Structure, and Thermoelastic Properties of $\text{LiSn}_2\text{Br}_3(\text{CN}_2)$ and $\text{Sn}_4\text{Br}_2(\text{CN}_2)_3$

Manuel Löber,<sup>[a]</sup> Markus Ströbele,<sup>[a]</sup> Carl P. Romao,<sup>[a, b]</sup> and Hans-Jürgen Meyer\*<sup>[a]</sup>

Tin carbodiimides have been reported with various compositions, prepared via solid-state metathesis reactions by heating tin halides and lithium carbodiimide at moderate temperatures. The formations of two new compounds,  $\text{LiSn}_2\text{Br}_3(\text{CN}_2)$  and  $\text{Sn}_4\text{Br}_2(\text{CN}_2)_3$  are monitored by differential thermal analysis (DTA), and crystal structures are reported as refined on basis of X-ray diffraction studies. The structure of  $\text{LiSn}_2\text{Br}_3(\text{CN}_2)$  can be

described by two interpenetrating frameworks of corner-linked coordination polyhedra, raising the possibility of negative thermal expansion (NTE) as investigated by density functional perturbation theory (DFPT). Like some previously reported tin carbodiimide compounds,  $\text{LiSn}_2\text{Br}_3(\text{CN}_2)$  was also found to be a semiconductor with an indirect band gap of 2.5 eV, as determined by DFT calculations.

## Introduction

The simplest tin carbodiimide, the pseudo-binary compound  $\text{Sn}(\text{CN}_2)$ , can be obtained from a reaction of  $\text{Li}_2(\text{CN}_2)$  and  $\text{SnCl}_2$ ; its crystal structure was determined from X-ray powder diffraction data. Band structure calculations and optical measurements revealed this compound to be a semiconductor with an indirect band gap in the order of 2 eV.<sup>[1]</sup>  $\text{Sn}(\text{CN}_2)$  has been investigated as potential battery material.<sup>[2]</sup>

With the addition of oxide into the previous reaction mixture,  $\text{Sn}_2\text{O}(\text{CN}_2)$  is obtained to form reddish-brown crystals somewhere above 400 °C.<sup>[3]</sup> The crystal structure of  $\text{Sn}_2\text{O}(\text{CN}_2)$  is related to that of  $\text{SnO}$ , based on an alternating layer sequence of tin atoms followed by alternating layers of either oxygen or carbodiimide. Band structure calculations, as well as optical reflectance measurements indicate  $\text{Sn}_2\text{O}(\text{CN}_2)$  to be a semiconductor with an indirect band gap around 1.5 eV and a direct band gap around 2 eV. Further studies revealed that  $\text{Sn}_2\text{O}(\text{CN}_2)$  can improve the efficiency of  $\text{CuWO}_4$  photoanodes used for photocatalytic water oxidation.<sup>[4]</sup>

Differential thermal analysis (DTA) of the SSM reaction between  $\text{Li}_2(\text{CN}_2)$  and  $\text{SnCl}_2$  revealed the formation of yet another unknown compound at low heating conditions ( $\approx 200\text{--}250$  °C) identified as  $\text{Sn}_4\text{Cl}_2(\text{CN}_2)_3$ .<sup>[1]</sup> In fact this compound could be shown to act as an intermediate phase in formation reactions of  $\text{Sn}(\text{CN}_2)$  and  $\text{Sn}_2\text{O}(\text{CN}_2)$ .<sup>[1,3]</sup>

DTA studies in the system  $\text{Li}_2(\text{CN}_2)$ ,  $\text{SnCl}_2$  and  $\text{SnO}$  did not only reveal the intermediate formation of  $\text{Sn}_4\text{Cl}_2(\text{CN}_2)_3$  but also to the new compound  $\text{Sn}_9\text{O}_5\text{Cl}_4(\text{CN}_2)_2$  around 300 °C. Band structure calculations and optical reflectance measurements again revealed semiconducting behavior with a band gap in the order of 3 eV.<sup>[5]</sup>

The orthorhombic crystal structure of  $\text{Sn}_9\text{O}_5\text{Cl}_4(\text{CN}_2)_2$  contains two tin-oxide clusters  $[\text{Sn}_8\text{O}_3]$  as a novel feature, in contrast to the common layered arrangements of metal atoms and (NCN) units in most structures with carbodiimides.

All these studies have evidenced the usefulness of solid-state metathesis (SSM) reactions for the discovery of new compounds and systems, especially when combined with thermal scanning and powder X-ray diffraction studies.<sup>[6]</sup>


Layered carbodiimides  $\text{A}_2\text{M}(\text{CN}_2)_3$  with tetravalent cations have been synthesized with  $\text{M}=\text{Sn}$ ,  $\text{Zr}$ , and  $\text{Hf}$ .<sup>[7]</sup> Their crystal structures are characterized by alternating layers of (NCN) units and metal atoms, revealing structural analogies to corresponding ternary oxides  $\text{A}_2\text{MO}_3$ . In addition, compounds  $\text{A}_2\text{MnSn}_2(\text{CN}_2)_6$  ( $\text{A}=\text{Li}$  and  $\text{Na}$ ) were discovered by SSM reactions with tetravalent tin.<sup>[8]</sup>


Tetravalent transition metal carbodiimides were reported for  $\text{M}(\text{CN}_2)_2$  ( $\text{M}=\text{Zr}$ ,  $\text{Hf}$ ) to exhibit near-zero thermal expansion.<sup>[9]</sup> The wine-rack topology of the crystal structure of  $\text{M}(\text{CN}_2)_2$  makes them flexible framework materials, and negative linear compressibility is predicted in  $\text{Hf}(\text{CN}_2)_2$ .

Due to the potential applications of tin carbodiimides as electronic materials, we have continued the exploration of the tin carbodiimide compositional space by reporting two bromide-containing compounds,  $\text{LiSn}_2\text{Br}_3(\text{CN}_2)$  and  $\text{Sn}_4\text{Br}_2(\text{CN}_2)_3$ , in this work, and study how  $\text{LiSn}_2\text{Br}_3(\text{CN}_2)$  differs from the isotopic  $\text{LiSr}_2\text{Cl}_3(\text{CN}_2)$  to demonstrate the role of tin. We have calculated the phonon band structure and thermal expansivity of  $\text{Sn}_4\text{Br}_2(\text{CN}_2)_3$  in order to assess whether it behaves like a flexible framework material.

[a] M. Löber, Dr. M. Ströbele, Dr. C. P. Romao, Prof. Dr. H.-J. Meyer  
Section for Solid State and Theoretical Inorganic Chemistry,  
Institute of Inorganic Chemistry, Eberhard Karls University Tübingen  
Auf der Morgenstelle 18, 72076 Tübingen, Germany  
E-mail: juergen.meyer@uni-tuebingen.de

[b] Dr. C. P. Romao  
Department of Materials, ETH Zürich  
Wolfgang-Pauli-Str. 27, 8093 Zürich, Switzerland

 Supporting information for this article is available on the WWW under <https://doi.org/10.1002/ejic.202100660>

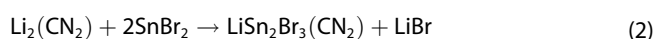
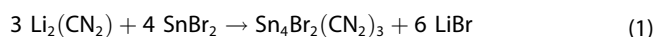
 © 2021 The Authors. European Journal of Inorganic Chemistry published by Wiley-VCH GmbH. This is an open access article under the terms of the Creative Commons Attribution Non-Commercial License, which permits use, distribution and reproduction in any medium, provided the original work is properly cited and is not used for commercial purposes.

## Results and Discussion

### Syntheses of $\text{Sn}_4\text{Br}_2(\text{CN}_2)_3$ and $\text{LiSn}_2\text{Br}_3(\text{CN}_2)$

Reactions between lithium carbodiimide ( $\text{Li}_2(\text{CN}_2)$ ) and tin bromide ( $\text{SnBr}_2$ ) were explored in two different ways, a) by heating mixtures in fused silica tubing in an oven, and b) by heating mixtures in fused silica tubing in a DTA analyzer. Preparation condition were adjusted after the composition of the new compounds were clarified.

The compounds  $\text{Sn}_4\text{Br}_2(\text{CN}_2)_3$  and  $\text{LiSn}_2\text{Br}_3(\text{CN}_2)$  can be synthesized by using different stoichiometric amounts of starting materials,  $\text{Li}_2(\text{CN}_2)$  and  $\text{SnBr}_2$ , in accordance with reactions (1) and (2) between 350 and 450 °C. As indicated by PXRD both compounds could be synthesized without any visible side phases (see SI).



When employing equimolar amounts of  $\text{Li}_2(\text{CN}_2)$  and  $\text{SnBr}_2$ , a mixture of  $\text{Sn}_4\text{Br}_2(\text{CN}_2)_3$  and the  $\text{Sn}^{4+}$ -containing  $\text{Li}_2\text{Sn}(\text{CN}_2)_3$  is formed. Tin carbodiimide,  $\text{Sn}(\text{CN}_2)$ , as formed when using equimolar mixtures of  $\text{Li}_2(\text{CN}_2)$  and either  $\text{SnCl}_2$  or  $\text{SnF}_2$ , was not observed here.

### Thermoanalytic Studies

DTA studies of both reactions, (1) and (2), were performed to investigate reaction pathways and formation conditions of compounds. The DTA of reaction (1) with the formation of  $\text{Sn}_4\text{Br}_2(\text{CN}_2)_3$  is shown in Figure 1. On heating, a broad exothermic effect appears between 150 °C and 205 °C. This exothermic effect can be assigned to the formation of

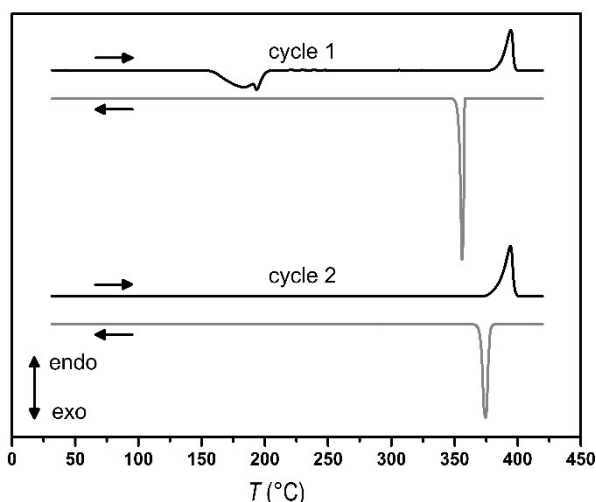


**Figure 1.** DTA of the reaction  $3\text{Li}_2(\text{CN}_2) + 4\text{SnBr}_2$  with the formation of  $\text{Sn}_4\text{Br}_2(\text{CN}_2)_3$  in cycle 1, with another heating and cooling cycle of the ( $\text{Sn}_4\text{Cl}_2(\text{CN}_2)_3$ , LiBr) product mixture given in cycle 2.

$\text{LiSn}_2\text{Br}_3(\text{CN}_2)$ . PXRD measurements of intermediate products between 150 and 250 °C still show the presence of some unreacted  $\text{Li}_2(\text{CN}_2)$  and  $\text{SnBr}_2$ , indicating a slow formation of  $\text{LiSn}_2\text{Br}_3(\text{CN}_2)$  within the broad exothermic effect. Within the continuing heating process  $\text{LiSn}_2\text{Br}_3(\text{CN}_2)$  slowly transforms into  $\text{Sn}_4\text{Br}_2(\text{CN}_2)_3$ , (starting at 250 °C) but without any noticeable thermal effect.

Finally, an endothermic effect at 395 °C upon heating and an exothermic effect at 356 °C upon cooling were observed and assigned as melting and recrystallisation of  $\text{Sn}_4\text{Br}_2(\text{CN}_2)_3$  and the coproduced LiBr. Those two effects are observed again in a second heating/cooling cycle.

A small endothermic depression at around 190 °C of the exothermic formation reaction may be caused by a eutectic melt formation between LiBr with still unreacted  $\text{SnBr}_2$ . This assumption is supported by a DTA of LiBr with  $\text{SnBr}_2$ , where an endothermic effect was observed around 190 °C upon heating and an exothermic effect upon cooling slightly below this temperature.

The formation of  $\text{LiSn}_2\text{Br}_3(\text{CN}_2)$ , represented in reaction (2) was also studied by DTA with similar thermal effects (see SI).

### Crystal structure of $\text{LiSn}_2\text{Br}_3(\text{CN}_2)$

The crystal structure of  $\text{LiSn}_2\text{Br}_3(\text{CN}_2)$  was solved and refined in the cubic space group  $Fd\bar{3}m$  from single-crystal X-ray diffraction data. Some details of the measurement and structure refinement are displayed in Table 1.

The structure is isotypic to the known structures of  $\text{LiM}_2\text{Br}_3(\text{CN}_2)$ , ( $M = \text{Sr}$  and  $\text{Eu}$ ,<sup>[10]</sup>  $\text{LiM}_2\text{I}_3(\text{CN}_2)$ , ( $M = \text{Sr}$ <sup>[11]</sup> and  $\text{Eu}$ <sup>[12]</sup>),  $\text{APb}_2\text{Cl}_3(\text{CN}_2)$ , ( $A = \text{Li}, \text{Na}, \text{Ag}$ ) and  $\text{APb}_2\text{Br}_3(\text{CN}_2)$ , ( $A = \text{Li}, \text{Na}$ ).<sup>[13]</sup> Unit cell parameters of isotypic compounds are depicted in Table 2, all determined at room temperature, except for the title compound. An indexed powder XRD pattern of  $\text{LiSn}_2\text{Br}_3(\text{CN}_2)$ , recorded at room temperature yielded 14.4128(7) Å, slightly larger than the value determined at 100 K (14.35722(9) Å). The unit cell of  $\text{LiSn}_2\text{Br}_3(\text{CN}_2)$  appears slightly larger than that of the

Empirical formula	$\text{LiSn}_2\text{Br}_3(\text{CN}_2)$	$\text{Sn}_4\text{Br}_2(\text{CN}_2)_3$
CSD code	2049524	2056459
Formula weight (g/mol)	524.08	754.67
Wavelength (Mo- $K_{\alpha}$ ) (Å)	0.71073	0.71073
Crystal system	Cubic	Monoclinic
Space group	$Fd\bar{3}m$	$P2_1/n$
Unit cell dimensions (Å)	$a = 14.35722(9)$	$a = 6.9597(1)$ $b = 9.3531(2)$ $c = 9.0323(2)$ $\beta = 106.349(2)$
Volume (Å <sup>3</sup> )	2959.45(6)	564.18(2)
Z	16	2
Density (calculated) (g/cm <sup>3</sup> )	4.71	4.44
2 Theta range for data collection (°)	8.03 to 52.56	7.89 to 52.73
Total number of reflections	16288	20167
Refined parameters	15	71
R1, wR2	0.029, 0.066	0.012, 0.025
GOOF	1.142	1.100

**Table 2.** Comparison of lattice parameters of  $\text{LiSn}_2\text{Br}_3(\text{CN}_2)_3$  with isotopic compounds.

Compound	$a$ [Å]
$\text{LiPb}_2\text{Cl}_3(\text{CN}_2)^{[a]}$	14.1892(1)
$\text{AgPb}_2\text{Cl}_3(\text{CN}_2)^{[a]}$	14.2559(6)
$\text{NaPb}_2\text{Cl}_3(\text{CN}_2)^{[a]}$	14.3155(5)
<b><math>\text{LiSn}_2\text{Br}_3(\text{CN}_2)^{[b]}</math></b>	<b>14.35722(9)</b>
$\text{LiPb}_2\text{Br}_3(\text{CN}_2)^{[a]}$	14.5270(5)
$\text{LiEu}_2\text{Br}_3(\text{CN}_2)^{[b]}$	14.572(1)
$\text{LiSr}_2\text{Br}_3(\text{CN}_2)^{[b]}$	14.641(1)
$\text{NaPb}_2\text{Br}_3(\text{CN}_2)^{[c]}$	14.7251(4)
$\text{LiEu}_2\text{I}_3(\text{CN}_2)^{[b]}$	15.1427(17)
$\text{LiSr}_2\text{I}_3(\text{CN}_2)^{[b]}$	15.2312(13)

[a] Rietveld refinement. [b] Single crystal. [c] Indexed XRD pattern.

related lead chloride compounds, but smaller than lead bromide carbodiimide, which is in line with larger ionic radii of  $\text{Br}^-$  and  $\text{Pb}^{2+}$ , versus  $\text{Cl}^-$  and  $\text{Sn}^{2+}$ .

The crystal structure of  $\text{LiSn}_2\text{Br}_3(\text{CN}_2)_3$  is comprised of tin tetrahedra that are capped by (NCN) units to form distorted  $[\text{Sn}_4(\text{CN}_2)_4]$  cubes (see Figure 2 (top)). The (NCN) units are coordinated by six tin atoms in an approximately octahedral coordination environment.

Tin is coordinated by six bromide and three carbodiimide ions with Sn–Br bond length of 3.23 and 3.48 Å (see Figure 2 (bottom)). The Sn–N distance of 2.48 Å are comparable to other known tin carbodiimide compounds. The symmetrical carbodiimide ion has a C–N bond distance of 1.21 Å, which is as long as in  $\text{Sn}(\text{CN}_2)^{[1]}$  Each  $[\text{Sn}_4(\text{CN}_2)_4]$  is connected to four other tin tetrahedra, forming a network like arrangement, shown in Figure 3 (top). Lithium is coordinated distorted octahedrally by bromide. Those octahedra are linked at the corners to an infinite network, as displayed in Figure 3 (bottom). The Li–Br

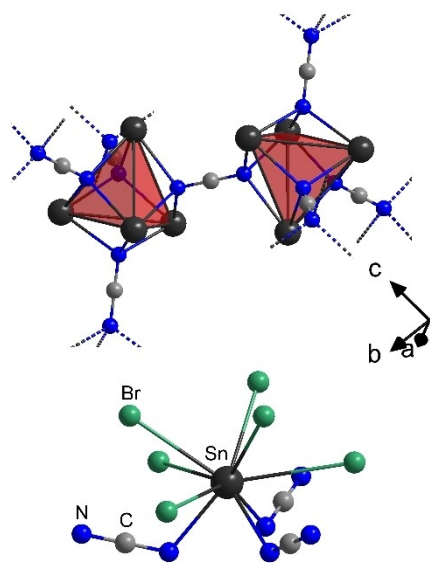


**Figure 2.** Top: Section of the framework of Sn tetrahedra (red) coordinated by (NCN) units. The dashed lines indicate the further linkage with other tin tetrahedra via Sn–N bonds. Bottom: Coordination environment of tin in  $\text{LiSn}_2\text{Br}_3(\text{CN}_2)$ .

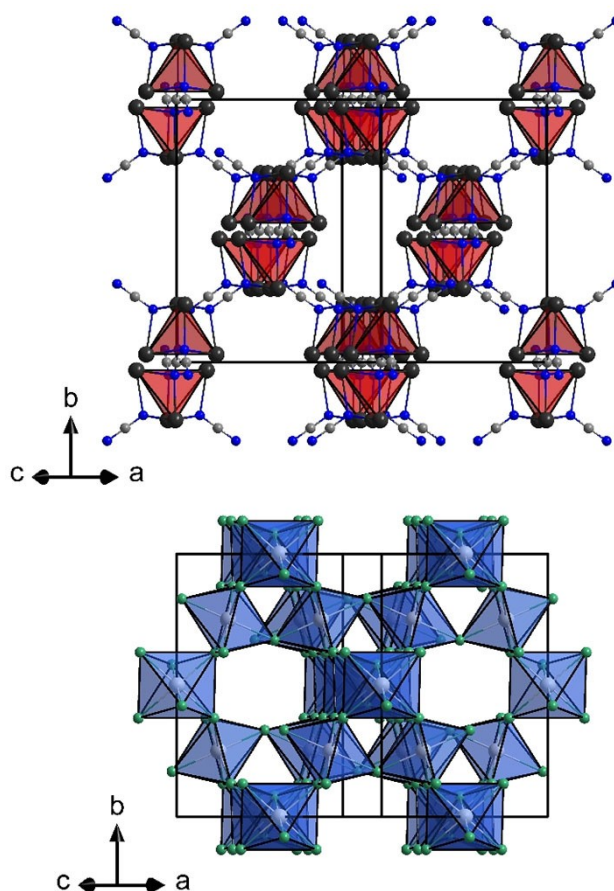


**Figure 3.** Top: Perspective view of the unit cell of  $\text{LiSn}_2\text{Br}_3(\text{CN}_2)$ . Tin is shown in black, carbon in grey and nitrogen in blue. Tin tetrahedra are indicated in red. Bottom: Perspective view of the unit cell of  $\text{LiSn}_2\text{Br}_3(\text{CN}_2)$  showing the structural arrangement of  $[\text{LiBr}_6]$  octahedra. Li is shown in light grey, Br in green.

bond distances of 2.78 Å are only somewhat longer than those in  $\text{LiBr}$  (2.74 Å).<sup>[14]</sup>

### Crystal structure of $\text{Sn}_4\text{Br}_2(\text{CN}_2)_3$

The crystal structure of  $\text{Sn}_4\text{Br}_2(\text{CN}_2)_3$  was solved and refined in the monoclinic space group  $P2_1/n$  from single-crystal XRD data. Some crystal structure and refinement data are given in Table 1. The crystal structure of  $\text{Sn}_4\text{Br}_2(\text{CN}_2)_3$  is isotopic to the already known compound  $\text{Sn}_4\text{Cl}_2(\text{CN}_2)_3$ , that was obtained from a reaction of  $\text{Li}_2(\text{CN}_2)$  and  $\text{SnCl}_2$  at a 3:4 molar ratio.<sup>[1]</sup> Due to the larger ionic radius of  $\text{Br}^-$  compared to  $\text{Cl}^-$  the unit cell parameters of  $\text{Sn}_4\text{Br}_2(\text{CN}_2)_3$  are slightly larger. The two crystallographically distinct tin atoms are both distorted octahedrally coordinated by three (NCN) units and three  $\text{Br}^-$  ions. The Sn–N distances are between 2.25 and 2.32 Å, the bond distances between Sn and Br are between 3.08 and 3.63 Å and comparable to those in  $\text{Sn}_4\text{Cl}_2(\text{CN}_2)_3$  (Sn–N 2.22–2.35 Å, Sn–Cl 2.93–3.69 Å). The C–N distances of the carbodiimide ion are 1.23 Å (coordinated planar by Sn) and 1.22/1.23 Å (coordinated

pseudo tetrahedrally by Sn) very similar to those in  $\text{Sn}_4\text{Cl}_2(\text{CN}_2)_3$ . The coordination environment of tin in  $\text{Sn}_4\text{Br}_2(\text{CN}_2)_3$  is shown in Figure 4 (top).

The overall crystal structure can be described by alternating layers of tin atoms with layers containing (NCN) units and bromide (Figure 4 (bottom)).

### Electronic Band Structure

Density functional theory was used to calculate the electronic band structure of  $\text{LiSn}_2\text{Br}_3(\text{CN}_2)$  (Figure 5).  $\text{LiSn}_2\text{Br}_3(\text{CN}_2)$  was found to be a semiconductor, with a calculated indirect band gap of 2.5 eV, giving it a slightly larger band gap than the related tin carbodiimides  $\text{Sn}(\text{CN}_2)$  and  $\text{Sn}_9\text{O}_5\text{Cl}_4(\text{CN}_2)_2$ .<sup>[1,5]</sup> The calculated electronic density of states (Figure 6) shows the states near the Fermi energy to have a mixture of N, Br, C, and Sn character, indicating the presence of highly delocalized electrons, a finding also evidenced in the low curvature of these bands.

### Vibrational Properties

The structure of  $\text{LiSn}_2\text{Br}_3(\text{CN}_2)$  can be described as two interpenetrating frameworks of corner-linked coordination polyhedra (Figure 3); in such framework structures we expect the

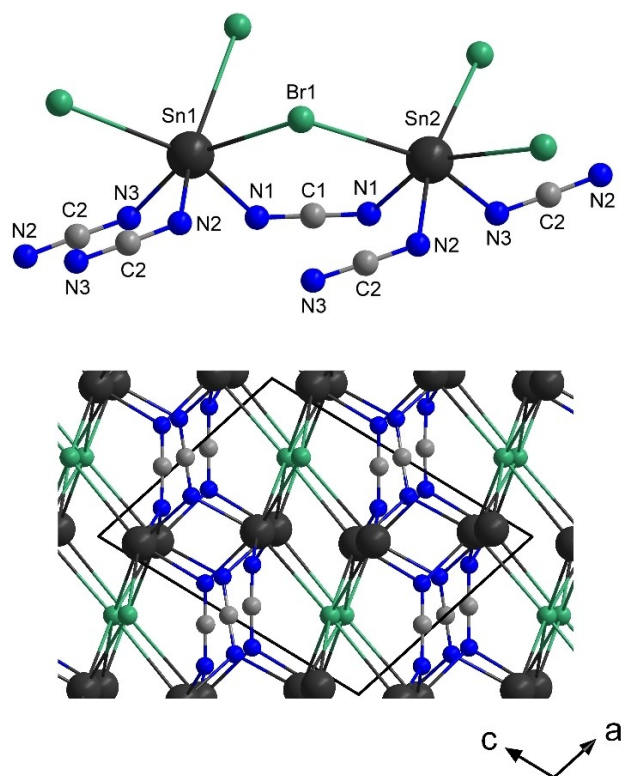


Figure 4. Top: Coordination environment of the two distinct crystallographic tin atoms. Bottom: View along the *ac* plane of a section of the structure of  $\text{Sn}_4\text{Br}_2(\text{CN}_2)_3$ , showing alternating layers of Sn and NCN/Br.

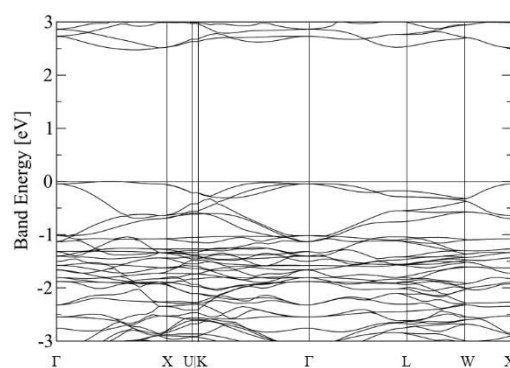


Figure 5. Calculated electronic band structure of  $\text{LiSn}_2\text{Br}_3(\text{CN}_2)$ . Special points in and paths through the Brillouin zone were selected following Reference.<sup>[15]</sup>

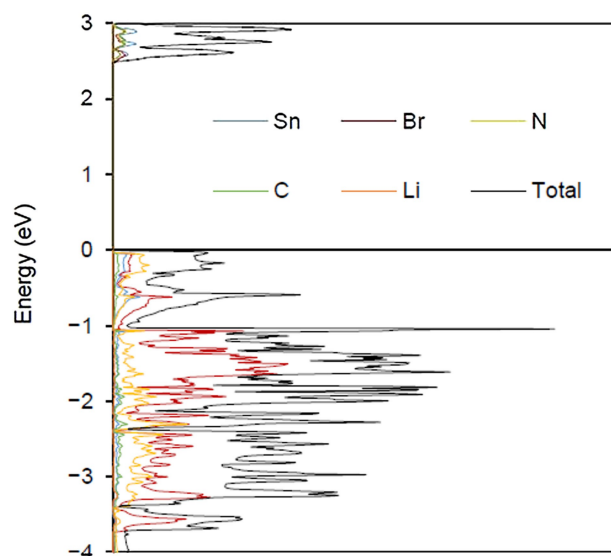
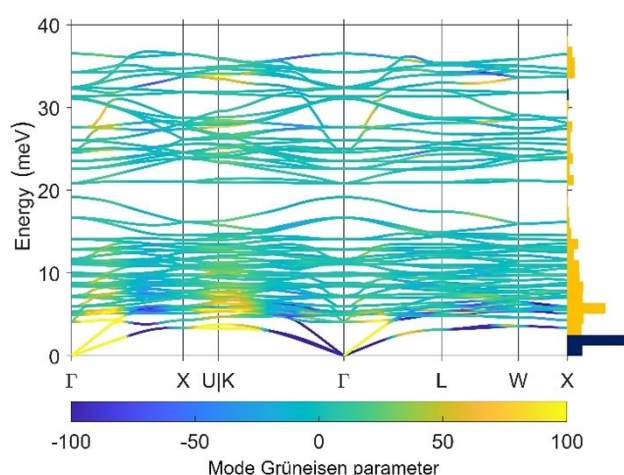


Figure 6. Calculated electronic density of states of  $\text{LiSn}_2\text{Br}_3(\text{CN}_2)$ , and its projections onto the atomic spheres.

presence of low-energy vibrational modes which can lead to unusual physical properties such as NTE (negative thermal expansion), as is seen in other carbodiimides such as  $\text{Si}(\text{CN}_2)_2$  and  $\text{Hf}(\text{CN}_2)_2$ .<sup>[9,16]</sup> Cubic materials which display NTE are of special interest due to their lack of thermal expansion anisotropy, which leads to thermal stress.<sup>[17]</sup> To investigate this possibility, we have used density functional perturbation theory (DFPT) to calculate the phonon band structure of  $\text{LiSn}_2\text{Br}_3(\text{CN}_2)$ , and its mode Grüneisen parameters (Figure 7), which measure the contribution of each mode to the overall thermal expansion within the quasiharmonic approximation.

As Figure 7 shows,  $\text{LiSn}_2\text{Br}_3(\text{CN}_2)$  does indeed have many low-energy phonons, as is expected of a framework material. Below 10 meV, these phonons have large mode Grüneisen parameters, both positive and negative, some being extremely large ( $>100$  and  $<-100$ ). Below 25 K, the modes with negative Grüneisen parameters (mainly from acoustic



**Figure 7.** Calculated low-energy phonon band structure of  $\text{LiSn}_2\text{Br}_3(\text{CN}_2)$ , with bands coloured by their mode Grüneisen parameters ( $\gamma$ , some values are off-scale). At right, a histogram of the density of states ( $\rho$ ) weighted by the Grüneisen parameters as  $\sum_k \rho_k(\omega) \gamma_k(\omega)$ , is shown, with positive values colored in gold and negative values in blue. Special points in and paths through the Brillouin zone were selected following Reference.<sup>[15]</sup>

bands) are predominant and NTE is predicted (Figure 8). However, as the temperature increases low energy optic bands with positive mode Grüneisen parameters contribute increasingly to the thermal expansion, leading to a positive coefficient of thermal expansion, which is predicted to reach a value of  $\alpha_t = 2.4 \times 10^{-6} \text{ K}^{-1}$  at 300 K. This value would still be considered anomalously low in comparison to most inorganic solids.<sup>[17]</sup>

Examination of the phonon eigenvectors (see SI) shows that the negative mode Grüneisen parameters of the acoustic bands can be attributed to librational (rocking) motions of all structural units (as expected for acoustic bands), with displacements transverse to the wave propagation direction, *i.e.*, the predicted NTE at low temperatures can be explained

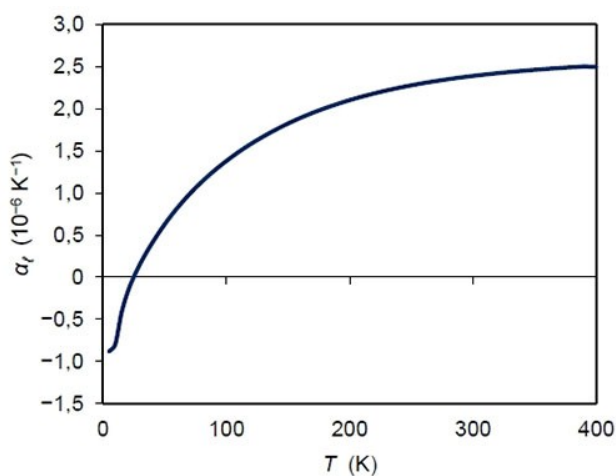


**Figure 8.** Calculated linear thermal expansion coefficient of  $\text{LiSn}_2\text{Br}_3(\text{CN}_2)$  between 5 and 400 K.

by the tension effect.<sup>[18]</sup> Along the  $\Gamma \rightarrow X$  direction, where large positive mode Grüneisen parameters are found, the motions of the structural units are closer to translations than librations.

As the structure of  $\text{LiSn}_2\text{Br}_3(\text{CN}_2)$  is amenable to ionic substitution, the effect of increasing the unit cell dimensions was studied by calculation of the phononic structure and coefficient of thermal expansion of  $\text{LiSr}_2\text{Br}_3(\text{CN}_2)$ . Similar ionic substitutions have been used to enhance NTE in oxide materials.<sup>[19]</sup> This substitution did not lead to significant changes in the phonon band structure, however the magnitudes of the mode Grüneisen parameters decreased significantly (see the Supporting Information). While  $\text{LiSr}_2\text{Br}_3(\text{CN}_2)$  is also predicted to show NTE at temperatures  $< 25 \text{ K}$ , at 300 K its thermal expansion is predicted to be much larger, with  $\alpha_t = 24 \times 10^{-6} \text{ K}^{-1}$ . This result suggests that the more covalent nature of the Sn–NCN bond results in more framework-like behaviour, outweighing the additional free space in the unit cell provided by the larger lattice constant. Comparison of the calculated elastic properties reveals  $\text{LiSr}_2\text{Br}_3(\text{CN}_2)$  ( $K = 40.8 \text{ GPa}$ ,  $G = 16.0 \text{ GPa}$ ,  $\nu = 0.32$ ) to be slightly softer than  $\text{LiSn}_2\text{Br}_3(\text{CN}_2)$  ( $K = 46.5 \text{ GPa}$ ,  $G = 16.6 \text{ GPa}$ ,  $\nu = 0.34$ ).

Although  $\text{LiSn}_2\text{Br}_3(\text{CN}_2)$  is not expected to display NTE, except perhaps at very low temperatures, the finding that it and other isotypic materials are framework materials with many low-energy phonons has important ramifications for applications. For example, the low-energy phonons act to decrease the thermal conductivity,<sup>[20]</sup> increase the ability to perform ionic substitutions,<sup>[21]</sup> and increase ionic conductivity.<sup>[22]</sup> Therefore, the flexible framework structure is expected to enhance the performance of  $\text{LiSn}_2\text{Br}_3(\text{CN}_2)$  as a potential battery or ion conducting material.

## Conclusion

Tin carbodiimide compounds are obtained under decent heating via SSM reactions to behave as wide gap semiconductors. The given compounds  $\text{Sn}_4\text{Br}_2(\text{CN}_2)_3$  and  $\text{LiSn}_2\text{Br}_3(\text{CN}_2)$  are formed from  $\text{SnBr}_2$  and  $\text{Li}_2(\text{CN}_2)$  near  $200^\circ\text{C}$  and are most efficiently prepared between  $350^\circ\text{C}$  and  $450^\circ\text{C}$ , both without any visible side phase, according to PXRD patterns.

$\text{Sn}_4\text{Br}_2(\text{CN}_2)_3$  is isotypic to  $\text{Sn}_4\text{Cl}_2(\text{CN}_2)_3$ , which has been shown to act as an intermediate compound in the formation of other ternary tin carbodiimides. The structure of  $\text{LiSn}_2\text{Br}_3(\text{CN}_2)$  is isotypic to a number of compounds related to the mineral Bideauxite. A remarkable feature of this compound is the appearance of two interpenetrating frameworks of corner-linked coordination polyhedral which can give rise to negative thermal expansion. DFPT calculations indeed show the presence of low-energy phonons related with large mode Grüneisen parameters, but NTE is expected at very low temperature only. The electronic structure of  $\text{LiSn}_2\text{Br}_3(\text{CN}_2)$  has been studied from the band structure and density of states (DOS), both determined by DFT calculations. The band structure and DOS show an indirect band gap of 2.5 eV, slightly higher than related tin

compounds, and a mixture of N, Br, C, and Sn character near the Fermi level, indicating high electron delocalization.

## Experimental Section

### Syntheses of $\text{LiSn}_2\text{Br}_3(\text{CN}_2)_3$ and $\text{Sn}_4\text{Br}_2(\text{CN}_2)_3$

Powders of  $\text{Li}_2(\text{CN}_2)$  and  $\text{SnBr}_2$  were mixed and pestled in a 1:2 ( $\text{LiSn}_2\text{Br}_3(\text{CN}_2)_3$ ) or 3:4 ( $\text{Sn}_4\text{Br}_2(\text{CN}_2)_3$ ) molar ratio under dry argon atmosphere. The reaction mixtures were transferred into silica ampoules and fused under vacuum. The ampoules were placed in a crucible furnace and heated to 350 °C ( $\text{LiSn}_2\text{Br}_3(\text{CN}_2)_3$ ) or 450 °C ( $\text{Sn}_4\text{Br}_2(\text{CN}_2)_3$ ) at 2 K/min, remained there for 20 h until cooling to room temperature at 2 K/min. Both compounds were obtained as colorless crystalline powders.

Colourless plate-like single crystals of  $\text{LiSn}_2\text{Br}_3(\text{CN}_2)_3$  were obtained when heating the 1:2 reaction mixture for 100 h at 350 °C until cooling to room temperature at 0.01 K/min. Also plate-like and colourless single crystals of  $\text{Sn}_4\text{Br}_2(\text{CN}_2)_3$  could be obtained when heating 3:4 mixtures to 400 °C at 2 K/min, kept there for 100 h and cooled to room temperature at 0.05 K/min.  $\text{LiSn}_2\text{Br}_3(\text{CN}_2)_3$  cannot be treated in air, but  $\text{Sn}_4\text{Br}_2(\text{CN}_2)_3$  behaves stable under atmospheric conditions. **X-ray Diffraction.** Powder X-ray diffraction (PXRD) pattern were recorded on a Stoe StadiP diffractometer (Stoe, Darmstadt) with Ge-monochromated  $\text{Cu-K}\alpha_1$  radiation and a Mythen1 detector.

Intensity data collections of single crystals of  $\text{LiSn}_2\text{Br}_3(\text{CN}_2)_3$  and  $\text{Sn}_4\text{Br}_2(\text{CN}_2)_3$  were recorded on a Rigaku XtaLAP Synergy-S single-crystal diffractometer, equipped with a HyPix-6000HE detector and monochromatic  $\text{Mo-K}\alpha$  radiation. The intensities were corrected using numerical methods and the CrysAlisPro 1.171.41.92a software (Rigaku Oxford Diffraction, 2021). The structure was solved by direct methods (SHELXS),<sup>[23]</sup> and full-matrix least-squares structure refinements, performed with SHELXL-2014<sup>[24]</sup> implemented in Olex2 1.3-ac4.<sup>[25]</sup>

**Thermoanalytic Measurements.** Differential thermal analysis (DTA) were performed using a Netsch STA 449F3 Jupiter (Netsch, Selb, Germany). The samples were sealed in homemade silica ampoules and analysed between room temperature and 430 °C at 2 K/min.

**Density Functional Theory.** Density functional theory (DFT) calculations were performed using the Abinit software package (v. 9).<sup>[26]</sup> Norm-conserving pseudopotentials were used as received from the Abinit library. Plane-wave basis set energy cutoffs and Monkhorst-Pack grid spacings were chosen following convergence studies (to 1 % in pressure).<sup>[27]</sup> The Perdew–Burke–Erzenhof exchange–correlation functional was used with the vdW-DFT-D3(BJ) dispersion correction.<sup>[28]</sup> Mode Grüneisen parameters were calculated using a tensile and a compressive perturbation of the lattice constant by 1 part in 10<sup>5</sup>. Structural relaxation was performed prior to calculation of the phonon band structure. Example input files are available as part of the Supporting Information.

Deposition Numbers 2049524 (for  $\text{LiSn}_2\text{Br}_3(\text{CN}_2)_3$ ) and 2060907 (for  $\text{Sn}_4\text{Br}_2(\text{CN}_2)_3$ ) contain the supplementary crystallographic data for this paper. These data are provided free of charge by the joint Cambridge Crystallographic Data Centre and Fachinformationszentrum Karlsruhe Access Structures service [www.ccdc.cam.ac.uk/structures](http://www.ccdc.cam.ac.uk/structures).

## Acknowledgements

Funding of this work by the Deutsche Forschungsgemeinschaft (DFG) through grant ME 914/25-2 and support by the state of Baden-Württemberg through bwHPC and the Deutsche Forschungsgemeinschaft (DFG) through grant no INST 40/575-1 FUGG (JUSTUS 2 cluster) are gratefully acknowledged. This project has received funding from the European Union's Horizon 2020 research and innovation programme under the Marie Skłodowska-Curie (MSC) grant agreement No 101030352. Open Access funding enabled and organized by Projekt DEAL.

## Conflict of Interest

The authors declare no conflict of interest.

**Keywords:** Carbodiimide · DFPT · DTA · Solid-State Reaction · Tin

- [1] M. Löber, K. Dolabdjian, M. Ströbele, C. P. Romao, H.-J. Meyer, *Inorg. Chem.* **2019**, *58*, 7845–7851.
- [2] C. Braun, L. Mereacre, W. Hua, T. Stuerzer, I. Ponomarev, P. Kroll, A. Slabon, Z. Chen, Y. Damour, X. Rocquefelte, J.-F. Halet, S. Indris, *ChemElectroChem* **2020**, *7*, 4550–4561.
- [3] K. Dolabdjian, A. L. Görne, R. Dronskowski, M. Ströbele, H.-J. Meyer, *Dalton Trans.* **2018**, *47*, 13378–13383.
- [4] Z. Chen, M. Löber, A. Rokicińska, Z. Ma, J. Chen, P. Kuśrowski, H.-J. Meyer, R. Dronskowski, A. Slabon, *Dalton Trans.* **2020**, *49*, 3450–3456.
- [5] M. Löber, C. S. Geißenhöner, M. Ströbele, S. Indris, C. P. Romao, H.-J. Meyer, *Inorg. Chem.* **2019**, *58*, 14560–14567.
- [6] H.-J. Meyer, *Dalton Trans.* **2010**, *39*, 5973–5982.
- [7] K. Dolabdjian, C. Castro, H.-J. Meyer, *Eur. J. Inorg. Chem.* **2018**, *2018*, 1624–1630.
- [8] A. J. Corkett, R. Dronskowski, *Dalton Trans.* **2019**, *48*, 15029–15035.
- [9] K. Dolabdjian, A. Kobald, C. P. Romao, H.-J. Meyer, *Dalton Trans.* **2018**, *47*, 10249–10255.
- [10] W. Liao, R. Dronskowski, *Z. Anorg. Allg. Chem.* **2005**, *631*, 1953–1956.
- [11] W. Liao, J. von Appen, R. Dronskowski, *Chem. Commun.* **2004**, 2302–2303.
- [12] W. Liao, C. Hu, R. K. Kremer, R. Dronskowski, *Inorg. Chem.* **2004**, *43*, 5884–5890.
- [13] K. Dolabdjian, H.-J. Meyer, *Z. Anorg. Allg. Chem.* **2017**, *643*, 1898–1903.
- [14] E. Posnjak, R. W. G. Wyckoff, *J. Wash. Acad. Sci.* **1922**, *12*, 248–251.
- [15] Y. Hinuma, G. Pizzi, Y. Kumagai, F. Oba, I. Tanaka, *Comput. Mater. Sci.* **2017**, *128*, 140–184.
- [16] a) L. Li, K. Refson, M. T. Dove, *J. Phys. Condens. Matter* **2020**, *32*, 465402; b) P. Kroll, M. Andrade, X. Yan, E. Ionescu, G. Miehe, R. Riedel, *J. Phys. Chem. C* **2012**, *116*, 526–531
- [17] C. P. Romao, K. J. Miller, C. A. Whitman, M. A. White, B. A. Marinkovic, in *Comprehensive Inorganic Chemistry II (Second Edition)* (Eds.: J. Reedijk, K. Poeppelmeier), Elsevier, Amsterdam, **2013**, pp. 127–151.
- [18] M. T. Dove, H. Fang, *Rep. Prog. Phys.* **2016**, *79*, 066503.
- [19] B. A. Marinkovic, M. Ari, R. R. de Avillez, F. Rizzo, F. F. Ferreira, K. J. Miller, M. B. Johnson, M. A. White, *Chem. Mater.* **2009**, *21*, 2886–2894.
- [20] C. Herring, *Phys. Rev.* **1954**, *95*, 954–965.
- [21] A. L. Goodwin, S. A. Wells, M. T. Dove, *Chem. Geol.* **2006**, *225*, 213–221.
- [22] K. Wakamura, *Phys. Rev. B* **1997**, *56*, 11593–11599.
- [23] G. M. Sheldrick, University of Göttingen (Göttingen, Germany) **1997**.
- [24] G. M. Sheldrick, *Acta Crystallogr.* **2015**, *C71*, 3–8.
- [25] O. V. Dolomanov, L. J. Bourhis, R. J. Gildea, J. A. K. Howard, H. Puschmann, *J. Appl. Crystallogr.* **2009**, *42*, 339–341.
- [26] a) X. Gonze, B. Amadon, G. Antonius, F. Arnardi, L. Baguet, J.-M. Beuken, J. Bieder, F. Bottin, J. Bouchet, E. Bousquet, N. Brouwer, F. Bruneval, G. Brunin, T. Gavignac, J.-B. Charraud, W. Chen, M. Gôte, S. Gottenier, J. Denier, G. Geneste, P. Ghosez, M. Giantomassi, Y. Gillet, O. Gingras, D. R. Hamann, G. Hautier, X. He, N. Helbig, N. Holzwarth, Y. Jia, F. Jollet, W.

- Lafargue-Dit-Hauret, K. Lejaeghere, M. A. L. Marques, A. Martin, C. Martins, H. P. C. Miranda, F. Naccarato, K. Persson, G. Petretto, V. Planes, Y. Puillon, S. Prokhorenko, F. Ricci, G.-M. Rignanese, A. H. Romero, M. M. Schmitt, M. Torrent, M. J. Van Setten, B. Van Troeye, M. J. Verstraete, G. Zérah, J. W. Zwanziger, *Comput. Phys. Commun.* **2020**, *248*, 107042; b) D. R. Hamann, X. Wu, K. M. Rabe, D. Vanderbilt, *Phys. Rev. B* **2005**, *71*, 035117; c) F. Bottin, S. Leroux, A. Knyazev, G. Zérah, *Comput. Mater. Sci.* **2008**, *42*, 329–336; d) B. Van Troeye, M. Torrent, X. Gonze, *Phys. Rev. B* **2016**, *93*, 144304.
- [27] D. Bende, F. R. Wagner, O. Sichevych, Y. Grin, *Angew. Chem.* **2017**, *129*, 1333–1338; *Angew. Chem. Int. Ed.* **2017**, *56*, 1313–1318.
- [28] a) J. P. Perdew, K. Burke, M. Ernzerhof, *Phys. Rev. Lett.* **1996**, *77*, 3865–3868; b) A. D. Becke, E. R. Johnson, *J. Chem. Phys.* **2006**, *124*, 221101; c) S. Grimme, J. Antony, S. Ehrlich, H. Krieg, *J. Chem. Phys.* **2010**, *132*, 154104.

---

Manuscript received: July 28, 2021  
Revised manuscript received: October 5, 2021





# European Journal of Inorganic Chemistry

Supporting Information

## Synthesis, Structure, and Thermoelastic Properties of $\text{LiSn}_2\text{Br}_3(\text{CN}_2)$ and $\text{Sn}_4\text{Br}_2(\text{CN}_2)_3$

Manuel Löber, Markus Ströbele, Carl P. Romao, and Hans-Jürgen Meyer\*

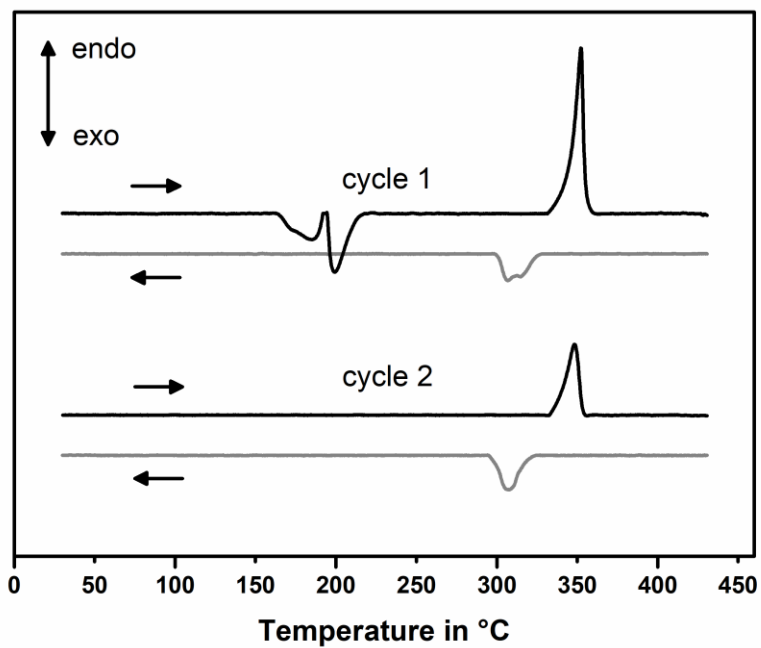


**Figure S1.** DTA of the reaction  $\text{Li}_2(\text{CN}_2) + 2\text{SnBr}_2$  with the formation of  $\text{LiSn}_2\text{Br}_3(\text{CN}_2)$  in cycle 1, with another heating and cooling cycle of the  $(\text{LiSn}_2\text{Br}_3(\text{CN}_2), \text{LiBr})$  product mixture given in cycle 2.

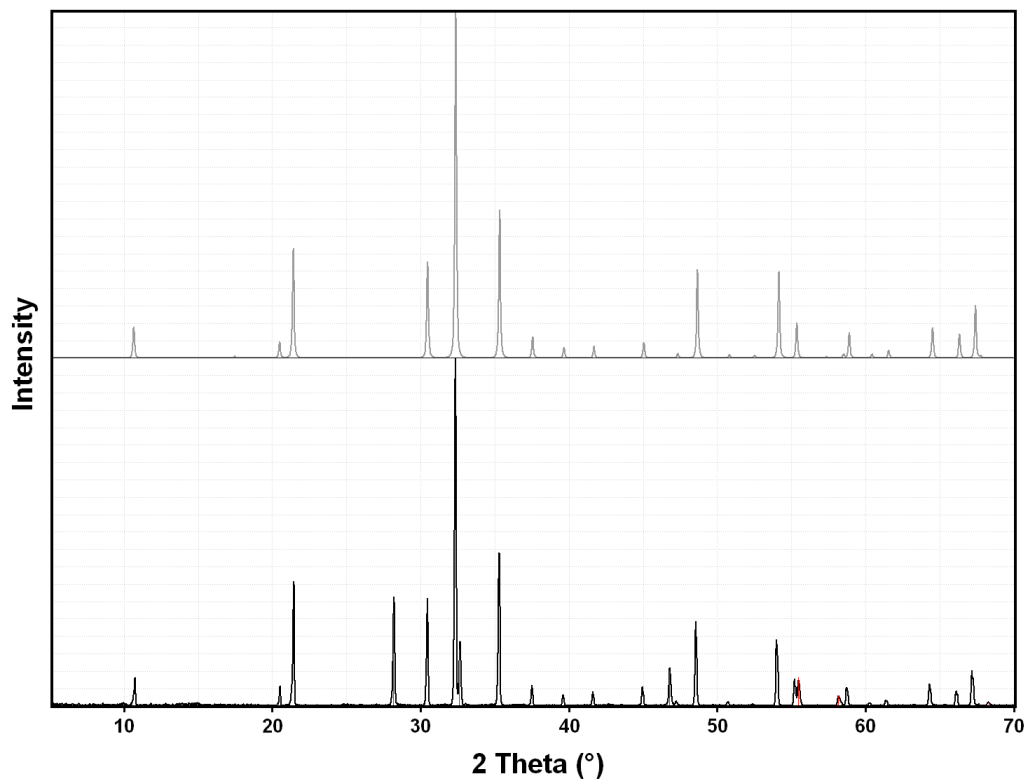


**Figure S2.** PXRD pattern of  $\text{LiSn}_2\text{Br}_3(\text{CN}_2) + \text{LiBr}$  shown in black in comparison with the calculated pattern, shown in grey. The red lines indicate Bragg positions and intensities of  $\text{LiBr}$ .

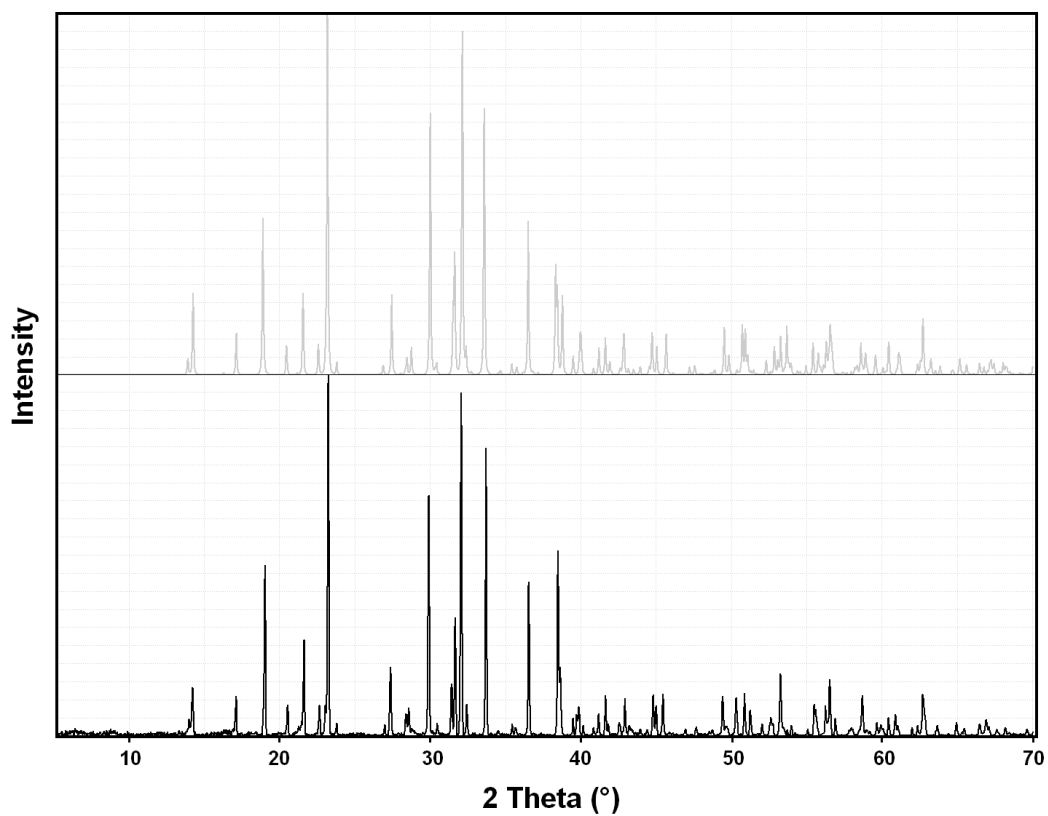


**Figure S3.** PXRD pattern of  $\text{Sn}_4\text{Br}_3(\text{CN}_2)_3$  shown in black in comparison with the calculated pattern, shown in grey. The metathesis salt  $\text{LiBr}$  was washed out with ethanol.

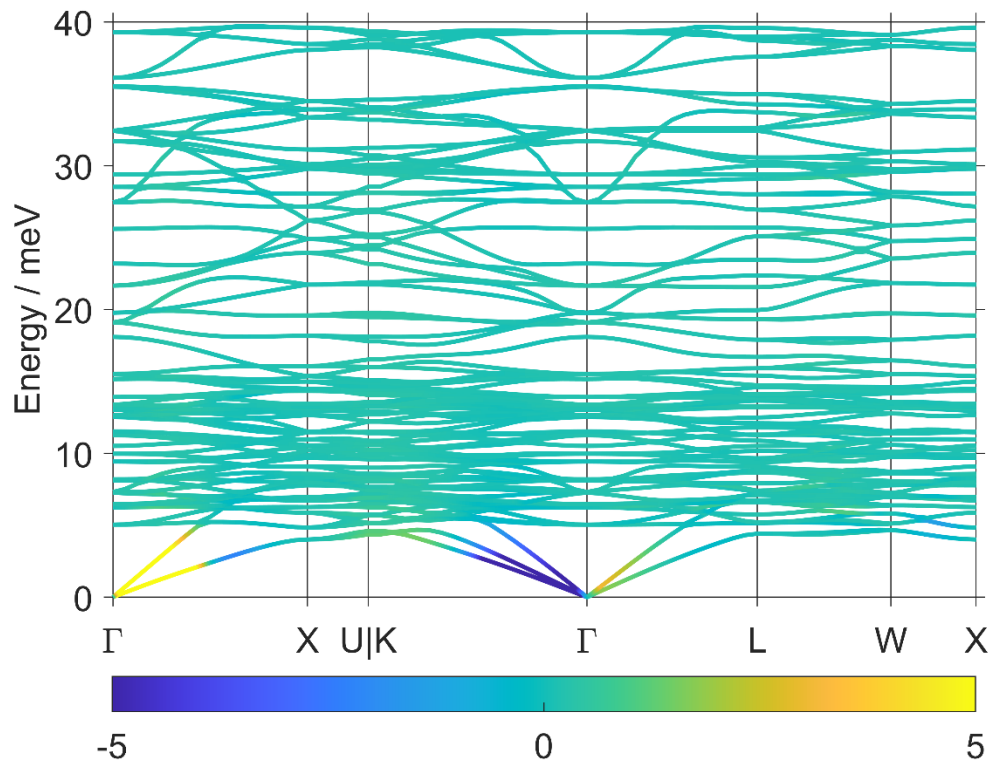


**Figure S4.** Calculated low-energy phonon band structure of  $\text{LiSr}_2\text{Br}_3(\text{CN}_2)$ , with bands coloured by their mode Grüneisen parameters ( $\gamma$ , some values are off-scale).

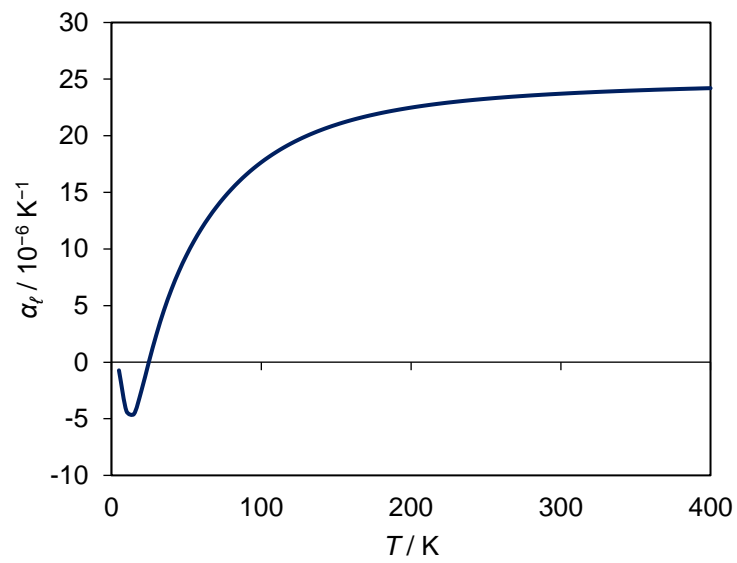
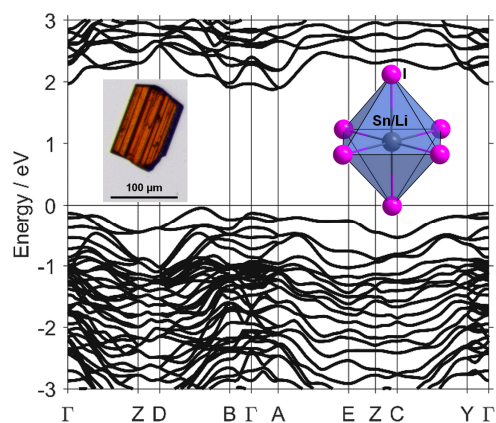


**Figure S5.** Calculated linear thermal expansion coefficient of  $\text{LiSr}_2\text{Br}_3(\text{CN}_2)$  between 5 and 400 K.

# Publication 8

The Lithium Iodostannate  $\text{LiSn}_3\text{I}_7$ : Synthesis, Properties and its Relationship to  $\text{SnI}_2$



<https://doi.org/10.1002/ejic.202100771>

Reprinted with permission from  
*Eur. J. Inorg. Chem.* **2021**, 2021, 4929–4934

Copyright © 2021 Wiley-VCH GmbH



# The Lithium Iodostannate $\text{LiSn}_3\text{I}_7$ : Synthesis, Properties and its Relationship to $\text{SnI}_2$

Manuel Löber,<sup>[a]</sup> Markus Ströbele,<sup>[a]</sup> Klaus Eichele,<sup>[b]</sup> Carl P. Romao,<sup>[a]</sup> and Hans-Jürgen Meyer<sup>\*[a]</sup>

The mixed lithium tin iodide  $\text{LiSn}_3\text{I}_7$  was prepared by reacting  $\text{LiI}$  and  $\text{SnI}_2$  at 300 °C. Single-crystal X-ray diffraction revealed a crystal structure related to that of  $\text{SnI}_2$ , with nearly identical coordination environments of tin atoms. The lithium ion in the structure of  $\text{LiSn}_3\text{I}_7$  shares one crystallographic position with a

tin atom in octahedral voids of  $(\text{LiSn})\text{Sn}_2\text{I}_7$ , as confirmed by solid-state  $^7\text{Li}$ ,  $^{119}\text{Sn}$  and  $^{127}\text{I}$  MAS NMR spectra. DFT band structure calculations show  $\text{LiSn}_3\text{I}_7$  to be a semiconductor with an indirect bandgap on the order of 2 eV.

## Introduction

Binary tin halides are a well-known group of compounds which include divalent and tetravalent tin compounds with  $\text{F}$ ,<sup>[1]</sup>  $\text{Cl}$ ,<sup>[2]</sup>  $\text{Br}$ <sup>[3]</sup> and  $\text{I}$ ,<sup>[4]</sup> as well as mixed-valence tin fluorides ( $\text{Sn}_3\text{F}_8$ <sup>[1c]</sup> and  $\text{Sn}_2\text{F}_6$ <sup>[1e]</sup>). Some promising properties have been reported from research on divalent binary tin halides. For example,  $\text{SnF}_2$  has been investigated as an anode material for lithium-ion batteries.<sup>[5]</sup> The luminescence of  $\text{SnCl}_2$ , as well as of  $\text{SnBr}_2$  have been studied.<sup>[6]</sup> Moreover both,  $\text{SnCl}_2$  and  $\text{SnBr}_2$ , are used as dopants for I-rich tin-based perovskite solar cells, which has improved their stability.<sup>[7]</sup>  $\text{SnCl}_2$  and  $\text{SnI}_2$  are used as precursors for the synthesis of perovskite solar cells.<sup>[8]</sup>

Ionic conductivity was reported for  $\text{SnI}_2$ .<sup>[9]</sup> Furthermore, some theoretical work on  $\text{SnI}_2$  has been carried out, such as the study of thermoelectric and optoelectronic properties of two-dimensional  $\text{SnI}_2$ .<sup>[10]</sup>

More complex systems like ternary tin halides are also known, including alkali halogenidostannates such as  $\text{CsSnCl}_3$ ,<sup>[11]</sup>  $\text{CsSnBr}_3$ <sup>[12]</sup> and  $\text{CsSnI}_3$ <sup>[13]</sup> which are studied for their potential use in perovskite solar cells<sup>[14]</sup> and have been described as less toxic alternatives to the prominent lead compounds  $\text{CsPbX}_3$  ( $X=\text{Cl}$ ,  $\text{Br}$ ,  $\text{I}$ ).<sup>[15]</sup>

Over the last decade, these lead-based perovskite solar cells have reached power conversion efficiencies (PCEs) of up to 25%<sup>[16]</sup> and are considered a potential replacement for silicon-

based solar cells, which suffer from a relatively low PCE, a complex production process (along with high  $\text{CO}_2$  emissions), and high cost.<sup>[17]</sup> Perovskite solar cells are based on an organic-inorganic metal halide with the general formula  $\text{ABX}_3$ , where A is a monovalent cation such as  $\text{MA}^+$  ( $\text{CH}_3\text{NH}_3^+$ ),  $\text{FA}^+$  ( $\text{HC}(\text{NH}_2)_2^+$ ) or  $\text{Cs}^+$ , B a divalent metal cation such as  $\text{Pb}^{2+}$  or  $\text{Sn}^{2+}$  and X a halide anion such as  $\text{Br}^-$  or  $\text{I}^-$ .<sup>[18]</sup> These compounds exhibit the cubic perovskite structure and are used as a light-harvesting-layer.<sup>[19]</sup> Perovskite-based solar cells are characterized by properties such as low synthesis cost, large absorption coefficient, long carrier diffusion length, low exciton binding energies, and many more, making them a promising candidate for applications.<sup>[20]</sup>

For best performances a relatively low bandgap of 1 to 1.4 eV is required, resulting in a theoretical PCE of 33%.<sup>[19]</sup> However, the bandgaps of lead halide perovskites are typically higher.<sup>[21]</sup> A major issue with organic-inorganic metal halides is their low stability to moisture, temperature, and irradiation, due to the used organic cations, so attempts are being made to replace them with inorganic ions, mainly  $\text{Cs}^+$ , with PCEs close to 20% being achieved recently.<sup>[22]</sup> A general critical issue with lead-based perovskite solar cells is the potential release of the toxic lead halide, which is easily dissolved by water.<sup>[15]</sup> Hence, extensive research has been conducted for several years on analogous compounds in which lead is replaced by the less toxic tin.<sup>[15,18,20,23]</sup> Despite the lower bandgap, the current best PCE of a tin-based perovskite solar cell is about 13%, well below the best performance of a lead-based solar cell. In addition, a major challenge is the low air stability of divalent tin halides, which are more easily oxidized from  $\text{Sn}^{2+}$  to  $\text{Sn}^{4+}$ , compared to lead compounds. To solve this issue various approaches like encapsulation of the tin halides or the use of reducing agents are made to prevent the tin halides from oxidation.<sup>[18]</sup>

Inorganic alkali metal-tin-halides are generally known to exist with  $\text{Na}$ ,<sup>[24]</sup>  $\text{K}$ ,<sup>[25]</sup>  $\text{Rb}$ <sup>[26]</sup> and  $\text{Cs}$ <sup>[11–13,27]</sup> but no ternary lithium-tin-halide has been reported in the literature. The only compounds containing the elements Li, Sn and I are  $\text{Li}_{6+x}\text{P}_{1-x}\text{Sn}_x\text{S}_5\text{I}$  with x varying between 0.05 and 0.3,<sup>[28]</sup> and two recently published lithium thiostannate spinels:  $\text{Li}_2\text{MSn}_3\text{S}_8$

[a] M. Löber, Dr. M. Ströbele, Dr. C. P. Romao, Prof. Dr. H.-J. Meyer  
Section for Solid-state and Theoretical Inorganic Chemistry  
Institute of Inorganic Chemistry  
Auf der Morgenstelle 18, 72076 Tübingen, Germany  
E-mail: juergen.meyer@uni-tuebingen.de

[b] Dr. K. Eichele  
Institute of Inorganic Chemistry  
Auf der Morgenstelle 18, 72076 Tübingen, Germany

Supporting information for this article is available on the WWW under <https://doi.org/10.1002/ejic.202100771>

© 2021 The Authors. European Journal of Inorganic Chemistry published by Wiley-VCH GmbH. This is an open access article under the terms of the Creative Commons Attribution Non-Commercial NoDerivs License, which permits use and distribution in any medium, provided the original work is properly cited, the use is non-commercial and no modifications or adaptations are made.

(M=Mg, Fe, Mn, Ni, Co) and  $\text{Li}_{1.66}\text{CuSn}_{3.33}\text{S}_8$ .<sup>[29]</sup> Moreover, the sulfidic compound  $\text{Li}_{0.6}[\text{Li}_{0.2}\text{Sn}_{0.8}\text{S}_2]$  was reported to be a lithium superionic conductor.<sup>[30]</sup>

In the course of our explorative studies of multinary tin carbodiimides<sup>[31]</sup> via solid-state metathesis reactions we have employed mixtures of  $\text{Li}_2(\text{CN})_2$  and  $\text{SnX}_2$ . During such studies we obtained single-crystals of a previously unknown lithium tin iodide, as side phase, with the composition  $\text{LiSn}_3\text{I}_7$ , which is the subject of this study.

## Results and Discussion

### Synthesis and Crystal Structure

Crystalline  $\text{LiSn}_3\text{I}_7$  is obtained when heating a 1:3 molar mixture of  $\text{LiI}$  and  $\text{SnI}_2$  at 200 °C, as confirmed by PXRD measurements.

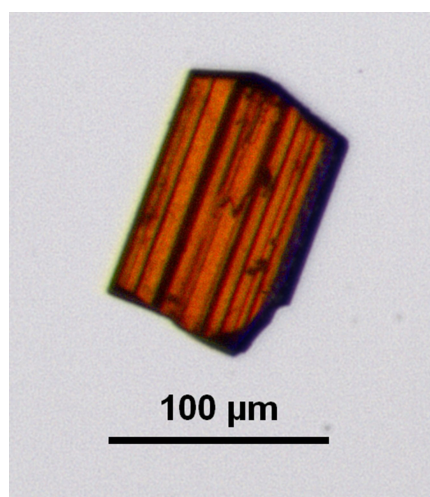


Figure 1. Brownish prismatic crystal of  $\text{LiSn}_3\text{I}_7$ .

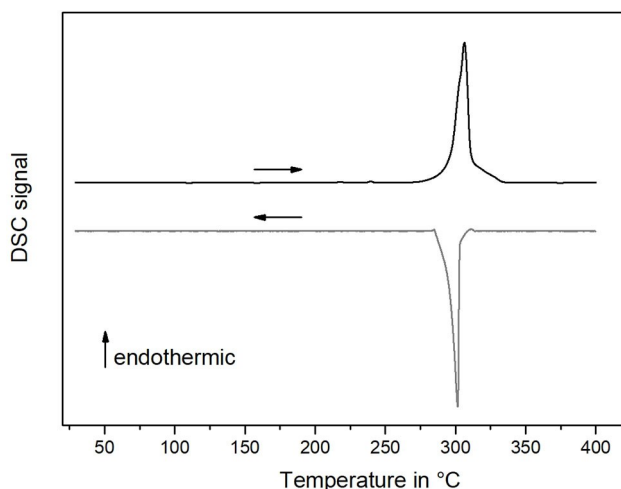
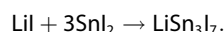


Figure 2. DSC measurement of a 3:1 molar mixture of  $\text{SnI}_2$  and  $\text{LiI}$  from room temperature to 400 °C in a cyclic heating-cooling procedure (see arrows).

Subsequent reactions at 300 °C were chosen to achieve higher yields and better crystallinity of the product:



A crystal of  $\text{LiSn}_3\text{I}_7$ , as obtained upon slow cooling, is depicted in Figure 1.

A DSC measurement (Figure 2) of the reaction mixture did not show a thermal feature that could be assigned to the formation of  $\text{LiSn}_3\text{I}_7$ . However, an endothermic effect was observed upon heating (at a rate of 2 °C/min) to slightly above 300 °C, (onset at 295 °C) as well as an exothermic effect upon cooling at 300 °C (onset at 303 °C), close to the melting point of  $\text{SnI}_2$  (320 °C<sup>[32]</sup>). These two effects are assigned to the melting and recrystallization of the title compound, which was confirmed visually when the reaction mixture was heated in a fused silica tube.

The crystal structure of  $\text{LiSn}_3\text{I}_7$  was solved and refined from recorded single-crystal X-ray diffraction data in the monoclinic space group  $C2/m$ . The  $\text{Li1/Sn1}$  ratio at the split position converged close to a 0.5/0.5 occupancy (see Table 2). Some details of the single-crystal measurement and the refinement are displayed in Table 1. Wyckoff positions, site occupation factors, atomic coordinates and isotropic displacement parameters of  $\text{LiSn}_3\text{I}_7$  are displayed in Table 2. Tin atoms occupy two distinct crystallographic positions in  $\text{LiSn}_3\text{I}_7$ , with approximately

Table 1. Crystallographic and refinement data of  $\text{LiSn}_3\text{I}_7$  in comparison to some relevant data of  $\text{SnI}_2$ .

	$\text{LiSn}_3\text{I}_7$	$\text{SnI}_2$ <sup>[4b]</sup>
CSD No.	2045613	
Space group	$C2/m$	$C2/m$
Unit cell dimensions (Å)	$a = 14.2850(4)$ $b = 4.4140(3)$ $c = 13.2188(3)$	$a = 14.17(5)$ $b = 4.54(2)$ $c = 10.87(4)$
Angle (°)	$\beta = 105.445(3)$	$\beta = 92.0(2)$
Volume (Å <sup>3</sup> )	797.78(3)	698.09(433)
Z	2	6
$\mu$ (Mo-K $\alpha$ ) mm <sup>-1</sup>	18.20	
Calculated density (gcm <sup>-3</sup> )	5.22	
2 $\theta$ range for data collection	9.60 to 59.15	
Total number of reflections	23279	
Independent reflections	1252	
Refined parameters	37	
$R_1$	0.0162	
$wR_2$	0.0347	
Goodness-of-fit on $F^2$	1.064	

Table 2. Wyckoff positions, site occupation factors (s.o.f.), atomic coordinates and isotropic displacement parameters ( $U_{eq}$  in Å<sup>2</sup>) for  $\text{LiSn}_3\text{I}_7$ .

Atom	Wyck.	s.o.f.	x	y	z	$U_{eq}$ <sup>[a]</sup>
Sn1	4i	0.513(2)	0.12272(4)	0	0.07202(5)	0.0162(2)
Li1	4i	0.487(2)	0.12272(4)	0	0.07202(5)	0.0162(2)
Sn2	4i		0.68327(2)	0	0.33761(3)	0.01645(8)
I1	4i		0.52252(2)	1/2	0.29788(2)	0.01332(7)
I2	4i		0.65220(2)	0	0.55092(2)	0.01012(7)
I3	4i		0.24040(2)	1/2	0.14310(2)	0.01930(8)
I4	2b		1/2	0	0	0.0223(1)

[a]  $U_{eq}$  is defined as one-third of the trace of the orthogonalized  $U_{ij}$  tensor.



octahedral and approximately mono-capped trigonal prismatic environments, as displayed in Figure 3. However, the octahedral site in the structure of  $\text{LiSn}_3\text{I}_7$  is a shared position that combines

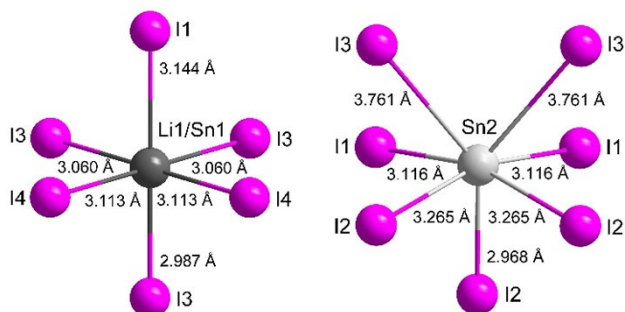


Figure 3. Approximately octahedral (Li1/Sn1) and capped trigonal prismatic (Sn2) coordination environments of lithium and tin in  $\text{LiSn}_3\text{I}_7$ .

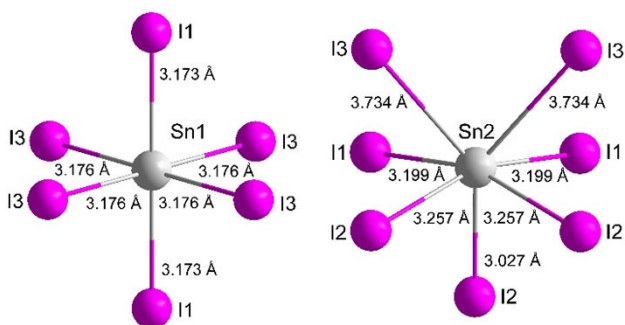


Figure 4. Approximately octahedral (Sn1) and capped trigonal prismatic (Sn2) coordination environments of tin in  $\text{SnI}_2$ .

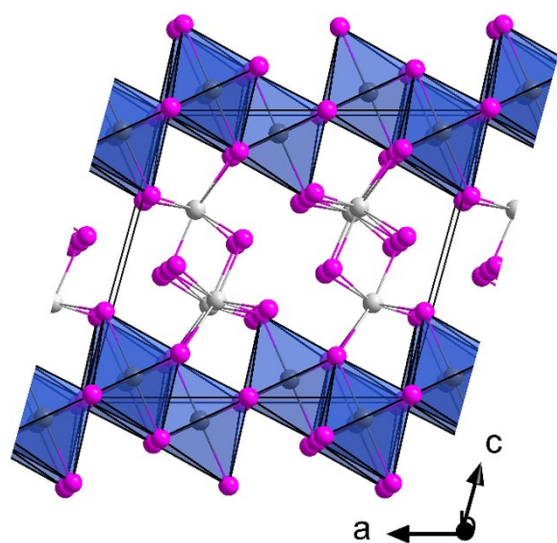


Figure 5. The crystal structure of  $\text{LiSn}_3\text{I}_7$  in the  $ac$  plane. Tin atoms are shown in grey, with the mixed Li1/Sn1 site being situated inside blue octahedra of iodide atoms (pink).

lithium (Li1) and tin (Sn1) as  $(\text{LiSn})\text{Sn}_2\text{I}_7$ . The split (Li1/Sn1) site is surrounded by three crystallographically distinct iodine atoms (I1, I3, I4), and the (Li1/Sn1)-I bond lengths vary between 2.99 and 3.14 Å (Figure 3).

A very similar environment of tin atoms can be found in the crystal structure of  $\text{SnI}_2$  which crystallizes in the same space group ( $C2/m$ ) and with related  $a$  and  $b$  lattice parameters (Table 1). A comparison of interatomic Sn-I distances in both compounds reveals significantly shorter values for the mixed Li1/Sn1 site than for Sn1 in  $\text{SnI}_2$ , as can be seen in Figure 3 and Figure 4. The range of Sn-I distances of the mixed Li1/Sn1 site in  $\text{LiSn}_3\text{I}_7$  (2.99 to 3.14 Å) covers more or less the bond lengths between the Li-I distance in cubic  $\text{LiI}$  (3.01 Å)<sup>[33]</sup> and the Sn-I distance in  $\text{SnI}_2$  (3.18 Å).

The seven-coordinated tin (Sn2) is surrounded by three crystallographically distinct iodine atoms (I1, I2 and I3) in both structures, ( $\text{SnI}_2$  and  $\text{LiSn}_3\text{I}_7$ ), whereby the longer distances with I3 are likely caused by a directional lone-pair effect of  $\text{Sn}^{2+}$  on the Sn2 position. Iodine atoms, octahedrally surrounding Sn1 in  $\text{SnI}_2$ , and (Li1/Sn1) in  $\text{LiSn}_3\text{I}_7$ , form infinite chains of trans-edge sharing octahedra, running parallel to their respective  $b$  axis directions (Figure 5 and Figure 6). An additional edge-sharing connectivity of octahedra is present in the structure of  $\text{LiSn}_3\text{I}_7$  parallel to the  $a$  axis. A comparative inspection of both structures shows that differences are essentially due to the shift of Sn1 away from the centre of symmetry (0,0,0), with the generation of another symmetry equivalent octahedral chain when going from the structure of  $\text{SnI}_2$  to that of  $\text{LiSn}_3\text{I}_7$  within the space group  $C2/m$ .

Disordered structures with lithium and tin are known to exist for the sulfidic compounds  $\text{Li}_x\text{Sn}_{1-x}\text{S}_2$ <sup>[34]</sup> with site occupation factors of 0.89 for Li and 0.11 for tin and for  $\text{Ba}_6\text{Li}_{2.67}\text{Sn}_{4.33}\text{S}_{16}$ <sup>[35]</sup> with site occupation factors for Li and Sn of 0.05 and 0.95, 0.08 and 0.92, 0.03 and 0.97.

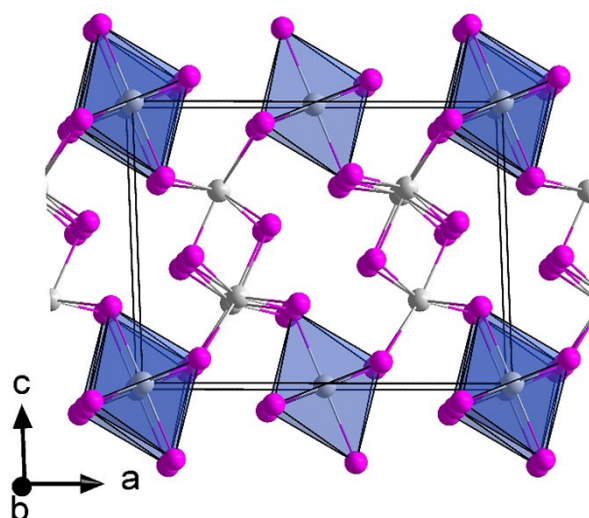


Figure 6. The crystal structure of  $\text{SnI}_2$  in the  $ac$  plane. Tin is shown in light grey and iodine in pink.

Similar unit cell parameters to those of  $\text{LiSn}_3\text{I}_7$  were reported for the compound  $\text{AgSn}_4\text{I}_9$  in the 1980s but without further crystal structure data.<sup>[36]</sup>

### Solid-State NMR

In order to study the incorporation of lithium into the structure of  $\text{SnI}_2$ , we have studied the  $^7\text{Li}$ ,  $^{127}\text{I}$ , and  $^{119}\text{Sn}$  solid-state NMR spectra of  $\text{LiSn}_3\text{I}_7$  and reference materials. The  $^7\text{Li}$  MAS NMR spectrum of  $\text{LiSn}_3\text{I}_7$  shows an intense, single peak at  $-3.9$  ppm ( $\Delta\nu_{1/2} = 255$  Hz), which is very similar to the chemical shift in  $\text{LiI}$ ,  $-4.3$  ppm ( $\Delta\nu_{1/2} = 249$  Hz), as shown in Figure 7. Given that the  $\text{Li-I}$  distances in  $\text{LiSn}_3\text{I}_7$ ,  $2.99\text{--}3.14$  Å, are very similar to those in  $\text{LiI}$ ,  $3.013$  Å,<sup>[33]</sup> this observation is plausible. However, in contrast to  $\text{LiI}$ , the  $^{127}\text{I}$  MAS NMR spectrum of  $\text{LiSn}_3\text{I}_7$  shows only a very weak and broad peak at  $405$  ppm ( $\Delta\nu_{1/2}$  ca.  $4.5$  kHz), compared to the very strong signal in  $\text{LiI}$  at  $411$  ppm ( $\Delta\nu_{1/2} = 1.1$  kHz) or  $\text{KI}$ ,  $199$  ppm ( $\Delta\nu_{1/2} = 230$  Hz). This can be ascribed to a small amount of residual  $\text{LiI}$  on the surface of  $\text{LiSn}_3\text{I}_7$  (not detectable by PXRD). The  $^{127}\text{I}$  chemical shift difference obtained between  $\text{LiI}$  and  $\text{KI}$  is in line with earlier reports in the literature and highlights the sensitivity of this chemical shift on the environment,<sup>[37]</sup> thus supporting the assignment of the weak broad peak to residual  $\text{LiI}$ . A  $^{127}\text{I}$  NQR study of the parent compound  $\text{SnI}_2$  indicated that the  $^{127}\text{I}$  nuclear quadrupole coupling constants are in the range  $284$  to  $406$  MHz,<sup>[38]</sup> much greater than the  $^{127}\text{I}$  Larmor frequency at our applied magnetic field. Hence, the iodine atoms in  $\text{SnI}_2$  or  $\text{LiSn}_3\text{I}_7$  are not expected to contribute to the  $^{127}\text{I}$  MAS NMR spectra.<sup>[39]</sup> The presence of iodine has a pronounced effect on the  $^{119}\text{Sn}$  MAS spectra of  $\text{LiSn}_3\text{I}_7$  and  $\text{SnI}_2$ , the latter presented recently<sup>[40]</sup> and reported to have a chemical shift of  $-529$  ppm. However, there are two crystallographically different tin sites present in  $\text{SnI}_2$ . Its  $^{119}\text{Sn}$  MAS NMR spectra shown in the literature, and obtained here for comparison, could indeed be interpreted in two different

ways: (1) a single site with associated spinning sidebands, or (2) as two overlapping sideband patterns. This ambiguity arises because of the intrinsically broad peaks (vide infra) and the achievable spinning rates imposed practically. The  $^{119}\text{Sn}$  MAS NMR spectrum of  $\text{SnI}_2$  obtained at a spinning rate of  $10$  kHz has been decomposed, in agreement with the crystal structure,<sup>[4b]</sup> into two different sideband families, with isotropic chemical shifts of  $\delta_{\text{iso}} = -433$  ( $\Delta\nu_{1/2} = 9.96$  kHz) and  $-529$  ppm ( $\Delta\nu_{1/2} = 6.60$  kHz), in a 1:2 ratio (see supporting information). The  $^{119}\text{Sn}$  MAS spectrum of  $\text{LiSn}_3\text{I}_7$  is very similar to that of  $\text{SnI}_2$ , but even broader:  $\delta_{\text{iso}} = -310$  ( $\Delta\nu_{1/2} = 10.5$  kHz) and  $-454$  ppm ( $\Delta\nu_{1/2} = 10.3$  kHz) and shifted by about  $80\text{--}120$  ppm to higher frequencies.

### Electronic Structure

The DFT-calculated electronic band structure of  $\text{LiSn}_3\text{I}_7$  is shown in Figure 8 below. In order to calculate the band structure, an approximate structure accounting for the disorder at the  $\text{LiI}/\text{SnI}$  sites had to be employed by the inclusion of two  $\text{Li}$  atoms per unit cell. The energy differences between the different orderings of the  $\text{Li}$  atoms were found to be fairly small, on the order of  $1$  kJ/mol. The ordering with the two  $\text{Li}$  atoms per unit cell in the same layer was found to be more stable than the one with  $\text{Li}$  atoms in different layers; the more stable ordering was used for the band structure calculation. As Figure 8 shows, this calculation predicts  $\text{LiSn}_3\text{I}_7$  to be a semiconductor, with an indirect bandgap of approximately  $2$  eV. The states near the Fermi level have predominantly  $\text{I}$  character, with some  $\text{Sn}$  character and also some states which do not project onto the atomic spheres and can be considered as interstitial or valence electrons. There are almost no valence states which project onto the  $\text{Li}$  spheres, indicating that  $\text{Li}$  is fully oxidised to  $\text{Li}^+$ . The band structure near the Fermi level is very similar to that of  $\text{SnI}_2$ , besides  $\text{SnI}_2$  having a somewhat smaller calculated bandgap ( $\approx 1.5$  eV).<sup>[41]</sup>

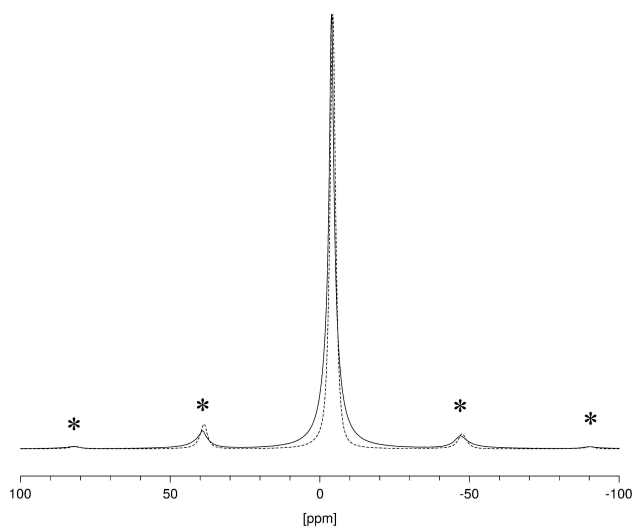


**Figure 7.**  $^7\text{Li}$  MAS NMR spectra of  $\text{LiSn}_3\text{I}_7$  and  $\text{LiI}$  (dashed line) at spinning rates of  $5$  kHz. Spinning sidebands are marked by asterisks.

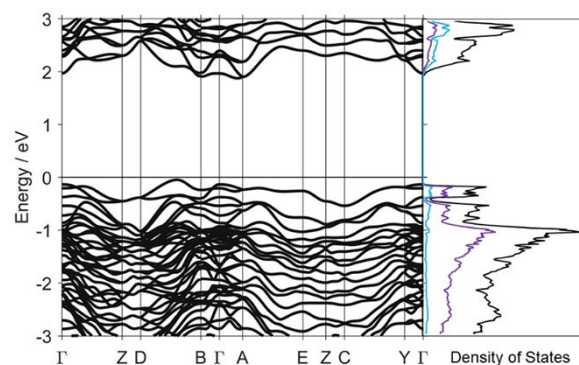


**Figure 8.** The calculated electronic band structure of  $\text{LiSn}_3\text{I}_7$ . The density of states (black) and its projection onto the  $\text{Sn}$  (blue) and  $\text{I}$  (purple) atomic spheres are shown at right. The density of states corresponding to  $\text{Li}$  in this energy region is negligible. Special points in and paths through the Brillouin zone were chosen following Ref. [42].

## Conclusion

The new compound  $\text{LiSn}_3\text{I}_7$  was prepared as a crystalline single-phase powder (according to PXRD) from  $\text{SnI}_2$  and  $\text{LiI}$  at  $300^\circ\text{C}$ , slightly below its melting point. The structure, as determined from a brownish single crystal, crystallizes in the same space group  $C2/m$  as  $\text{SnI}_2$ . Moreover, there is an intriguing structural relationship between  $\text{LiSn}_3\text{I}_7$  and  $\text{SnI}_2$ . One lithium and one tin atom share a mixed Li/Sn position in the structure (as  $(\text{LiSn})\text{Sn}_2\text{I}_7$ ) situated in an octahedral environment of iodine atoms. The  $^7\text{Li}$  solid-state MAS NMR spectrum of Li in  $\text{LiSn}_3\text{I}_7$  is only slightly different from that of the corresponding signal in  $\text{LiI}$ . DFT band structure calculations predict  $\text{LiSn}_3\text{I}_7$  to be a semiconductor with an indirect bandgap in the order of 2 eV, in accordance with the orange to brown body colour of the crystalline powder.

## Experimental Section

### Synthesis

The starting materials  $\text{SnI}_2$  (Sigma-Aldrich, anhydrous, 99.99%) and  $\text{LiI}$  (Sigma-Aldrich, anhydrous beads, 99.999%) were mixed and pestled under dry argon atmosphere (glove box) in a 3:1 molar ratio (100 mg), filled into a silica ampoule (length  $\approx 5$  cm, ID  $\approx 1$  cm) and fused therein under vacuum. The sample was heated to  $300^\circ\text{C}$  at 2 K/min in a crucible furnace for 20 h and cooled to room temperature at 2 K/min. The reaction product was obtained as an orange to brownish crystalline powder in high yield ( $> 95\%$ ), without any side phase being visible in the powder XRD diffraction pattern. Orange to brownish prismatic single crystals were obtained, when cooling the above-mentioned reaction mixture to room temperature, using a cooling rate of 0.1 K/min.

Both crystals and powder cannot be treated in air and decompose after few minutes.

### Thermoanalytic Studies

A study of the reaction by differential scanning calorimetry (DSC) was performed with a DSC 204 F1 Phoenix (Fa. Netzsch, Selb, Germany). The starting materials were enclosed in a gold-plated (5  $\mu\text{m}$ ) steel autoclave (volume 100  $\mu\text{L}$ ; BFT 94; Bächler Feintech AG, Hölstein, Switzerland) under a dry argon atmosphere (glovebox). The reaction of educts was analyzed between room temperature and  $400^\circ\text{C}$  at a heating and cooling rate of 2 K/min.

### Powder X-ray Diffraction

PXRD patterns were recorded on well-ground powders using a StadiP diffractometer (Stoe, Darmstadt) with Ge-monochromated  $\text{Cu-K}\alpha_1$  radiation and a Mythen1 Detector.

### Single-Crystal X-ray Diffraction

Data collection was performed on a Rigaku XtaLAB Synergy-S single-crystal X-ray diffractometer equipped with HyPix-6000HE detector and monochromated  $\text{Mo-K}\alpha$  radiation ( $\lambda = 0.71073 \text{ \AA}$ ) at 100 K. The X-ray intensities were corrected for absorption with a numerical method using CrysAlisPro 1.171.41.67a (Rigaku Oxford Diffraction, 2020). The structure was solved by direct methods

(SHELXS)<sup>[43]</sup> and full-matrix least-squares structure refinements, performed with SHELXL-2014<sup>[44]</sup> as implemented in Olex2 1.3-ac4.<sup>[45]</sup>

### Density Functional Theory

Density functional theory (DFT) calculations were performed using the Abinit software package (v. 9) using the projector-augmented wave (PAW) method.<sup>[46]</sup> Monkhorst-Pack grids of k-points<sup>[47]</sup> and plane-wave basis set energy cutoffs were chosen after convergence studies to 1% in pressure. Structural relaxation to a pressure  $< 1$  MPa was performed prior to calculation of the electronic band structure. The Perdew-Burke-Erzenhof exchange-correlation functional was used<sup>[48]</sup> with the dispersion correction of Grimme.<sup>[49]</sup> Example input files are available as part of the Supporting Information.

### Solid-state NMR

Solid-state NMR spectra were obtained on a Bruker Avance III HD 300 wide-bore NMR spectrometer ( $B_0 = 7.05$  T) operating at 116.64 ( $^7\text{Li}$ ), 60.04 ( $^{127}\text{I}$ ), or 111.92 MHz ( $^{119}\text{Sn}$ ). Samples were packed into 4 mm o.d. zirconia rotors under the inert atmosphere of a glove box. Spectra were acquired after a  $1 \mu\text{s}$  pulse ( $30^\circ$  pulse). Referencing against  $\Xi = 38.863797\%$  ( $^7\text{Li}$ ), 20.007486% ( $^{127}\text{I}$ ), or 37.290632% ( $^{119}\text{Sn}$ )<sup>69</sup> was achieved by the substitution method: an external sample of  $\text{CHCl}_3$  in acetone in a zirconia rotor was spun at 1.5 kHz and the external magnetic field was adjusted such that the  $^1\text{H}$  chemical shift of  $\text{CHCl}_3$  matched a predetermined chemical shift wrt. external 1% TMS in  $\text{CHCl}_3$ .

Deposition Number 2045613 (for  $\text{LiSn}_3\text{I}_7$ ) contains the supplementary crystallographic data for this paper. These data are provided free of charge by the joint Cambridge Crystallographic Data Centre and Fachinformationszentrum Karlsruhe Access Structures service [www.ccdc.cam.ac.uk/structures](http://www.ccdc.cam.ac.uk/structures).

## Acknowledgements

Funding if this work by the Deutsche Forschungsgemeinschaft (DFG) through grant ME 914/25-2 and support by the state of Baden-Württemberg through bwHPC and the Deutsche Forschungsgemeinschaft (DFG) through grant no INST 40/575-1 FUGG (JUSTUS 2 cluster) are gratefully acknowledged. Open Access funding enabled and organized by Projekt DEAL.

## Conflict of Interest

The authors declare no conflict of interest.

**Keywords:** DFT · Semiconductor · Solid-state NMR · Solid-state reaction · Tin halide

- [1] a) G. Bergerhoff, *Acta Crystallogr.* **1962**, *15*, 509; b) R. Hoppe, W. Dähne, *Naturwissenschaften* **1962**, *49*, 254–255; c) M. F. A. Dove, R. King, T. J. King, *J. Chem. Soc. Chem. Commun.* **1973**, 944–945; d) G. Denes, J. Pannetier, J. Lucas, *J. Solid State Chem.* **1980**, *33*, 1–11; e) N. Ruchaud, C. Mirambet, L. Fournes, J. Grannec, J. L. Soubeyrou, *Z. Anorg. Allg. Chem.* **1990**, *590*, 173–180.

- [2] a) J. M. Van den Berg, *Acta Crystallogr.* **1961**, *14*, 1002–1003; b) J. M. Leger, J. Haines, A. Atouf, *J. Phys. Chem. Solids* **1996**, *57*, 7–16; c) H. Reuter, R. Pawlak, *Z. Anorg. Allg. Chem.* **2000**, *626*, 925–929.
- [3] a) P. Brand, H. Sackmann, *Acta Crystallogr.* **1963**, *16*, 446–451; b) I. Abrahams, D. Z. Demetriou, *J. Solid State Chem.* **2000**, *149*, 28–32; c) P. Eckold, W. Hügel, R. E. Dinnebie, R. Niewa, *Z. Anorg. Allg. Chem.* **2015**, *641*, 1467–1472.
- [4] a) R. G. Dickinson, *J. Am. Chem. Soc.* **1923**, *45*, 958–962; b) R. A. Howie, W. Moser, I. C. Trevena, *Acta Crystallogr.* **1972**, *B28*, 2965–2971.
- [5] S. Bouazza, A. Saberi, M. Willert-Porada, *Mater. Lett.* **2011**, *65*, 1334–1336.
- [6] a) J. Nara, S. Adachi, *J. Appl. Phys.* **2011**, *109*, 083539; b) Y. Yamasaki, N. Ohno, *Int. J. Mod. Phys. B* **2001**, *15*, 4009–4012.
- [7] A. Baltakesmez, B. Güzeldir, Y. Alkan, M. Sağlam, M. Biber, *Opt. Mater.* **2020**, *110*, 110524.
- [8] N. Kumari, S. R. Patel, J. V. Gohel, *J. Mater. Sci. Mater. Electron.* **2018**, *29*, 18144–18150.
- [9] T. A. Kuku, *Solid State Ionics* **1986**, *20*, 217–222.
- [10] A. Betal, J. Bera, S. Sahu, *Comput. Mater. Sci.* **2021**, *186*, 109977.
- [11] F. R. Poulsen, S. E. Rasmussen, *Acta Chem. Scand.* **1970**, *24*, 150–156.
- [12] J. D. Donaldson, J. Silver, S. Hadjiminolis, S. D. Ross, *J. Chem. Soc. Dalton Trans.* **1975**, 1500–1506.
- [13] P. Mauersberger, F. Huber, *Acta Crystallogr.* **1980**, *B36*, 683–684.
- [14] L.-J. Chen, C.-R. Lee, Y.-J. Chuang, Z.-H. Wu, C. Chen, *J. Phys. Chem. Lett.* **2016**, *7*, 5028–5035.
- [15] G. Nasti, A. Abate, *Adv. Energy Mater.* **2020**, *10*, 1902467.
- [16] K. J. Savill, A. M. Ulatowski, L. M. Herz, *ACS Energy Lett.* **2021**, *6*, 2413–2426.
- [17] U. Krishnan, M. Kaur, M. Kumar, A. Kumar, *J. Photonics Energy* **2019**, *9*, 021001.
- [18] J. Cao, F. Yan, *Energy Environ. Sci.* **2021**, *14*, 1286–1325.
- [19] Q. Tai, K.-C. Tang, F. Yan, *Energy Environ. Sci.* **2019**, *12*, 2375–2405.
- [20] A. Toshiwal, V. Kheraj, *Sol. Energy* **2017**, *149*, 54–59.
- [21] J. Werner, T. Moot, T. A. Gossett, I. E. Gould, A. F. Palmstrom, E. J. Wolf, C. C. Boyd, M. F. A. M. van Hest, J. M. Luther, J. J. Berry, M. D. McGehee, *ACS Energy Lett.* **2020**, *5*, 1215–1223.
- [22] F.-Z. Qiu, M.-H. Li, J.-J. Qi, Y. Jiang, J.-S. Hu, *Aggregate* **2021**, *2*, 66–83.
- [23] a) T. C. Jellicoe, J. M. Richter, H. F. J. Glass, M. Tabachnyk, R. Brady, S. E. Dutton, A. Rao, R. H. Friend, D. Credgington, N. C. Greenham, M. L. Böhm, *J. Am. Chem. Soc.* **2016**, *138*, 2941–2944; b) J. Li, C. C. Stoumpos, G. G. Trimarchi, I. Chung, L. Mao, M. Chen, M. R. Wasielewski, L. Wang, M. G. Kanatzidis, *Chem. Mater.* **2018**, *30*, 4847–4856; c) C. Liu, J. Tu, X. Hu, Z. Huang, X. Meng, J. Yang, X. Duan, L. Tan, Z. Li, Y. Chen, *Adv. Funct. Mater.* **2019**, *29*, 1808059; d) X. Liu, Y. Wang, T. Wu, X. He, X. Meng, J. Barbaud, H. Chen, H. Segawa, X. Yang, L. Han, *Nat. Commun.* **2020**, *11*, 2678.
- [24] a) R. R. McDonald, A. C. Larson, D. T. Cromer, *Acta Crystallogr.* **1964**, *17*, 1104–1108; b) G. Bergerhoff, L. Goost, *Acta Crystallogr.* **1970**, *B26*, 19–23; c) G. Benner, R. Hoppe, *J. Fluorine Chem.* **1990**, *48*, 219–227; d) Z. Zhang, H. D. Lutz, *J. Solid State Chem.* **1995**, *115*, 158–164.
- [25] a) J. A. Lerbscher, J. Trotter, *Acta Crystallogr.* **1976**, *B32*, 2671–2672; b) T. Higashi, S. Syoyama, K. Osaki, *Acta Crystallogr.* **1979**, *B35*, 144–146; c) S. Vilminot, R. Bachmann, H. Schulz, *Solid State Ionics* **1983**, *9*, 559–562; d) J. D. Foulon, J. Durand, A. Larbot, L. Cot, A. Soufiane, *Eur. J. Solid State Inorg. Chem.* **1993**, *30*, 87–99; e) D. Becker, H. P. Beck, *Z. Anorg. Allg. Chem.* **2004**, *630*, 1924–1932.
- [26] a) J. A. A. Ketelaar, A. A. Rietdijk, C. H. van Staveren, *Recl. Trav. Chim. Pays-Bas* **1937**, *56*, 907–908; b) W. Werker, *Recl. Trav. Chim. Pays-Bas* **1939**, *58*, 257–258; c) T. B. Brill, R. C. Gearhart, W. A. Welsh, *J. Magn. Reson.* **1974**, *13*, 27–37; d) G. Thiele, B. R. Serr, *Z. Kristallogr. Cryst. Mater.* **1995**, *210*, 64–64; e) P. Berastegui, S. Hull, S. G. Eriksson, *J. Solid State Chem.* **2010**, *183*, 373–378; f) T. T. Tran, P. S. Halasyamani, *J. Solid State Chem.* **2014**, *210*, 213–218.
- [27] a) M. J. Durand, J. L. Galigne, A. Lari-Lavassani, *J. Solid State Chem.* **1976**, *16*, 157–160; b) I. Abrahams, D. Z. Demetriou, R. T. Kroemer, H. Taylor, M. Motevalli, *J. Solid State Chem.* **2001**, *160*, 382–387; c) C. C. Stoumpos, C. D. Malliakas, M. G. Kanatzidis, *Inorg. Chem.* **2013**, *52*, 9019–9038; d) D. H. Fabini, G. Laurita, J. S. Bechtel, C. C. Stoumpos, H. A. Evans, A. G. Kontos, Y. S. Raptis, P. Falaras, A. Van der Ven, M. G. Kanatzidis, R. Seshadri, *J. Am. Chem. Soc.* **2016**, *138*, 11820–11832; e) B. M. Benin, D. N. Dirin, V. Morad, M. Wörle, S. Yakunin, G. Rainò, O. Nazarenko, M. Fischer, I. Infante, M. V. Kovalenko, *Angew. Chem. Int. Ed.* **2018**, *57*, 11329–11333; *Angew. Chem.* **2018**, *130*, 11499–11503.
- [28] S. Ohno, B. Helm, T. Fuchs, G. Dewald, M. A. Kraft, S. P. Culver, A. Senyshyn, W. G. Zeier, *Chem. Mater.* **2019**, *31*, 4936–4944.
- [29] M. A. Quintero, S. Hao, S. V. Patel, J.-K. Bao, X. Zhou, Y.-Y. Hu, C. Wolverton, M. G. Kanatzidis, *Chem. Mater.* **2021**, *33*, 2080–2089.
- [30] T. Holzmann, L. M. Schoop, M. N. Ali, I. Moudrakovski, G. Gregori, J. Maier, R. J. Cava, B. V. Lotsch, *Energy Environ. Sci.* **2016**, *9*, 2578–2585.
- [31] M. Löber, K. Dolabdjian, M. Ströbele, C. P. Romao, H.-J. Meyer, *Inorg. Chem.* **2019**, *58*, 7845–7851.
- [32] C. S. Yoder, S. Shenk, R. W. Schaeffer, B. Chan, M. Molinaro, S. Morissey, C. H. Yoder, *J. Chem. Educ.* **1997**, *74*, 575.
- [33] D. Fischer, A. Müller, M. Jansen, *Z. Anorg. Allg. Chem.* **2004**, *630*, 2697–2700.
- [34] A. Kuhn, T. Holzmann, J. Nuss, B. V. Lotsch, *J. Mater. Chem. A* **2014**, *2*, 6100–6106.
- [35] R.-H. Duan, R.-A. Li, P.-F. Liu, H. Lin, Y. Wang, L.-M. Wu, *Cryst. Growth Des.* **2018**, *18*, 5609–5616.
- [36] R. Blachnik, U. Stöter, *Thermochim. Acta* **1987**, *112*, 47–50.
- [37] a) H. Shigenobu, H. Kikuko, *Bull. Chem. Soc. Jpn.* **1990**, *63*, 913–919; b) H. Shigenobu, H. Kikuko, *J. Phys. Chem. Solids* **1992**, *53*, 239–248; c) C. M. Schurz, R. Niewa, T. Schleid, *Solid State Sci.* **2020**, *99*, 106047; d) W. Gauß, S. Günther, A. R. Haase, M. Kerber, D. Kessler, J. Kronenbitter, H. Krüger, O. Lutz, A. Nolle, P. Schrade, M. Schüle, G. E. Sieglösch, *Z. Naturforsch. A* **1978**, *33*, 934–939.
- [38] T. J. Bastow, H. J. Whitfield, *J. Magn. Reson.* **1980**, *37*, 269–274.
- [39] C. M. Widdifield, D. L. Bryce, *J. Phys. Chem. A* **2010**, *114*, 10810–10823.
- [40] J. Pascual, G. Nasti, M. H. Aldamasy, J. A. Smith, M. Flatken, N. Phung, D. Di Girolamo, S.-H. Turren-Cruz, M. Li, A. Dallmann, R. Avolio, A. Abate, *Mater. Adv.* **2020**, *1*, 1066–1070.
- [41] P. Ravindran, A. Delin, R. Ahuja, B. Johansson, S. Auluck, J. M. Wills, O. Eriksson, *Phys. Rev. B* **1997**, *56*, 6851–6861.
- [42] Y. Hinuma, G. Pizzi, Y. Kumagai, F. Oba, I. Tanaka, *Comput. Mater. Sci.* **2017**, *128*, 140–184.
- [43] G. M. Sheldrick, University of Göttingen (Göttingen, Germany), **1997**.
- [44] G. M. Sheldrick, *Acta Crystallogr.* **2015**, *C71*, 3–8.
- [45] O. V. Dolomanov, L. J. Bourhis, R. J. Gildea, J. A. K. Howard, H. Puschmann, *J. Appl. Crystallogr.* **2009**, *42*, 339–341.
- [46] a) X. Gonze, B. Amadon, G. Antonius, F. Arnardi, L. Baguet, J.-M. Beuken, J. Bieder, F. Bottin, J. Bouchet, E. Bousquet, N. Brouwer, F. Bruneval, G. Brunin, T. Gavnignac, J.-B. Charraud, W. Chen, M. Gôté, S. Gottenier, J. Denier, G. Geneste, P. Ghosez, M. Giantomassi, Y. Gillet, O. Gingras, D. R. Hamann, G. Hautier, X. He, N. Helbig, N. Holzwarth, Y. Jia, F. Jollet, W. Lafargue-Dit-Hauret, K. Lejaeghere, M. A. L. Marques, A. Martin, C. Martins, H. P. C. Miranda, F. Naccarato, K. Persson, G. Petretto, V. Planes, Y. Puillon, S. Prokhorenko, F. Ricci, G.-M. Rignanese, A. H. Romero, M. M. Schmitt, M. Torrent, M. J. van Setten, B. Van Troeye, M. J. Verstraete, G. Zerah, J. W. Zwanziger, *Comput. Phys. Commun.* **2020**, *248*, 107042; b) M. Torrent, F. Jollet, F. Bottin, G. Zerah, X. Gonze, *Comput. Mater. Sci.* **2008**, *42*, 337–351; c) F. Bottin, S. Leroux, A. Knyazev, G. Zerah, *Comput. Mater. Sci.* **2008**, *42*, 329–336.
- [47] H. J. Monkhorst, J. D. Pack, *Phys. Rev. B* **1976**, *13*, 5188.
- [48] J. P. Perdew, K. Burke, M. Ernzerhof, *Phys. Rev. Lett.* **1996**, *77*, 3865–3868.
- [49] S. Grimme, J. Antony, S. Ehrlich, H. Krieg, *J. Chem. Phys.* **2010**, *132*, 154104.

Manuscript received: September 2, 2021  
Revised manuscript received: October 6, 2021

# European Journal of Inorganic Chemistry

Supporting Information

## The Lithium Iodostannate $\text{LiSn}_3\text{I}_7$ : Synthesis, Properties and its Relationship to $\text{SnI}_2$

Manuel Löber, Markus Ströbele, Klaus Eichele, Carl P. Romao, and Hans-Jürgen Meyer\*

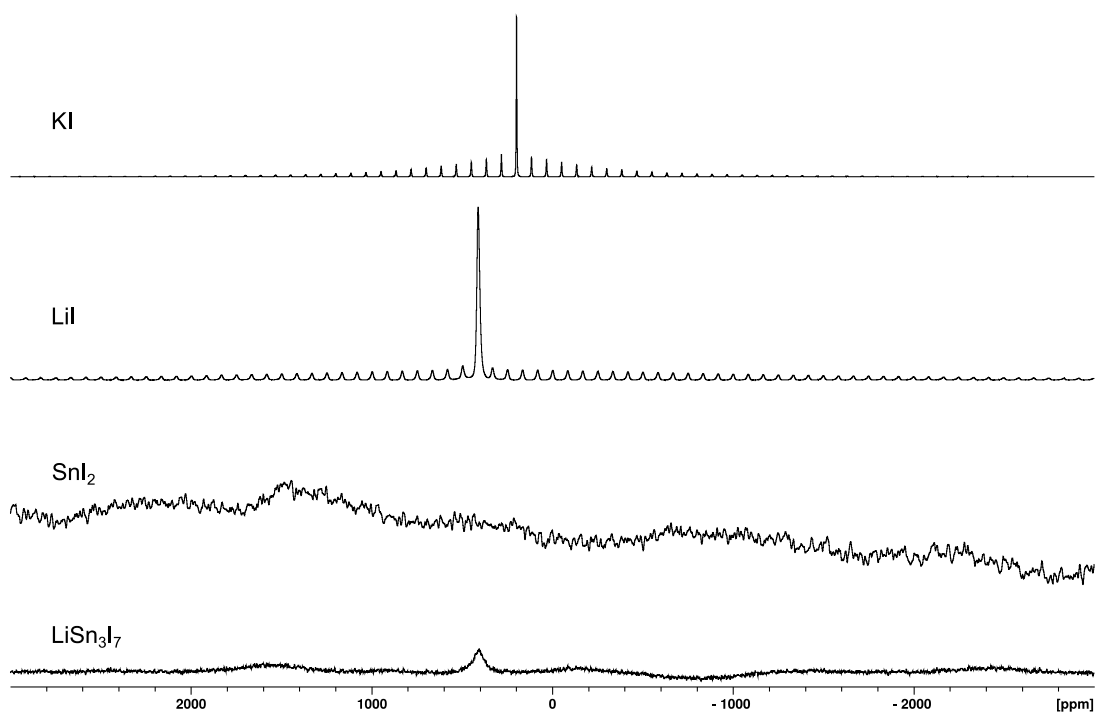


Figure S1.  $^{127}\text{I}$  MAS NMR spectra of  $\text{LiSn}_3\text{I}_7$ ,  $\text{SnI}_2$ ,  $\text{LiI}$ ,  $\text{KI}$  at spinning rates of 5 kHz.

```

"#1" "CSA mas" "amp" 1612.7 "pos(ppm)" -529.865 "wid(ppm)" 58.9918 "g1" 1 "dCS(ppm)" 100 "etaCS" 0
"#2" "CSA mas" "amp" 413.727 "pos(ppm)" -432.879 "wid(ppm)" 88.9876 "g1" 1 "dCS(ppm)" -150 "etaCS" 0
ro : 10000/

```

Model Integration

```

# Name Peak Model % Intens
1 "" "CSA mas" 67.19 13674456.35
2 "" "CSA mas" 32.81 6678680.52

```

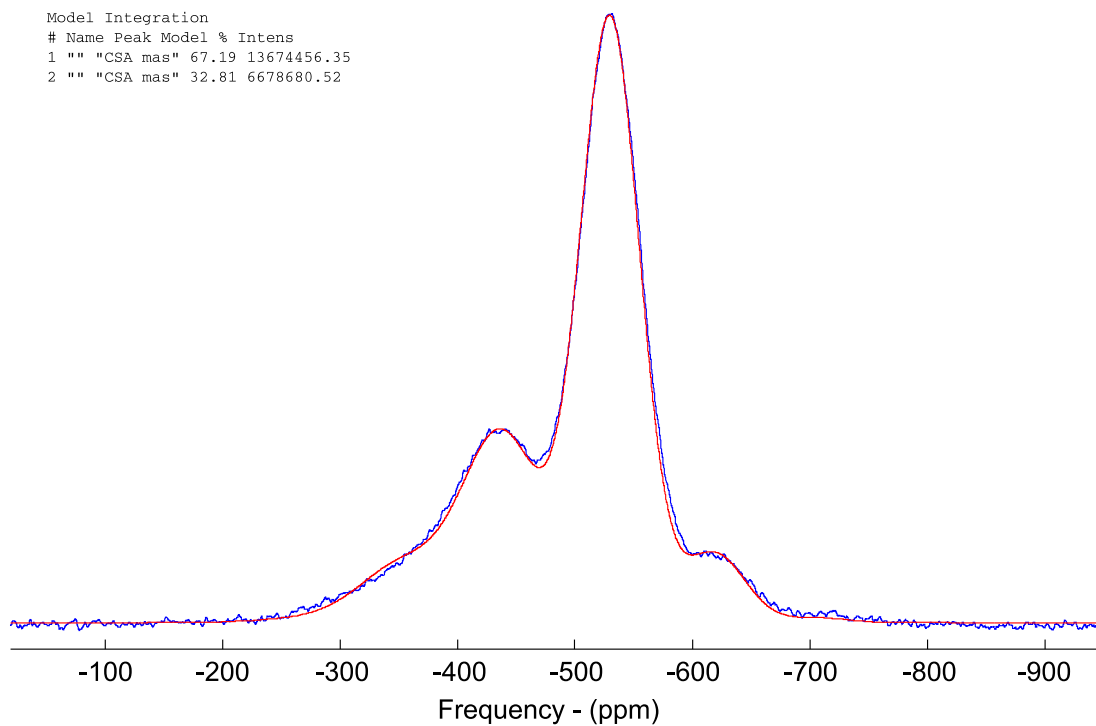


Figure S2:  $^{119}\text{Sn}$  MAS NMR spectrum of  $\text{SnI}_2$  (blue) at a spinning rate of 10 kHz and decomposition using DMFit (red).<sup>1</sup>

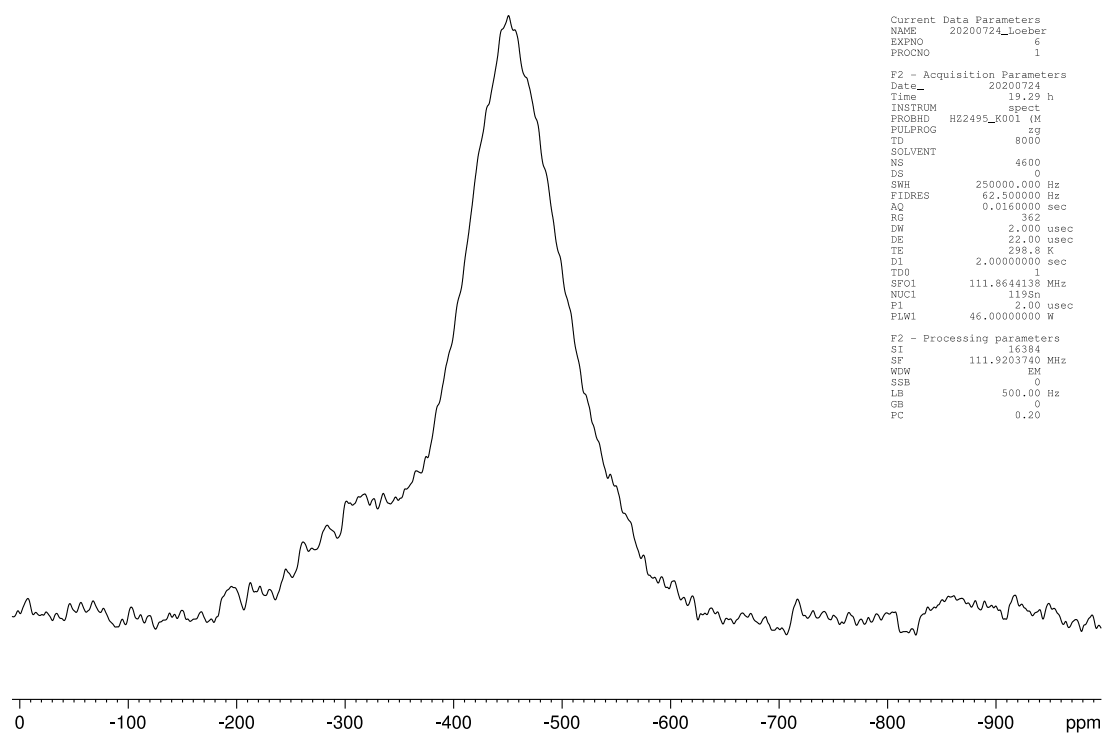


Figure S3:  $^{119}\text{Sn}$  MAS NMR spectrum of  $\text{LiSn}_3\text{I}_7$  at a spinning rate of 10 kHz.

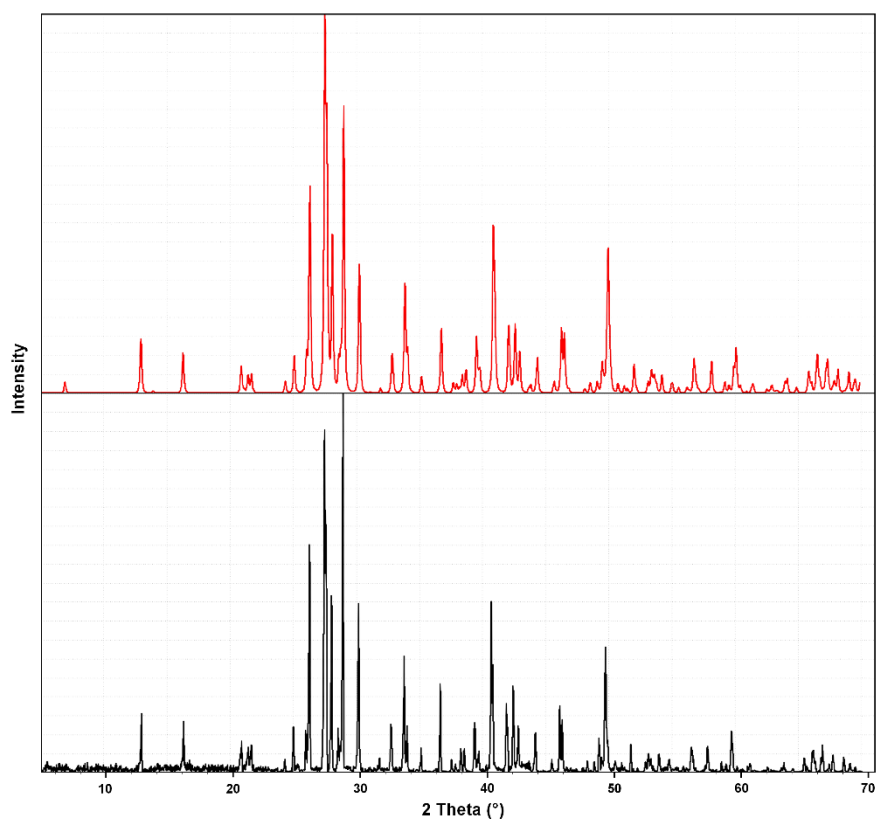


Figure S4: Recorded PXRD pattern of  $\text{LiSn}_3\text{I}_7$ , (shown in black) compared to the calculated pattern, (shown in red).

## References

- 1 D. Massiot, F. Fayon, M. Capron, I. King, S. Le Calvé, B. Alonso, J. O. Durand, B. Bujoli, Z. Gan and G. Hoatson, *Magn. Reson. Chem.*, 2002, **40**, 70-76.

## DFT Input files:

### lisni7.in

```
#autoparal 1

#paral_kgb 1

ndtset 3
jdtset 1 2 3

nkpt2 313

iscf2 -2
iscf3 -3

pawprtdos3 2
prtdos3 3

kptopt3 1
kptrlatt3 0 9 6 6 0 6 6 6 9 0
nshiftk3 1
shiftk3 0 0 0

kptrlatt1      0   3   2   2   0   2   2   3   0
nshiftk1 1
shiftk1 0 0 0

kptopt2 0

getwfk 0
getwfk2 1
getden 0
getden2 1
getden3 1
vdw_xc 6
vdw_tol 1d-11
pawxcdev 0

fband 1

occopt 6
tsmear 0.01

pawfatbnd2 1
natsph2 22
iatsph2 1 2 3 4 5 6 7 8 9 10 11 12 13 14 15 16 17 18 19 20 21 22
```



```

nstep 5000
kptrlen 35

ecut 18
ecutsm 0.5

pawecutdg 128

kptopt 1

tolwfr 1d-24
prtcif 0
prtden1 1
prtden 0
prtwf1 1
prtwf 0
prteig 1
prtgssr 0

```

# Structural parameters

```

          acell      2.7112270684E+01  8.4227211718E+00  2.5471275357E+01 Bohr
          rprim      9.9997956957E-01  0.0000000000E+00 -6.3922171241E-03
                   0.0000000000E+00  1.0000000000E+00  0.0000000000E+00
          xred      -2.7035055879E-01  0.0000000000E+00  9.6276195155E-01
                   5.2575318289E-01  5.0000000000E-01  3.0117863564E-01
                   4.8136864192E-01  5.0000000000E-01  7.1101321609E-01
                   9.8136067576E-01  0.0000000000E+00  7.1099199080E-01
                   2.5805753205E-02  0.0000000000E+00  3.0118338890E-01
                   6.5620110797E-01  0.0000000000E+00  5.5710541460E-01
                   3.5145252502E-01  0.0000000000E+00  4.5231650623E-01
                   8.5141728326E-01  5.0000000000E-01  4.5230530407E-01
                   1.5622846575E-01  5.0000000000E-01  5.5709716461E-01
                   2.2799678301E-01  5.0000000000E-01  8.5546084321E-01
                   7.4806374379E-01  5.0000000000E-01  1.3462898736E-01
                   2.4800760211E-01  0.0000000000E+00  1.3458943676E-01
                   7.2798911779E-01  0.0000000000E+00  8.5547483624E-01
                   4.9566083677E-01  0.0000000000E+00 -1.2832065151E-02
                   -4.3485574085E-03  5.0000000000E-01 -1.2887098437E-02
                   6.8785169618E-01  0.0000000000E+00  3.4770752750E-01
                   3.2352398903E-01  0.0000000000E+00  6.6736027520E-01
                   8.2350429486E-01  5.0000000000E-01  6.6735509924E-01
                   1.8790867679E-01  5.0000000000E-01  3.4771309225E-01
                   1.2480275336E-01  0.0000000000E+00  9.1970682557E-01
                   8.7732603806E-01  0.0000000000E+00  6.6391752486E-02
                   3.7728621003E-01  5.0000000000E-01  6.6381545381E-02
                   6.2483917982E-01  5.0000000000E-01  9.1975732145E-01

natom      22
ntypat     3
typat      1 1 1 1 1 1 1 1 1 1 1 1 1 2 2 2 3 2 2 3
znucl      53 50 3

```

```

kpt 0.0000000000 0.0000000000 0.0000000000
     0.0000000000 0.0192307692 0.0000000000
     0.0000000000 0.0384615385 0.0000000000
     0.0000000000 0.0576923077 0.0000000000
     0.0000000000 0.0769230769 0.0000000000
     0.0000000000 0.0961538462 0.0000000000
     0.0000000000 0.1153846154 0.0000000000
     0.0000000000 0.1346153846 0.0000000000
     0.0000000000 0.1538461538 0.0000000000
     0.0000000000 0.1730769231 0.0000000000
     0.0000000000 0.1923076923 0.0000000000
     0.0000000000 0.2115384615 0.0000000000

```

0.0000000000	0.2307692308	0.0000000000
0.0000000000	0.2500000000	0.0000000000
0.0000000000	0.2692307692	0.0000000000
0.0000000000	0.2884615385	0.0000000000
0.0000000000	0.3076923077	0.0000000000
0.0000000000	0.3269230769	0.0000000000
0.0000000000	0.3461538462	0.0000000000
0.0000000000	0.3653846154	0.0000000000
0.0000000000	0.3846153846	0.0000000000
0.0000000000	0.4038461538	0.0000000000
0.0000000000	0.4230769231	0.0000000000
0.0000000000	0.4423076923	0.0000000000
0.0000000000	0.4615384615	0.0000000000
0.0000000000	0.4807692308	0.0000000000
0.0000000000	0.5000000000	0.0000000000
0.0000000000	0.5000000000	0.0625000000
0.0000000000	0.5000000000	0.1250000000
0.0000000000	0.5000000000	0.1875000000
0.0000000000	0.5000000000	0.2500000000
0.0000000000	0.5000000000	0.3125000000
0.0000000000	0.5000000000	0.3750000000
0.0000000000	0.5000000000	0.4375000000
0.0000000000	0.5000000000	0.5000000000
0.0000000000	0.4807692308	0.5000000000
0.0000000000	0.4615384615	0.5000000000
0.0000000000	0.4423076923	0.5000000000
0.0000000000	0.4230769231	0.5000000000
0.0000000000	0.4038461538	0.5000000000
0.0000000000	0.3846153846	0.5000000000
0.0000000000	0.3653846154	0.5000000000
0.0000000000	0.3461538462	0.5000000000
0.0000000000	0.3269230769	0.5000000000
0.0000000000	0.3076923077	0.5000000000
0.0000000000	0.2884615385	0.5000000000
0.0000000000	0.2692307692	0.5000000000
0.0000000000	0.2500000000	0.5000000000
0.0000000000	0.2307692308	0.5000000000
0.0000000000	0.2115384615	0.5000000000
0.0000000000	0.1923076923	0.5000000000
0.0000000000	0.1730769231	0.5000000000
0.0000000000	0.1538461538	0.5000000000
0.0000000000	0.1346153846	0.5000000000
0.0000000000	0.1153846154	0.5000000000
0.0000000000	0.0961538462	0.5000000000
0.0000000000	0.0769230769	0.5000000000
0.0000000000	0.0576923077	0.5000000000
0.0000000000	0.0384615385	0.5000000000
0.0000000000	0.0192307692	0.5000000000
0.0000000000	0.0000000000	0.5000000000
0.0000000000	0.0000000000	0.4375000000
0.0000000000	0.0000000000	0.3750000000
0.0000000000	0.0000000000	0.3125000000
0.0000000000	0.0000000000	0.2500000000
0.0000000000	0.0000000000	0.1875000000
0.0000000000	0.0000000000	0.1250000000
0.0000000000	0.0000000000	0.0625000000
0.0000000000	0.0000000000	0.0000000000
-0.0500000000	0.0000000000	0.0500000000
-0.1000000000	0.0000000000	0.1000000000
-0.1500000000	0.0000000000	0.1500000000
-0.2000000000	0.0000000000	0.2000000000
-0.2500000000	0.0000000000	0.2500000000
-0.3000000000	0.0000000000	0.3000000000
-0.3500000000	0.0000000000	0.3500000000
-0.4000000000	0.0000000000	0.4000000000
-0.4500000000	0.0000000000	0.4500000000
-0.5000000000	0.0000000000	0.5000000000

-0.5000000000	0.0192307692	0.5000000000
-0.5000000000	0.0384615385	0.5000000000
-0.5000000000	0.0576923077	0.5000000000
-0.5000000000	0.0769230769	0.5000000000
-0.5000000000	0.0961538462	0.5000000000
-0.5000000000	0.1153846154	0.5000000000
-0.5000000000	0.1346153846	0.5000000000
-0.5000000000	0.1538461538	0.5000000000
-0.5000000000	0.1730769231	0.5000000000
-0.5000000000	0.1923076923	0.5000000000
-0.5000000000	0.2115384615	0.5000000000
-0.5000000000	0.2307692308	0.5000000000
-0.5000000000	0.2500000000	0.5000000000
-0.5000000000	0.2692307692	0.5000000000
-0.5000000000	0.2884615385	0.5000000000
-0.5000000000	0.3076923077	0.5000000000
-0.5000000000	0.3269230769	0.5000000000
-0.5000000000	0.3461538462	0.5000000000
-0.5000000000	0.3653846154	0.5000000000
-0.5000000000	0.3846153846	0.5000000000
-0.5000000000	0.4038461538	0.5000000000
-0.5000000000	0.4230769231	0.5000000000
-0.5000000000	0.4423076923	0.5000000000
-0.5000000000	0.4615384615	0.5000000000
-0.5000000000	0.4807692308	0.5000000000
-0.5000000000	0.5000000000	0.5000000000
-0.4500000000	0.5000000000	0.4500000000
-0.4000000000	0.5000000000	0.4000000000
-0.3500000000	0.5000000000	0.3500000000
-0.3000000000	0.5000000000	0.3000000000
-0.2500000000	0.5000000000	0.2500000000
-0.2000000000	0.5000000000	0.2000000000
-0.1500000000	0.5000000000	0.1500000000
-0.1000000000	0.5000000000	0.1000000000
-0.0500000000	0.5000000000	0.0500000000
0.0000000000	0.5000000000	0.0000000000
-0.0625000000	0.5000000000	0.0000000000
-0.1250000000	0.5000000000	0.0000000000
-0.1875000000	0.5000000000	0.0000000000
-0.2500000000	0.5000000000	0.0000000000
-0.3125000000	0.5000000000	0.0000000000
-0.3750000000	0.5000000000	0.0000000000
-0.4375000000	0.5000000000	0.0000000000
-0.5000000000	0.5000000000	0.0000000000
-0.5000000000	0.4807692308	0.0000000000
-0.5000000000	0.4615384615	0.0000000000
-0.5000000000	0.4423076923	0.0000000000
-0.5000000000	0.4230769231	0.0000000000
-0.5000000000	0.4038461538	0.0000000000
-0.5000000000	0.3846153846	0.0000000000
-0.5000000000	0.3653846154	0.0000000000
-0.5000000000	0.3461538462	0.0000000000
-0.5000000000	0.3269230769	0.0000000000
-0.5000000000	0.3076923077	0.0000000000
-0.5000000000	0.2884615385	0.0000000000
-0.5000000000	0.2692307692	0.0000000000
-0.5000000000	0.2500000000	0.0000000000
-0.5000000000	0.2307692308	0.0000000000
-0.5000000000	0.2115384615	0.0000000000
-0.5000000000	0.1923076923	0.0000000000
-0.5000000000	0.1730769231	0.0000000000
-0.5000000000	0.1538461538	0.0000000000
-0.5000000000	0.1346153846	0.0000000000
-0.5000000000	0.1153846154	0.0000000000
-0.5000000000	0.0961538462	0.0000000000
-0.5000000000	0.0769230769	0.0000000000
-0.5000000000	0.0576923077	0.0000000000

-0.5000000000	0.0384615385	0.0000000000
-0.5000000000	0.0192307692	0.0000000000
-0.5000000000	0.0000000000	0.0000000000
-0.4375000000	0.0000000000	0.0000000000
-0.3750000000	0.0000000000	0.0000000000
-0.3125000000	0.0000000000	0.0000000000
-0.2500000000	0.0000000000	0.0000000000
-0.1875000000	0.0000000000	0.0000000000
-0.1250000000	0.0000000000	0.0000000000
-0.0625000000	0.0000000000	0.0000000000

0 0 0

### **lisni7.files**

lisn3i7.in  
lisn3i7.out  
lisn3i7i  
lisn3i7o  
tmp  
I.GGA\_PBE-JTH.xml  
Sn.GGA\_PBE-JTH.xml  
Li.GGA\_PBE-JTH.xml